CRYSTALLIZATION AND MELTING IN GEOLOGICAL FLUID MECHANICS

Richard Allan Jarvis

St. John's College

A dissertation submitted for the
degree of Doctor of Philosophy
at the University of Cambridge

April 1991

Crystallization and Melting in Geological Fluid Mechanics

R.A. Jarvis

The new field of *geological fluid mechanics* seeks to apply theoretical fluid dynamical techniques to the wide range of phenomena observed in geological systems. During the formation of igneous rocks, fluid mechanical processes can affect the final composition of the solid product. In this dissertation, two particular processes are studied, each of which involves a moving boundary between solid and liquid phases.

The first problem addressed is the formation of compositionally stratified igneous rock by the solidification of magma chambers, which are large reservoirs of molten rock within the Earth's crust. As the magma freezes, the composition of the rock formed differs from the melt from which it originates and consequently variations in the composition of the magma occur which can drive strong convective motions. These motions in turn alter the composition of the magma, and therefore the rock that is formed. The freezing of a magma chamber is modelled here by the crystallization of a binary alloy (such as an aqueous salt solution) from one sidewall of a rectangular enclosure. The model equations for solid growth and thermal and compositional convection are solved numerically. The results for the compositional stratification in the solid product are shown to be in good agreement with experiments conducted in the past. It is also demonstrated that a fluid whose viscosity is dependent upon both its temperature and composition can be modelled by a fluid of constant viscosity, provided a suitable effective viscosity is chosen.

The second process studied is the thermal erosion of channels by lava flows. Lavas erupted in the Archaean (2.5 to 4 billion years ago) were much less viscous than most magmas erupted today, and were likely to have exhibited turbulent flow. As the lava flowed away from its source, it melted the seafloor over which it flowed. Consequently, the lava became contaminated by the seafloor material, which altered the composition of the rock formed when the lava finally solidified. A two-dimensional model has already been proposed which predicts the rate of erosion and degree of contamination of a lava flow of infinite width. Here, that model is significantly extended, to allow prediction of the cross-sectional shape of the erosion channels. It is shown that the finite nature of the channel width, due either to the finite length of the erupting fissure or due to channelling of the lava flow by topography, can have an order of magnitude effect on the extent of the contamination of the lava by the seafloor. In addition, a mechanism is proposed and studied for the observed instability of channel splitting, in which an island forms near the centre of the lava flow.

To Sarah and to my parents

Preface and Acknowledgements

I claim that all of the work contained in this dissertation is original except where references to the contrary are made within the text. It is the result of my own research and includes nothing that is the outcome of work done in collaboration. No parts of this dissertation have been submitted for a degree, diploma or similar qualification in any other university.

First, I would like to thank my supervisor, Prof. H. E. Huppert for his excellent advice and guidance over the last three years. His comments on earlier drafts of the material presented here proved particularly invaluable.

During the course of my studies, I have benefited from many discussions on many topics. In particular, I would like to thank Andy Woods, Grae Worster, John Lister, Huw Davies, Arieh Iserles, Dan Moore and Paul Hammerton. Valuable comments on previous drafts of this dissertation were provided by Andy Woods, John Lister and Huw Davies. I would also like to thank Steve Belcher, Paul Hammerton, Ollie Harlen, Oliver Jensen and Keith Julien for helping to provide such a pleasant working environment in DAMTP.

During the summer of 1989, I attended the Summer School in Geophysical Fluid Dynamics at Woods Hole Oceanographic Institution. I am grateful to the Steering Committee for a thoroughly enjoyable experience.

Finally, I would like to express my deep gratitude to St. John's College, Cambridge for their provision of a Benefactors' Studentship, without which none of this dissertation would have been possible. With regard to this, I acknowledge the contribution of my tutor, Patrick Sims-Williams.

CONTENTS

Chapter 1

Introduction

1.1 The origin of igneous rocks

Igneous rocks are formed by the solidification of molten rock, which is called *magma* when within the earth and *lava* when extruded on the surface. Periodically, magma is released from the Earth's crust by processes associated with volcanic eruptions, either on land or at sea. If inviscid, lava erupts more or less quietly, sometimes flowing many kilometres from the source. Viscous, gas-rich lava may erupt more explosively. Still more hazardous are *pyroclastic flows*, which are rapidly flowing currents of hot air laden with rock and fine ash. Pyroclastic flows are often called *nuées ardentes*, or 'glowing clouds'. Light ash can be transported laterally hundreds of kilometres after being carried vertically by up to at least 45 km in buoyant eruption columns. A less spectacular style of igneous rock formation occurs when large regions of magma residing within the Earth's crust are cooled by the surrounding rock, or by hydrothermal circulations. Rocks formed by the cooling of such regions are termed *igneous intrusions*, or *plutons*. An intrusion may subsequently be revealed at the surface by erosion of the overlying crust.

A rich diversity of rock compositions can be observed, which reflects the wide variety of magma types and styles of solidification. Table 1.1 lists the major-element compositions for some selected magmas. Typically, magmas are multicomponent melts, predominantly composed of silica (SiO_2). The viscosity of a magma is primarily determined by its silica content and temperature. Relatively inviscid *basaltic* lavas flow quite easily upon eruption, unlike the viscous, silica-rich *rhyolites*, which have been observed to erupt mainly as domes. *Komatiitic* lavas were erupted only in the Archaean (2.5–4 Ga ago), and were even less viscous than basalts because of their high magnesium content and temperature (Hall 1987).

The original source of magmas is the *mantle*, which extends to about 2000 km below the Earth's surface. Melt is formed within the mantle by the partial melting of the rock matrix. Magma can also be formed by the remelting of crustal material. The formation of magma, and the sites at which igneous rocks are formed, are closely related to the *plate tectonics* of the Earth. The Earth's crust and the underlying brittle part of the mantle comprise the *lithosphere*, which is made up of a number of large *plates* which are constantly in motion with respect to one another. The motion of these plates is believed to be driven by weak, large-scale convection within the mantle, either involving the whole

	Rhyolite	*Andesite*	*Basalt*	*Komatiite*
SiO_2	72.8	57.9	49.2	46.9
TiO_2	0.3	0.9	1.8	0.2
Al_2O_3	13.3	17.0	15.7	3.7
Fe_2O_3	1.5	3.3	3.8	—
FeO	1.1	4.0	7.1	10.2
MgO	0.4	3.3	6.7	33.0
CaO	1.1	6.8	9.5	5.3
Na_2O	3.5	3.5	2.9	0.5
K_2O	4.3	1.6	1.1	0.2

Table 1.1. Average compositions of selected magmas, expressed as the weight percentage of various common compounds (from Hall 1987, Huppert & Sparks 1985*b*). Note that rhyolite typically has higher proportions of SiO_2, and lower proportions of Fe_2O_3, FeO and MgO than basalt. Komatiitic magmas are very magnesian (>18 wt% by definition) and require a high degree of partial melting.

mantle or just the upper 670 km (Wilson 1989). The relationship between volcanism and plate tectonics is sketched in Figure 1.1. Plates diverge at mid-ocean ridges, where fresh oceanic crust is continuously being formed, and converge at subduction zones, where one plate slides below the other and is subducted into the mantle. Melt formed by the partial melting of the upper mantle at depth is generally buoyant with respect to the rock matrix and may migrate upwards by a process known as compaction (McKenzie 1984, 1985). The rock matrix is compacted by the overlying rock, thus squeezing out the buoyant melt. Magmas formed by the partial melting of the mantle are typically basaltic in composition, though there may be some *picrites* or komatiites, which are richer in magnesium, as shown in Table 1.1. As the melt rises, it is focused towards the mid-ocean ridges by the mantle convection. At subduction zones, melt is formed by a more complicated process. Volatiles, such as water, are transported into the mantle by the subducting slab. The volatiles can reduce the local liquidus temperature, leading to partial melting of the mantle. In addition, the slab may melt, and so the mantle melt mixes with the remelted crustal material. The composition of the fresh magma may be anything from rhyolitic to basaltic (Wilson 1989).

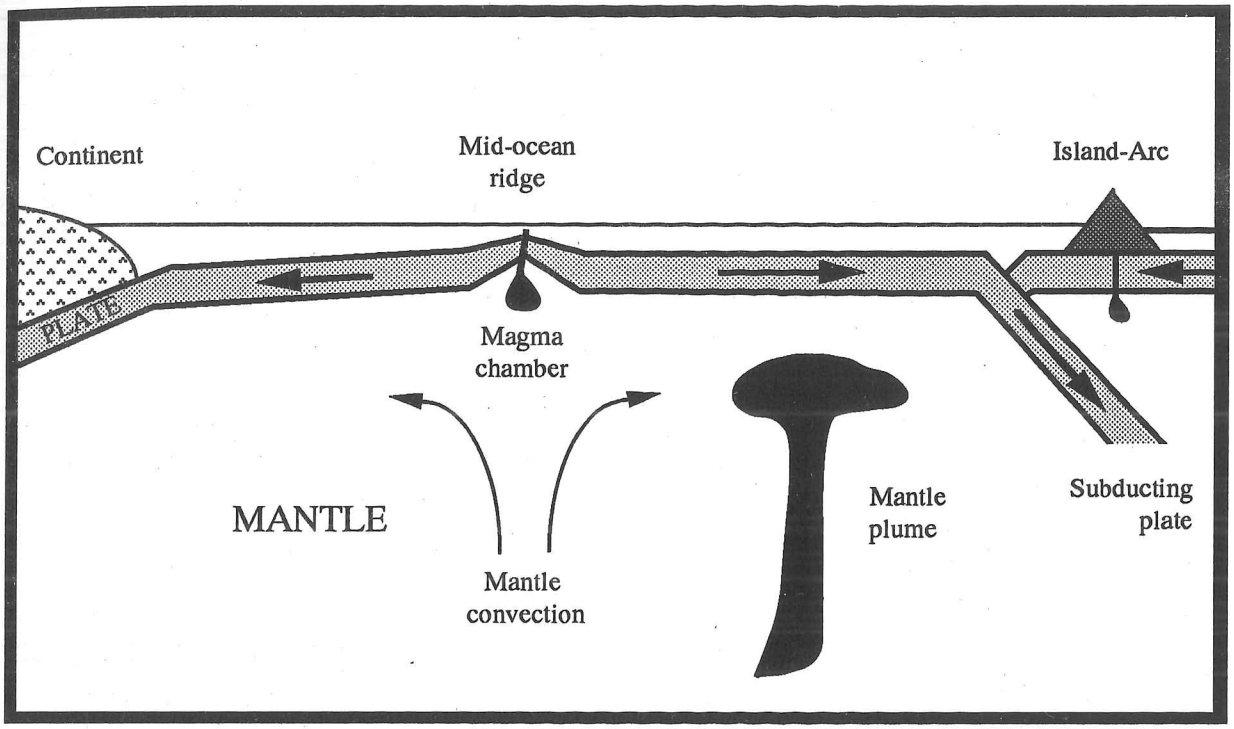

Figure 1.1. Sketch depicting the relationship between plate tectonics and volcanism. Melt formed deep in the upper mantle migrates towards mid-ocean ridges through the action of mantle convection. Subducting plates transport volatiles into the mantle, which leads to partial melting and the arc-island style of volcanism. Anomalous features, such as mantle plumes, can also transport melt to the surface of the Earth.

However, this does not explain why the composition of the crust differs from that of the primary melts formed by partial melting in the mantle. Igneous rocks commonly have compositions ranging from basaltic to rhyolitic, while the composition of mantle melts is typically basaltic to komatiitic. The key to this problem lies in the multicomponent nature of magmas. When a multicomponent melt crystallizes, the composition of the solid formed is not generally the same as that of the melt from which it originates. Therefore, the melt in the neighbourhood of the crystallizing rock becomes depleted in some minerals and enriched in others. This mechanism by which the composition of a magma may be altered is called *fractional crystallization.* Most minerals formed by the solidification of magma are relatively poor in silica. Therefore, fractional crystallization leads to silica enrichment in the melt. The magma *evolves* from a basaltic composition towards a rhyolitic composition.

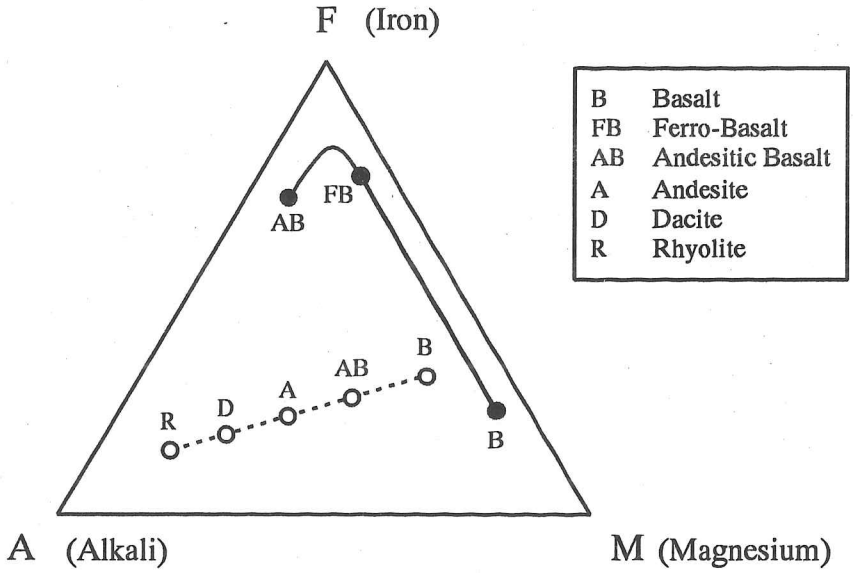

Figure 1.2. AFM diagram showing the relative proportions of alkalis (A), iron (F) and magnesium (M) in magmas which differentiate according to ●——●——● the tholeiitic trend, and o- - -o- - -o the calc-alkaline trend of fractionation. The iron may appear as either of the oxides FeO, Fe_2O_3 while the magnesium appears as magnesium oxide (MgO). Common alkalis in magmas are potassium oxide (K_2O) and sodium oxide (Na_2O).

Fractional crystallization is believed to occur primarily in *magma chambers*, which are large reservoirs of melt emplaced within the Earth's crust, but may also occur in conduits. The magma chambers are supplied by melt migrating upwards from the mantle. As the magma cools, it begins to solidify and the melt becomes fractionated. A number of processes have been suggested for the subsequent separation of the solid phase from the residual melt, the two most probable of which are *crystal settling* and *convective fractionation* (Wilson 1989). The density of the crystals formed upon cooling differs by about 10% from that of the melt (Hall 1987). Therefore, in a quiescent magma chamber, heavy crystals will settle at a rate determined by the viscosity of the magma. Similarly, light crystals rise. However, it has been argued that magma chambers are not generally quiescent, but convect (Huppert & Sparks 1980, Sparks *et al.* 1984). Fluid cooled from below or from the sides exhibits *thermal convection.* In addition, variations in composition due to fractional crystallization can drive *compositional convection*, which may dominate in many circumstances. The convection may be either turbulent or laminar, depending upon

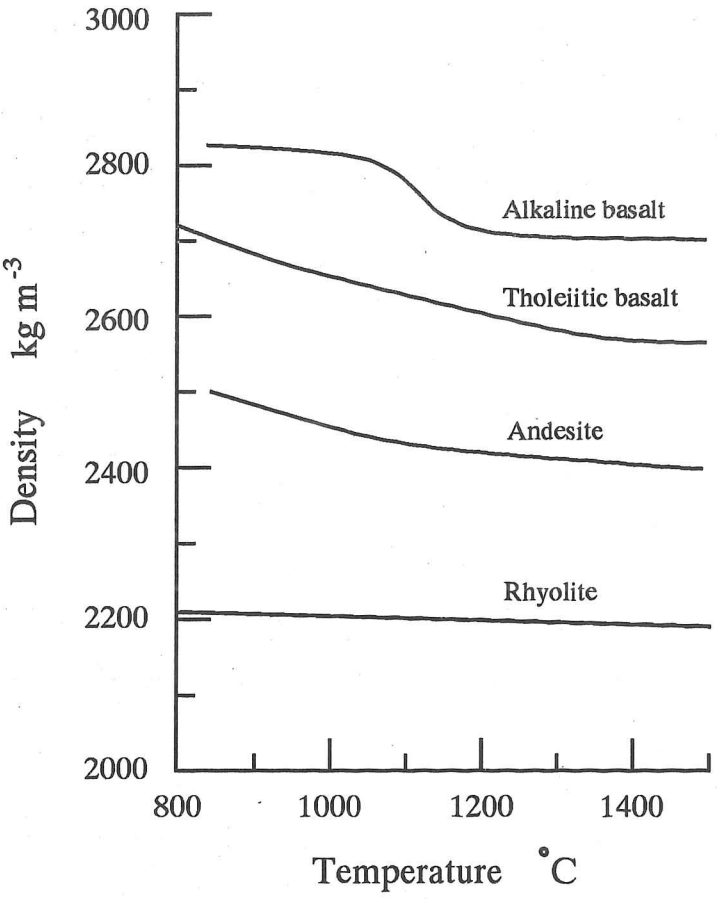

Figure 1.3. The density of various magmas plotted against temperature. All magmas becomes less dense as they become hotter. It is also apparent that density depends strongly upon the composition of the magma. Andesites and rhyolites are more silicic than tholeiitic basalt and have a lower iron content (see Table 1.1). The alkaline olivine basalt has a comparable iron content to the tholeiitic basalt, but is richer in magnesium and hence is heavier. The data were obtained experimentally by Murase & McBirney (1973).

the nature of the cooling, the sites at which crystals form, the geometry of the magma chamber and the viscosity of the magma. Magma crystallizing primarily from the side leads to laminar convection (Nilson *et al.* 1985). The residual melt rises in a boundary layer flow to the roof of the magma chamber if it is relatively light, or sinks to the floor if it is heavy. The fractionated magma forms a stably stratified region at the roof (or floor) of the chamber. Magma cooled from above, or cooled from below with a light residual melt released upon crystallization, convects turbulently and is well-mixed (Huppert 1986). Observations of crystal accumulates at the base of some igneous intrusions is not

inconsistent with the concept of the magma convecting turbulently. Crystals may still settle out of the thin, relatively stagnant viscous boundary layer at the base of the magma chamber (Martin & Nokes 1988, Koyaguchi *et al.* 1990). The attraction of convective fractionation as a mechanism is that the magma at the roof (or floor) of the magma chamber can be significantly fractionated in a relatively short time while the bulk fluid remains approximately unaltered. Evidence for convectional fractionation therefore hinges upon inferences from erupted and solidified lavas of substantially evolved melts being produced at too rapid a rate for crystal settling to have been the dominant separation mechanism.

Whether a fractionating magma chamber is characterised by relatively light fluid rising to the top of the chamber or by heavy fluid descending to the floor depends upon the composition and temperature of the magma. Two common trends of fractionation can be identified. The *calc-alkaline* trend of fractionation (o---o---o) is characterised by the transition from basalt to *andesite* to rhyolite (Figure 1.2). The melt becomes depleted in the heaviest element, iron (Fe), as *olivine* preferentially forms. Olivine is a mineral composed of an aggregate of varying proportions of its two end-members *forsterite* (Mg_2SiO_4) and *fayalite* (Fe_2SiO_4). The other main trend of fractionation is the *tholeiitic* trend of fractionation (•—•—•), in which substantial iron-enrichment occurs because the primary mineral crystallizing out is *plagioclase*, which contains no iron. The basalt evolves to a ferro-basalt until it becomes saturated in iron, at which point *magnetite* forms. Tholeiitic basalts are observed in all tectonic settings. However, calc-alkaline magmas appear to be restricted entirely to convergent plate boundaries, and are common in *island-arc* volcanism (see Figure 1.1). Because of their exclusive setting, rocks formed from calc-alkaline magmas provide useful information about historic plate movements (Wilson 1989).

The density of an evolved magma is primarily dependent upon its iron content. The densities of selected magmas are plotted in Figure 1.3 (after Murase & McBirney 1973). Variations in density due to compositional effects clearly dominate over variations in density due to thermal effects. For a magma fractionating along the tholeiitic trend, the evolved magma is relatively heavy because it is iron-enriched. Conversely, the residual melt for a magma evolving along the tholeiitic trend of fractionation is light. Therefore, the two different trends of fractional crystallizations can lead to very different fluid dynamical regimes.

1.2 Scope of the present study

Fluid dynamical processes, combined with crystallization and melting, play a major role during the formation of igneous rocks. In this dissertation, attention is focused upon two problems in which fluid motions affect the composition of the rock formed. One problem involves crystallization and the other involves melting.

Some information about processes within magma chambers can be obtained from observations of erupted materials. However, more can be learned from studying wholly solidified magma chambers, or igneous intrusions. A striking feature of many igneous intrusions is that they exhibit compositional stratification. The *layering* of intrusions may either be continuous or discrete, and can be caused by a number of processes. In Chapters 2 and 3, we concentrate on one process for the formation of compositionally stratified rock, *viz.* thermal and compositional convection within the solidifying magma chamber.

The essential features of a crystallizing magma can be modelled by a simple eutectic binary alloy (McBirney *et al.* 1985). For example, a dilute aqueous salt solution forms nearly pure ice upon crystallization, thus releasing salty water at the solid/melt interface. The heavy, salty water sinks to the base of the enclosure in the same way as a fractionated tholeiitic basalt in a magma chamber. Similarly, a calc-alkaline magma can be modelled by a concentrated salt solution, for which light, fresh fluid is released at the advancing solidification front. Experiments have been conducted by Leitch (1985, 1987) and Huppert *et al.* (1987) for an aqueous sodium carbonate solution solidifying from one sidewall of a rectangular tank. It was demonstrated that the composition of the solid product was strongly affected by the convective motions within the fluid. The implication for solidifying magmatic bodies is that many of the layering features observed in igneous intrusions may have been similarly determined by fluid motions.

In Chapter 2, we present a numerical model for the crystallization of a binary alloy at a sidewall. The moving interface between the solid and liquid interface is treated as planar, neglecting the effects of constitutional supercooling, and the fluid is assumed to have constant viscosity. For this geometry, the flow in magma chambers is likely to be laminar (Nilson *et al.* 1985). The experiments of Leitch (1985, 1987) and Huppert *et al.* (1987) suggested that the qualitative features of the compositional layering in the solid

are determined by the rate at which the zone of fractionated fluid fills the enclosure — the *box-filling* timescale. By conducting a scaling analysis, we are able to demonstrate that the variation in solid composition due to convective effects may be described both qualitatively and quantitatively by a single nondimensional parameter, which is determined by the ratio of the box-filling timescale to the timescale for complete solidification of the chamber. The scaling analysis allows us to model the experiments of Leitch (1985, 1987) and Huppert *et al.* (1987) by numerical calculations performed at lower Rayleigh numbers. Similarly, the experimental results are shown to be directly applicable to solidifying magma chambers. We compare our numerical results with the experiments with mixed success. However, when the planar interface assumption is valid, the disagreement between calculation and experiment is not significantly greater than the experimental error.

In Chapter 3, the model of Chapter 2 is extended to fluids of variable viscosity. We concentrate on the situation in which light fluid is released at the solidification front. The viscosity of a magma may vary by up to 12 orders of magnitude from the interior of a magma chamber to the solid/melt interface (Spera *et al.* 1982, Nilson *et al.* 1985). The magma adjacent to the solidification front is both cold and highly silicic. Consequently its viscosity increases due to both compositional and thermal effects. In general, variable viscosity effects are treated by constructing an appropriate average, or effective, viscosity. By analysing the model of Nilson *et al.* (1985) for flow in a double-diffusive boundary layer, we obtain a suitable effective viscosity for determining the rate of box-filling for a fractionating melt whose viscosity depends upon both composition and temperature. We then demonstrate numerically that the same effective viscosity determines the compositional stratification in the solid that is grown. The form of the effective viscosity indicates that increased viscosity due to thermal effects plays a greater role than the variation in viscosity due to compositional effects. Our investigations suggest that a magma of variable viscosity convecting in laminar fashion at high Rayleigh numbers can be modelled by a fluid of constant viscosity convecting at much lower Rayleigh numbers.

The second problem addressed is the erosion of channels by hot, turbulent lava flows. Komatiitic lavas were erupted only in the Archaean and typically exhibited turbulent flow, melting the ground over which they flowed (Huppert *et al.* 1984). This resulted in the lava becoming contaminated by the crustal material. Komatiites have aroused great interest, chiefly because they provide a route towards an understanding of the composition and

temperature of the Archaean mantle. It is therefore important to know how much they may have become contaminated by the crust upon eruption and emplacement.

Huppert *et al.* (1984) and Huppert & Sparks (1985*a*) constructed a two-dimensional model for the thermal erosion of an erodible bed by a hot, turbulent gravity current in which the channel width was effectively infinite and the erosion steady. In Chapter 4, a new model is presented for the evolution of the cross-sectional geometry of erosion channels. Under certain simplifying conditions, we are able solve analytically for the channel shape as a function of the total depth eroded alone. By adapting the earlier model of Huppert and co-workers, we are able to find a solution for the lava contamination as a function of the lava temperature. We proceed to compare the erosion of a channel of finite width with the erosion of a channel of infinite width. We then investigate the stability of the channel geometry to perturbations. In their experiments with hot water eroding a channel in solid wax, Huppert & Sparks (1985*a*) observed that the channel geometry frequently become unstable, with the channel splitting into two. We suggest that the instability is due to inefficient cross-stream mixing of the lava. By combining our model for the evolution of the channel shape with a parameterised model for the proposed instability mechanism, we are able to demonstrate by linear stability analysis that the most unstable mode indeed corresponds to the channel splitting into two.

Finally, in Chapter 5, we summarise the work presented in this dissertation and consider the geological implications. Prospects for future investigations are indicated.

Chapter 2

Crystallization of a binary alloy at a vertical wall

I: Constant viscosity

2.1 Introduction

When a multicomponent alloy solidifies, the composition of the solid formed is not generally the same as the composition of the melt from which it originates. Consequently, the fluid in the vicinity of the solidification front is depleted in those components which are preferentially incorporated into the solid phase, and enriched in those components which are rejected. This process is termed *fractional crystallization.* Variations in composition in a fluid generally imply variations in density and so the asymmetric segregation of alloy components between the solid and liquid phases can drive significant convective motions in the fluid.

In this chapter, we investigate the interaction between solidification and convection for a binary alloy, which has just two components, crystallizing at a vertical boundary. In particular, we focus on how the redistribution of components in the melt by convection can lead to spatial variations in the composition of the solid grown. This is of special interest to geologists, metallurgists and crystal growers, albeit for differing reasons. Metallurgists generally wish to suppress variations in the composition of the solid. Impurities in a metal casting can significantly weaken the solid alloy. Similarly, crystal growers seek a homogeneous product.

Geologists, on the other hand, wish to interpret existing rock features to understand the physical processes which led to their formation. Compositional stratification has been observed in many intrusive igneous bodies, for example the Skaergaard intrusion in east Greenland and the Muskox intrusion in northern Canada. Generally, the observed variations in rock composition are in the form of layers, either discrete or continuous (Hess 1989). There are many styles of layering. *Modal* layering is typically characterised by heavy minerals (such as olivine and pyroxene) being found towards the base of intrusions, and lighter minerals (such as plagioclase) occurring towards the top. *Cryptic* layering is when there is a regular, sometimes continous, variation in the composition of a particular mineral. For example, in the Skaergaard intrusion, the plagioclase varies continuously from 66% anorthite at the base of the Layered Series to 30% anorthite in the uppermost layers (Wager & Brown 1968).

A variety of mechanisms have been proposed to explain the layering of igneous intrusions, no one of which can explain all observed features. Some examples of layering may

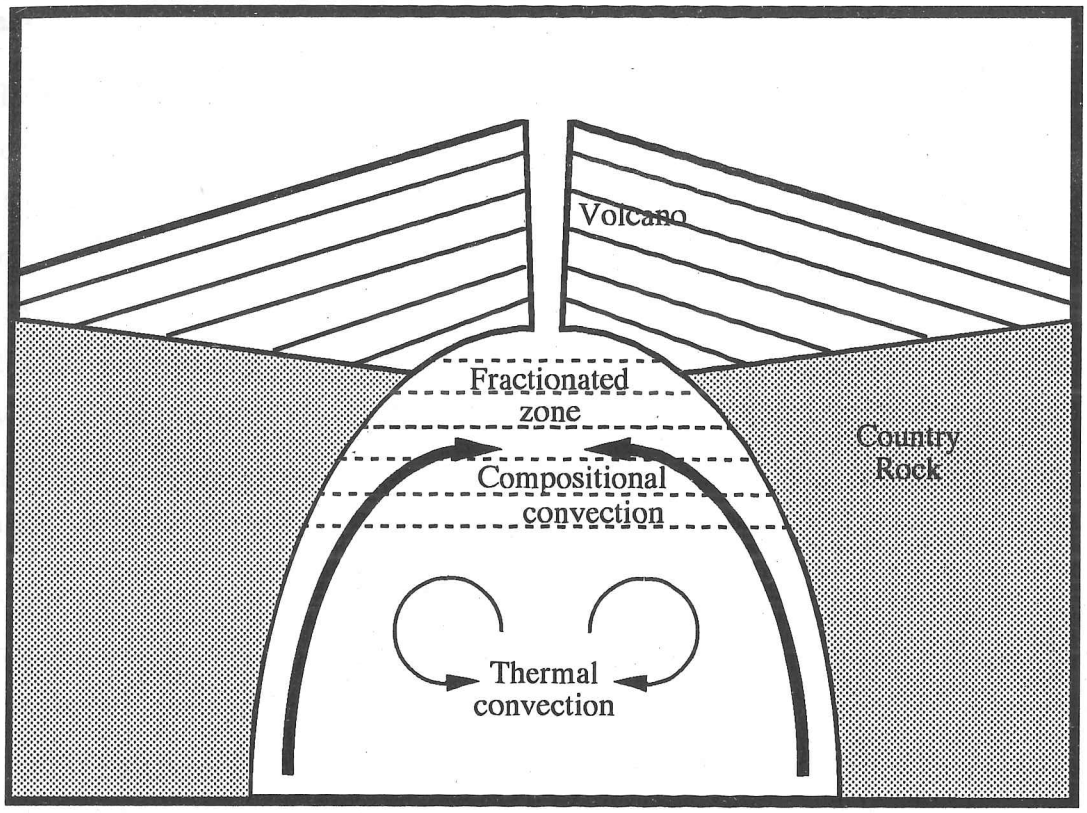

Figure 2.1. Diagram of a calc-alkaline magma chamber below a mature andesitic volcano. The volcano is layered from successive eruptions and the magma chamber below is surrounded by country rock, for example gneiss. As the chamber solidifies from its boundaries, light fluid is released which collects at the roof of the magma chamber in a fractionated zone. Within the the bulk of the magma chamber, there may be some thermal convection (after McBirney 1980).

reflect a compositional stratification in the magma. One mechanism for stratification in the melt is convective fractionation (Sparks *et al.* 1984, McBirney *et al.* 1985, Worster & Leitch 1985). The fluid released at the solid/melt interface has a different density from the bulk fluid, which can drive convection. If crystallization occurs at a sidewall, the residual melt rises or falls in a thin boundary layer, according to its density. Magma evolving along the tholeiitic trend of fractionation becomes heavier, largely because it is enriched in iron which has been rejected by the solid phase. The evolved melt descends to the base of the chamber, forming a stratified region of fluid. The stratification produced in the fluid is reflected in the solid rock subsequently formed as the solidification front

advances into the stratified region.

In Figure 2.1, a volcanic calc-alkaline magma chamber is sketched. The magma is cooled by the country rock and convects thermally in the bulk of the magma chamber due to the cooling from the sidewalls and above. The melt at the margins of the chamber is depleted in the heaviest component, iron, because iron-rich minerals such as olivine ($(Fe, Mg)_2SiO_4$) are preferentially incorporated into the solid. Despite being colder, the melt adjacent to the solidification front is less dense than the bulk fluid and is therefore buoyant. Consequently, calc-alkaline magma chambers are characterised by a graded zone of light fluid in the upper region of the chamber (McBirney 1980). Lavas erupted from such a magma chamber would have andesitic composition.

Convective fractionation is by no means the only process occurring in an evolving magma chamber. Other forms of fractionation, such as crystal settling or Soret diffusion, may predominate in certain circumstances. The picture is further confused by the continued supply of fresh melt to the base of the magma chamber and by the loss of magma from the upper regions through eruption. One of the reasons why the Skaergaard intrusion is so important is that it appears to have formed from a magmatic body which completely solidified without being replenished or tapped. However, in order to understand physical processes, it is necessary first to isolate them. Only when a process is understood can its interactions with other mechanisms be properly addressed.

Some workers (Chen & Turner 1980, Turner & Gustafson 1981, Leitch 1985, 1987, McBirney *et al.* 1985, Huppert *et al.* 1987) have modelled convective magma chamber processes by drawing an analogy with aqueous salt solutions. Although such solutions are only binary alloys, the effects of fractional crystallization in a multicomponent magma can be reproduced by careful choice of the salinity of the solution. Experiments can be conducted which exhibit either tholeiitic or calc-alkaline behaviour. When dilute aqueous salt solutions freeze, nearly pure ice is formed and the residual liquid is relatively salty and dense. For concentrated aqueous salt solutions, salt is preferentially incorporated into the solid as hydrated salt crystals form. The residual liquid is fresh and therefore light. Hence, tholeiitic magmas can be modelled by dilute salt solutions and calc-alkaline magmas by concentrated salt solutions. The nature of the convection at high Prandtl numbers is determined by the Grashof number, which is the same for the experiments as

in typical magma chambers (Nilson *et al.* 1985). The reduced scale of the experiments is balanced by the lower viscosity of the water compared with magma. In most of the experiments conducted with aqueous salt solutions crystallizing at a sidewall, the residual melt rises or falls, depending upon its density, in a thin laminar boundary layer adjacent to the advancing solidification front (Nilson *et al.* 1985, Leitch 1985).

Although solidification is likely to occur on more than one boundary, the analysis of a crystallizing alloy is simplified by considering solidification to occur at only one boundary. For a discussion of the interaction between convection and solidification for crystallization of a binary alloy at a horizontal boundary, the reader is referred to the review by Huppert (1990). When crystallization occurs at a horizontal boundary, one or both of the compositional and thermal fields may be unstable (Huppert & Worster 1985). This can lead to turbulent convection. By assuming the fluid to be well mixed by the convection, and by parameterising the thermal and compositional fluxes at the solidification front in terms of the Rayleigh number of the convection, it is possible to construct one-dimensional models for the growth and stratification of the solid (Turner *et al.* 1986, Woods & Huppert 1989, Kerr *et al.* 1989). However, for solidification at a sidewall, the convection is often laminar, particularly under magmatic conditions (Nilson *et al.* 1985), and variations in solid and liquid composition occur both in the vertical direction (due to the effects of gravity) and in the direction of growth of the solid. Therefore, the problem is fundamentally two-dimensional (at least) and must be solved numerically.

The solidification of a melt from one sidewall of a rectangular enclosure has been studied both for a pure melt (Ramachandran *et al.* 1981, Ho & Viskanta 1984) and for a binary alloy (Thompson & Szekely 1987, 1988, Bennon & Incropera 1987*b*, Beckermann & Viskanta 1988). The model of Thompson & Szekely (1987, 1988) assumes a planar interface between the solid and liquid phases and predicted the formation of double-diffusive layers in the melt once it had become compositionally stratified. However, the parameter regime studied by Thompson & Szekely (1987, 1988) is one in which no compositional stratification occurs in the solid. The models of Bennon & Incropera (1987*b*) and Beckermann & Viskanta (1988) account for the possibility of morphological instability of the solid/melt interface and are able to model convection through the dendritic (mushy) two-phase layer which lies between the solid and liquid phases. Neither model includes the possibility of solid stratification.

In this chapter, we adopt the planar interface approximation of Thompson & Szekely (1987, 1988) to study the solidification of a binary alloy from a sidewall. In particular we calculate the compositional variations in the resultant solid. We begin in §2.2 by describing how stratification may occur in a binary alloy growing in the absence of convective motions. In §2.3, we discuss the nature of the convection induced by the horizontal variation in composition and temperature. By considering the flow in the boundary layer adjacent to the solidification front, we are able to demonstrate by scaling arguments that, under certain conditions, both the pattern and the magnitude of the compositional layering in the solid can be described by a single nondimensional number P. The aqueous sodium carbonate experiments of Leitch (1985, 1987) and Huppert *et al.* (1987) were conducted at fairly high Rayleigh numbers ($\gtrsim 10^9$). In §2.4, we use the scaling anaylsis of §2.3 to model the experiments by performing numerical calculations at much lower Rayleigh numbers ($\sim 10^6$). Finally, in §2.5, the numerical results are discussed and placed in the context of layering in magma chambers.

2.2 Diffusion controlled growth of a binary alloy

The simplest case of a multicomponent alloy is a *binary alloy*, which is made up of two components, denoted A and B. Examples of binary alloys are bronze, where the two components are copper (Cu) and zinc (Zn); aqueous salt solutions, composed of water (H_2O) and salt (*e.g.* NaCl, NH_4Cl, Na_2CO_3); and gallium-germanium (Ga–Ge) mixtures. Magmas are strictly multicomponent alloys, but they can often be modelled by binary alloys (McBirney *et al.* 1985). Although composed of several components, with many possibilities for segregation between solid and liquid phases, the convective behaviour is determined simply by whether the fluid released at the solid/melt interface is relatively heavy or relatively light.

2.2.1 Equilibrium phase diagram

The composition of a binary alloy may be quantified as the weight percentage of solute B in solvent A. In the solid phase, the composition is a local average, over a scale larger than the crystal sizes. When in thermodynamic equilibrium, the phase of a binary alloy is determined by its composition C and temperature T. Figure 2.2 shows a typical *equilibrium phase diagram.* Along the horizontal axis, the composition varies from pure A to pure B. Alloys of composition A and B are termed the *equilibrium end-members.* For an aqueous sodium carbonate solution, pure A is ice (H_2O) and pure B is hydrated sodium carbonate ($Na_2CO_3.10H_2O$). For temperatures greater than the liquidus temperature $T_L(C)$ (*i.e.* above the *liquidus*), the alloy is liquid. The liquid phase is sometimes termed the *melt.*

The dotted lines in Figure 2.2 represent lines of equal density. The lines are nearly vertical, demonstrating that composition typically has a greater effect on density than temperature. Figure 2.2 is based on the actual phase diagram for an aqueous sodium carbonate solute, whose density increases with composition (wt% Na_2CO_3) and decreases with temperature. The minimum temperature at which the liquid phase may exist in equilibrium is represented by the eutectic point, denoted E. The eutectic temperature is T_E and the eutectic composition is C_E. Alloys cooler than the eutectic temperature (*i.e.* below the *solidus*) are solid. If the temperature of the alloy is above the solidus and below the liquidus, crystals of A or B are formed, depending upon whether the

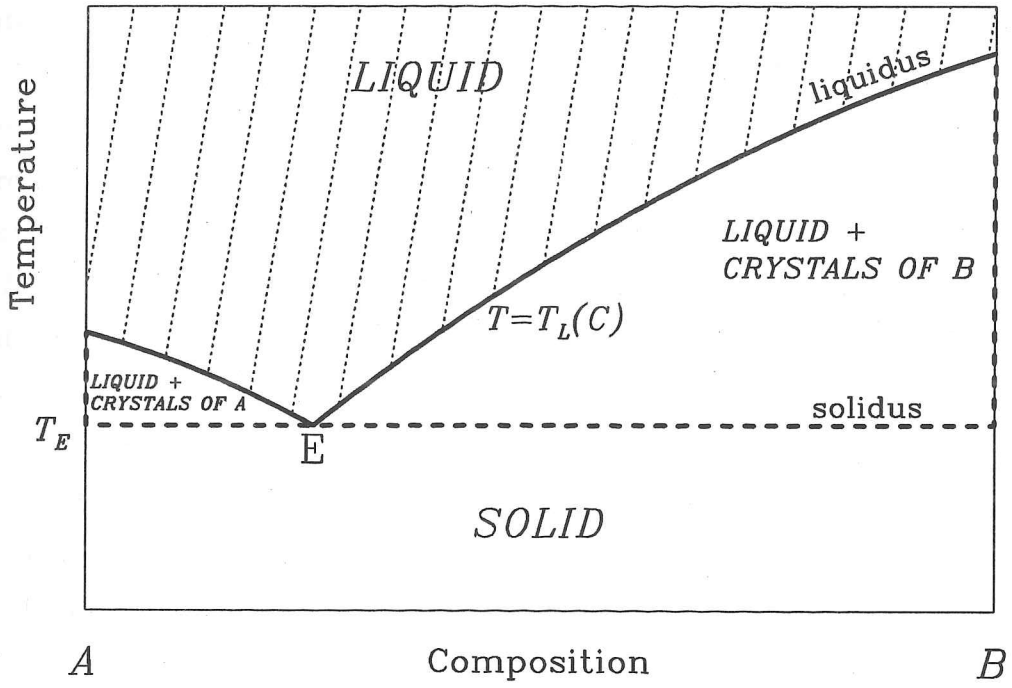

Figure 2.2. Typical equilibrium phase diagram for a binary alloy. The alloy can be described by its local temperature T and composition C. The composition is defined to be the proportion of B in the solution solute B in solvent A. The thick solid line (——) is the liquidus curve and the thick dashed line (– – –) is the solidus curve. The near-vertical dotted lines are contours of liquid density, indicating the relative effects of composition and temperature.

alloy composition is below or above eutectic. The composition of the residual fluid is given by the liquidus curve. The crystals may grow *homogeneously* or *heterogeneously*. Homogeneous nucleation occurs when a crystal forms spontaneously in the bulk of the fluid. However, heterogeneous growth, in which crystals form at a boundary, is favoured because less supercooling is required for nucleation. Consequently, an alloy cooled from a boundary generally solidifies against that boundary.

The segregation of components between the solid and liquid phases is also determined by the phase diagram. Consider a solid growing into a fluid of initial composition C_0, with $C_A < C_0 < C_B$, where C_A is the composition of pure A and C_B is the composition of pure A. An alloy with composition less than the eutectic composition ($C_0 < C_E$) is termed a *subeutectic* alloy. Similarly, if $C_0 > C_E$, the alloy is *supereutectic*. The temperature T is continuous across the solid/melt interface and the interface temperature T_i and

composition C_l of the liquid adjacent to the solidification front are related by the liquidus relation $T_i = T_L(C_l)$. The minimum interfacial temperature is the eutectic temperature T_E. The composition C_s of the solid is determined by the solidus curve (dashed line in Figure 2.2). If $C_0 < C_E$ and $T_i > T_E$, the solid grown is pure A ($C_s = C_A$) and the interfacial liquid composition $C_l > C_0$. If $C_0 > C_E$ and $T_i > T_E$, the solid grown is pure B ($C_s = C_B$) and the interfacial liquid composition $C_l < C_0$. If the interfacial temperature is eutectic ($T_i = T_E$), the fluid has eutectic composition and the composition of the solid may take any value between C_A and C_B. If the initial composition is eutectic ($C_0 = C_E$), the alloy evolves as a pure melt, freezing at the single temperature T_E. The solid formed also has eutectic composition. Note that a subeutectic alloy forms solid of subeutectic composition, and the liquid interfacial composition C_l may not exceed the eutectic composition C_E. Similarly, a supereutectic alloy may only form supereutectic solid and must remain supereutectic.

The above description is simplified, and there are many complicating factors. For example, the interfacial liquid temperature T_l is never exactly equal to the liquidus temperature, but must be slightly below to drive the crystal growth. By definition, solidification is a non-equilibrium process and so the assumption of equilibrium thermodynamics is an approximation. The effect of the supercooling required to drive the growth is negligible in general (Langer 1980), except when it leads to qualitative changes in the evolution of a crystallizing system. For example, supercooling of a melt may allow solidification at a boundary other than the cooling boundary if a suitable nucleation site exists (Kerr *et al.* 1989). Here we assume quasi-static growth, in which the alloy adjusts to thermodynamic equilibrium more rapidly than the system is evolving. We have also assumed that the solidus is vertical for $T > T_E$. For an aqueous sodium carbonate solution, in which the two components are H_2O (A) and Na_2CO_3 (B), the solidus is almost vertical and there is little variation in solid composition provided $T_i > T_E$.

Other alloys, such as some binary systems occurring in a geological context, may have very different phase diagrams. In Figure 2.3, the phase diagrams for the binary anorthite-silica and albite-anorthite systems are shown. Anorthite-silica is a classical binary eutectic system, but albite-anorthite differs quite markedly. When the melt solidifies to form plagioclase, Ca and Al are preferentially incorporated into the solid, and so the residual melt is rich in Na and Si. There is no intermediate eutectic composition for which the binary

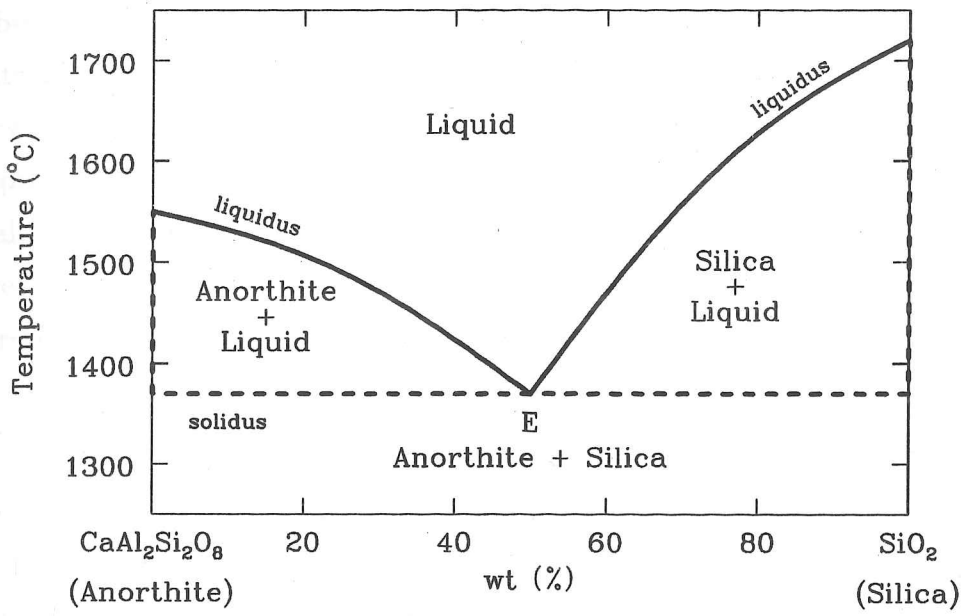

(a)

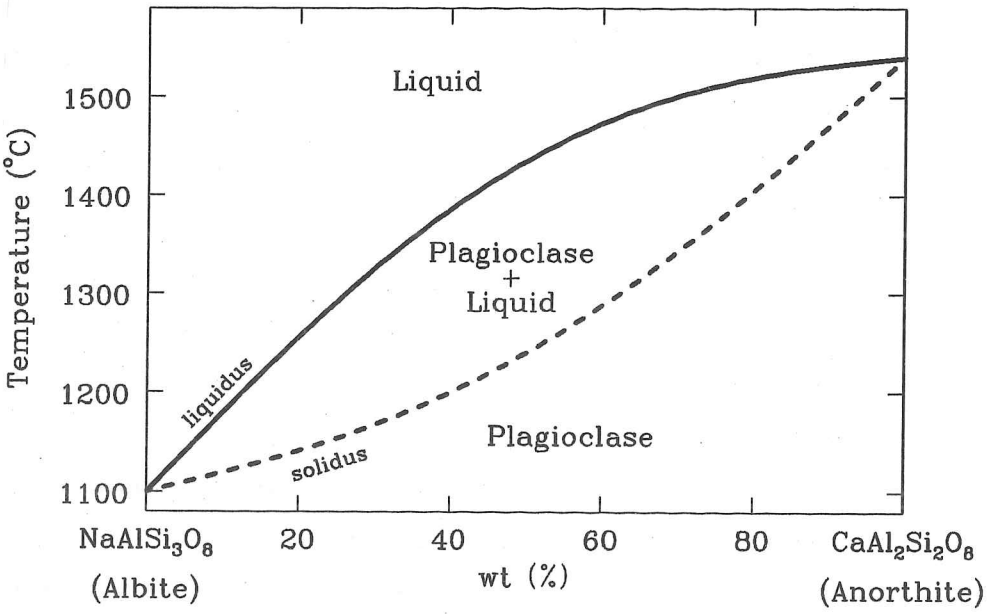

(b)

Figure 2.3. Phase diagrams for binary systems common in magmas. Figure (*a*) shows the anorthite-silica system and (*b*) the albite-anorthite system. Thick solid curves (——) are the liquidi and thick dashed curves (– – –) are the solidi. Anorthite-silica has a similar phase diagram to Figure 2.2. However, albite-anorthite is very different and there is no eutectic point. Formation of plagioclase leads to Na-enrichment in the residual melt. At a given interfacial temperature, the composition of the liquid adjacent to the solidification front is given by the liquidus curve and the composition of the solid grown is given by the solidus curve (from Hall 1987).

melt behaves as a pure melt. For any intermediate melt composition, the solid formed consists of an aggregate of albite and anorthite. Ternary (three-component) and quaternary (four-component) melts have also been identified and studied. A more complete description of the phase diagrams for basaltic magmas is provided by Morse (1980). In general, the number of components in a melt is the minimum number of chemical species required to describe the composition of the melt over the entire range of temperatures and pressures of interest.

The equilibrium phase diagram shown in Figure 2.2 suggests two growth regimes for growth with a planar solid/melt interface, which here are termed *liquidus* and *eutectic* growth. Liquidus growth occurs when the interfacial temperature T_i is above the eutectic. The solid formed is either pure A or pure B and consequently there is no compositional stratification in the solid. In the eutectic growth regime, the liquid at the solid/melt interface has eutectic composition and temperature. The composition of the solid grown varies from C_E to C_A or C_B, depending upon whether the alloy has sub- or supereutectic composition. The solid composition is determined by the compositional flux (here defined as the flux of component B) into, or out of the solid. If the bulk fluid is supereutectic, component B preferentially crystallizes and so the fluid adjacent to the solid/melt interface is depleted in component B. For an aqueous sodium carbonate solution, component B (Na_2CO_3) is heavier than component A (H_2O), and so the fluid released at the solidification front is generally lighter than the bulk fluid, as the density of the fluid depends more strongly upon its composition than upon its temperature. Similarly, a crystallizing subeutectic aqueous salt solution releases heavy fluid at the solid/melt interface. Therefore, supereutectic aqueous salt solutions have been used to model calc-alkaline magma chambers, in which the solid formed is rich in heavy components, such as iron, and the fluid released is relatively light. Subeutectic aqueous salt solutions are used to model tholeiitic magma chambers, in which the fluid released is often relatively heavy (McBirney *et al.* 1985).

For eutectic growth, the specific manner in which crystals of component A are incorporated into the matrix of crystals of component B, or *vice versa*, varies with the solidification conditions and from alloy to alloy. There are two main classes of behaviour for eutectic solidification, termed *normal* and *anomalous* (Porter & Easterling 1981). In normal structures, the two components form either a rod-like or a lamellar structure. In

a rod-like structure, the minor component (A for a supereutectic melt) appears as rods embedded in the major component (B), with the axes of symmetry of the rods parallel to the direction of growth. A lamellar eutectic consists of alternate sheets of each component, each sheet lying parallel to the direction of growth. For normal eutectic growth, the solid/liquid interface is essentially planar. The particular choice of normal structure is determined by minimization of the interfacial energy between the components A and B, and is therefore varies between alloys. Anomalous structures occur when one of the solid components is capable of faceting. For example, anomalous growth may occur when a supereutectic sodium carbonate solution freezes. Large hydrated salt crystals ($Na_2CO_3.10H_2O$) protrude from the solid into the liquid and the solid/melt interface has a craggy appearance (Leitch 1985). In this chapter, a planar interface and normal structure are assumed throughout. In §2.4, we see that anomalous solidification of supereutectic sodium carbonate solutions leads to some differences between experiments and the theory presented here.

2.2.2 Diffusion controlled growth

In the absence of fluid motions, the rate of growth of the solid is limited by diffusive processes. For liquidus growth into a supereutectic solution, the growth is controlled by the rate at which composition can be transported diffusively to the solidification front so that crystals of pure B may form. Similarly, for liquidus solidification of a subeutectic solution, composition must be transported away from the solid/melt interface. However, if the temperature at the solid/melt interface is eutectic, the solidification is thermally controlled. In the eutectic regime, growth is limited by the rate at which the latent heat released upon solidification and the heat flux from the liquid can be conducted through the solid away from the solid/melt interface.

Consider solid growing from the boundary $z = 0$ into the semi-infinite half-space $z > 0$. At time $t = 0$, the region $z > 0$ is occupied by fluid at constant temperature T_0 and composition C_0. At $t = 0+$, the temperature of the boundary is instantaneously reduced to the constant value $T_C < T_E$. Note that the equivalent problem for a pure melt $C = C_A$ or C_B is the classical Stefan problem (Carslaw & Jaeger 1959). For a binary alloy, the thermal and compositional evolutions of the melt and solid are described by

the diffusion equation. Diffusion of composition within the solid phase is neglected. The diffusion equations for the solid temperature T_s, the melt temperature T_l and the melt composition C_l are

$$\rho_s c_{ps} \frac{\partial T_s}{\partial t} = \frac{\partial}{\partial z}\left(k_s \frac{\partial T_s}{\partial z}\right) \qquad 0 < z < h(t)\,; \tag{2.2.1}$$

$$\rho_l c_{pl} \frac{\partial T_l}{\partial t} = \frac{\partial}{\partial z}\left(k_l \frac{\partial T_l}{\partial z}\right) \qquad z > h(t)\,; \tag{2.2.2}$$

$$\frac{\partial C_l}{\partial t} = \frac{\partial}{\partial z}\left(\kappa_C \frac{\partial C_l}{\partial z}\right) \qquad z > h(t)\,, \tag{2.2.3}$$

where ρ_l and ρ_s respectively are the densities of the liquid and solid phases; c_{pl} and c_{ps} are the thermal capacities; k_l and k_s are the thermal conductivities; and κ_C is the molecular diffusivity of composition in the melt. The thermal diffusivities of the liquid and solid phases are $\kappa_{Tl} = k_l/\rho_l c_{pl}$ and $\kappa_{Ts} = k_s/\rho_s c_{ps}$, and typically $\kappa_C \ll \kappa_{Tl}, \kappa_{Ts}$. In general, the physical properties of the alloy vary with composition and with phase. However, we will make the approximation that the physical properties of the alloy (k, c_p, κ_C) are constant within each phase, and that there is no volumetric expansion or contraction upon solidification ($\rho_s = \rho_l$). Within the liquid phase, there is little variation in the physical properties of the alloy. The thermal properties of the solid phase are constant if the composition of the solid is constant and if the eutectic structure is normal (*i.e.* rod-like or lamellar). Differences between the thermal properties of the solid and liquid phases are likely because of the difference in structure. For example, a crystalline matrix is in general a better conductor of heat then a disorganised fluid.

At the solidification front $z = h(t)$, the temperature is continuous ($T_l = T_s = T_i$). The latent heat released upon solidification and the heat flux from the liquid are balanced by the heat flux into the solid, and so

$$\rho_s \mathcal{L} \dot{h} = k_s \frac{\partial T_s}{\partial z} - k_l \frac{\partial T_l}{\partial z}\,, \tag{2.2.4}$$

where $\mathcal{L}$ is the latent heat of fusion. The solid composition for $z < h(t)$ is constant with respect to time and is denoted $C_s(z)$. The composition of the newly formed solid is determined by the composition of the liquid alloy adjacent to the solidification front

and the diffusive flux of composition towards, or away from, the solid/melt interface. By conducting a local mass balance at $z = h(t)$, we obtain the following expression for $C_s(h)$,

$$(C_s - C_l)\dot{h} = \kappa_C \frac{\partial C_l}{\partial z}. \tag{2.2.5}$$

The model is closed by two boundary conditions for the temperature, the solid composition and the melt composition at the solid/melt interface. For liquidus growth, the liquid temperature and composition are constrained by the liquidus relation and the solid is pure A or pure B, *i.e.*

$$\begin{aligned} T_i &= T_L(C_l)\,; \\ C_s &= C_A \quad \text{or} \quad C_B\,. \end{aligned} \tag{2.2.6}$$

For eutectic growth, the interfacial temperature and liquid composition are eutectic at the solid/melt interface. Therefore, the boundary conditions at $z = h(t)$ are

$$\begin{aligned} T_i &= T_E\,; \\ C_l &= C_E\,. \end{aligned} \tag{2.2.7}$$

The partial differential equations (2.2.1)–(2.2.3), combined with the boundary conditions described above, admit a similarity solution with similarity variable (Worster 1986)

$$\eta = \frac{z}{2\sqrt{\kappa_{Tl} t}}. \tag{2.2.8}$$

The solution for the liquidus growth regime (boundary conditions (2.2.6)) has been studied extensively by Worster (1986). That a similarity solution also exists for the eutectic regime was noted by Woods & Huppert (1989). Here, we consider the eutectic regime as we wish to investigate compositional stratification in the solid. Therefore boundary condition (2.2.7) applies and the solutions for T_s, T_l and C_l take the form

$$T_s = T_C + (T_E - T_C)\,\frac{\operatorname{erf}(\eta/\sqrt{\gamma})}{\operatorname{erf}(\lambda/\sqrt{\gamma})}\,; \tag{2.2.9}$$

$$T_l = T_0 + (T_E - T_0)\,\frac{\operatorname{erfc}(\eta)}{\operatorname{erfc}(\lambda)}\,; \tag{2.2.10}$$

$$C_l = C_0 + (C_E - C_0)\,\frac{\operatorname{erfc}(\eta/\sqrt{D})}{\operatorname{erfc}(\lambda/\sqrt{D})}\,, \tag{2.2.11}$$

where

$$h(t) = 2\lambda\sqrt{\kappa_{Tl}t} \tag{2.2.12}$$

and $\gamma = \kappa_{Ts}/\kappa_{Tl}$; $D = \kappa_C/\kappa_{Tl}$. The growth rate parameter λ can be found by substituting (2.2.9), (2.2.10) and (2.2.12) into the heat balance (2.2.4). After some algebra, we obtain

$$\frac{\mathcal{L}}{c_{ps}} = \frac{(T_E - T_C)}{G(\lambda/\sqrt{\gamma})} - \frac{\rho_l c_{pl}}{\rho_s c_{ps}} \frac{(T_0 - T_E)}{F(\lambda)} . \tag{2.2.13}$$

The solid composition is constant and is obtained by substituting the solution (2.2.11) for the melt composition into the mass balance (2.2.5), *i.e.*

$$C_s = C_E + \frac{(C_0 - C_E)}{F(\lambda/\sqrt{D})} . \tag{2.2.14}$$

The functions $F(x)$ and $G(x)$ are defined by

$$\begin{aligned} F(x) &= \sqrt{\pi}\, x\, e^{x^2} \text{ erfc } x\,; \\ G(x) &= \sqrt{\pi}\, x\, e^{x^2} \text{ erf } x\,. \end{aligned} \tag{2.2.15}$$

Equation (2.2.13) shows that the growth is controlled by the thermal conditions alone. The growth rate factor λ increases as the cooling temperature T_C and the far-field temperature T_0 decrease. For the liquidus growth regime (Worster 1986), the interfacial temperature and composition in the liquid are functionally related (equation (2.6)) and the condition that the solid grown must be pure A (or B) means that the growth is limited by the rate at which composition can be transported diffusively from (or to) the solid/melt interface. Relaxing this restriction, with the solid taking up as much or as little component B as it is able, means that the compositional field has no effect upon the growth rate and the solid grows at the same rate as for an alloy of eutectic composition.

The function $F(x)$ is monotonically increasing on the range $0 \leq x < \infty$ such that $F(0) = 0$ and $F(x) \to 1$ as $x \to \infty$ (Abramowitz & Stegun 1964). Therefore the solid composition C_s is always greater than the far-field composition C_0. For large growth rates ($\lambda \gg 1$), the solid composition C_s approaches C_0. Equation (2.2.14) suggests unphysically high values of the solid composition as $\lambda \to 0$. At a sufficiently low growth rate λ_{crit}, the

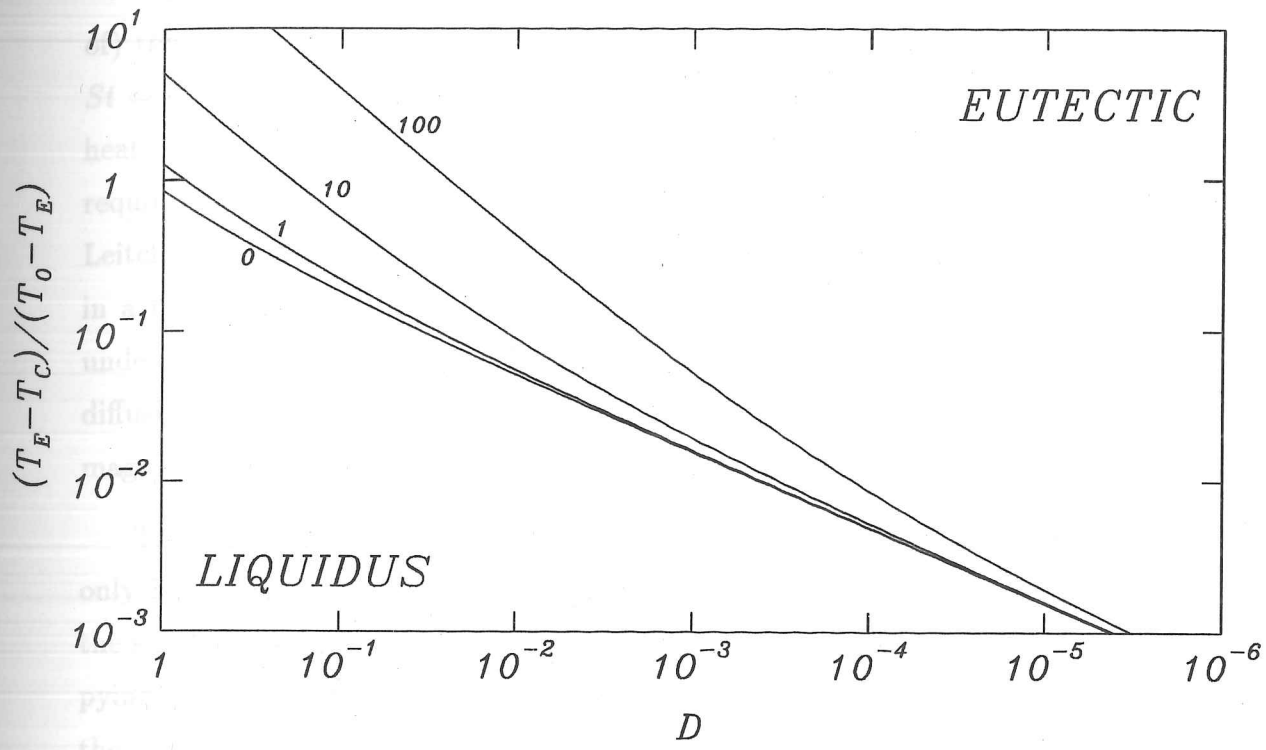

Figure 2.4. Critical curves for nondimensional undercooling $(T_E - T_C)/(T_0 - T_E)$ plotted against nondimensional compositional diffusivity $D = \kappa_C/\kappa_{Tl}$. The far-field composition $C_0 = \frac{1}{2}(C_E + C_M)$, where $C_M = C_A$ or C_B. Curves are plotted for four different values of the Stefan number $St = \mathcal{L}/c_{pl}(T_0 - T_E)$, namely $S = 0$, $S = 1$, $S = 10$ and $S = 100$. For large values of the diffusivity D, the compositional flux is sufficiently high for pure A or B to form (*LIQUIDUS* regime). The solid growth rate is too rapid for large undercoolings and low Stefan numbers, and so pure A (or B) cannot form (*EUTECTIC* regime).

growth regime changes to liquidus and boundary condition (2.2.6) applies. The critical growth rate λ_{crit} is given by substituting C_M for C_s in equation (2.2.14), where C_M is the appropriate equilibrium end-member composition (C_A or C_B). That is, λ_{crit} is the root of

$$F(\lambda_{\text{crit}}/\sqrt{D}) = \frac{(C_0 - C_E)}{(C_M - C_E)}. \tag{2.2.16}$$

The growth rate λ is affected by the undercooling $T_E - T_C$, while the solid composition is determined by the compositional diffusivity D. Figure 2.4 shows how the growth regime changes from eutectic to liquidus as (*i*) the undercooling is decreased and so the growth rate slows, allowing the formation of the appropriate pure end-member; or (*ii*) the compositional diffusivity increases, increasing the compositional flux into (or out

of) the solid. Critical curves are plotted for four different values of the Stefan number $St = \mathcal{L}/c_{pl}(T_0 - T_E)$. A large value of the Stefan number corresponds to a high latent heat of fusion, and therefore growth is slower. Consequently, greater undercooling is required to produce eutectic growth for high Stefan numbers. In the experiments of Leitch (1985, 1987) and Huppert *et al.* (1987), the Stefan number is less than ten, and in a typical magma chamber, $0.1 \lesssim St \lesssim 10$ (see §2.3.2 below). The nondimensional undercooling $(T_E - T_C)/(T_0 - T_E)$ is generally greater than unity and the nondimensional diffusivity $D \lesssim 10^{-2}$. Therefore, the conditions of the laboratory experiments and in magma chambers are consistent with the eutectic growth regime.

The similarity solution (2.2.9)–(2.2.12) for eutectic growth of a binary alloy is valid only for a semi-infinite domain with constant far-field conditions in the melt. However, the similarity solution provides some insight into the solidification of a liquid alloy occupying a finite domain with changing far-field conditions. If the far boundary is insulated, the region will eventually become completely solid. For a supereutectic solution solidifying in a finite domain, the formation of solid rich in component B must eventually lead to a decrease in the far-field melt composition by mass conservation. Consequently, the solid composition decreases with distance away from the cooling boundary. The final solid formed has eutectic composition. In general, the influence of the far-field conditions is felt across the compositional boundary layer, and the solid composition reflects the far-field composition. Consequently, if a two-dimensional cavity is occupied by compositionally stratified fluid, the solid grown might also be expected to exhibit compositional stratification.

2.2.3 Constitutional supercooling

The similarity solution (2.2.9)–(2.2.12) presupposes a planar interface between the solid and liquid phases. However, if the compositional gradient at the solid/melt boundary is sufficiently large, the solidification front may become unstable. For example, the solid/melt interface may become highly convoluted, with long thin dendrites surrounded by interstitial fluid. This type of geometrical instability is termed *morphological instability* and occurs because the melt is locally cooler than its liquidus temperature, *i.e.* the melt is *constitutionally supercooled.*

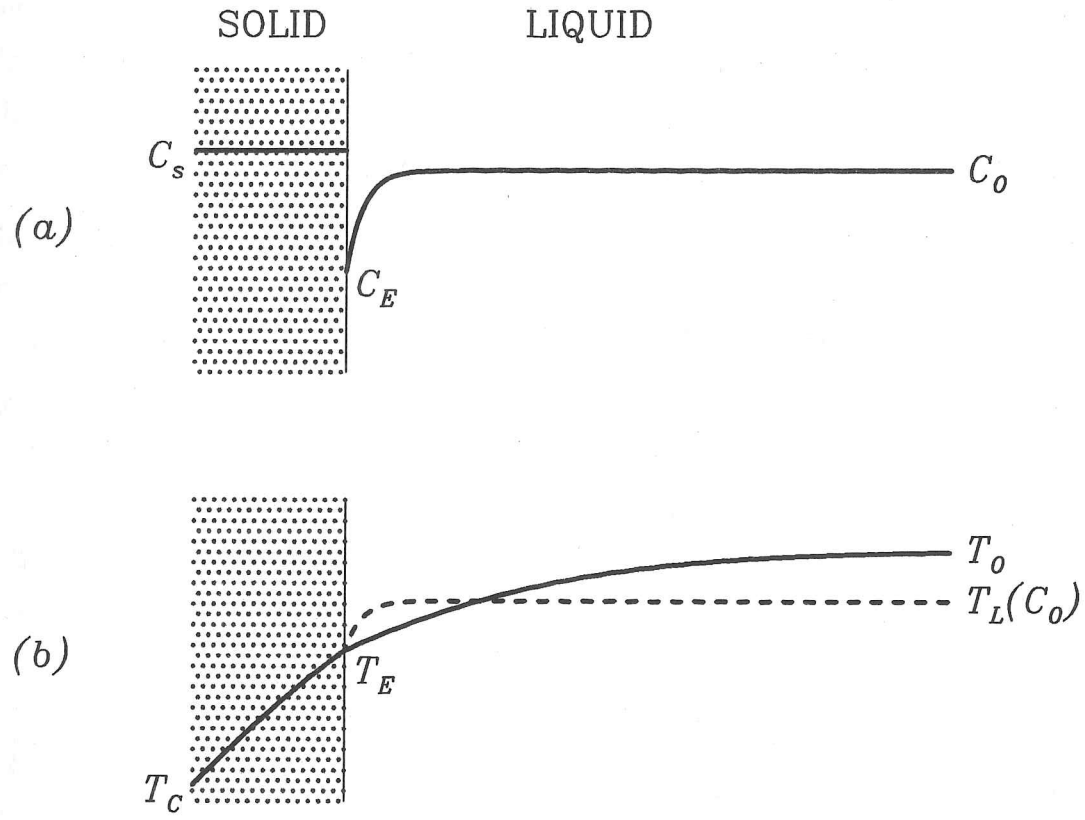

Figure 2.5. Typical profiles for (a) composition and (b) temperature ahead of an advancing solid/melt interface. In (b), the liquidus temperature $T_L(C)$ is plotted as a dashed line (- - -), demonstrating that the fluid may be locally supercooled ahead of the solidification front.

Figure 2.5 demonstrates typical composition and temperature profiles in a growing solid and in the melt immediately ahead of the solidification front. The compositional boundary layer (Figure 2.5(a)) is thinner than the thermal boundary layer (Figure 2.5(b)) because of the relatively low molecular diffusivity of composition compared with the thermal diffusivity. Consequently, the melt ahead of the solidification front may become constitutionally supercooled locally, *i.e.* $T < T_L(C)$. For a planar interface advancing at a constant velocity, Mullins & Sekerka (1964) demonstrated that the interface becomes unstable when

$$(k_l + k_s)^{-1} \left\{ k_l \frac{\partial T_l}{\partial z}\bigg|_{z=h} + k_s \frac{\partial T_s}{\partial z}\bigg|_{z=h} \right\} < \Gamma \frac{\partial C_l}{\partial z}\bigg|_{z=h}, \tag{2.2.17}$$

where $\Gamma = T_L'(C)$, the slope of the liquidus curve. The nature of the solid/melt interface once instability occurs is dependent upon the particular alloy under consideration. When

a supereutectic aqueous ammonium chloride (NH_4Cl) solution becomes supercooled, the solid/melt interface becomes dendritic, with a two-phase *mush* region between the melt and the eutectic solid. At the base of the mush, there is a eutectic front at which the temperature and interstitial fluid composition are eutectic.

Mathematical mush models have been applied to a variety of situations (Hills *et al.* 1983, Huppert & Worster 1985, Worster 1986, Kerr *et al.* 1989), with some success. If the dendrite spacing is sufficiently small, the mush may be described in terms of its local porosity, or liquid fraction, and equations formulated for the growth of such a region. The interface between the two-phase and liquid region is reasonably sharp, and so a mush/melt interface may be defined. For other alloys, the interface morphology is less regular. In particular, the solid/melt interface for a supereutectic aqueous sodium carbonate solution growing into stagnant fluid is characterised by large, faceted, plate-like crystals ($Na_2CO_3.10H_2O$) extending from the eutectic front into the melt (Chen & Turner 1980). In this case, the conditions are far removed from those for which the mathematical mush models are valid.

In the presence of strong fluid motions, either laminar or turbulent, the thickness of the crystal layer is reduced. For laminar flow past supereutectic sodium carbonate crystallizing at a sidewall (Leitch 1985) and for turbulent convection above the same alloy cooled from below (Woods & Huppert 1989), the crystal layer is no more than 2mm thick. Woods & Huppert (1989) showed that a planar interface model more than adequately explained their experimental observations, in particular the compositional stratification in the solid. In this chapter, the same planar interface approximation is made and the effects of constitutional supercooling are neglected.

In the following section, we consider how compositional stratification in the solid may be affected by convective motions driven by the gradients in composition and temperature across an alloy cooled from the side. By considering only the most important physical processes which determine the solid stratification we are able to demonstrate how the pattern of layering observed in the solid product is determined by a single compound nondimensional parameter.

2.3 Convection and compositional layering

In this section, we include the effects of convection driven by compositional and thermal variations in the melt during the solidification of a binary alloy from a sidewall. Redistribution of composition by convective motions can lead to strong compositional stratification in the solid product. We identify the principal physical processes involved in determining the pattern of solid stratification. By performing a scaling analysis, we are able to show that the effects of laminar convection upon the solid stratification can be collapsed into a single nondimensional parameter P. This allows comparison between numerical calculations performed in §2.4 below and experiments with aqueous salt solution conducted by Leitch (1985, 1987) and Huppert *et al.* (1987). We tentatively suggest that the numerical and experimental predictions for the solid stratification may be applied directly to the solidification of magma chambers. This provides a working estimate of the degree of solid stratification which may be expected as a result of convective processes alone.

2.3.1 Governing equations

For convection in an incompressible fluid, it is usual to make the Boussinesq approximation that density variations are small compared with the average fluid density. In addition, we assume that the density ρ of the fluid depends linearly upon its temperature T and composition C, *viz.*

$$\rho = \rho_0 \left(1 - \alpha(T - T_{\text{ref}}) + \beta(C - C_{\text{ref}})\right) , \tag{2.3.1}$$

where ρ_0, T_{ref} and C_{ref} are reference values and α and β are respectively the thermal and compositional coefficients of expansion. For an aqueous salt solution, an increase in temperature reduces the density of the solution, while an increase in composition (salinity) increases the density. In this case, therefore, both α and β are positive. As an extension to the Boussinesq approximation, we neglect the change in density associated with the change in phase from liquid to solid.

The particular geometry studied in this chapter, and in the following chapter, is sketched in Figure 2.6. A two-dimensional square box of length L and depth H is filled with liquid binary alloy. A magma chamber solidifying at both sidewalls could be modelled

by two such boxes placed side-by-side. The initial temperature of the liquid is T_0 and its initial composition is C_0. At $t = 0+$, the temperature at one of the vertical sidewalls, $x = 0$, is reduced to a temperature T_c, so that crystallization immediately commences at that boundary. All other boundaries remain insulated. For $t > 0$, the region $0 < x < h(y,t)$ has solidified, and the region $h < x < L$ is still liquid. The fluid velocity $\mathbf{u}$ is zero on the rigid boundaries $y = 0$, $y = H$ and $x = L$. In addition, $\mathbf{u} = 0$ at the moving solid/melt interface $x = h(y,t)$. The fluid adjacent to the interface is not pushed by the moving solid but is incorporated into the solid phase. This is a consequence of our assumption that there is no change of density upon phase change. If the alloy were to expand upon freezing, a normal velocity away from the solidification front would be induced in the fluid. Conversely, if the alloy were to contract upon freezing, a normal velocity towards the solidification front would result.

The Boussinesq equations for the fluid velocity $\mathbf{u}$, the liquid temperature T_l, the solid temperature T_s and the liquid composition C_l are

$$\rho_0 \left(\frac{\partial \mathbf{u}}{\partial t} + \mathbf{u}.\nabla \mathbf{u} \right) = -\nabla p + \mu \nabla^2 \mathbf{u} + \rho \mathbf{g}\,; \tag{2.3.2}$$

$$\rho_0 c_{pl} \left(\frac{\partial T_l}{\partial t} + \mathbf{u}.\nabla T_l \right) = \nabla.(k_l \nabla T_l)\,; \tag{2.3.3}$$

$$\rho_0 c_{ps} \frac{\partial T_s}{\partial t} = \nabla.(k_s \nabla T_s)\,; \tag{2.3.4}$$

$$\frac{\partial C_l}{\partial t} + \mathbf{u}.\nabla C_l = \kappa_c \nabla^2 C_l\,, \tag{2.3.5}$$

where p is the fluid pressure, μ is the dynamic viscosity of the fluid, and $\mathbf{g}$ is the acceleration due to gravity. The partial differential system (2.3.2)–(2.3.5) is closed by the incompressibility condition

$$\nabla.\mathbf{u} = 0\,. \tag{2.3.6}$$

For material properties, such as the heat capacity c_p, the subscripts s and l correspond to the solid and liquid phases respectively. As in §2.2, the thermal conductivities k and heat capacities c_p are assumed to be constant for each of the solid and liquid phases. Chemical diffusion of composition in the solid phase is neglected. In this chapter, the viscosity μ is assumed to be constant. This is a valid assumption for aqueous salt solutions, but less so for magmas, in which order-of-magnitude variations in viscosity occur as the temperature

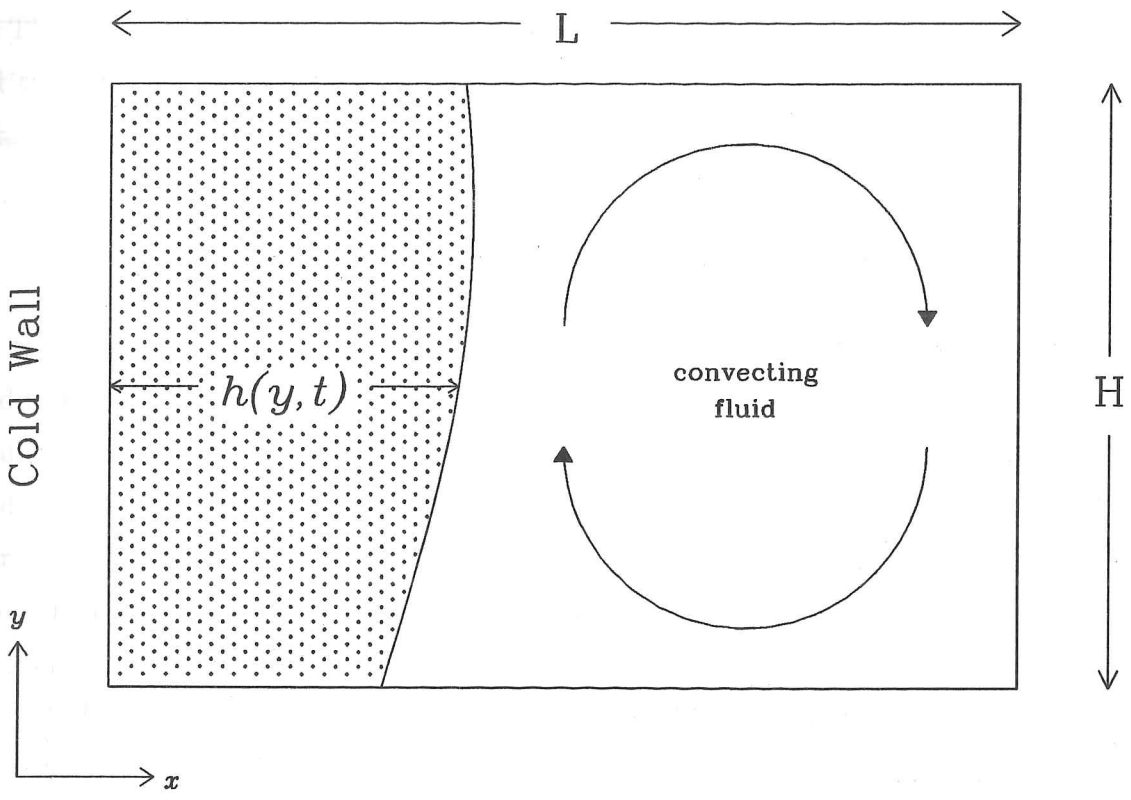

Figure 2.6. Sketch of the geometry for the sidewall crystallization experiments and calculations. The stippling represents the solid region $0 < x < h(y,t)$.

and composition of the magma vary across the width of a magma chamber. The effects of variable viscosity are discussed at greater length in Chapter 3.

If the temperature T_c of the cooling boundary is below the eutectic temperature T_E, the melt completely solidifies after some time. The rate of advance V_h of the solidification front is controlled by the rate at which the heat supplied by the melt and the latent heat released upon solidification can be transported away from the solid/melt interface. In general, the solid/melt interface is not parallel to the cooling boundary, and so we write

$$\rho_0 \mathcal{L} V_h = k_s \frac{\partial T_s}{\partial n}\bigg|_{x=h-} - k_l \frac{\partial T_l}{\partial n}\bigg|_{x=h+}, \tag{2.3.7}$$

where $\partial/\partial n$ is the derivative taken normal to the solidification front $x = h(y,t)$ and into the fluid.

The composition C_s of the solid grown is determined by the composition of the melt and the diffusive flux from the melt at the solid/melt interface. Applying a local mass balance at $x = h(y,t)$, we obtain

$$\left(C_s\big|_{x=h-} - C_l\big|_{x=h+}\right) V_h = \kappa_C \left.\frac{\partial C_l}{\partial n}\right|_{x=h+} . \tag{2.3.8}$$

For the thermal and compositional fields, four boundary conditions are required at the solidification front $x = h(y,t)$ — one each for T_l, C_l, V_h and C_s. Two of these boundary conditions are provided by equations (2.3.7) and (2.3.8). The remaining two boundary conditions are determined by the equilibrium phase diagram (Figure 2.2). For equilibrium growth with a planar interface, there are two distinct solidification regimes, termed liquidus growth and eutectic growth, as described in §2.2.2. For relatively weak undercooling or high solutal diffusivity, the solid grown is one of the two equilibrium end-members A or B, depending upon the whether the initial composition is below or above the eutectic composition. Under conditions of equilibrium growth, the interfacial temperature and composition in the melt are constrained to lie upon the liquidus curve. For liquidus growth, the two remaining boundary conditions at $x = h(y,t)$ are

$$\begin{aligned} T_l &= T_L(C_l)\,; \\ C_s &= C_A \text{ or } C_B\,. \end{aligned} \tag{2.3.9}$$

A similarity solution analogous to that described in §2.2.2 can be obtained for the liquidus growth regime if the liquidus function $T_L(C_l)$ is linear (Worster 1986). For a supereutectic aqueous Na_2CO_3 solution, the gradient $\partial T_L/\partial C_l$ is 1.7 °C (wt% Na_2CO_3)$^{-1}$ and the end-members A and B have compositions $C_A = 0$ wt% Na_2CO_3 (pure ice) and $C_B = 37$ wt% Na_2CO_3 (hydrated salt crystal). The liquidus regime for solidification of a binary alloy from a vertical sidewall was studied by Thompson & Szekely (1987, 1988). Their work was motivated primarily by metallurgical applications and was aimed towards an understanding of the fluid dynamical processes which occur when an alloy solidifies, in particular the formation of double-diffusive layers. Thompson & Szekely (1987, 1988) did not study the consequent compositional stratification in the solid.

For solidifying magma chambers, the undercooling by the country rock is likely to be too great for liquidus growth to occur. Assuming that the solid/melt interface remains

planar, the temperature and composition at the interface are eutectic and the solid composition determined by the compositional flux (equation (2.3.8)). This is the eutectic regime, in which the final two boundary conditions at $x = h(y,t)$ are

$$\begin{aligned} C_l &= C_E\,; \\ T_l &= T_E\,. \end{aligned} \tag{2.3.10}$$

This is the regime of interest, in which variations in compositional fluxes along the solidification front can lead to compositional layering in the solid. When the composition and temperature at the solid/melt interface are constant along the interface, as in the eutectic growth regime, (2.3.7) and (2.3.8) can be rewritten as follows,

$$\mathcal{L}\dot{h} = f\left(k_s\frac{\partial T_s}{\partial x} - k_l\frac{\partial T_l}{\partial x}\right)\,; \tag{2.3.11}$$

$$(C_s - C_l)\dot{h} = f\kappa_C\frac{\partial C_l}{\partial x}\,, \tag{2.3.12}$$

where the shape factor $f = \left(1 + (\partial h/\partial y)^2\right)^{-1}$. If the variations in melt composition and temperature along the solid/melt interface are small, equations (2.3.11) and (2.3.12) can be considered good approximate expressions (Thompson & Szekely 1988).

The governing equations (2.3.2)–(2.3.5) suggest a simple nondimensionalisation based upon the length of the enclosure and the timescale for diffusion of heat across the enclosure. Hereinafter, lengths are scaled by L, time by L^2/κ_{Tl} and temperatures and compositions by the reference differences ΔT and ΔC respectively. There is no change in notation to primed variables. It should be evident whether or not any given expression is dimensional or nondimensional since the former will generally include dimensional material constants, and the latter will include one or more of the important nondimensional groups described below. Any possible ambiguities are explained where necessary.

In addition to the nondimensionalisation, the curl of (2.3.2) has been taken to eliminate the pressure p. This leads to the vorticity–streamfunction formulation, in which the vorticity $\boldsymbol{\omega} = \nabla \wedge \mathbf{u} = (0,0,\omega)$ The unit vector $\mathbf{k} = (0,0,1)$ is directed out of the page in Figure 2.6. The incompressibility condition (2.3.6) means that we may define a streamfunction ψ, which is given by $\mathbf{u} = \nabla \wedge (\psi\mathbf{k})$. Therefore, the partial differential

equations (2.3.2)–(2.3.5) become

$$\frac{1}{Pr}\left(\frac{\partial \omega}{\partial t} + \mathbf{u}.\nabla\omega\right) = Ra_{_T}\frac{\partial T_l}{\partial x} - Ra_{_C}\frac{\partial C_l}{\partial x} + \nabla^2\omega\,; \tag{2.3.13}$$

$$\frac{\partial T_l}{\partial t} + \mathbf{u}.\nabla T_l = \nabla^2 T_l\,; \tag{2.3.14}$$

$$\frac{\partial T_s}{\partial t} = \gamma\nabla^2 T_s\,; \tag{2.3.15}$$

$$\frac{\partial C_l}{\partial t} + \mathbf{u}.\nabla C_l = \frac{1}{Le}\nabla^2 C_l\,; \tag{2.3.16}$$

$$\nabla^2\psi = -\omega\,, \tag{2.3.17}$$

where

$$\mathbf{u} = (\psi_y, -\psi_x)\,. \tag{2.3.18}$$

Pr is the Prandtl number, $Ra_{_T}$ and $Ra_{_C}$ respectively are the thermal and compositional Rayleigh numbers, γ is the ratio of the solid thermal diffusivity to liquid thermal diffusivity, and Le is the Lewis number, *i.e*

$$Pr = \frac{\nu}{\kappa_{_{Tl}}} \qquad Ra_{_T} = \frac{g\alpha\Delta T L^3}{\nu\kappa_{_{Tl}}} \qquad Ra_{_C} = \frac{g\beta\Delta C L^3}{\nu\kappa_{_{Tl}}}$$
$$\gamma = \frac{\kappa_{_{Ts}}}{\kappa_{_{Tl}}} \qquad Le = \frac{\kappa_{_{Tl}}}{\kappa_{_C}} \tag{2.3.19}$$

The kinematic viscosity $\nu = \mu/\rho_0$. Throughout this thesis, the compositional Rayleigh number is based upon the thermal diffusivity $\kappa_{_{Tl}}$, rather than the solutal diffusivity $\kappa_{_C}$. In general, this is a more convenient choice. However, when applying general results obtained for thermal convection to situations where compositional effects dominate, the correct Rayleigh number is that based on the solutal diffusivity $\kappa_{_C}$. To avoid confusion by introducing two different compositional Rayleigh numbers, the Rayleigh number based on $\kappa_{_{Tl}}$ is denoted $Ra_{_C}$ and is defined by (2.3.19). The Rayleigh number based on $\kappa_{_C}$ is then $Le\,Ra_{_C}$.

In the eutectic growth regime, for which the boundary conditions (2.3.10) apply, the interfacial thermal and compositional balances (2.3.11) and (2.3.12) become

$$St\,\dot{h} = f\left(K\frac{\partial T_s}{\partial x} - \frac{\partial T_l}{\partial x}\right)\,; \tag{2.3.20}$$

and

$$(C_s - C_E)\,\dot{h} = f\,\frac{1}{Le}\frac{\partial C_l}{\partial x}\,, \tag{2.3.21}$$

where $St = \mathcal{L}/c_{pl}\Delta T$ is the Stefan number and $K = k_s/k_l$. If the dimensional undercooling is $\Delta T_s = T_E - T_C$, then the ratio $St\Delta T/K\Delta T_s$ represents the magnitude of the latent heat released upon solidification compared with the capacity of the solid to conduct heat away from the solid/melt interface. Large values of the Stefan number imply that the growth is controlled by the latent heat release and is slow. Small values of the Stefan number imply that solidification rates are rapid, unless limited by the heat supplied from the melt. When the heat supplied by the melt is small compared with the latent heat released upon crystallization, we see from (2.3.20) that the nondimensional timescale for the enclosure to become completely solidified is

$$t_S \sim St\Delta T/K\Delta T_s = \widehat{St}\,. \tag{2.3.22}$$

The modified Stefan number $\widehat{St}$ is that based on the thermal properties of the solid and the temperature difference between the cold wall and the solidification front, *i.e.* the undercooling. Equation (2.3.22) is valid for large Stefan numbers. When the heat supplied by the melt is not negligible, t_S is larger than that predicted by (2.3.22). Equation (2.3.21) implies that for large values of the Lewis number Le, high compositional gradients are required in the vicinity of the solidification front to create $O(1)$ variations in the solid composition. For an aqueous salt solution, $Le = O(10^2)$, and in a magma chamber $Le = O(10^2 - 10^5)$ (Nilson *et al.* 1985). It is therefore almost certain that the melt adjacent to the solidification front is constitutionally supercooled. Typically, this leads to morphological instability (Mullins & Sekerka 1964) and the solid/melt interface becomes highly convoluted, with a two-phase region (commonly termed a *mushy zone*) lying between the wholly solid and wholly liquid regions.

For some crystallizing systems, for example supereutectic aqueous ammonium nitrate, the mushy region has a fine structure of thin, needle-like crystals surrounded by interstitial fluid. In this case, the mush may be treated as a continuum, described by a local porosity, or liquid fraction. Mathematical models for such systems have been studied successfully for a variety of physical situations (Hills *et al.* 1983, Huppert & Worster 1985, Worster

1986, Bennon & Incropera 1987*a*, Kerr *et al.* 1989), most of which do not involve flow within the mushy layer. Numerical models of dendritic solidification (Bennon & Incropera 1987*b*, Beckermann & Viskanta 1988) have revealed that significant redistribution of composition occurs in the melt through convection within the porous mushy zone. No discussion of the composition of the solid phase was provided by Bennon & Incropera (1987*b*), nor by Beckermann & Viskanta (1988). However, there are considerable uncertainties involved in such analyses. Most importantly, the strength of convection within the mushy zone is strongly dependent upon the permeability of the mush, a property which is difficult to quantify. In addition, the range of alloys for which a continuum mush model is valid may be limited. In particular, for a supereutectic aqueous sodium carbonate solution, the solid/melt interface typically has a craggy appearance (Leitch 1985), with a layer of faceted hydrated salt crystals protruding into the compositional boundary layer. When growing into stagnant fluid, this layer can be quite thick (Chen & Turner 1980). However, Leitch (1985) and Woods & Huppert (1989) found that the dendritic layer can be quite thin ($\lesssim 2$ mm) when growing into a convecting fluid. Woods & Huppert (1989) showed that under such conditions, the stratification of the solid formed from an alloy cooled from below can be modelled reasonably accurately by assuming a planar interface between the solid and liquid phases.

It remains briefly to describe the rest of the boundary conditions. In nondimensional variables, the alloy occupies the domain $0 < x < 1$, $0 < y < \mathcal{A}$, where $\mathcal{A} = H/L$ is the aspect ratio of the enclosure. At the floor and roof boundaries $y = 0$ and $y = \mathcal{A}$, there is no flux of heat or mass, and so $\partial T_s/\partial y = \partial T_l/\partial y = \partial C_l/\partial y = 0$. At the cold wall $x = 0$, $T_s = T_C$ and the far wall $x = 1$ is insulated and impermeable, *i.e.* $\partial T_l/\partial x = \partial C_l/\partial x = 0$. At all melt boundaries, the no-slip condition $\mathbf{u} = 0$ is applied which, combined with the condition of no normal flow, implies that

$$\psi = \frac{\partial \psi}{\partial n} = 0 \quad \text{at} \quad x = h, 1 \text{ and } y = 0, \mathcal{A}. \tag{2.3.23}$$

The governing equations (2.3.13)–(2.3.17) cannot be solved analytically for the geometry considered here, and therefore must be solved numerically. The details of the numerical scheme used to obtain the results below are provided in the Appendix to this chapter. Convective flows in magma chambers are typically characterised by Rayleigh

numbers in excess of 10^{15}. Calculation of such flows requires greater computing power than is currently available. The Rayleigh numbers in the experiments conducted by Leitch (1985, 1987) and Huppert *et al.* (1987) are lower ($10^9 - 10^{11}$), but still require substantial computational resources if we are to resolve the fine detail of the compositional boundary layer in the melt adjacent to the solidification front. However, by considering the essential physical processes involved in determining the solid stratification, we are able to demonstrate below that the compositional stratification in the solid resulting from high Rayleigh number, high Lewis number convection can be the same as the solid stratification resulting from convection characterised by lower Rayleigh numbers and lower Lewis numbers, provided that a certain nondimensional parameter is the same in both cases. This enables us to study how convective processes within a solidifying magma chamber lead to variegation in the solid product, and to see how the experiments conducted by Leitch (1985, 1987) and Huppert *et al.* (1987) relate to geological situations.

2.3.2 Scaling analysis

The model presented in the above subsection is valid only when the convection is laminar. To aid discussion, the values of various physical quantities are presented in Table 2.1 for experimental conditions and for a magma chamber of approximately unit aspect ratio and with length 1 km. The Rayleigh numbers in the experiments are close to the critical value for transition of the boundary layer flow to turbulence. For free convection at a vertical wall, the compositional Rayleigh number $Ra_{_H}$, based upon the thermal diffusivity $\kappa_{_{Tl}}$ and the depth H of the tank, has a critical value for the onset of flow instability given by (Nilson *et al.* 1985)

$$Le\, Ra_{_H} \sim 10^9\, Sc^n, \tag{2.3.24}$$

where $0.5 \lesssim n \lesssim 2.5$ and $Sc = \nu/\kappa_{_C}$ is the Schmidt number. The range of values for the index n reflects a variety of sources. Elder (1965) proposed the value $n = 0.5$, based upon his experiments. Asymptotic analysis of the boundary layer equations in the limit $Sc \to \infty$ and constant heat flux at the wall leads to the value $n = 2.5$ (Hieber & Gebhart 1971).

Alternatively, one could construct a Reynolds number based on the thickness of the viscous boundary layer. The condition that the flow becomes turbulent at $Re = 300$

Quantity	Na_2CO_3–$10H_2O$	Magma chamber	Units
c_{pl}	3.9×10^3	1.3×10^3	$J\,kg^{-1}\,°C^{-1}$
c_{ps}	1.3×10^3	1.3×10^3	$J\,kg^{-1}\,°C^{-1}$
κ_{Tl}	1.3×10^{-7}	5.0×10^{-7}	m^2s^{-1}
κ_{Ts}	9.0×10^{-7}	5.0×10^{-7}	m^2s^{-1}
ν	2.3×10^{-6}	$10^{-2} - 10$	m^2s^{-1}
κ_C	4.0×10^{-10}	$10^{-9} - 10^{-12}$	m^2s^{-1}
ρ_0	1.0×10^3	2.45×10^3	$kg\,m^{-3}$
$\mathcal{L}$	3.1×10^5	5.0×10^5	$J\,kg^{-1}$
α	2.0×10^{-4}	2.5×10^{-5}	$°C^{-1}$
β	1.0×10^{-2}		$(wt\%\,Na_2CO_3)^{-1}$
$\Delta\rho_C$		2.5×10^2	$kg\,m^{-3}$

Table 2.1. Physical constants for aqueous sodium carbonate system at 0°C, obtained from various sources, including Leitch (1985), Woods (1989) and Weast (1971), and for magma chambers (Nilson *et al.* 1985). For the magma chamber, a characteristic density change $\Delta\rho_C$ is listed rather than β, the coefficient of expansion due to variations in composition. An equivalent value for β is given by $\Delta\rho_C/\rho_0\Delta C$.

yields the value $n = 2$ (Nilson *et al.* 1985). In the complete freezing experiments of Leitch (1985), the compositional Rayleigh number $Ra_H = 8 \times 10^9$, while for the stratified solution studied by Huppert *et al.* (1987), $Ra_H = 5 \times 10^{10}$. For an aqueous sodium carbonate solutions just above or within its freezing range, $Le = 330$ and $Sc \sim 6000$, and so the boundary layer for the complete freezing experiments is laminar if the index $n \gtrsim 2$ (Leitch 1985). For the experiments of Huppert *et al.* (1987), Ra_H is also below the critical value for most values of the index n ($n \gtrsim 1.2$). Substantial departures from laminar flow do not occur until Ra_H is much higher than the critical value for the onset of turbulence, and so it is assumed here that the boundary layer flow is laminar in all experiments. It is interesting to note that the ranges of compositional Rayleigh numbers $Le\,Ra_C = O(10^{17} - 10^{22})$ and Schmidt numbers $Sc = O(10^7 - 10^{12})$ for magma chambers are also such that it is unclear whether the flow is laminar or turbulent. The flow is

Quantity	Na_2CO_3–$10H_2O$	Magma chamber	Units
c_{pl}	3.9×10^3	1.3×10^3	$J\,kg^{-1}\,°C^{-1}$
c_{ps}	1.3×10^3	1.3×10^3	$J\,kg^{-1}\,°C^{-1}$
κ_{Tl}	1.3×10^{-7}	5.0×10^{-7}	m^2s^{-1}
κ_{Ts}	9.0×10^{-7}	5.0×10^{-7}	m^2s^{-1}
ν	2.3×10^{-6}	$10^{-2} - 10$	m^2s^{-1}
κ_C	4.0×10^{-10}	$10^{-9} - 10^{-12}$	m^2s^{-1}
ρ_0	1.0×10^3	2.45×10^3	$kg\,m^{-3}$
$\mathcal{L}$	3.1×10^5	5.0×10^5	$J\,kg^{-1}$
α	2.0×10^{-4}	2.5×10^{-5}	$°C^{-1}$
β	1.0×10^{-2}		$(wt\%\,Na_2CO_3)^{-1}$
$\Delta\rho_C$		2.5×10^2	$kg\,m^{-3}$

Table 2.1. Physical constants for aqueous sodium carbonate system at 0°C, obtained from various sources, including Leitch (1985), Woods (1989) and Weast (1971), and for magma chambers (Nilson *et al.* 1985). For the magma chamber, a characteristic density change $\Delta\rho_C$ is listed rather than β, the coefficient of expansion due to variations in composition. An equivalent value for β is given by $\Delta\rho_C/\rho_0\Delta C$.

yields the value $n = 2$ (Nilson *et al.* 1985). In the complete freezing experiments of Leitch (1985), the compositional Rayleigh number $Ra_H = 8 \times 10^9$, while for the stratified solution studied by Huppert *et al.* (1987), $Ra_H = 5 \times 10^{10}$. For an aqueous sodium carbonate solutions just above or within its freezing range, $Le = 330$ and $Sc \sim 6000$, and so the boundary layer for the complete freezing experiments is laminar if the index $n \gtrsim 2$ (Leitch 1985). For the experiments of Huppert *et al.* (1987), Ra_H is also below the critical value for most values of the index n ($n \gtrsim 1.2$). Substantial departures from laminar flow do not occur until Ra_H is much higher than the critical value for the onset of turbulence, and so it is assumed here that the boundary layer flow is laminar in all experiments. It is interesting to note that the ranges of compositional Rayleigh numbers $Le\,Ra_C = O(10^{17} - 10^{22})$ and Schmidt numbers $Sc = O(10^7 - 10^{12})$ for magma chambers are also such that it is unclear whether the flow is laminar or turbulent. The flow is

always laminar if $n \gtrsim 2$ (Leitch 1985). However, the criterion (2.3.21) applies to a fluid of constant viscosity. Magma close to the solid/melt interface is much more viscous than the bulk fluid, and so the boundary layer Reynolds number is smaller, implying that the boundary layer flow is almost certainly laminar (Nilson *et al.* 1985).

When the lighter component of the alloy is preferentially incorporated into the solid, the cooler fluid adjacent to the solidification front becomes enriched in the heavier component and flows downwards. Compositional and thermal buoyancy effects combine constructively to produce a unidirectional boundary layer flow. This occurs in a crystallizing aqueous salt solution of subeutectic composition, where salt is rejected by the solid phase. Similarly, when tholeiitic magmas solidify, heavy components, such as iron, are rejected from the solid phase and the melt adjacent to the interface becomes enriched in the heavier components (McBirney *et al.* 1985). The most famous example of a solidified tholeiitic magma chamber is the Skaergaard Intrusion in east Greenland (McBirney & Noyes 1979).

More interesting fluid dynamically is the case in which the solid formed is rich in the heavier component. This occurs in supereutectic aqueous salt solutions and for fractionating calc-alkaline magmas. The fluid adjacent to the solid/melt interface may be lighter than the bulk fluid, despite being cooler, because it is depleted in the heavy component. In general, density differences due to variations in composition are greater than density differences due to variations in temperature. However, the compositional boundary layer next to the solid/melt interface is typically much narrower than the thermal boundary layer because the chemical diffusivity of composition is generally much smaller than the thermal diffusivity of the melt ($Le \gtrsim 10^2$). The thermal and compositional buoyancy effects compete with each other, the structure of the boundary being determined (Nilson 1985, Nilson *et al.* 1985) by the Lewis number Le and the buoyancy ratio Γ, where Γ is defined by

$$\Gamma = \frac{\alpha \Delta T}{\beta \Delta C} = \frac{Ra_T}{Ra_C}. \tag{2.3.25}$$

The buoyancy ratio Γ represents the relative magnitudes of the thermal and compositional buoyancy forces, while the Lewis number Le represents the relative ranges of influence of thermal and compositional effects. In general, for a crystallizing supereutectic salt solution, or for a calc-alkaline magma chamber, $\Gamma \ll 1$ and $Le \gg 1$. For $\Gamma\, Le^{1/3} \gtrsim 1$, the

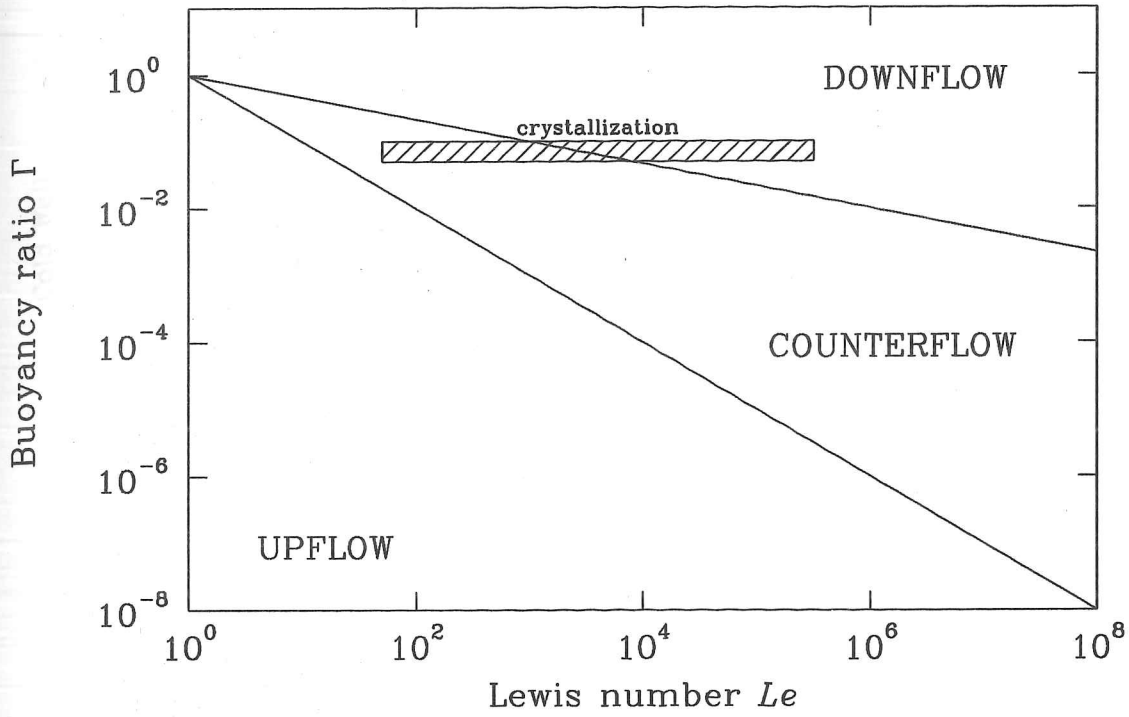

Figure 2.7. Parameter ranges for thermally-dominated downflow, compositionally-dominated upflow and counterflow for the boundary layer adjacent to a solid/melt interface from which light fluid is rejected. The shaded region corresponds to parameter values typical for crystallization in a magma chamber or in the laboratory (after Nilson 1985).

boundary layer flow is thermally dominated and therefore exhibits unidirectional downflow. If $\Gamma Le \lesssim 1$, compositional effects dominate and there is unidirectional upflow. For $Le^{-1} \lesssim \Gamma \lesssim Le^{-1/3}$, the boundary layer exhibits counterflow, with the fluid close to the solid melt interface rising upwards and the fluid farther away sinking downwards. The results of Nilson (1985) and Nilson *et al.* (1985) are presented in Figure 2.7, in which the parameter ranges corresponding to crystallizing magma chambers are represented by the shaded box. The parameter ranges for the complete freezing experiments of Leitch (1985) lie in the left-hand side of the shaded box. For an enclosure in which all boundaries are insulated, with the exception of the cooling wall, the melt cools more rapidly than it becomes compositionally homogenised. Therefore, the buoyancy ratio Γ decreases as solidification proceeds and counter-flow becomes more likely. For a fluid of variable viscosity, Nilson *et al.* (1985) showed that counter-flow is almost certain if the magma viscosity varies by a factor of at least 10^5 from the interior to the boundary.

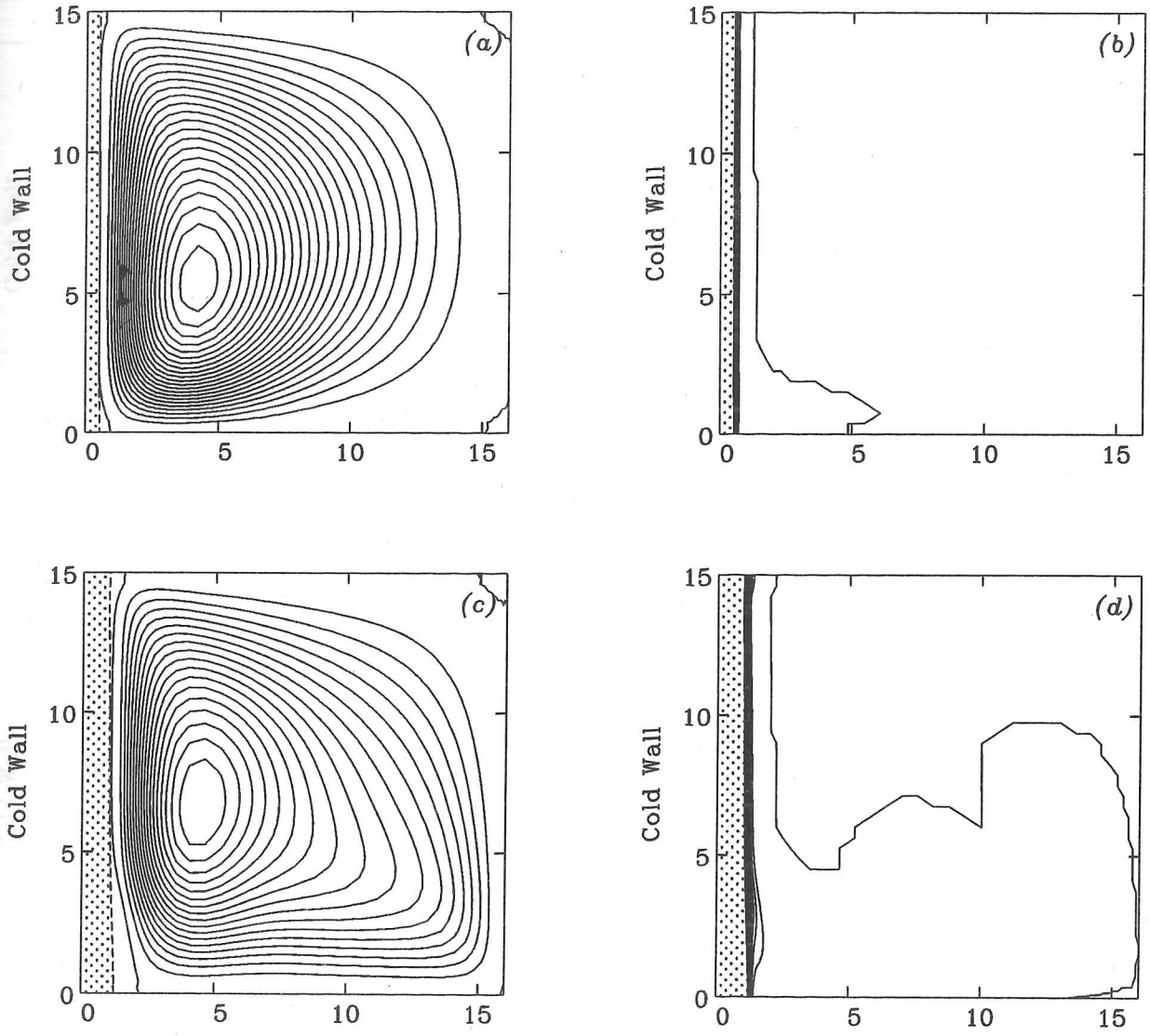

Figure 2.8. Figures (*a*)–(*d*). See end of figure for caption.

Numerical calculations of flow at high Rayleigh numbers are computationally expensive. Indeed, for Rayleigh numbers as high as 10^{15}, or even higher, it is not possible to solve numerically for the flow with the resources currently available. However, although the details differ, the essential physical processes are the same for low and high Rayleigh number flows, providing the flow remains laminar. Figure 2.8 shows the calculated flow and compositional fields at various times during the complete solidification of a supereu-

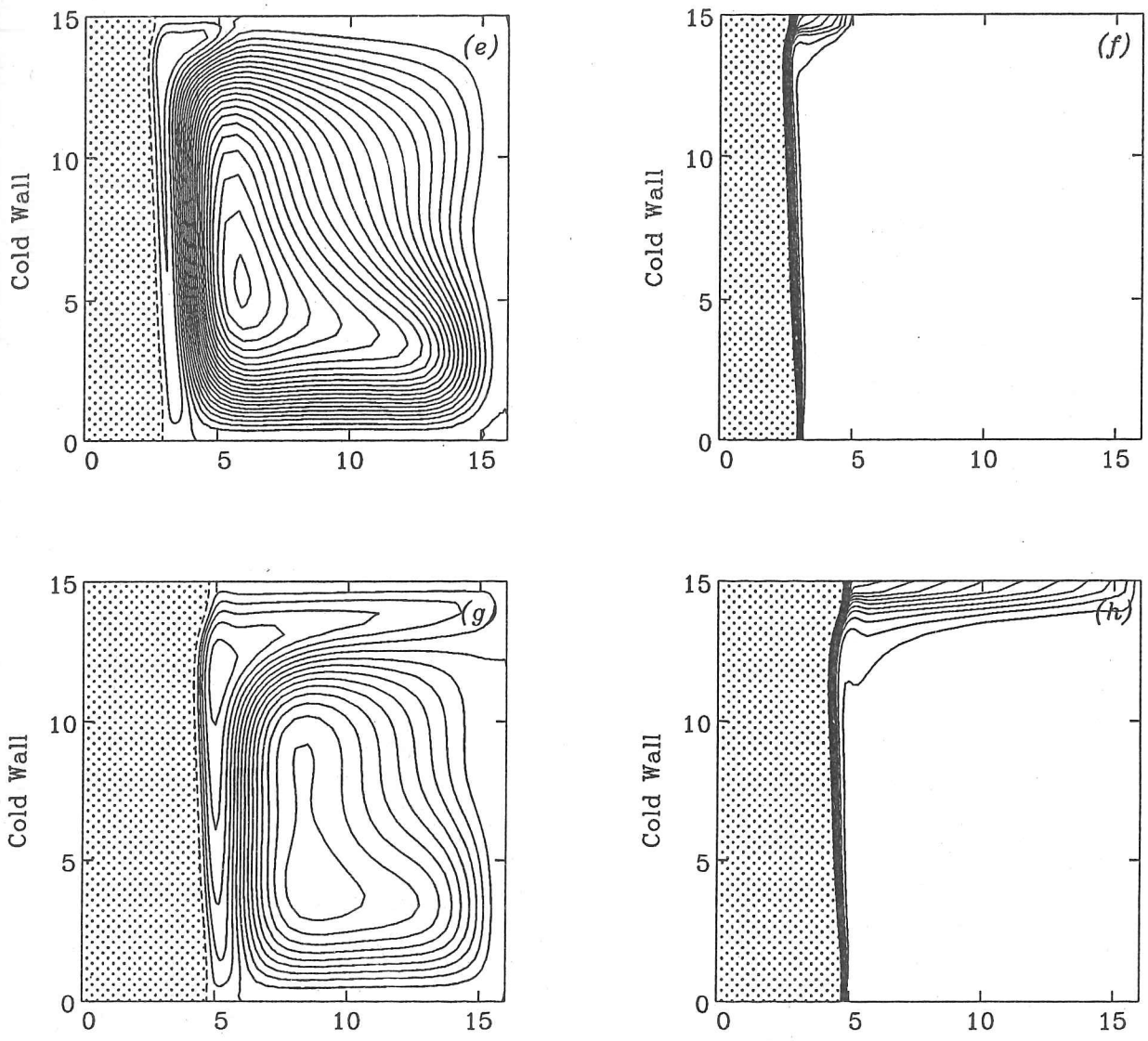

Figure 2.8. Figures (e)–(h). See end of figure for caption.

tectic aqueous sodium carbonate solution. At first, there is a single anti-clockwise thermal convection cell. However, a thin compositionally-dominated boundary layer soon forms towards the base and roof of the tank. Figure 2.8(d) shows a widening in the compositional boundary layer towards the top of the lower compositionally-dominated cell. By $t = 106$ mins., the fluid along the whole of the solidification front is rising. The light fluid intrudes into the interior at the roof of the tank (Figure 2.8(e)) and forms a stratified

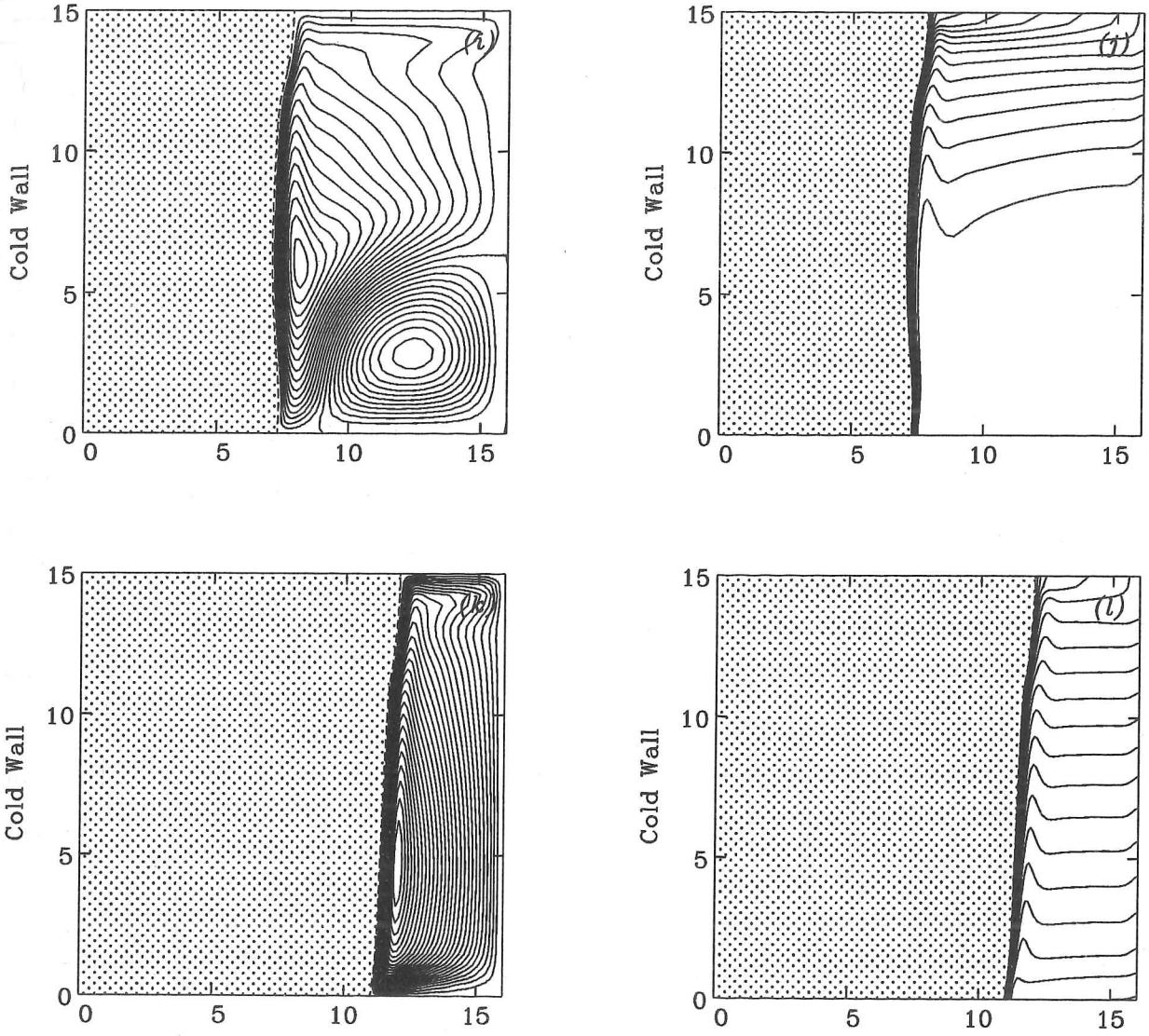

Figure 2.8. Figures (i)–(l). Calculated streamlines and liquid composition for the crystallization of a homogeneous supereutectic sodium carbonate solution, conditions as listed in Table 2.3(a), at times: (a), (b) 7 mins; (c), (d) 27 mins; (e), (f) 106 mins; (g), (h) 210 mins; (i), (j) 7 hours; (k), (l) 14 hours. The axes are marked in cm. At early times, the flow is thermally dominated and anticlockwise. At later times, the flow is dominated by compositional effects and is clockwise.

region (Figure 2.8(h), which grows downwards from the roof of the tank (Figure 2.8(j)). The stratification is strongest towards the roof of the tank, which is typical of a laminar filling-box (Worster & Leitch 1985). For a turbulent filling-box (Turner 1979), the stratification weakens with height.

As the fluid cools, the thermal forcing weakens and the thermal convection cell decays. The compositional cell continues to grow until, by $t = 7$ hrs., the original thermal cell is restricted to the bottom right-hand corner of the tank. Eventually, the convection is wholly compositionally driven and in the clockwise sense (Figure 2.8(k)). The streamline patterns in the upper part of Figure 2.8(i), and in Figure 2.8(k), are similar to those observed by Worster & Leitch (1985) in their laminar filling-box experiments. In the experiments of Worster & Leitch (1985), the convection was purely thermal, being driven by heating at one sidewall of a small rectangular tank. There is a slight inertial overshoot in the boundary layer and a double flow reversal in the horizontal direction at the top-right of the tank. Similar features were observed by Thompson & Szekely (1987), who associated the flow reversal with the formation of a double-diffusive cell. In fact, such features are entirely typical of single-component laminar free convection (Worster & Leitch 1985).

Complete freezing experiments conducted by Leitch (1985, 1987) and Huppert *et al.* (1987) have demonstrated that the compositional stratification in the solid is strongly dependent upon convective transport in the melt. Contours of solid composition obtained experimentally by Leitch (1985) for the complete freezing of a supereutectic aqueous sodium carbonate solution are presented in Figure 2.9. Typically, the solid formed earliest has composition close to that of the melt from which it originates. As the experiments proceed, the solid growth rate $\dot{h}$ decreases. In the absence of convection, the compositional boundary layer thickens diffusively with time so that the compositional flux from the melt $F_C \sim t^{-1/2}$. Since the growth rate $\dot{h} \sim t^{-1/2}$ also, equation (2.3.21) implies that the solid composition remains constant. However, when the fluid is convecting, the compositional boundary layer has approximately constant thickness after a brief period of growth (Patterson & Imberger 1980). There is no visible thickening of the compositional boundary layer after the first half hour of the calculation (Figures 2.8(d)–(l)). Hence, the compositional flux is maintained and so the solid composition increases with distance away from the cold wall as the growth rate decreases. The bulk fluid is continously being

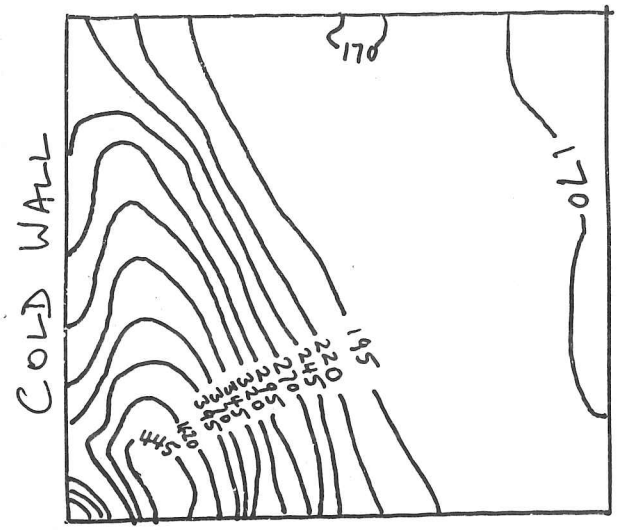

Figure 2.9. Contour plot of solid composition for the complete freezing of a homogeneous supereutectic aqueous sodium carbonate solution. The experimental conditions are listed in Table 2.3(a). The contours are labelled in kg Na_2CO_3 m^{-3}. As a guide, 170 kg m^{-3} is equivalent to 6.2 wt% Na_2CO_3 (C_E) and 445 kg m^{-3} is equivalent to 16.2 wt% Na_2CO_3. The solid composition was measured by cutting the solid up into sections and allowing them to melt. The solid block has length 16 cm and depth 15 cm (traced from original figure of Leitch 1985).

depleted of heavy component as it passes through the compositional boundary layer. In addition, the compositional boundary layer thickens as it rises, and so the compositional flux F_C decreases with height. Therefore, the solid composition decreases with height above the floor of the enclosure. Consequently, contours of equal solid composition slope upwards away from the cold wall.

As the experiment proceeds, the light fluid descends from the roof of the enclosure (Figure 2.8(j)). This is reflected in the composition of the solid further from the cold wall. Starting at the roof of the enclosure, the solid composition begins to decrease away from the cold wall, and the contours in Figure 2.9 begin to dip downwards away from the cold wall. Eventually the entire tank becomes stratified and the solid composition decreases away from the cold wall at all heights. Therefore, a maximum in solid composition occurs at the floor of the tank. The position of the maximum with respect to the cold wall corresponds to the thickness of solid grown when the stratified layer in the fluid reaches the base of the tank. For the remainder of the experiment, the solid composition decreases

monotonically as the liquid is gradually depleted of solute. The final solid formed has eutectic composition. Note that for a subeutectic aqueous salt solution (see Figure 2.18 in §2.4), the boundary layer flow is downwards and so the stratified region grows from the floor of the tank. Therefore, a minimum in solid composition occurs at the roof of the enclosure.

The distance of the maximum (or minimum) in solid composition away from the cold wall depends primarily upon the ratio of the timescale t_{BF} for box-filling to the timescale t_S for solidification. The solidification timescale t_S is given by equation (2.3.22) above. To determine the box-filling timescale t_{BF}, we must analyse the compositional boundary layer close to the solidification front. If the thickness of the boundary layer is very much less than the height of the tank, we may make the usual boundary layer approximation in which variations with respect to x are very much greater than variations with respect to y. Ignoring thermal effects, equations (2.3.13) and (2.3.15) become

$$\frac{1}{Pr}\left(\frac{\partial \omega}{\partial t} + u\frac{\partial \omega}{\partial x} + v\frac{\partial \omega}{\partial y}\right) = -Ra_C\frac{\partial C}{\partial x} + \frac{\partial^2 \omega}{\partial x^2}\,; \tag{2.3.26}$$

$$\frac{\partial C_l}{\partial t} + u\frac{\partial C_l}{\partial x} + v\frac{\partial C_l}{\partial y} = \frac{1}{Le}\frac{\partial^2 C_l}{\partial x^2}\,, \tag{2.3.27}$$

where

$$\omega = \frac{\partial v}{\partial x} \tag{2.3.28}$$

and

$$\frac{\partial u}{\partial x} + \frac{\partial v}{\partial y} = 0\,. \tag{2.3.29}$$

At first, the fluid velocity is negligible and the compositional boundary layer grows diffusively (Patterson & Imberger 1980). Therefore, the compositional boundary layer has thickness

$$\delta_C \sim Le^{-1/2}t^{1/2}\,. \tag{2.3.30}$$

The momentum equation (2.3.26) is dominated by a balance between buoyancy and vis-

cous forces, and so

$$\frac{\omega}{\delta_C^2} \sim \frac{Ra_C}{\delta_C} . \tag{2.3.31}$$

Equations (2.3.28) and (2.3.31) imply that the upward velocity v is given by

$$v \sim \omega \delta_C \sim Ra_C \delta_C^2 . \tag{2.3.32}$$

The compositional boundary layer continues to grow diffusively until the advective terms in (2.3.27) become of equal magnitude to the diffusion term. This occurs when

$$\frac{v}{y} \sim \frac{1}{Le} \frac{1}{\delta_C^2} , \tag{2.3.33}$$

i.e. when the compositional boundary layer has reached thickness

$$\delta_C \sim \left(\frac{y}{Ra_C Le} \right)^{1/4} \tag{2.3.34}$$

and the magnitude of the upward velocity is

$$v \sim \left(\frac{y Ra_C}{Le} \right)^{1/2} . \tag{2.3.35}$$

This occurs at the nondimensional time $\tau \sim (y\, Le/Ra_C)^{1/4}$. Therefore, a steady state in which advection of composition towards the wall balances diffusion of composition away from the wall is reached very rapidly for high Rayleigh numbers. For $t_s \gg \tau$, we may consider the boundary layer flow to be quasi-steady for most of the solidification process. However, we also require the rate of growth of the solid to be small compared with typical values of the normal velocity u in the boundary layer. For situations in which the solid growth rate is large, the thickness of the compositional boundary layer is determined by a balance between diffusion away from the solidification front and the flux of fluid into the solid phase as the boundary layer fluid solidifies. The validity of our assumption that the boundary layer flow is determined by a balance between advection and diffusion is examined below, *a posteriori*.

The flux of light fluid intruding into the interior at the top of the tank is given by $v\delta_C$, measured at the base of the stratified fluid layer (Worster & Leitch 1985). The initial nondimensional volume of the fluid-filled enclosure is $\mathcal{A}$. Therefore, we define the box-filling timescale to be $t_{BF} \sim \mathcal{A}/v\delta_C$. Here, t_{BF} may exceed t_S, the timescale for solidification. However, the size of the fluid region decreases as solidification proceeds and so box-filling always occurs before the alloy becomes entirely solid. Nevertheless, for the bulk of the solidification process, the box-filling rate is characterised by the timescale t_{BF}. Therefore, substituting for v and δ_C from (2.3.35) and (2.3.34), we obtain

$$t_{BF} \sim \mathcal{A}^{1/4} Le^{3/4} {Ra_C}^{-1/4}, \tag{2.3.36}$$

and so the ratio of box-filling and solidification timescales is

$$\frac{t_{BF}}{t_S} \sim \mathcal{A}^{1/4} \left(\frac{Le^{3/4} {Ra_C}^{-1/4}}{\widehat{St}} \right). \tag{2.3.37}$$

Now, the nondimensional flux of composition from the fluid into (or out of) the solid is given by

$$F_C \sim \frac{1}{Le} \frac{1}{\delta_C}. \tag{2.3.38}$$

From equation (2.3.21), we see that the difference $\Delta C_s = |C_s - C_E|$ between the solid composition and the eutectic composition is

$$\Delta C_s \sim \frac{F_C}{\dot{h}}. \tag{2.3.39}$$

If the thermal flux from the melt is neglected, equation (2.3.20) implies that the solid growth rate $\dot{h} \sim (\widehat{St}\, h)^{-1}$ when the solid thickness is h. Therefore, substituting from (2.3.34) for δ_C into (2.3.38), we obtain

$$\Delta C_s \sim \frac{h}{y^{1/4}} \left(\frac{Le^{3/4} {Ra_C}^{-1/4}}{\widehat{St}} \right)^{-1}. \tag{2.3.40}$$

Equation (2.3.40) implies that, before box-filling occurs, the absolute difference between the solid composition and the eutectic composition increases with distance away from

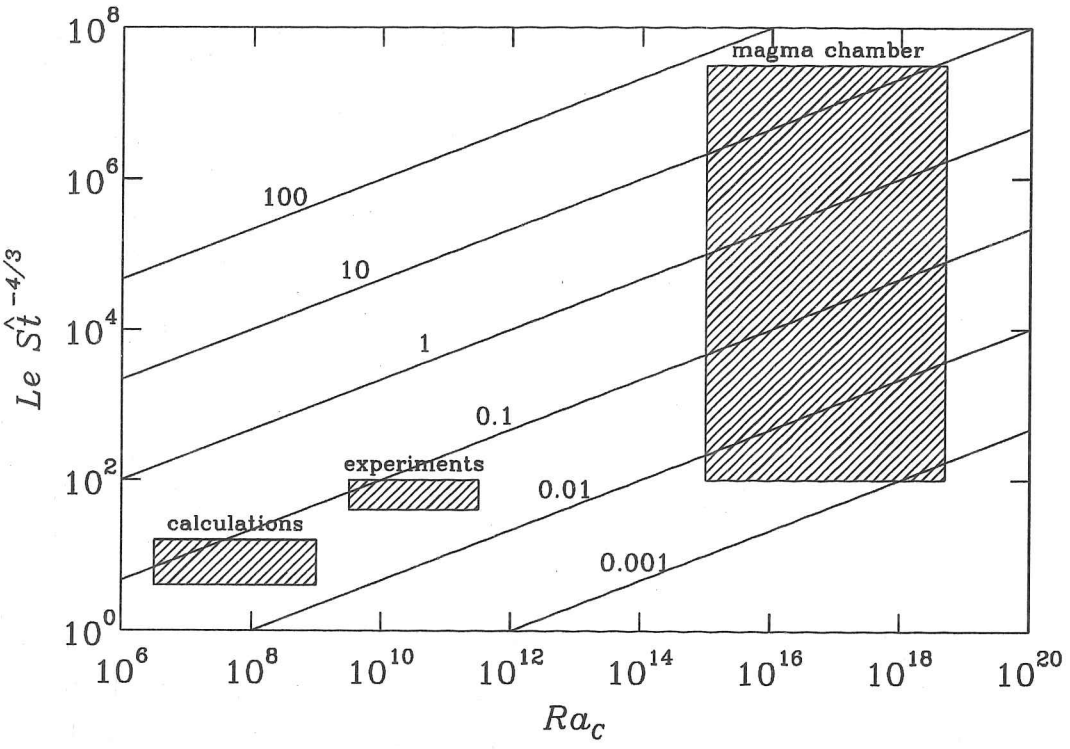

Figure 2.10. Contours of the parameter P, defined by equation (2.3.41), for a range of values of the compositional Rayleigh number Ra_C and $Le\,\widehat{St}^{-4/3}$, where Le is the Lewis number and $\widehat{St}$ is the modified Stefan number (see equation (2.3.22)). The aspect ratio $\mathcal{A} = 1$. Curves are plotted for $P = 0.001$, 0.01, 0.1, 1, 10 and 100, where the parameter P represents the ratio of timescales for box-filling and solidification. Small values of P correspond to rapid rates of box-filling and a high degree of compositional stratification. Shaded areas represent parameter values typical of magma chambers (dimension $\sim$ 1 km), the laboratory experiments of Leitch (1985, 1987) and Huppert *et al.* (1987), and the numerical calculation presented in this chapter.

the cold wall and decreases in the downstream direction, as observed in experiments (Figure 2.9). We therefore see that the widening of the compositional boundary layer in the downstream direction leads to vertical stratification in the solid even when the bulk fluid is homogeneous. The solid towards the base of the chamber becomes enriched in heavy component, independent of the direction of boundary layer flow, as long as it is compositionally dominated or counterflowing.

Comparison between equations (2.3.37) and (2.3.40) reveals that both qualitative and quantitative agreement can be expected between magma chambers with $Ra_C \sim 10^{15}$, laboratory experiments with $Ra_C \sim 10^{11}$ and numerical calculations with $Ra_C \sim 10^7$,

provided that the combination of parameters

$$P = \frac{\mathcal{A}^{1/4} Le^{3/4} {Ra_c}^{-1/4}}{\widehat{St}} \tag{2.3.41}$$

is the same in all three cases. Larger values of P correspond to relatively slow box-filling, due to rapid solidification ($\widehat{St} \ll 1$), weak convection, a thin compositional boundary layer ($Le \gg 1$), or a tall chamber geometry ($\mathcal{A} \gg 1$). For $P \gg 1$, the fluid is largely homogeneous and the compositional stratification in the solid is determined by boundary layer thickening and the gradual reduction in the growth rate of the solid. Therefore, the solid is enriched in the heavier component towards the base of the tank and the solid composition approaches the appropriate equilibrium end-member with distance away from the cold wall. Consequently, the contours of solid composition dip downwards away from the cold wall for a subeutectic aqueous sodium carbonate solution and slope upwards for a supereutectic solution. For $P \ll 1$, box-filling is rapid and the fluid composition gradually approaches the eutectic as solidification proceeds. The fluid is heaviest at the base of the tank. The solid composition reflects the fluid composition and approaches the eutectic as one moves away from the cold wall. Therefore, for a subeutectic aqueous sodium carbonate solution, the contours slope upwards. For a supereutectic solution, the contours slope downwards. For the complete solidification of an alloy, the compositional layering in the solid must exhibit both types of behaviour. At first, the fluid is homogeneous and so the solid composition is determined by the thickening of the compositional boundary layer and the decreasing rate of growth of the solid. Eventually, however, the fluid must evolve everywhere towards the eutectic composition to conserve mass, and the solid composition is then determined by the box-filling process. The parameter P determines the relative durations of each style of behaviour.

The above scaling analysis is valid if the solid growth rate $\dot{h} \ll u$. The incompressibility condition (2.3.29) implies that $u \sim v\delta_c/y$. The solidification rate $\dot{h} \sim 1/\widehat{St}\, h$, where h is the solid thickness. Therefore, substituting from (2.3.34) and (2.3.35) for δ_c and v, we see that $\dot{h} \ll u$ when

$$\frac{y^{1/4}}{h}\left(\frac{Le^{3/4} {Ra_c}^{-1/4}}{\widehat{St}}\right) \ll 1\,. \tag{2.3.42}$$

Therefore, the effect of the moving boundary upon the boundary layer is negligible if $P \ll h$. Note that this restriction applies only to the quantitative predictions of the

scaling analysis. Qualitative descriptions in this section of the compositional stratification in the solid remain correct.

Figure 2.10 shows how P varies with $Le\widehat{St}^{-4/3}$ and Ra_c when the aspect ratio is unity ($\mathcal{A} = 1$). Shaded boxes in Figure 2.10 represent typical parameter regimes for magma chambers of dimension ~ 1 km, for the experiments conducted by Leitch (1985, 1987) and Huppert *et al.* (1987), and for the numerical calculations presented below in §2.4. Magma chambers are characterised by high Lewis and Rayleigh numbers. However, for the higher values of the Lewis number ($Le \gtrsim 10^4$), the boundary layer flow will be thermally dominated (Figure 2.7) and significantly affected by the moving boundary ($P \gtrsim 1$). The scalings outlined above are not valid therefore for the top half of the figure. We see that the range of values of P is the same (0.01–0.1) for the experiments of Leitch (1985, 1987) and Huppert *et al.* (1987) as for a magma chamber of dimension ~ 1 km. The parameter P is sufficiently small* for the scaling analysis presented above to be valid for most of the solidification process. The experiments of Leitch (1985, 1987) and Huppert *et al.* (1987) were designed so that the compositional Grashof number $Gr_c = Ra_c/Pr$ was the same for the experiments as for a typical magma chamber. This choice of scaling leads to similar fluid dynamical behaviour in the limit $Pr \to \infty$, but has no direct bearing upon the solid composition. We have been able to show, with the scaling analysis presented here, that some confidence can also be expressed in their experimental results for the solid stratification. Equally, numerical calculations performed at low values of the Lewis and Rayleigh numbers can exhibit similar values of P and therefore can be confidently expected to agree with the experiments. In §2.4, some of the experiments of Leitch (1985) and Huppert *et al.* (1987) are modelled numerically and similarities and differences are discussed.

To confirm the validity of the scaling represented by the parameter P, three calculations were performed, for the parameters listed in Table 2.2. Cross-sections of the solid composition at the base of the tank, the mid-depth $\mathcal{A}/2$ and the roof of the tank are plotted in Figure 2.11. Two of the runs were for the same value of P (solid and dotted lines), while the third run had a higher value of P (dashed line). At the base of the tank, and at the mid-depth (Figures 2.11(a), (b)), there is excellent agreement between the two runs with the same value of P. For the higher value of P, box-filling occurs later and the maximum solid composition is lower, as suggested by equations (2.3.37) and

* However, if the aspect ratio $\mathcal{A} \ll 1$, most solidification in a magma chamber may occur on horizontal boundaries, in which case the model presented here will be invalid despite P being small.

	Ra_T	Ra_C	Le	P	$C_{\max}$ wt% Na_2CO_3	$x_{\max}$ cm
(i)	6.6×10^6	3.9×10^7	30	0.021	20.5	5.9
(ii)	1.6×10^7	9.1×10^7	40	0.021	20.3	6.0
(iii)	6.6×10^6	3.9×10^7	40	0.025	17.4	6.8

Table 2.2. Nondimensional parameters Ra_T, Ra_C and Le for three simulations conducted to demonstrate the dependence of the final solid composition upon $P = Le^{3/4} Ra_C{}^{-1/4} \hat{St}^{-1}$, where $\hat{St} = 8$ for all three runs. All other constants are as for the complete freezing of a homogeneous supereutectic Na_2CO_3 solution (Leitch 1985), and are given in Tables 2.1 and 2.3(*a*). Also listed here are the maximum solid composition $C_{\max}$ and the distance $x_{\max}$ of the maximum from the cold wall. The maximum occurs at the base of the tank in all cases.

(2.3.41) respectively. At the roof of the tank, there is no such agreement. The boundary layer theory presented above assumes that the compositional boundary layer continues to entrain as it rises. Consequently the boundary layer thickness $\delta_C \sim y^{1/4}$ (equation (2.3.34)). However, at the roof of the tank, the boundary layer must detrain, with the rising fluid intruding horizontally into the interior. Therefore, the scaling (2.3.41) for the solid composition is not valid at $y = \mathcal{A}$. It is interesting to note the quality of agreement at the base of the tank, since the boundary layer theory is strictly not valid there because of the presence of the lower boundary. Note also that thermal convection is not absent from the calculations presented in Figure 2.11, further demonstrating the robustness of the scaling analysis presented above.

In the numerical calculations, high-Rayleigh-number situations are modelled by conducting calculations at lower Lewis numbers. Reducing the Lewis number increases the influence of the compositional buoyancy force over the thermal buoyancy force (Figure 2.7). Therefore, when thermal effects are important, calculated box-filling rates are likely to be slightly more rapid than those observed experimentally. However, thermally-dominated upflow is less likely than Figure 2.7 suggests. Weak turbulence in the boundary layer can enhance the diffusive transport of composition and so the effective Lewis number is much lower than that suggested by the molecular diffusivity of composition (Leitch 1985).

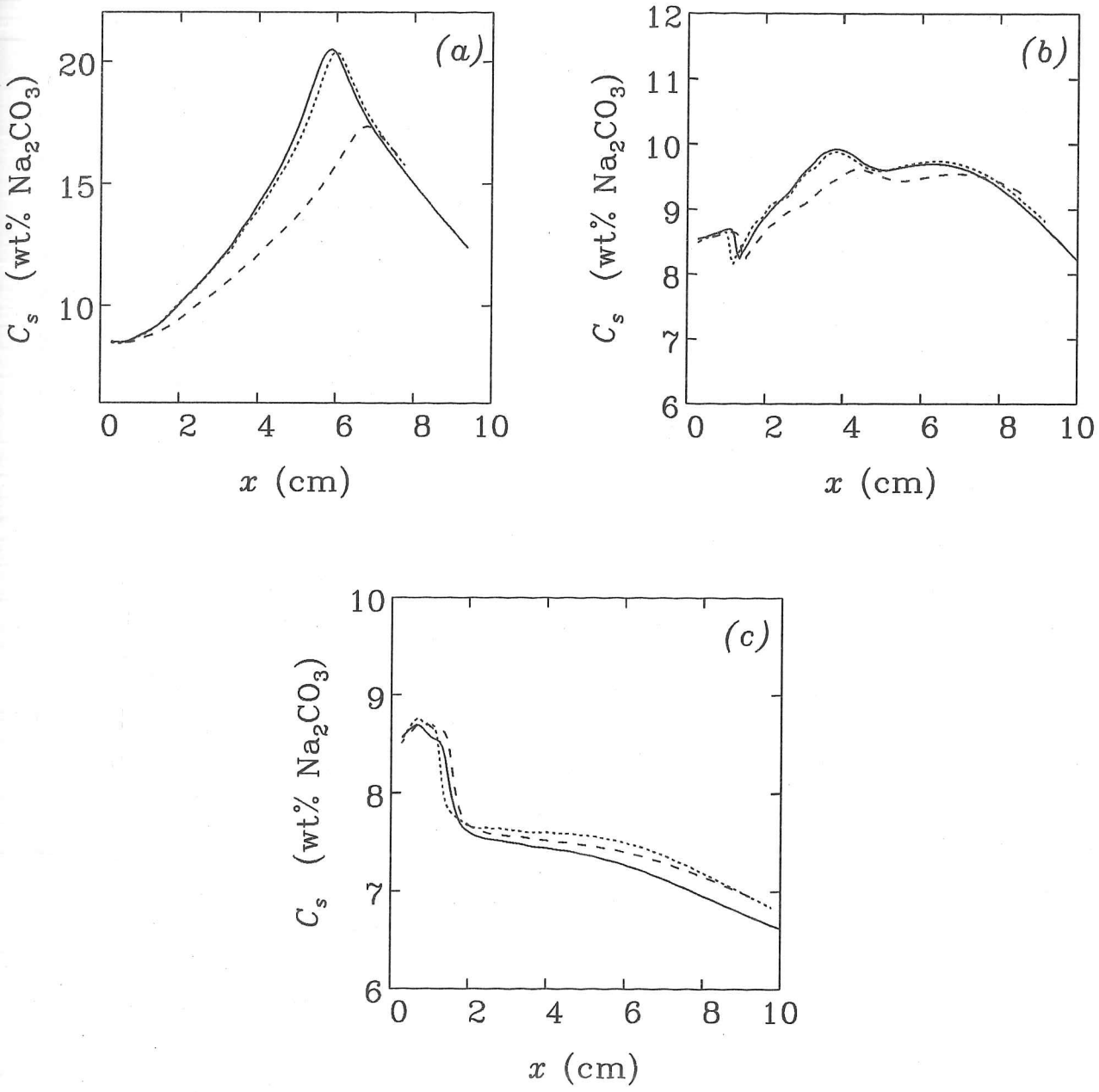

Figure 2.11. Cross-sections of solid composition calculated for an initially homogeneous supereutectic aqueous sodium carbonate solution at (*a*) the base of the tank, (*b*) the mid-height $H/2$ and (*c*) the top of the tank. The three lines are for three different sets of values of Le, Ra_T and Ra_C (as listed in Table 2.2): —— (*i*); ····· (*ii*); – – –(*iii*). The values of $P = Le^{3/4} Ra_C{}^{-1/4} \widehat{St}^{-1}$ for (*i*) and (*ii*) are the same.

The scaling analysis presented in this section applies only to the growth of a binary alloy in the eutectic regime. The scaling (2.3.34) of the boundary layer thickness is dependent upon the absence of a suitable length scale in the x-direction. For rapid solidification rates ($P \gg h$), a length scale is provided by the (dimensional) rate of advance $\dot{h}$ of the solid/melt interface and the compositional diffusivity κ_C. The diffusion of composition towards (or away from) the solidification front is balanced by the rate at which the solid incorporates (or rejects) composition. The compositional boundary layer has approximately constant thickness and there is little or no variation in composition with height. Consequently, contours of solid composition lie almost parallel to the solidification front. The analysis is also invalid for dendritic crystal growth, in which the transport of composition is controlled by the permeability of the porous mush (Lowell 1985).

Similar compositional stratification has been observed by Hebditch (1975) in experiments with lead–tin (Pb–Sn) castings. For metallurgical systems, however, the solid/melt interface is rarely planar and in the experiments of Hebditch (1975) the solidification was dendritic in nature. However, the similarity between the experimental results of Leitch (1985) and Hebditch (1975) serves to demonstrate that the qualitative nature of the solid stratification is independent of the particular mechanism by which the solid is formed, so long as the composition of the solid reflects the composition of the liquid into which it is growing.

2.4 Numerical results

Three representative problems are discussed here, all motivated by experiments with aqueous sodium carbonate solutions (Leitch 1985, Huppert *et al.* 1987). The first is the complete freezing of an initially homogeneous supereutectic solution; the second the complete freezing of an initially homogeneous subeutectic solution; and the third the partial solidification of two enclosures of differing dimensions, filled with a compositionally stratified supereutectic solution. The values of the various physical constants which are common to all experiments are listed in Table 2.1, while those that differ between experiments, most notably the box dimensions and the initial composition, are presented in Table 2.3. Those nondimensional parameters which are common to all experiments are $Pr = 17.7$, $\gamma = 6.9$, $Le = 330$ and $St = 40$. The Stefan number is based on a reference temperature difference $\Delta T = 2.1\,^{\circ}C$.

The compositional Rayleigh numbers for the experiments are rather large (10^9–10^{11}) for direct numerical calculation. In §2.3.2, it was shown that solidification of a binary alloy for laminar, compositionally-dominated flow at high Lewis and Rayleigh numbers can be modelled by calculations at lower Lewis and Rayleigh numbers, provided that P, defined by (2.3.41) remains unaltered.

2.4.1 Homogeneous supereutectic solution

The experiment first chosen for comparison with numerical solutions was conducted by Leitch (1985), and is also discussed in Huppert *et al.* (1987). A tank 16 cm long and 15 cm deep was filled with a compositionally homogeneous supereutectic aqueous sodium carbonate solution and completely frozen by cooling from one vertical sidewall. The solid product was then cut up and analysed to determine the distribution of the solute Na_2CO_3. The experimental conditions are listed in Table 2.3(a), with the exception of the temperature at the cold wall. In general, it is not possible to maintain a constant temperature at the cold wall throughout such an experiment. For this particular experiment (and for the complete freezing of a homogeneous subeutectic solution, described below), records are available of the cold wall temperature (Leitch 1985). The time evolution of

	Ra_T	Ra_C	C_0 wt% Na_2CO_3	T_0 °C	L cm	H cm	t_{ref} hrs
(a)	5.4×10^7	8.1×10^9	8.8	18	16	15	54.7
(b)	5.4×10^7	8.1×10^9	4.0	22	16	15	54.7
(c)	1.0×10^8	1.6×10^{10}	6.2 – 13.0	15.5	20	30	85.5
(d)	2.8×10^9	4.2×10^{11}	6.2 – 13.0	15.5	60	30	769.2

Table 2.3. Experimental values for thermal and compositional Rayleigh numbers Ra_T and Ra_C, initial composition C_0, initial temperature T_0, length L and depth H of box, and dimensional timescale $t_{\rm ref} = L^2/\kappa_{Tl}$ for *(a)* complete freezing of homogeneous supereutectic solution (Leitch 1985); *(b)* complete freezing of homogeneous subeutectic solution (Leitch 1985); *(c)* partial freezing of smaller volume of stratified supereutectic solution (Huppert *et al.* 1987); and *(d)* partial freezing of larger volume of stratified supereutectic solution (Huppert *et al.* 1987). Ra_T and Ra_C are based on reference values $\Delta T = 2.1\,°\mathrm{C}$ and $\Delta C = 6.2$ wt% Na_2CO_3 respectively.

the dimensional temperature at the cold wall is approximated here by

$$T_C = [-36 + 26\exp(-t/t_0)]\,°\mathrm{C}\,, \tag{2.4.1}$$

where $t_0 \sim 2$ hours is the timescale for the reduction in the temperature to its minimum of around $-36\,°C$. The experiment took just under 24 hours to complete.

A contour plot of the composition of the solid product was presented above (Figure 2.9), in §2.3.2. From the version of Figure 2.9 given in Huppert *et al.* (1987), graphs of solid composition versus distance from the cold wall can be constructed for various heights above the base of the tank (Figure 2.12). The effect of convective motions upon the solid composition is evident from Figures 2.9 and 2.12. If convective transport were unimportant, there would be no variation in solid composition with height y, and consequently the contours of composition would lie parallel to the solidification front.

Numerical calculations were performed at the reduced Lewis number $Le = 33$ and reduced Rayleigh numbers $Ra_T = 5.4 \times 10^4$ and $Ra_C = 8.1 \times 10^6$, as suggested by the definition (2.3.41) of the scaling parameter P. The results are plotted in Figure 2.13. The qualitative features of the experimental results of Leitch (1985) have been reproduced

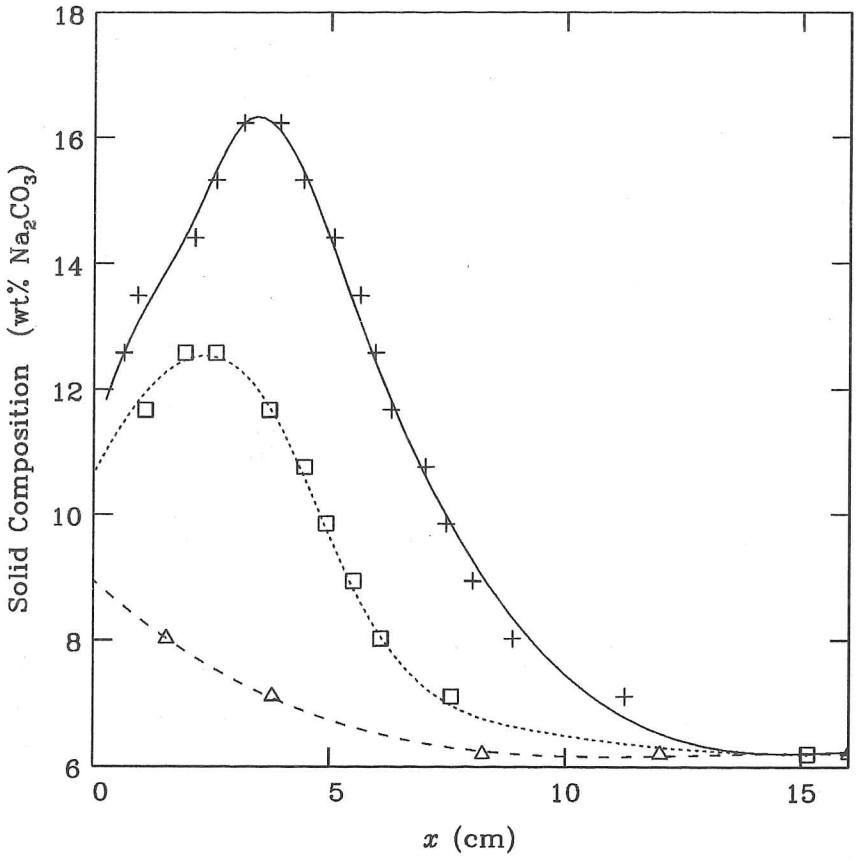

Figure 2.12. Cross-sections of solid composition at the base of the tank (———), the mid-height $H/2$ ($\cdots\cdots$) and the top of the tank ($- - -$) for the complete freezing of a homogeneous supereutectic aqueous sodium carbonate solution. Data points are denoted by + at the base, □ for the mid-height and △ for the top of the tank. Experimental conditions as listed in Table 2.3(a). Figure constructed from the data of Leitch (1985).

successfully — the maximum in solid composition at the base of the tank; the initial increase in composition, followed by a decrease in composition, with distance from the cold wall; and the decrease in composition with height above the base of the tank. However, the numerical and experimental values of solid composition do not tally and the predicted position of the local maximum is too far from the cold wall.

One interesting feature of Figure 2.13(b) is the rapid drop in solid composition between 1 and 2 cm from the far wall at the mid-height $H/2$ (dotted line in Figure 2.13(b)). This is reflected in Figure 2.13(a) by the thin elliptical contour towards the left of the figure and is due to the growth of the inner, compositionally dominated boundary layer. As

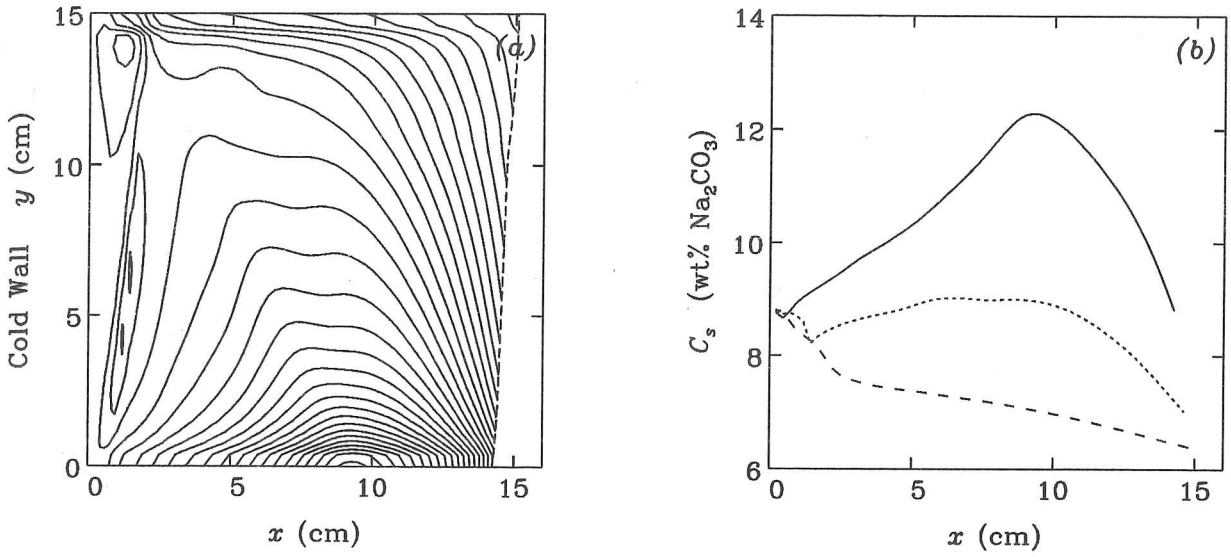

Figure 2.13. Calculation for the complete freezing of a homogeneous supereutectic sodium carbonate solution (Table 2.3(a)). Solid composition is presented (a) as a contour plot, and (b) in cross-sections at various heights: ——— base of tank; · · · · · · mid-height $H/2$; – – –top of tank.

described in §2.3 (see Figure 2.8), this layer initially appears as a small triangular cell at the solid/melt interface at the base of tank. Towards the top of this cell, there is a small region where flow is away from the interface. At this position, the compositional flux F_C is substantially reduced by the advective transport of composition away from the solidification front. As the compositional cell grows, this outflow region moves up the interface. Figure 2.14 shows the evolution of solid composition with time for the heights $H/4$, $H/2$ and $3H/4$. At very early times, the convection is thermally dominated, and so the boundary layer is thickest at the base of the tank. Hence, the solid composition increases with height above the base. There then follows a rapid drop in C_s, first at $H/4$ and last at $3H/4$. This drop corresponds to the top of the embryonic compositionally dominated cell reaching each height in turn. By $t = 30$ minutes, the solid composition everywhere decreases with height y. The boundary layer flow is now compositionally dominated and the compositional boundary layer thickens as it rises. This leads to a decrease in compositional flux with height.

In the calculation, box-filling occurs at a dimensional time of around 11 hours, when only 65% of the volume of the tank is still liquid. This agrees with the timescale $t_{\text{BF}} \sim$

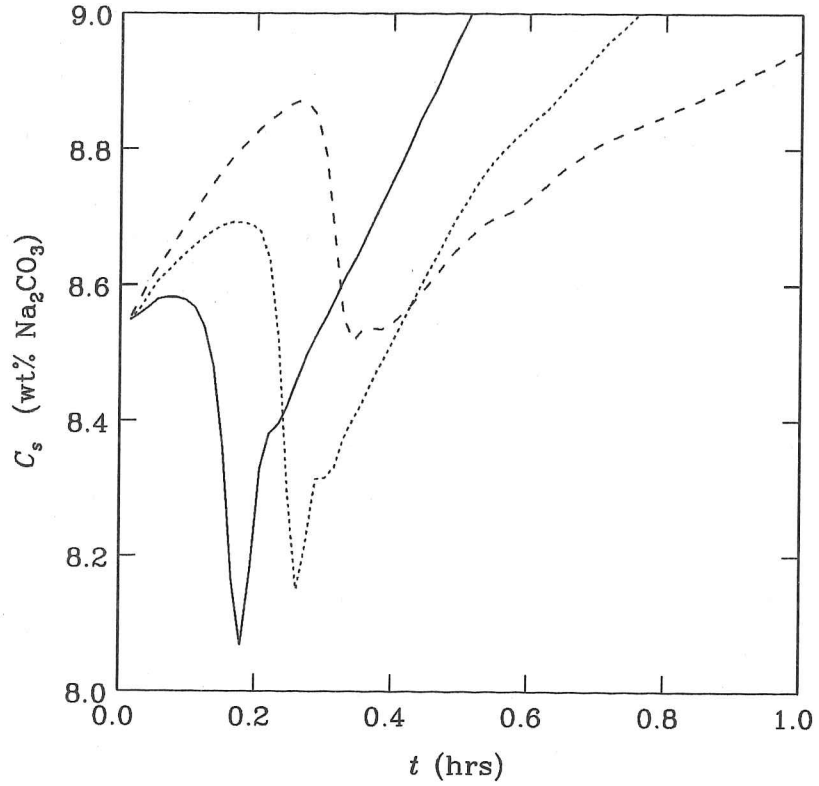

Figure 2.14. Solid composition calculated for an initially homogeneous supereutectic sodium carbonate solution (Table 2.3(a)) at heights $H/4$ (——), $H/2$ (· · · · ·) and $3H/4$ (– – –) to demonstrate the monotonic increase in solid composition with height at early times; the sharp drop in solid composition associated with the growth of the compositionally dominated convection cell; and the monotonic decrease in solid composition with height at later times.

13 hours predicted by the modified laminar box-filling model of Leitch (1985), which took account of the decrease in the volume of fluid as the alloy solidified. However, in the experiments, box-filling was observed to occur after only 5 hours (Leitch 1985). Moreover, the remaining volume of fluid is greater (70%) in the experiments than for the simulation (35%) as less solid has grown. Therefore, the stratification occurs over 4 times more rapidly in the experiment than is predicted by laminar box-filling theory. This disparity is recognised by Leitch (1985), who proposed that it is due to the roughness of the solid/melt interface. Hydrated sodium carbonate crystals ($Na_2CO_3.10H_2O$) are much larger than ice crystals and the solid/melt interface has a craggy appearance. The crystals therefore present a greater surface area than they would if the interface were

planar, and so the rate of release of light fluid is increased. An alternative explanation is that the rate of diffusion of composition in the compositional boundary layer is enhanced by turbulent diffusion. Fluid released from the upper surface of a protruding crystal would rise in a plume until entrained into the general boundary layer flow (Leitch 1985). Consequently, the boundary layer exhibits weakly turbulent behaviour. This enhances the lateral diffusion of composition and thickens the compositional boundary layer, thereby increasing the upward flux of light, fractionated fluid.

2.4.2 Homogeneous subeutectic solution

The solid/melt interface for the solidification of a subeutectic aqueous sodium carbonate solution is typically much smoother than the solid/melt interface for a solidifying supereutectic solution. As the solution cools, ice preferentially forms, with molecules of Na_2CO_3 incorporated into the crystal matrix. The solidification front is smoother for the subeutectic solution principally because ice crystals are much smaller than hydrated sodium carbonate crystals. Consequently, we expect better agreement between experiments and the planar interface, laminar flow theory presented here. The fluid adjacent to the solidification front is cold and rich in solute, and therefore heavy. Thus the boundary layer flow is downwards at all times. A stratified layer of heavy fluid intrudes into the interior at the base of the tank. The heavy layer grows as solidification proceeds, until the whole tank is compositionally stratified.

A complete freezing experiment for a homogeneous subeutectic aqueous sodium carbonate solution was conducted by Leitch (1985), under the conditions listed in Table 2.3(*b*). Figure 2.15 shows a contour plot of the solid composition for the experiment. Instead of a maximum in solid composition at the base of the tank, there is now a minimum in solid composition at the roof. The minimum composition is 60 kg Na_2CO_3 m^{-3}, which is equivalent to 2.1 wt% Na_2CO_3. The position of the minimum corresponds to the box-filling time t_{BF} as before; this time there is agreement with the theoretical value (Leitch 1985), unlike for the experiment with a supereutectic solution.

For this experiment, the cold wall took longer to drop to its minimum temperature. Using the original data of Leitch (1985) for the cold wall temperature, T_C is approximated

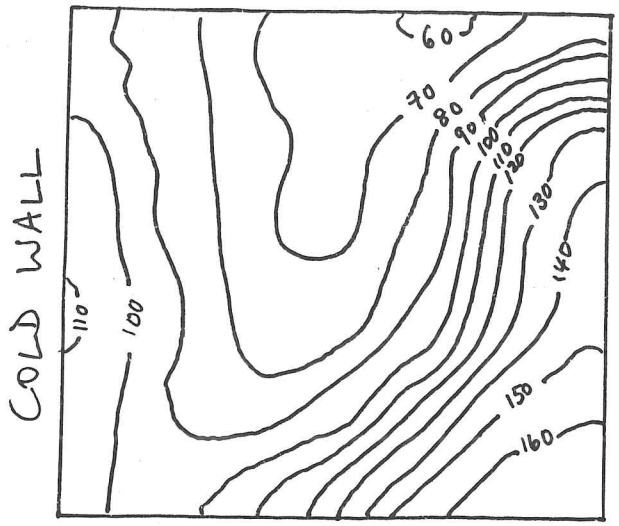

Figure 2.15. Contour plot of solid composition for the complete freezing of a homogeneous subeutectic aqueous sodium carbonate solution. The experimental conditions are listed in Table 2.3(*b*). The contours are labelled in kg Na_2CO_3 m^{-3}. As a guide, 170 kg m^{-3} is equivalent to 6.2 wt% Na_2CO_3 (C_E) and 60 kg m^{-3} is equivalent to 2.1 wt% Na_2CO_3. The solid composition was measured by cutting the solid up into sections and allowing them to melt. The solid block has length 16 cm and depth 15 cm (traced from original figure of Leitch 1985).

here by

$$T_C = [-36 + 26\exp(-t/t_1)]\,^{\circ}\mathrm{C}\,, \tag{2.4.2}$$

where $t_1 \sim 5$ hours. For the numerical calculations, the Lewis number is reduced by a factor of 10, and the Rayleigh numbers by a factor of 10^3, as in the calculations for a supereutectic solution (§2.4.1 above). The calculated solid composition is plotted in Figure 2.16, both as a contour plot and in cross-section for various heights. The most notable feature is the strong minimum in solid composition around 1 cm from the cold wall at the roof of the tank. The negative solid composition is an artefact of our mathematical model and represents the compositional flux becoming sufficiently large at the solidification front for equilibrium end-member A (pure ice) to form. For consistency, the boundary condition (2.3.9), corresponding to liquidus growth, should be applied at the solid/melt interface close to the roof of the tank, rather than the boundary condition (2.3.10), which corresponds to eutectic growth. However, application of boundary condition (2.3.9) on part of the solid/melt interface $x = h$ and (2.3.10) on the remainder of

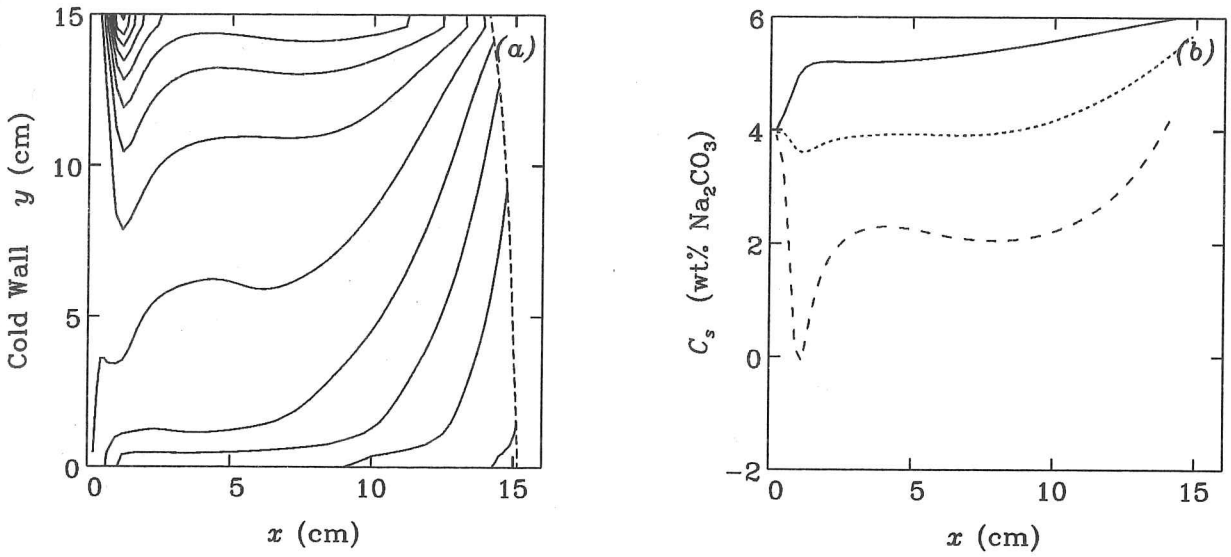

Figure 2.16. Calculation for the complete freezing of a homogeneous subeutectic sodium carbonate solution (Table 2.3(b)). Solid composition is presented (a) as a contour plot, and (b) in cross-sections at various heights: ——— base of tank; · · · · · · mid-height $H/2$; – – –top of tank.

the interface leads to poor convergence. In the experiments of Leitch (1985) and Huppert *et al.* (1987), the solid composition is nowhere equal to C_A or C_B, which means that neither equilibrium end-member was obtained. Therefore, we choose not to model the liquidus regime and assume eutectic growth everywhere. This may lead to predictions of negative solid composition for a subeutectic sodium carbonate solution. Similarly, for a supereutectic sodium carbonate solution, solid compositions greater than the composition of pure B may be predicted.

The strong minimum in the predicted solid composition close to the cold wall occurs because of the strong inflow of warm fluid towards the solidification front at the roof of the tank. In the experiment, this suppresses the nucleation of crystals in that region and growth is restricted initially to the base of the tank (Leitch 1985). Solidification only starts at the roof of the tank when the solution there has become sufficiently supercooled for an initial quench layer to form, and this only occurs when the heat available from the solution has been reduced substantially. However, the simple solidification model presented here assumes immediate nucleation and growth at all heights. The strong input of heat from the interior serves only to *slow* the crystal growth. Since the difference in

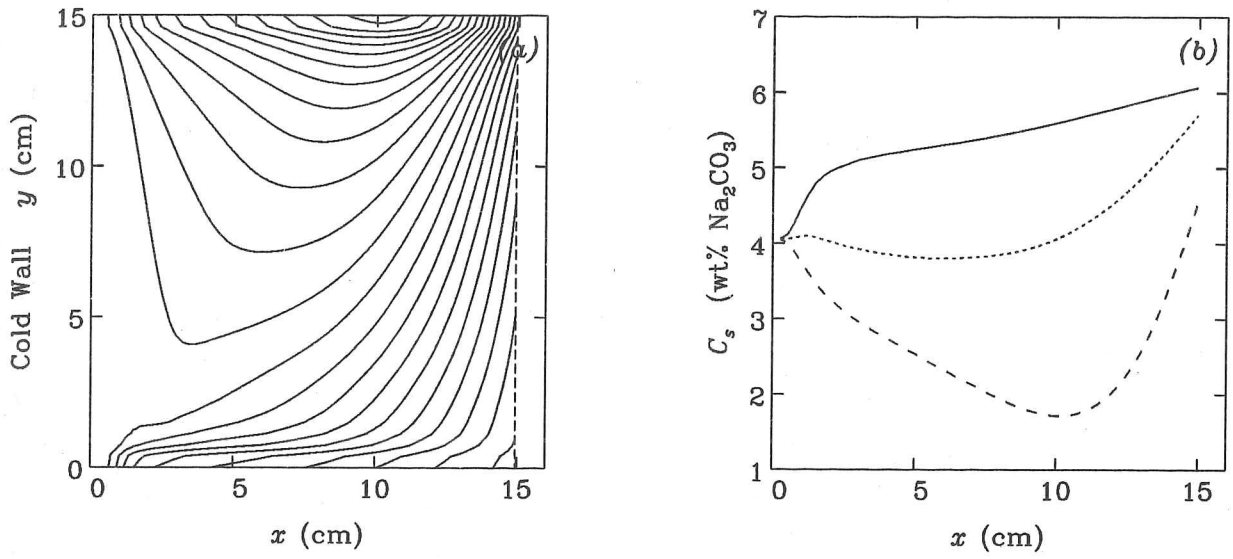

Figure 2.17. Calculation for the complete freezing of a homogeneous subeutectic sodium carbonate solution (Table 2.3(*b*)). Thermal effects have been removed by setting the initial temperature $T_0 = T_E$. Solid composition is presented (*a*) as a contour plot, and (*b*) in cross-sections at various heights: ——— base of tank; ····· mid-height $H/2$; – – –top of tank.

composition between the solid and the liquid at the solid/melt interface is proportional to $1/\dot{h}$ (equation (2.3.21)), this leads to the strong minimum in predicted solid composition close to the cold wall. The presence of the minimum close to the cold wall is therefore due to incorrect modelling of the early stages of solidification.

We note that the compositional stratification in the solid is primarily determined by compositional convection. Therefore, a further calculation was performed in which thermal effects were removed by setting the initial fluid temperature to be equal to the eutectic temperature ($T_0 = T_E$). The results are plotted in Figure 2.17. The predicted minimum solid composition is now equal to 1.7 wt% Na_2CO_3, compared with the experimental minimum which is 2.1 wt% Na_2CO_3. The predicted position of the minimum is 10.3 cm from the cold wall (compared with the experimental value 10.8 cm). It should be noted that the method of measurement of Leitch (1985), *i.e.* cutting the solid in a finite number of blocks, inevitably leads to smearing of the results. In other words, the minimum value of the solid composition is underestimated. Figure 2.17 therefore represents excellent agreement and is strong evidence that the model presented here correctly describes the solid stratification for a subeutectic salt solution. In particular, the composition of the

solid is determined locally by the diffusive compositional flux at the solidification front, and the convective transport of composition, both in the bulk flow and in the upflowing compositional boundary layer, determines the global distribution of composition in the solid.

2.4.3 Stratified supereutectic solution

Finally, we discuss briefly some simulations for an initially stratified supereutectic solution. Two experiments were performed by Huppert *et al.* (1987) to demonstrate that the angles of inclination of the contours of solid composition are dependent upon the size of the chamber into which the solid is growing. A square enclosure was split into two smaller enclosures (of volumes 4800 cm^3 and 14400 cm^3) by placing the cooling plate vertically inside the tank. The experimental conditions are listed in Table 2.3 (*c*), (*d*) and contour plots of the solid composition are presented in Figure 2.18. Note that Figure 2.18(*b*) differs slightly from that originally published in Huppert *et al.* (1987). There is now a local maximum in solid composition at the base of the smaller tank. Figure 2.18(*b*) has been constructed from the original experimental data, kindly supplied by one of the co-authors, Mark Hallworth.

For the smaller chamber, the liquid solution is rapidly depleted in solute, and so the solid composition decreases with distance away from the cold wall. For a larger chamber, however, the far-field liquid composition is maintained and the compositional flux is maintained by the convection. As the solid growth slows, there is an increase in solid composition with distance away from the cooling boundary. In addition, the solid stratification reflects the stratification in the liquid, and so the solid composition decreases with height. Therefore, the contours of solid composition slope downwards away from the cold wall for the smaller tank and slope upwards away from the cold wall for the larger tank.

For the purposes of numerical calculation, the experimental values of the Lewis number were again reduced by a factor of 10 and the Rayleigh numbers by a factor of 10^3. The streamlines and contours of liquid composition are plotted after 24 hours in Figure 2.19. The strength of the convection is comparable in the two chambers. For the larger chamber, however, the compositional stratification is stronger than in the smaller chamber.

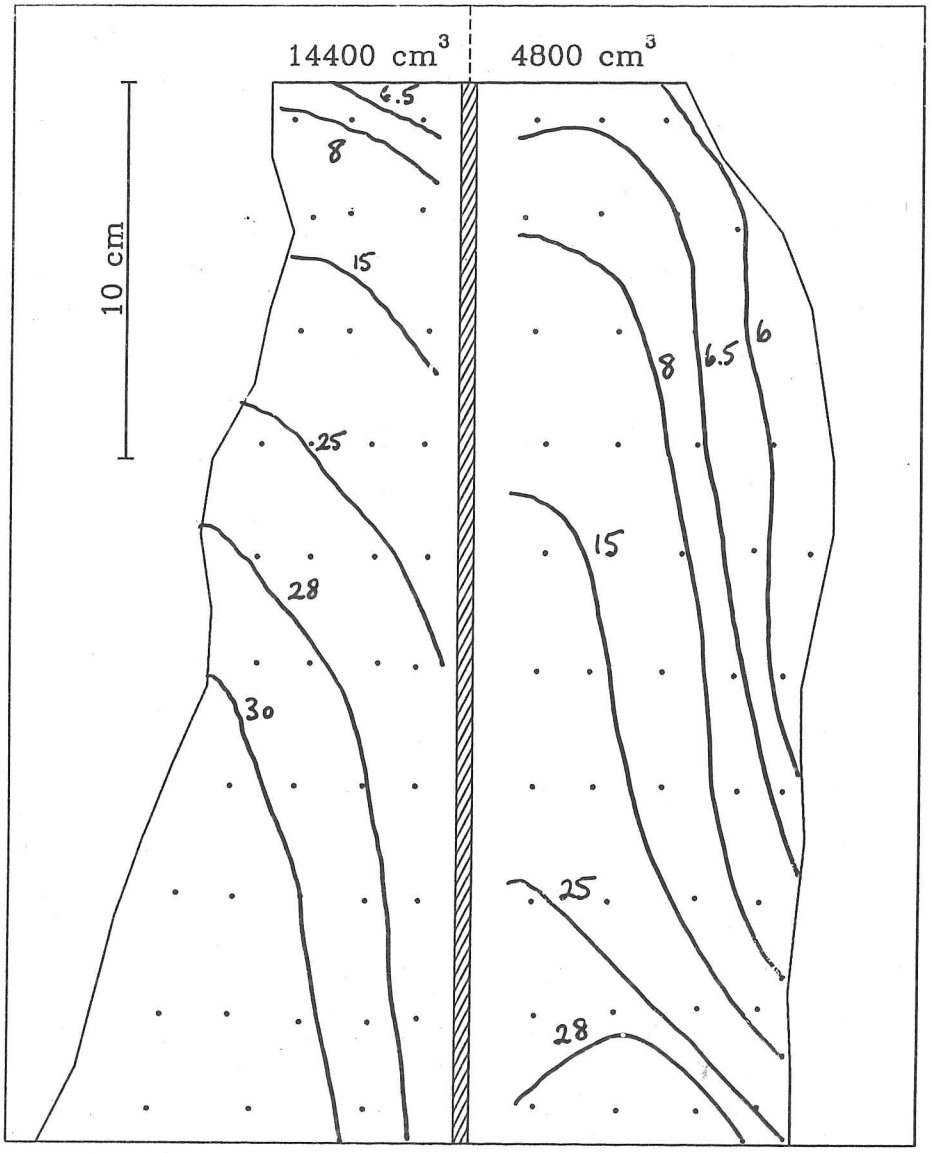

Figure 2.18. Contour plots of solid composition for the partial freezing (after 24 hours) of a stratified supereutectic aqueous sodium carbonate solution in (*a*) a larger chamber, volume 14400 cm^3, and (*b*) a smaller chamber, volume 4800 cm^3. The experimental conditions are listed in Table 2.3(*c*) and (*d*) respectively. The contours are labelled in wt% Na_2CO_3. Data points are marked as dots. Note that (*b*) differs from the original published figure (Huppert *et al.* 1987).

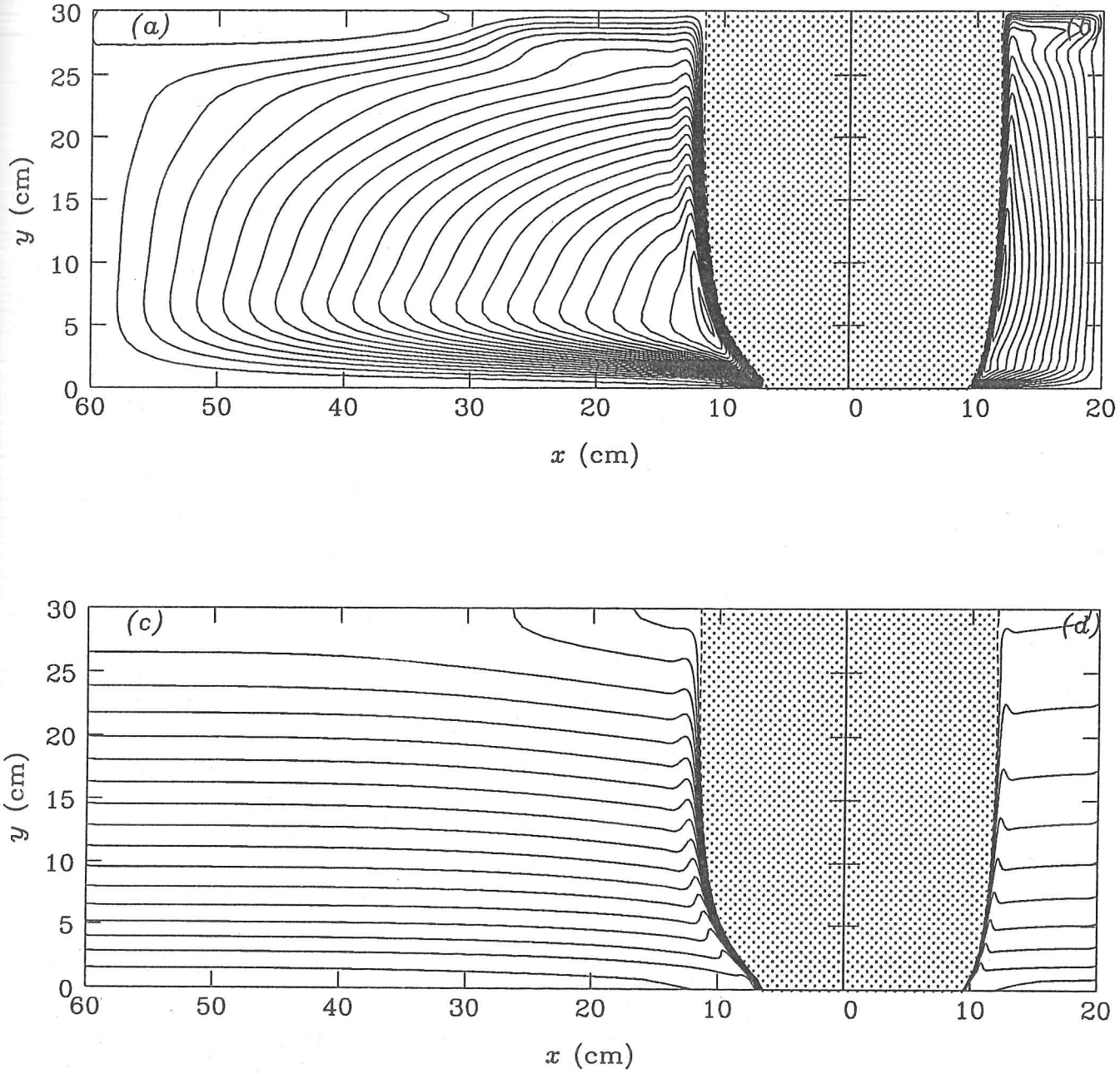

Figure 2.19. Calculated streamlines and liquid composition after 24 hours for the partial crystallization of a stratified supereutectic aqueous sodium carbonate solution for: (*a*), (*c*) the larger tank, and (*b*), (*d*) the smaller tank. The cold boundary is at $x = 0$. Original experimental conditions are listed in Table 2.3(*c*), (*d*).

The fluid in the smaller chamber has become significantly depleted in solute by the end of the calculation. Calculated values for solid composition are plotted in Figure 2.20. Agree-

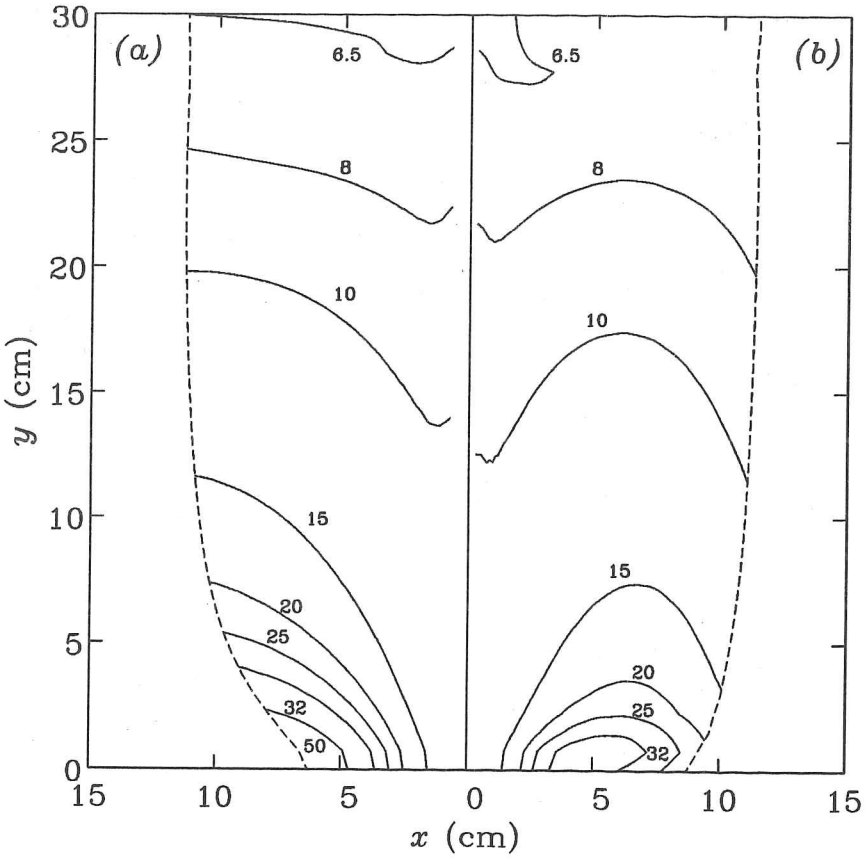

Figure 2.20. Calculated solid composition for the partial crystallization of a stratified supereutectic aqueous sodium carbonate solution in: (*a*) the larger tank, and (*b*) the smaller tank. Original experimental conditions are listed in Table 2.3(*c*), (*d*). Contours are labelled in wt% Na_2CO_3.

ment between the experiments and the numerical calculations is poor. For the smaller chamber, the predicted maximum composition is just under 37 wt% Na_2CO_3 (almost pure $Na_2CO_3.10H_2O$). The maximum in the experiment is around 30 wt% Na_2CO_3. The predicted position of the maximum is again too far from the cold wall and the contours of solid composition have only just started to dip downwards after 24 hours (the run time for the experiment). This is probably due to the disparity in box-filling timescales, discussed in §2.3.1, between laminar theory and the experiments with supereutectic sodium carbonate solutions.

For the larger tank (Figure 2.20(*a*)), the major qualitative features are again reproduced — the upwards inclination of the contours and the maximum at the base of the tank — but the quantitative agreement is very poor. This is most probably due to the

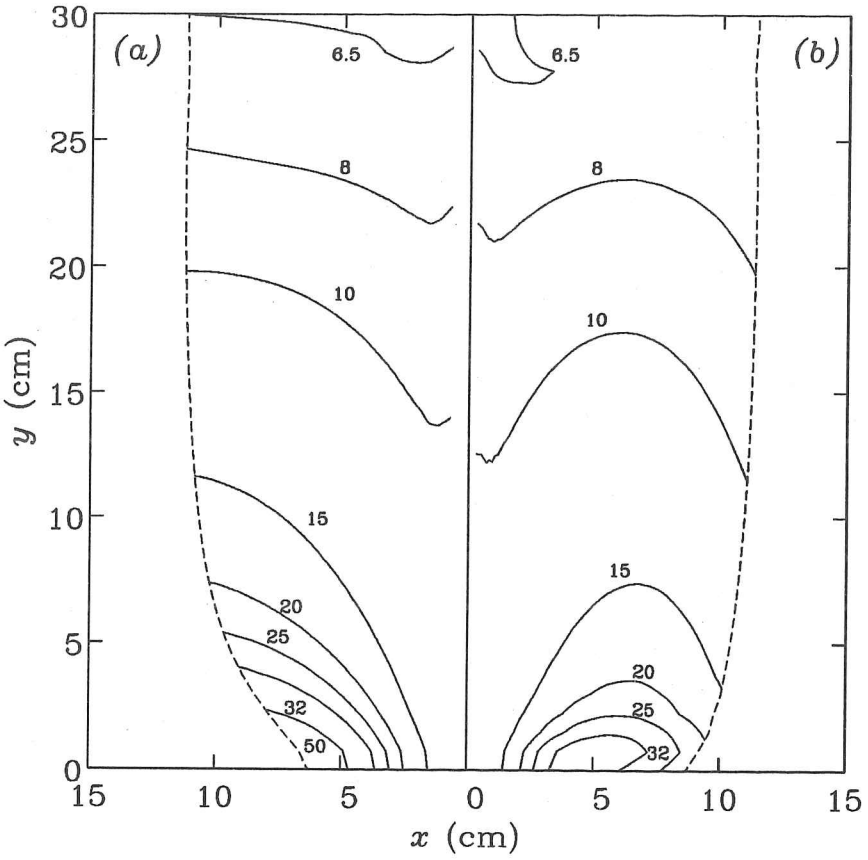

Figure 2.20. Calculated solid composition for the partial crystallization of a stratified supereutectic aqueous sodium carbonate solution in: (*a*) the larger tank, and (*b*) the smaller tank. Original experimental conditions are listed in Table 2.3(*c*), (*d*). Contours are labelled in wt% Na_2CO_3.

ment between the experiments and the numerical calculations is poor. For the smaller chamber, the predicted maximum composition is just under 37 wt% Na_2CO_3 (almost pure $Na_2CO_3.10H_2O$). The maximum in the experiment is around 30 wt% Na_2CO_3. The predicted position of the maximum is again too far from the cold wall and the contours of solid composition have only just started to dip downwards after 24 hours (the run time for the experiment). This is probably due to the disparity in box-filling timescales, discussed in §2.3.1, between laminar theory and the experiments with supereutectic sodium carbonate solutions.

For the larger tank (Figure 2.20(*a*)), the major qualitative features are again reproduced — the upwards inclination of the contours and the maximum at the base of the tank — but the quantitative agreement is very poor. This is most probably due to the

planar interface assumption becoming invalid. At the base of the larger tank, a dendritic layer approximately 5cm thick was observed (Huppert *et al.* 1987). The dendritic layer is thickest towards the base of the tank because of the greater compositional constrast between the solid/melt interface and the bulk fluid. Consequently, the horizontal compositional gradient in the melt is greatest at the base of the tank, which therefore exhibits the greatest degree of supercooling. Although the qualitative evolution of the system is unaffected by the presence of a two-phase region, the scaling law developed in §2.3.2 is no longer valid and therefore quantitative agreement between experiments and calculations cannot be expected.

2.5 Discussion

In this chapter, we have investigated how convective processes in the fluid can affect the composition of an alloy solidifying from the side. The model studied here is based upon a simple eutectic binary alloy growing from one sidewall of a two-dimensional rectangular enclosure. The melt has constant viscosity and exhibits laminar convection, dominated by compositional effects. The solid/melt interface is assumed to be planar, the effects of constitutional supercooling being neglected. Under these conditions, it has proved possible to conduct a scaling analysis in which we showed that the pattern of compositional stratification in the solid is both qualitatively and quantitatively dependent upon a single compound nondimensional parameter $P = \mathcal{A}^{1/4} Le^{3/4} {Ra_c}^{-1/4} \widehat{St}^{-1}$. The scaling analysis is valid for $P \ll 1$. This enabled us to model experimental conditions by conducting numerical calculations at significantly reduced Rayleigh numbers.

The parameter P represents the rate at which light (or heavy) fluid released at the solidification front fills the chamber, compared with the rate at which the chamber becomes entirely solid. In the context of fractionation of magmas, larger values of P represent more rapid rates of evolution of the melt, for both tholeiitic and calc-alkaline trends of fractionation. The general pattern of solid stratification is that heavy components are more prevalent towards the base of the solid. This occurs even when the bulk fluid is homogeneous, through the action of the compositional boundary layer. The compositional stratification is continuous, which would correspond to cryptic layering in an igneous intrusion. For larger values of P, the solid composition typically tends to the eutectic composition with distance away from the cold wall, while for smaller values of P, the solid composition moves towards the appropriate equilibrium end-member.

Comparison between numerical calculations and the experiments conducted by Leitch (1985, 1987) and Huppert *et al.* (1987) produced agreement which ranged from excellent to poor. The critical approximation is the assumption of a planar crystal/melt interface. For a subeutectic aqueous sodium carbonate solution, the planar interface model, combined with the scaling of Rayleigh and Lewis numbers suggested by the dimensional analysis in §2.3, led to accurate numerical simulation of the experiments. The disagreement was not significantly greater than the experimental error. However, for supereutectic solutions, agreement was less good. This was largely because the morphology of the crystal/melt

interface in the experiments was not planar.

A striking difference between the calculations and the original experiments is the absence of double-diffusive layering in the calculated flows. This is probably due to insufficient vertical resolution in our calculations. Double-diffusive layering was successfully predicted by Thompson & Szekely (1988), using a similar numerical method, for a situation in which the height of the double-diffusive cells was approximately one tenth of the height of the enclosure. In addition, Thompson & Szekely considered the case of a heated far wall $x = L$, and so a substantial horizontal thermal gradient was maintained throughout the calculation. It has been suggested that the discrete stratification produced in the fluid by this form of instability may be responsible for the sharp interfaces between layers observed in some igneous intrusions (McBirney & Noyes 1979). However, despite the presence of double-diffusive layers, the observed solid stratification was continuous in the experiments of Huppert *et al.* (1987) with supereutectic stratified solutions. This was chiefly because the layers were not static, but migrated vertically and sometimes merged. Therefore, the absence of double-diffusive layering in the calculations is perhaps not critical in modelling the experiments.

It is unlikely that an individual magma chamber would crystallize only from its sidewalls, exhibit simple fractionation behaviour with a planar solid/interface and be allowed to completely solidify without being replenished by fresh melt, or lose mass by erupting. It is equally unlikely, however, that a coherent picture of the evolution of a magma chamber can be presented by simultaneously considering all possible physical processes. In this chapter, a single process has been isolated and studied. Any one geological feature has generally been formed by the interaction of many processes. However, each important physical process must first be understood in isolation before more complete interpretation may be attempted.

The work presented here suggests many possible avenues for future investigations. Immediately possible is a study of crystallization from an inclined floor or roof, provided that the boundary is sufficiently close to the vertical for the convection to be laminar. Experimental results for such a geometry already exist (Huppert *et al.* 1987). More fundamentally, it may be necessary to construct a more complete model of the solidification process which includes a two-phase mushy zone between the solid and liquid phases.

Lowell (1985) found that the rate at which fractionated fluid rises to the roof of the chamber depends strongly upon the permeability $\bar{K}$ of the mush. For fractionation within a two-phase mushy region, the nondimensional box-filling timescale t_{BF} is proportional to $\bar{K}^{-1/2} {Ra_C}^{-1/2} Le^{1/2}$ (Lowell 1985). We see immediately that the scalings derived in §2.3.2 would no longer be valid. Another possible avenue to explore is the evolution of multicomponent systems, or binary systems with different phase diagrams from the simple eutectic binary alloy characterised by the equilibrium phase diagram in Figure 2.1.

In the following chapter, we investigate how variations in the viscosity of the melt, due to differences in both temperature and composition, affect the layering mechanism described in this chapter.

Appendix. Numerical methods

A large variety of numerical schemes have been developed to solve solidification problems (Crank 1984), and these fall broadly into two groups — front-tracking and front-fixing methods. Front-tracking methods employ a fixed grid for the whole domain, both solid and liquid, and track the solidification front, which generally occurs between mesh points. Latent heat is treated as a source term in the heat equations and is applied to the mesh points adjacent to the solid/melt interface. These methods are relatively fast, and have good global conservation properties, but the detail close to the phase interface is poorly resolved. When a binary alloy crystallizes at a vertical wall, there is a thin compositional boundary layer close to the solidification front. The composition of the solid grown is very sensitive to the compositional flux at the solidification front, and so it is important to resolve compositional boundary layer accurately at all times. To do so with a fixed grid would require a fine grid across the entire domain, which is computationally impractical.

Instead, in the front-fixing methods, the solid and liquid regions are each mapped onto the domain $[0,1] \times [0,1]$. In transforming the independent variables, the governing partial differential equations become more complicated, but each computational domain is now rectangular and the solidification front is fixed in the transformed coordinates. Therefore, the mesh need only be refined in the vicinity of the (known) solidification front. The inner boundary layer associated with the compositional buoyancy forcing is of width $\delta_c \sim (Le\, Ra_c)^{-1/4}$ (Patterson & Imberger 1980, Worster & Leitch 1985), and it is necessary to fit at least 4 grid points into this region. In the horizontal x-direction in the liquid region, 65 grid points are used, the grid spacing being an even 0.04 for most of the domain, decreasing by a factor of 1.2 per grid point to around 3×10^{-5} immediately adjacent to the solid/melt interface. The grids in the y-direction and in the x-direction for the solid are both uniform, with 41 grid points in the y-direction and 21 grid points in the x-direction for the solid. The numerical scheme below has been tested on finer (73×49 and 73×57) grids and at smaller timesteps to determine accuracy and grid and timestep independence. The effect of refining the grid upon the predicted solid composition for a typical calculation is presented in Figure 2.21. The solid compositions for the three calculations at the mid-height $H/2$ are indistinguishable, demonstrating that the horizontal resolution is sufficient. There are small differences towards the top and bottom of the tank, corresponding to incomplete resolution of the viscous boundary

layers at the horizontal surfaces, but convergence is clearly being approached. The lowest value 41 is taken for the vertical resolution to shorten calculation times.

The governing equations (2.3.13)–(2.3.17) are nonlinear and coupled, and so cannot be solved directly at each timestep. A global iteration is required, with successive guesses for all variables (including the interface velocity $\dot{h}$) at the new timestep being updated until some convergence criterion is satisfied. Generally 5 to 6 global iterations are sufficient at each timestep. For the parabolic equations, the Alternating Direction Implicit (ADI) method introduced by Peaceman & Rachford (1955) is employed, while a multigrid method has been used for the potentially expensive inversion of $\nabla^2\psi = -\omega$. The similarity solution (2.2.9)–(2.2.13) for crystallization in the absence of convection presented in §2.2 implies that the solid growth rate $\dot{h}$ is infinite at $t = 0$. To avoid difficulties associated with large solidification rates as $t \to 0$, all calculations are started at the nondimensional time 10^{-4} from the similarity solutions for zero flow in §2.2.

A single timestep on a CONVEX vector computer takes 2–6 cpu seconds, with a typical complete freezing experiment requiring up to 30000 timesteps, and so around 30 cpu hours may be required for a full production run. This cost can increase dramatically, however, for larger Rayleigh numbers, for which greater spatial resolution is required. In most cases, the calculations are halted when only half of the original volume of molten alloy has solidified, reducing the required cpu time by a factor of four.

A.1 Coordinate transformation

As the solid grows, the interface position $h(y,t)$ varies with height y owing to the convective redistribution of heat in the liquid. Therefore, both solid ($0 \le x \le h$, $0 \le y \le \mathcal{A}$) and liquid ($h \le x \le 1$, $0 \le y \le \mathcal{A}$) regions are non-rectangular. A simple transformation of coordinates (Crank 1984) maps both regions onto the rectangular domain $[0,1] \times [0,1]$, *viz.*

$$\zeta = x/h \qquad 0 \le x \le h\,; \qquad (2.A.1a)$$

$$\xi = (x-h)/(1-h) \qquad h \le x \le 1\,; \qquad (2.A.1b)$$

$$\eta = y/\mathcal{A}\,; \qquad (2.A.1c)$$

$$\tau = t\,. \qquad (2.A.1d)$$

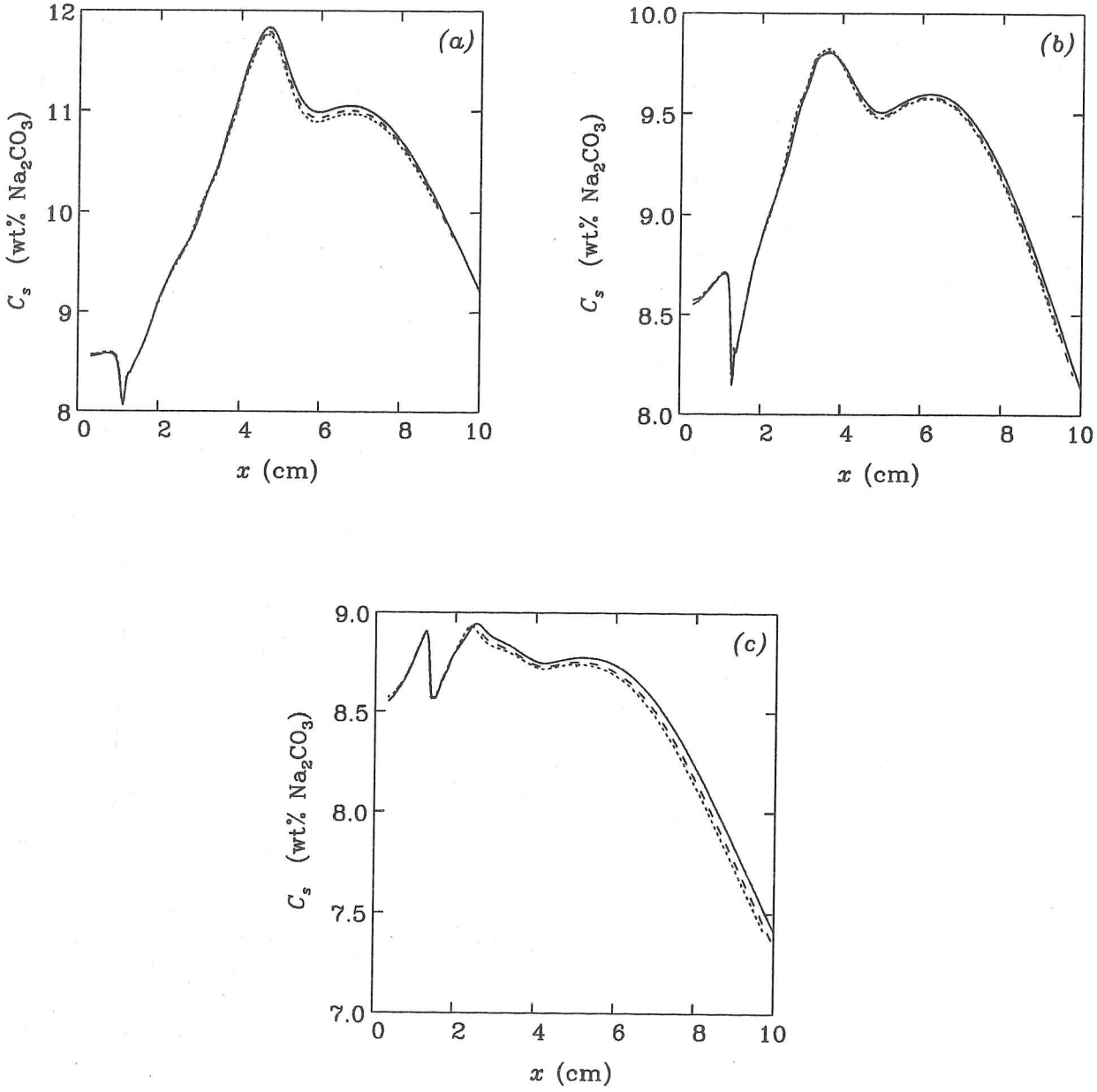

Figure 2.21. Typical solutions for solid composition C_s plotted against distance x from the cold wall at heights (*a*) the quarter-height $H/4$; (*b*) the mid-height $H/2$; and (*c*) the three-quarter height $3H/4$, calculated for three different grids: —— 65×41; – – –73×49; ····· 73×57. Note that each figure has a different scale. The length of the tank is 16 cm and eutectic composition for an aqueous sodium carbonate solution is $C_E = 6.2$ wt% Na_2CO_3.

Treating h as a function of η and τ, the partial first derivatives transform as follows for the solid and liquid regions respectively,

$$\left.\begin{aligned} \frac{\partial}{\partial x} &\rightarrow \frac{1}{h}\frac{\partial}{\partial \zeta} \\ \frac{\partial}{\partial y} &\rightarrow \frac{1}{\mathcal{A}}\left(\frac{\partial}{\partial \eta} - \frac{\zeta h_\eta}{h}\frac{\partial}{\partial \zeta}\right) \\ \frac{\partial}{\partial t} &\rightarrow \frac{\partial}{\partial \tau} - \frac{\zeta h_\tau}{h}\frac{\partial}{\partial \zeta} \end{aligned}\right\} \qquad 0 \leq x \leq h\,; \qquad (2.A.2a)$$

$$\left.\begin{aligned} \frac{\partial}{\partial x} &\rightarrow \frac{1}{(1-h)}\frac{\partial}{\partial \xi} \\ \frac{\partial}{\partial y} &\rightarrow \frac{1}{\mathcal{A}}\left(\frac{\partial}{\partial \eta} - \frac{(1-\xi)h_\eta}{(1-h)}\frac{\partial}{\partial \xi}\right) \\ \frac{\partial}{\partial t} &\rightarrow \frac{\partial}{\partial \tau} - \frac{(1-\xi)h_\tau}{(1-h)}\frac{\partial}{\partial \xi} \end{aligned}\right\} \qquad h \leq x \leq 1\,. \qquad (2.A.2b)$$

From these the more complicated forms of the transformed second derivatives can be found. The transformation (2.A.2) is equivalent to using a curvilinear mesh which lies parallel to the solidification front and moves as the solid region grows and the liquid region shrinks. The additional terms introduced by this transformation fall into two categories — mesh curvature terms in h_η and $h_{\eta\eta}$, and pseudo-advective terms in h_τ. Many workers have chosen to neglect most of the additional terms produced by this transformation (Thompson & Szekely 1988, Ramachandran *et al.* 1981, Ho & Viskanta 1984), including the pseudo-advective terms. This is known as the pseudo-stationary approximation. Tests with a one-dimensional freezing model have demonstrated that neglect of the pseudo-advective terms is valid when only the evolution of the solidification front with time is required. However, the approximation leads to significant numerical errors in the compositional flux at the interface. Therefore, the pseudo-advective terms cannot be neglected when calculating the composition of the solid grown. Test calculations with the full two-dimensional numerical model described here have shown that the mesh curvature terms may be neglected. This is partly because the insulation boundary conditions at $y = 0$ and $y = \mathcal{A}$ imply that $h_\eta = 0$ at the top and bottom boundaries, and partly because the Jacobian terms $\mathbf{u}.\nabla\mathbf{f} = J(f,\psi)_{x,y}$ occurring on the left-hand side of (2.3.13), (2.3.14) and (2.3.16) transform to new Jacobians, namely $J(f,\psi)_{\xi,\eta}$ divided by $\mathcal{A}(1-h)$.

A.2 Global iteration

To solve the full nonlinear system of partial differential equations (2.3.13)–(2.3.17), a global iterative procedure is required. This is both because of the nonlinear coupling between equations and because of the presence of the h_τ terms introduced by the coordinate transformation (2.*A*.1). The solution to the system (2.3.13)–(2.3.17) at the nth timestep is first considered to be equal to the solution at the $(n-1)$th timestep, except for the interface position and interface velocity, which are assumed to have changed according to $t^{1/2}$ and $t^{-1/2}$ respectively. At each global iteration, the nonlinear terms in the equations (2.3.13)–(2.3.16) are approximated by the latest estimate for the solution at the nth timestep. The equations are solved repeatedly until successive estimates for the solution converge and the heat balance (2.3.20) at the solid/melt interface ($\zeta = 1$, $\xi = 0$) is satisified. The order of solution at each global iteration is as follows: first the vorticity ω, followed by the streamfunction ψ, the solid and liquid temperatures T_s and T_l and the liquid composition C_l. The next estimate for the interface velocity h_τ is obtained by substituting the latest solutions for T_s and T_l into the heat balance (2.3.20). Once the solution has converged at the nth timestep, the solid composition is calculated from the mass conservation condition (2.3.21).

For the partial differential equations (2.3.13)–(2.3.17), there are corresponding boundary conditions for each of the variables ψ, T_s, T_l and C_l. However, there is no explicit boundary condition for the vorticity ω. Instead, the boundary conditions for ω must be derived from the no-slip condition $\mathbf{u} = 0$. This is natural, as it is an adverse anomaly of vorticity which acts to slow down the flow in the vicinity of the rigid boundary. The scheme most commonly used to determine the wall vorticity is derived from the Taylor expansion of the streamfunction ψ at the grid-point nearest the wall. For example, for the boundary $y = 0$,

$$\psi(x,\Delta y) = \psi(x,0) + \Delta y \frac{\partial \psi}{\partial y}(x,0) + \frac{1}{2}\Delta y^2 \frac{\partial^2 \psi}{\partial y^2}(x,0) + \ldots \qquad (2.A.3)$$

Since $\mathbf{u} = 0 \Rightarrow \psi_y = 0$ and $\psi = 0 \Rightarrow \psi_{xx} = 0$ at $(x,0)$, we may substitute $\omega = -\psi_{xx} - \psi_{yy}$ into (2.*A*.3) to obtain

$$\omega(x,0) = \tilde{\omega}_w = -\frac{2}{\Delta y^2}\psi(x,\Delta y) + O(\Delta y^2)\,. \qquad (2.A.4)$$

New guesses $\omega_w^{n,k+1}$ for the wall vorticity ω_w require under-relaxation of the form

$$\omega_w^{n,k+1} = \omega_w^{n,k} + \gamma(\tilde{\omega}_w - \omega_w^{n,k}), \qquad (2.A.5)$$

where $\gamma \ll 1$, to ensure stability of the iterative scheme.

The global iterative scheme is considered to have converged once the maximum absolute change $|h_\tau^{n,k+1} - h_\tau^{n,k}|$ in the interface velocity is less than 5×10^{-5} and the maximum relative change $|\omega_w^{n,k+1} - \omega_w^{n,k}|/|\omega_w^{n,k}|$ in the wall vorticity is less than 5×10^{-5}. Generally 5 or 6 global iterations are required at each timestep to ensure convergence.

A.3 Parabolic solver

The equations (2.3.13)–(2.3.16) for the vorticity ω, the solid and liquid temperatures T_s and T_l, and the liquid composition C_l are all parabolic partial differential equations of the general form

$$\frac{\partial f}{\partial \tau} + A\frac{\partial f}{\partial \xi} + B\frac{\partial f}{\partial \eta} = \nu^{(\xi)}\frac{\partial^2 f}{\partial \xi^2} + \nu^{(\eta)}\frac{\partial^2 f}{\partial \eta^2} + g, \qquad (2.A.6)$$

where A, B, $\nu^{(\xi)}$, $\nu^{(\eta)}$ and g are functions of ξ and η. The cross-derivative terms in $\partial^2 f/\partial\xi\partial\eta$ which arise from the transformation (2.A.2), are incorporated into g on the right-hand side and can be calculated for the kth iteration on the nth timestep from the latest approximate solution $f^{n,k-1}$. The general equation (2.A.6) is solved by using the Alternating Direction Implicit (ADI) method of Peaceman & Rachford (1955). Each timestep is split into two. In the first half-step, (2.A.6) is integrated in the ξ-direction alone, while in the second it is integrated in the η-direction. Each half-step is therefore solved by the method of lines, with each half-step involving the inversion of a number of tridiagonal systems. The discretization for the ADI method is written:

$$\frac{2}{\Delta\tau}(\tilde{f}_{ij} - f_{ij}^n) + (A_1\Delta_\xi^{\mathrm{up}} - \nu_1^{(\xi)}\Delta_{\xi\xi})\tilde{f}_{ij} = -(B_1\Delta_\eta^{\mathrm{up}} - \nu_1^{(\eta)}\Delta_{\eta\eta})f_{ij}^n + g\,; \qquad (2.A.7a)$$

$$\frac{2}{\Delta\tau}(f_{ij}^{n+1} - \tilde{f}_{ij}) + (B_2\Delta_\eta^{\mathrm{up}} - \nu_2^{(\eta)}\Delta_{\eta\eta})f_{ij}^{n+1} = -(A_2\Delta_\xi^{\mathrm{up}} - \nu_2^{(\xi)}\Delta_{\xi\xi})\tilde{f}_{ij} + g\,. \qquad (2.A.7b)$$

A_1 and A_2 are suitable approximations for A_{ij}, and similarly B_1 and B_2 for B_{ij}; $\nu_1^{(\xi)}$ and $\nu_2^{(\xi)}$ for $\nu_{ij}^{(\xi)}$; and $\nu_1^{(\eta)}$ and $\nu_2^{(\eta)}$ for $\nu_{ij}^{(\eta)}$. The symbols Δ_x and Δ_{xx} represent discretizations

of the first and second spatial derivatives. To ensure diagonal dominance in the implicit tridiagonal equations for $\tilde{f}_{ij}$ and f_{ij}^{n+1}, upwinding is employed on the left-hand sides of (2.A.7), denoted by the superscript 'up' on the first derivatives. This scheme has only first-order accuracy in time because non-centred differences have been taken for the first derivatives. A variety of schemes have been suggested for recovery of second-order accuracy (Peyret & Taylor 1983), but none of these proved suitable. For example, a scheme in which the first derivatives on the right-hand sides of (2.A.7) were downwinded proved unstable. Upwinding ensures the diagonal dominance of the tridiagonal forms (which can be solved by a simple, well-known algorithm). For centred differencing, the necessity of diagonal dominance would lead to a restriction upon the size of the timestep.

Suitable choices for A_1, A_2 and B_1, B_2 are

$$A_1 = A_2 = \frac{1}{2}(A_{ij}^n + A_{ij}^{n+1}), \qquad B_1 = B_{ij}^n, \qquad B_2 = B_{ij}^{n+1}, \tag{2.A.8}$$

and the following estimates for the diffusion coefficients are made,

$$\nu_1^{(\xi)} = \nu_2^{(\xi)} = \frac{1}{2}(\nu^{(\xi)n} + \nu^{(\xi)(n+1)}) \qquad \nu_1^{(\eta)} = \nu_2^{(\eta)} = \frac{1}{2}(\nu^{(\eta)n} + \nu^{(\eta)(n+1)}). \tag{2.A.9}$$

When A, B, $\nu^{(\xi)}$ and $\nu^{(\eta)}$ are constant, the ADI scheme is unconditionally stable (Peyret & Taylor 1983). When coupled with a model for solid growth, accuracy is important. Ideally, the timestep should be much smaller than the timescale for variations in solid thickness h. It was demonstrated in §2.2 that $h_\tau \to \infty$ as $\tau \to 0$. To avoid the singularity as $\tau \to 0$, all calculations were started from the similarity solution presented in §2.2 at $\tau = 10^{-4}$. For most calculations, a timestep $\Delta\tau = 2 \times 10^{-5}$ was found to be sufficiently small. However, for larger Rayleigh numbers, a finer mesh is required in the fluid region adjacent to the moving interface, and consequently the timestep must be smaller. At late stages of solidification, the liquid region becomes very narrow. This reduces the real grid size $\Delta x = (1 - h)\Delta\xi$. It was found that the numerical calculations tend to break down when the chamber is about 90% solidified because the timestep is no longer sufficiently small for accuracy and the global iteration fails to converge.

The boundary conditions for f_{ij}^{n+1} are those of §2.3 applied at the $(n+1)$th timestep, but the boundary values of $\tilde{f}_{ij}$ are unknown — $\tilde{f}_{ij}$ is not simply the value of f_{ij} at a

half-timestep. If we subtract (2.*A*.7*a*) from (2.*A*.7*b*), we obtain

$$\tilde{f}_{ij} = \frac{1}{2}(f_{ij}^n + f_{ij}^{n+1}) + \frac{\Delta\tau}{4}\left((B_2\Delta_\eta^{\rm up} - \nu_2^{(\eta)}\Delta_{\eta\eta})f_{ij}^{n+1} - (B_1\Delta_\eta^{\rm up} - \nu_1^{(\eta)}\Delta_{\eta\eta})f_{ij}^n\right) \quad (2.A.10)$$

Aside from any conditions of stability, if an upwind-downwind scheme had been used to obtain second-order accuracy, equation (2.*A*.10) would no longer hold. The lack of an exact expression for $\tilde{f}_{ij}$ at the boundaries would introduce a truncation error into the scheme (Peyret & Taylor 1983), and so second-order accuracy would have been lost in any case.

Although there is no timestep restriction associated with stability of the ADI scheme, it is still necessary to preserve accuracy. The advective term A_{ij} is strongly dependent upon the solidification rate h_τ and so care must be taken to ensure that the timestep is much smaller than the timescale for changes in h_τ. This is clearly impossible for very early times, as $h_\tau \propto \tau^{-1/2}$. However, for the bulk for the calculations, a timestep of 10^{-5} was found to be sufficiently small.

A.4 Elliptic solver

The most expensive part of any numerical scheme for solving the streamfunction-vorticity formulation of the unsteady Navier-Stokes equations is the Poisson solver for the streamfunction equation (2.3.18), namely $\nabla^2\psi = -\omega$. The scheme commonly used (Thompson & Szekely 1988, Ramachandran *et al.* 1981) is a Gauss-Seidel point relaxation with successive over-relaxation (SOR). This is not particularly competitive for a regular mesh and constant coefficients in the elliptic equation. However, when the general Poisson equation

$$\nabla^2 f = g \quad (2.A.11)$$

is transformed to the new independent variables ξ and η by the transformation (2.*A*.2), it takes the general form

$$X_2\frac{\partial^2 f}{\partial\xi^2} + XY\frac{\partial^2 f}{\partial\xi\partial\eta} + Y_2\frac{\partial^2 f}{\partial\eta^2} + X_1\frac{\partial f}{\partial\xi} + Y_1\frac{\partial f}{\partial\eta} = g, \quad (2.A.12)$$

where X_2, XY, Y_2, X_1 and Y_1 are non-constant in time and space. This makes it impossible to fix an optimal over-relaxation parameter for all time, and so the SOR scheme

becomes even less competitive. In this chapter, the general elliptic equation (2.*A*.12) is solved by a multigrid scheme, in which the finite difference equations are solved on a variety of grids of differing sizes. An approximate solution is obtained for the finest grid, and the error is reduced by solving on coarser and coarser grids in the manner described below. The solution is then obtained for each of the fine grids in succession by interpolation, until a new approximate solution has been found for the finest mesh. This multigrid strategy is known as a V-cycle. A good overall description of multigrid methods is provided by Sonneveld *et al.* (1985). At each grid level, only 4 relaxations of the solution are made, and no more than 2 or 3 V-cycles are required to obtain convergence. The multigrid scheme described here has been tested for a simple model elliptic problem and converges at least four times as quickly as an optimal SOR method.

The cross-derivative term $XY\,\partial^2 f/\partial\xi\partial\eta$ is incorporated into the right-hand side of (2.*A*.12) as before. Equation (2.*A*.12) may then be written in finite difference form to give the linear matrix equation

$$\mathbf{A}\mathbf{f} = \mathbf{r}\,. \tag{2.A.13}$$

For a grid sized $M \times N$, $\mathbf{f}$ has MN elements and $\mathbf{A}$ has $(MN)^2$ elements. In each row, $\mathbf{A}$ has only 5 non-zero elements, and is therefore very sparse. It is impractical to solve (2.*A*.13) by inverting $\mathbf{A}$, and instead relaxation methods are used. One example of a relaxation method is the Gauss-Seidel point relaxation, which is used in the SOR method. If we write $\mathbf{A} = \mathbf{L} + \mathbf{U}$, where $\mathbf{L}$ has elements only on or below the diagonal, and $\mathbf{U}$ has elements only above the diagonal, then (2.*A*.13) may be written

$$\mathbf{L}\mathbf{f}^k = \mathbf{r} - \mathbf{U}\mathbf{f}^{k-1}\,, \tag{2.A.14}$$

where $\mathbf{f}^k$ is the kth estimate of the solution $\mathbf{f}$. Successive direct solution of (2.*A*.14), with an over-relaxation to accelerate convergence, eventually converges. Now consider the error in the kth estimate $\mathbf{f}^k$, which is

$$\mathbf{e}^k = \mathbf{r} - \mathbf{A}\mathbf{f}^k\,. \tag{2.A.15}$$

The error $\mathbf{e}^k$ can be written as a sum of normal modes, with wavelengths ranging from the smallest grid scale to the scale of the whole computational domain. The relaxation scheme

(2.A.14) quickly removes the small-wavelength components of the error $\mathbf{e}^k$, but is much slower at removing the large-wavelength components. Solving for the error $\mathbf{e}^k$ on coarser grids with only a few relaxation steps on each grid can remove these large-wavelength components much more rapidly. This is the motivation behind multigrid schemes. In the multigrid scheme used in this chapter we use a line relaxation scheme — the Gauss-Seidel zebra. Writing $\mathbf{A} = \mathbf{T} + \mathbf{Q}$, where $\mathbf{T}$ is block-tridiagonal and $\mathbf{Q}$ holds the two members of $\mathbf{A}$ which are far from the diagonal, (2.A.13) can now be written

$$\mathbf{T}\mathbf{f}^k = \mathbf{r} - \mathbf{Q}\mathbf{f}^{k-1}, \tag{2.A.16}$$

which can easily be inverted. The cross-derivative term has already been amalgamated into the right-hand side by taking the solution for $\mathbf{f}$ at the previous global iterate, rather than using the latest iterate $\mathbf{f}^k$. Equation (2.A.16) can then be written in the 5-point form

$$a_{i,j} f^k_{i-1,j} + b_{i,j} f^k_{i+1,j} + e_{i,j} f^k_{i,j} = r_{i,j} - c_{i,j} f^{k-1}_{i,j-1} - d_{i,j} f^{k-1}_{i,j+1} \tag{2.A.17}$$

for $2 \leq i \leq M-1$ and $2 \leq j \leq N-1$. Given the right-hand side of (2.A.17), the left-hand side can be solved directly for $1 \leq i \leq M$, one value of j at a time. A single Gauss-Seidel zebra sweep consists of two half-sweeps, solving for all odd values of j on the first half-sweep and for all the even values of j on the second half-sweep. Alternatively, the tridiagonal inversions can be performed by columns, rather than by rows. Since the mesh considered here is regular in the j-direction and highly irregular in the i-direction, tridiagonal inversion by rows leads to much better rates of convergence.

The multigrid algorithm proceeds as follows. The largest grid size $M \times N$ is chosen so that $M-1$ and $N-1$ are both divisible by some power of two, at least 2^3. At each coarsening, every other grid point is taken, and the grid size at level $l+1$ is $M^{(l+1)} \times N^{(l+1)}$, where

$$M^{(l+1)} = 1 + (M^{(l)} - 1)/2 \qquad \text{and} \qquad N^{(l+1)} = 1 + (N^{(l)} - 1)/2 \tag{2.A.18}$$

The finest grid is denoted level 0, and $M^{(0)} = M$, $N^{(0)} = N$. Consider the following

problem at level l:

$$\mathbf{A}^{(l)}\mathbf{f}^{(l)} = \mathbf{r}^{(l)}\,. \tag{2.A.19}$$

The operators $\mathbf{A}^{(0)}$ and $\mathbf{r}^{(0)}$ are equivalent to $\mathbf{A}$ and $\mathbf{r}$ in equation (2.A.13), where $\mathbf{A}^{(0)}$ is obtained directly from the finite difference equation (2.A.12). After a few relaxations by the Gauss-Seidel zebra scheme, the latest estimated solution at level l is $\tilde{\mathbf{f}}^{(l)}$, and the residual error is $\mathbf{r}^{(l)} - \mathbf{A}^{(l)}\tilde{\mathbf{f}}^{(l)}$. Note that the ordering of the zebra relaxation results in the residual being zero at even values of j. The coarse-grid correction comes from solving

$$\mathbf{A}^{(l+1)}\mathbf{f}^{(l+1)} = \mathbf{r}^{(l+1)}\,, \tag{2.A.20}$$

where

$$\mathbf{r}^{(l+1)} = R^{(l+1,l)}(\mathbf{r}^{(l)} - \mathbf{A}^{(l)}\tilde{\mathbf{f}}^{(l)})\,. \tag{2.A.21}$$

This provides a coarse-grid corrected estimate $\mathbf{f}^{(l)}_{\text{corr}}$ for $\mathbf{f}$ at level l, namely

$$\mathbf{f}^{(l)}_{\text{corr}} = \tilde{\mathbf{f}}^{(l)} + P^{(l,l+1)}\mathbf{f}^{(l+1)}\,. \tag{2.A.22}$$

The operator $R^{(l+1,l)}$ is the *restriction* operator. The simplest restriction is *injection*, in which the residual at the coarser grid $l+1$ is taken directly from the corresponding points on the finer grid l. Since it is the odd values of j which are thereby included in the coarser grid, it is essential that the odd-even ordering in the Gauss-Seidel zebra relaxation is adhered to. The operator $P^{(l,l+1)}$ is the *prolongation* operator whereby the 'solution' $\mathbf{f}^{(l+1)}$ on the coarser grid is interpolated onto the finer grid. Here again the simplest choice is made, namely *bilinear interpolation.*

The matrix operator $\mathbf{A}^{(l+1)}$ at the coarser level $l+1$ is not obtained directly from the differential equation (2.A.12), but rather from the matrix operator $\mathbf{A}^{(l)}$ at level l. Substituting for $\mathbf{r}^{(l+1)}$ from (2.A.21) into equation (2.A.20), we obtain

$$\mathbf{A}^{(l+1)}\mathbf{f}^{(l+1)} = R^{(l+1,l)}(\mathbf{r}^{(l)} - \mathbf{A}^{(l)}\tilde{\mathbf{f}}^{(l)})\,, \tag{2.A.23}$$

which implies that

$$R^{(l+1,l)}(\mathbf{r}^{(l)} - \mathbf{A}^{(l)}\mathbf{f}^{(l)}_{\text{corr}}) = R^{(l+1,l)}(\mathbf{r}^{(l)} - \mathbf{A}^{(l)}\tilde{\mathbf{f}}^{(l)} - \mathbf{A}^{(l)}P^{(l,l+1)}\mathbf{f}^{(l+1)})\,,$$

and so

$$R^{(l+1,l)}(\mathbf{r}^{(l)} - \mathbf{A}^{(l)}\mathbf{f}^{(l)}_{\rm corr}) = \mathbf{r}^{(l+1)} - R^{(l+1,l)}\mathbf{A}^{(l)}P^{(l,l+1)}\mathbf{f}^{(l+1)}\,. \qquad (2.A.24)$$

Therefore, to minimise the residual $\mathbf{r}^{(l)} - \mathbf{A}^{(l)}\mathbf{f}^{(l)}_{\rm corr}$ for the corrected solution on the finer grid (assuming that the $(l+1)$th level has been solved exactly), the best choice for $\mathbf{A}^{(l+1)}$ is (Sonneveld *et al.* 1985)

$$\mathbf{A}^{(l+1)} = R^{(l+1,l)}\mathbf{A}^{(l)}P^{(l,l+1)}\,. \qquad (2.A.25)$$

During the coarsening half of each V-cycle, 4 zebra relaxations are applied at each level l to the equation (2.A.19), leaving a residual error $\mathbf{r}^{(l)} - \mathbf{A}^{(l)}\tilde{\mathbf{f}}^{(l)}$. This residual is then reduced to a coarser grid $l+1$ by the operation (2.A.21) with half as many mesh points in each direction, and the process is repeated until the coarsest possible grid has been reached. This requires storing the current solution at each level l. The coarsest grid is usually so small that direct methods, such as Gaussian elimination may be used to solve (2.A.19). Once the solution $\mathbf{f}^{(l+1)}$ at level $l+1$ has been obtained, it is interpolated to the grid on level l by applying the prolongation operator $P^{(l,l+1)}$. This provides the coarse-grid correction to the solution $\mathbf{f}^{(l)}$ at level l through equation (2.A.22). The errors introduced by the interpolation have a characteristic wavelength corresponding to the smallest scale of the grid at level l and so are quickly reduced by 4 further relaxations. This process is then repeated until the finest grid (level 0) has been reached. At level 0, an additional relaxation sweep is performed to determine whether or not the solution $\mathbf{f}^{(0)}$ has converged. If the maximum relative change in $\mathbf{f}^{(0)}$ is less than 10^{-5}, convergence is assumed. If convergence has not been attained, a further V-cycle is made. In general, no more than 3 V-cycles are required to obtain convergence.

In the above, it has been assumed implicitly that line relaxation by Gauss-Seidel zebra sweep can be applied at all levels $l+1$. This means that for all levels $l+1$, equation (2.A.20) must have the 5-point form

$$a^{(l+1)}_{i,j} f^{(l+1)}_{i-1,j} + b^{(l+1)}_{i,j} f^{(l+1)}_{i+1,j} + c^{(l+1)}_{i,j} f^{(l+1)}_{i,j-1} + d^{(l+1)}_{i,j} f^{(l+1)}_{i,j+1} + e^{(l+1)}_{i,j} f^{(l+1)}_{i,j} = r^{(l+1)}_{i,j} \qquad (2.A.26)$$

for the multigrid scheme described here to work. If (2.A.19) can be written in 5-point form for level l, it can be shown by explicitly expanding equation (2.A.25) that equation

(2.A.20) may also be written in 5-point form if restriction is by injection and prolongation is by bilinear interpolation. Since equation (2.A.19) can be written in 5-point form for level 0, the rest follows by induction. It suffices here to state that

$$\begin{aligned}
a_{i,j}^{(l+1)} &= (1-\alpha^{2i-2})a_{2i-1,2j-1}^{(l)} \\
b_{i,j}^{(l+1)} &= \alpha^{2i} b_{2i-1,2j-1}^{(l)} \\
c_{i,j}^{(l+1)} &= (1-\beta^{2j-2})c_{2i-1,2j-1}^{(l)} \\
d_{i,j}^{(l+1)} &= \beta^{2j} d_{2i-1,2j-1}^{(l)} \\
e_{i,j}^{(l+1)} &= \alpha^{2i-2} a_{2i-1,2j-1}^{(l)} + (1-\alpha^{2i}) b_{2i-1,2j-1}^{(l)} \\
&\quad + \beta^{2j-2} c_{2i-1,2j-1}^{(l)} + (1-\beta^{2j}) d_{2i-1,2j-1}^{(l)} + e_{2i-1,2j-1}^{(l)}
\end{aligned} \tag{2.A.27}$$

for $2 \le i \le M^{(l+1)} - 1$ and $2 \le j \le N^{(l+1)} - 1$. The interpolation factors α^{2i} and β^{2j} are given by

$$\alpha^{2i} = \frac{X_{2i} - X_{2i-1}}{X_{2i+1} - X_{2i}} \quad \text{and} \quad \beta^{2j} = \frac{Y_{2j} - Y_{2j-1}}{Y_{2j+1} - Y_{2j}}, \tag{2.A.28}$$

where X_i is the ξ-coordinate and Y_j the η-coordinate of the mesh point (i,j) on the finer grid l.

Chapter 3

Crystallization of a binary alloy at a vertical wall

II: Variable viscosity

3.1 Introduction

The model presented in Chapter 2 for the solidification of a binary alloy assumes that the fluid has constant viscosity. This is a reasonable assumption for aqueous salt solutions over a limited range of temperatures, but less so for magmas under natural conditions. The viscosity of a silicate melt is strongly dependent upon its temperature and composition. The viscosity of an andesitic magma, for example, increases by a factor of 10^5 as it cools from 1500 °C to below 1000 °C, with the most rapid increase occurring when crystals begin to form within the melt (Murase & McBirney 1973).

The boundary-layer flow for steady natural convection in a fluid of variable viscosity in contact with a cold vertical wall has been studied theoretically both for a thermally convecting melt (Spera *et al.* 1982) and for double-diffusive convection (Nilson *et al.* 1985). In both models, the viscosity of the fluid increased markedly in the vicinity of the vertical wall, by as much as 12 orders of magnitude, albeit over differing length scales. In the purely thermal model of Spera *et al.* (1982), the magmatic viscosity increases exponentially with temperature and the region of high viscosity therefore scales as the thickness of the thermal boundary layer. The increased viscosity in the neighbourhood of the wall reduces the vertical velocity in the boundary layer by no more than a single order of magnitude, even when the viscosity increase is at its greatest. Nilson *et al.* (1985) considered a model in which both compositional and thermal buoyancy forcings were present, with the viscosity dependent upon composition alone, and showed that a fluid with variable viscosity can be modelled by a fluid of constant viscosity if a suitable average, or effective, viscosity is chosen.

In this chapter, we investigate how the compositional stratification in an alloy crystallizing from a vertical sidewall is affected by temperature- and composition-dependent viscosity in the melt. We concentrate on the case in which light fluid is released at the solid/melt interface, *e.g.* a supereutectic aqueous salt solution or a magma fractionating along the calc-alkaline trend. Below, we briefly describe how the rheology of a magma changes with its temperature and composition. This enables us to obtain a sensible parametrised model for viscosity variations. In §2, we describe how the model of Chapter 2 is modified by considering variable viscosity and discuss how the scaling analysis of §2.3.2 in Chapter 2 may be altered. In §3, some numerical calculations are described

which show how the composition of solid growing into a variable-viscosity liquid binary alloy varies from that of a solid growing into an fluid of constant viscosity. We are able to demonstrate that the scaling analysis developed in Chapter 2 may still be applied, both qualitatively and quantitatively, to a variable-viscosity fluid by employing a suitable effective viscosity. Finally, the results presented in this chapter are discussed in §4.

3.1.1 The rheology of magma

Magmas exhibit a wide range of rheologies. Erupted basalts can flow freely and rapidly from their source, while rhyolites flow very slowly, often exhibiting non-Newtonian behaviour. The viscosity of a magma is in general dependent upon three quantities — temperature, composition of major elements and volatile content. In Figure 3.1, experimental results for the viscosity of various magmas are plotted against temperature (from McBirney & Murase 1984). Although there is a clear decrease in viscosity with increasing temperature, it is the compositional effects which dominate in determining the viscosity. The viscosity of a rhyolitic magma is several orders of magnitude greater than that of a basalt at the same temperature. In general, the viscosity of a magma is increased by the presence of the elements Si, Al and K, and reduced by the presence of Na, Ca, Fe and Mg (Murase 1962). Reference to Table 1.1 demonstrates that rhyolites differ from basalts in that they have higher Si and K contents, but lower proportions of Ca, Fe and Mg. The Al and Na contents do not vary appreciably as a magma evolves from basalt to rhyolite.

Several methods exist for the calculation of the viscosity of a magma from its major-element composition (Bottinga & Weill 1972, Shaw 1972, McBirney & Murase 1984) based on experiments with molten rock. The method of McBirney & Murase (1984) includes the substantial effect of suspended crystals, which increases the magma viscosity. The effective viscosity μ of a crystal-rich magma is often estimated from the empirical Einstein-Roscoe equation

$$\mu = \mu_0(1 - R\phi)^{-2.5}, \tag{3.1.1}$$

where μ_0 is the viscosity of the magma alone and ϕ is the volume fraction of crystals. The constant R reflects the manner in which the crystals are packed. Marsh (1981) has suggested that a value $R = 1.67$ is appropriate for magmatic liquids. This is based

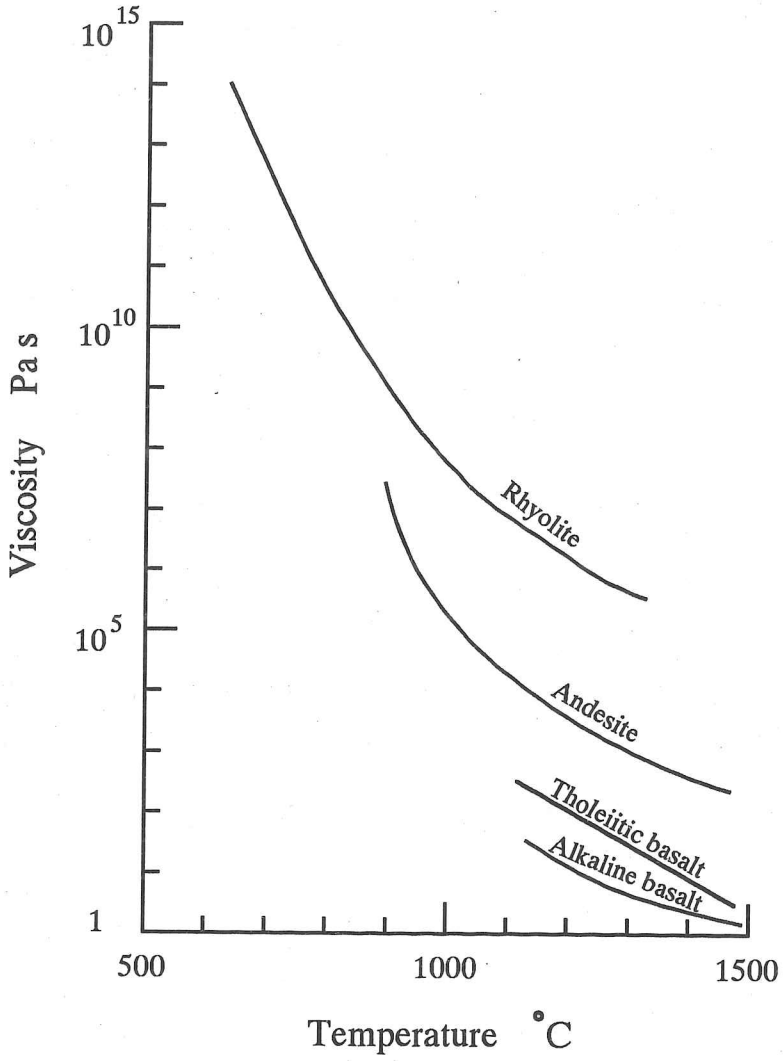

Figure 3.1. Experimentally determined viscosities for selected magmas as a function of temperature (from Murase & McBirney 1973). The progression from tholeiitic basalt to rhyolite is marked by an increase in silica (SiO_2) content. Alkali basalts typically have a high sodium oxide (Na_2O) content.

on the premise that the magma becomes immobile ($\mu \rightarrow \infty$) when the crystal content reaches 60%. Of significant importance is the volatile content, *e.g.* dissolved gases and water, which also has a strong effect on magma viscosity (Hall 1987). For example, 1 wt% of water lowers the viscosity of silica-rich magmas by nearly an order of magnitude (McBirney & Murase 1984). However, it is not always possible to determine the volatile content of the parent magma of an igneous rock because it can be significantly depleted in volatiles before and during eruption.

The increase in viscosity with silica content is due chiefly to the strength of the SiOSi bridging bonds (Hess 1989). The higher the temperature of the fluid, the weaker are the bonds, and polymerization is more likely for highly silicic melts. Therefore, the viscosity decreases with temperature and increases with silicity. Basaltic melts are approximately Newtonian, but rhyolites exhibit distinctly non-Newtonian behaviour. Typically, rhyolites exhibit shear-thinning behaviour, which is common in polymerized liquids. The transition between Newtonian and non-Newtonian behaviour has not been determined precisely, but probably occurs in magmas of rhyolitic to dacitic composition (Hess 1989). This corresponds to about 63–69 wt% SiO_2 (Wilson 1989). Magma which has evolved from a basaltic primary magma by fractional crystallization only shows such high silicity for relatively high degrees of fractionation. Therefore we may consider the flow to be Newtonian for the purposes of this study.

For a magma undergoing fractional crystallization, the fluid released at the solid/melt interface is colder and has a higher SiO_2 content than the bulk fluid. Therefore, the viscosity of the magma increases towards the solidification front both because of thermal effects and because of compositional effects. The picture is complicated by the presence of suspended crystals and volatiles, whose effects are not modelled here. Here, we make the choice

$$\mu = \mu_0 \left(\frac{\mu_w}{\tilde{\mu}}\right)^{(C_0-C)/(C_0-C_E)} \left(\frac{\tilde{\mu}}{\mu_0}\right)^{(T_0-T)/(T_0-T_E)}, \qquad (3.1.2)$$

where the initial (far-field) viscosity, temperature and composition are μ_0, T_0 and C_0 respectively; and viscosity, temperature and composition at the solid/melt interface are μ_w, T_E and C_E. The relative increase in viscosity due to thermal effects is $\tilde{\mu}/\mu_0$ and the relative increase in viscosity due to compositional effects is $\mu_w/\tilde{\mu}$. The models of Spera *et al.* (1982) and Nilson *et al.* (1985) correspond to $\tilde{\mu} = \mu_w$ and $\tilde{\mu} = \mu_0$ respectively. Equation (3.1.2) is the simplest parametrisation for a fluid whose viscosity is dependent upon both temperature and viscosity, and the dynamics can be described in terms of just three viscosities μ_0, $\tilde{\mu}$ and μ_w. For a fluid whose viscosity is given by equation (3.1.2), the viscosity is initially equal to μ_0 away from the cold boundary. The viscosity increases exponentially to $\tilde{\mu}$ at the outer edge of the compositional boundary layer, which is much thinner than the thermal boundary layer. There is then a further exponential rise due to compositional effects from $\tilde{\mu}$ to μ_w at the solidification front.

3.2 Theoretical considerations

In this section, we describe how the convection equations are altered by the inclusion of a variable viscosity. We then analyse the numerical results of Nilson *et al.* (1985) for boundary layer flow when compositional and thermal effects oppose each other, and argue that the effect of a temperature-dependent viscosity differs markedly from that of a composition-dependent viscosity. We propose a suitable effective viscosity for the application of the results of Chapter 2 for a fluid of constant viscosity to a fluid whose viscosity depends upon both composition and temperature.

3.2.1 Governing equations

The governing equations for a fluid with variable viscosity are the same as those for a fluid of constant viscosity, *i.e.* equations (2.3.2)–(2.3.6) in Chapter 2, with the exception of the momentum equation (2.3.2). For non-constant μ, the Boussinesq momentum equation is

$$\rho_0 \left(\frac{\partial \mathbf{u}}{\partial t} + \mathbf{u}.\nabla \mathbf{u} \right) = \nabla.\boldsymbol{\sigma} + \rho \mathbf{g}, \qquad (3.2.1)^*$$

where the density ρ is given by equation (2.3.1) in Chapter 2. We proceed as in §2.3 by taking the curl of the momentum equation and scaling all lengths by L and time by L^2/κ_{Tl}. Because μ is no longer constant, there are some additional terms in the vorticity equation. The nondimensional partial differential equations for the vorticity ω, liquid and solid temperatures T_l and T_s and the liquid composition C_l are

$$\frac{1}{Pr}\left(\frac{\partial \omega}{\partial t} + (\mathbf{u} - 2\nabla\chi).\nabla\omega \right) = Ra_T \frac{\partial T_l}{\partial x} - Ra_C \frac{\partial C_l}{\partial x} + \chi \nabla^2 \omega + \omega \nabla^2 \chi + 2\varepsilon_{3jk} \frac{\partial u_i}{\partial x_k} \frac{\partial^2 \chi}{\partial x_i \partial x_j}\,; \qquad (3.2.2)$$

$$\frac{\partial T_l}{\partial t} + \mathbf{u}.\nabla T_l = \nabla^2 T_l\,; \qquad (3.2.3)$$

$$\frac{\partial T_s}{\partial t} = \gamma \nabla^2 T_s\,; \qquad (3.2.4)$$

$$\frac{\partial C_l}{\partial t} + \mathbf{u}.\nabla C_l = \frac{1}{Le}\nabla^2 C_l\,; \qquad (3.2.5)$$

$$\nabla^2 \psi = -\omega\,, \qquad (3.2.6)$$

* where $\boldsymbol{\sigma} = -p\mathbf{I} + \mu\left[\nabla\mathbf{u} + (\nabla\mathbf{u})^{\mathrm{T}}\right]$ is the stress tensor.

where

$$\mathbf{u} = (\psi_y, -\psi_x)\,. \tag{3.2.7}$$

The nondimensional numbers Pr, Ra_T and Ra_C are defined as in equation (2.3.19), Chapter 2, using the initial (or far-field) kinematic viscosity $\nu_0 = \mu_0/\rho_0$. The definitions of γ and Le remain unchanged. The function χ describes the variations in viscosity due to temperature T and composition C. From (3.1.2), χ is given by

$$\chi = \left(\frac{\mu_w}{\tilde{\mu}}\right)^{(C_0-C)/(C_0-C_E)} \left(\frac{\tilde{\mu}}{\mu_0}\right)^{(T_0-T)/(T_0-T_E)}\,. \tag{3.2.8}$$

The boundary conditions are unaltered from Chapter 2. In this chapter, we continue to employ the simple eutectic binary alloy model. The growth regime is eutectic (see §2.2) and so the temperature T and liquid composition C_l at the solid/melt interface are T_E and C_E respectively. Therefore, equation (3.2.8) implies that initially $\chi \to 1$ far from the solidification front and $\chi = \mu_w/\mu_0$ at the solidification front. The equations (3.2.2)–(3.2.6) are solved using the same scheme as employed for a fluid of constant viscosity (see Appendix, Chapter 2), with the exception of the terms $\omega\nabla^2\chi$ and $\varepsilon_{3jk}(\partial u_i/\partial x_k)\,(\partial^2\chi/\partial x_i\partial x_j)$ on the right-hand side of (3.2.2). For each timestep, these two terms are evaluated at the previous timestep and thereafter treated as constant for the remainder of the timestep.

3.2.2 Scaling analysis

The scaling analysis presented in §2.3.2 is valid only for a fluid of constant viscosity. If the fluid viscosity increases by several orders of magnitude in the neighbourhood of the vertical wall, the boundary layer flow is substantially altered (Spera *et al.* 1982, Nilson *et al.* 1985). The fluid immediately adjacent to the wall is almost stagnant, with the width of the stagnant region increasing with the viscosity increase μ_w/μ_0. However, Nilson *et al.* (1985) were able to demonstrate that results for fluids of constant viscosity can be applied to fluids with variable viscosity by choosing a suitable average viscosity. Nilson *et al.* (1985) considered a suitable effective viscosity to be the weighted average

$$\mu_{\text{eff}} = (\mu_{\text{min}})^{4/5}(\mu_{\text{max}})^{1/5}\,, \tag{3.2.9}$$

which implies that the flow is controlled by the smaller viscosity. There is no single average

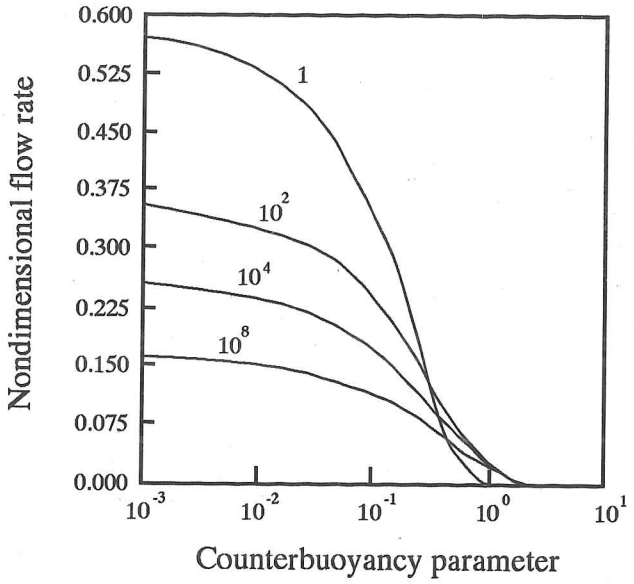

Figure 3.2. The nondimensional upward flow rate in the upflowing compositional boundary layer plotted against the counterbuoyancy parameter $\Gamma\, Le^{1/3}$ for differing values of the viscosity variation μ_w/μ_∞, where μ_∞ is the far-field viscosity and μ_w is the velocity at the vertical wall. The nondimensional upward flow rate has been scaled by $4^{-3/4} Le^{-3/4} {Ra_c}^{1/4}$ (in our notation), where Ra_c is based on the weighted average viscosity $\mu_{\text{eff}} = \mu_\infty^{4/5} \mu_w^{1/5}$ (after Nilson *et al.* 1985).

viscosity which can describe all features of the flow. The choice (3.2.9) of Nilson and co-workers appears to be based on their calculations for the maximum upward velocity in the rising compositional boundary layer flow. However, the aim of such boundary layer studies has been to determine the rate at which light, fractionated fluid collects at the roof of the chamber. This is given by the total upward flux in the compositional boundary layer. Therefore, the choice of an effective viscosity should be motivated by the upward flow rate, rather than the maximum upward velocity.

Figure 3.2 shows the nondimensional upward flow rate for the boundary layer flow plotted against the counterbuoyancy parameter $\Gamma\, Le^{1/3}$ as calculated by Nilson *et al.* (1985) for differing values of μ_w/μ_0. Small values of $\Gamma\, Le^{1/3}$ correspond to the compositional upflow dominating the thermal downflow. In our notation, the nondimensional flow rate is scaled by $4^{-3/4} Le^{-3/4} {Ra_c}^{1/4}$, with the Rayleigh number Ra_c defined in terms of the effective viscosity μ_{eff} given by equation (3.2.9). To within a numerical factor, this agrees with the nondimensional flow rate given by the product $v\delta_c$, where v and δ_c are given by

equations (2.3.34) and (2.3.35) respectively in Chapter 2. Figure 3.2 demonstrates that the choice (3.2.9) for the effective viscosity leads to order-of-magnitude agreement for the non-dimensional box-filling. However, the curves in Figure 3.2 can be collapsed further by making a different choice for the effective viscosity. The nondimensional flow rate halves when the viscosity ratio μ_w/μ_0 increases from 1 to $\sim 10^4$, or from 10^2 to $\sim 10^8$. This suggests that the average (3.2.9) is weighted too much in favour of the smaller viscosity for $1 < \mu_w/\mu_\infty < 10^8$, where μ_∞ is the far-field viscosity in the notation of Nilson *et al.* (1985). For smaller values of μ_w/μ_∞, the nondimensional flow rate (as plotted) is approximately proportional to $(\mu_w/\mu_\infty)^{-0.075}$, which corresponds to a decrease by a factor of 2 for an increase in μ_w/μ_∞ of a factor of 10^4. Therefore, since $Ra_c \propto \mu_{\rm eff}^{-1}$, the dimensional flow rate is approximately proportional to $\mu_{\rm eff}^{-0.25}(\mu_w/\mu_\infty)^{-0.075} = \bar{\mu}_{\rm eff}^{-1/4}$ where

$$\bar{\mu}_{\rm eff} = (\mu_\infty \mu_w)^{1/2} . \tag{3.2.10}$$

We therefore conclude that for relatively small variations in viscosity due to compositional effects ($1 < \mu_w/\mu_\infty < 10^6$), a better weighted average is the geometric mean of the minimum and maximum viscosities, as given by equation (3.2.10).

We now seek to apply the results of Nilson *et al.* (1985), which were obtained for viscosity μ dependent upon composition alone to the case of a fluid whose viscosity is dependent upon both composition and temperature. For $Le \gg 1$, the thermal boundary layer is much thicker than the compositional boundary layer. Therefore, from (3.2.8), we see that the nondimensional viscosity ($\chi \sim \tilde{\mu}/\mu_0$) is effectively uniform at the outer edge of the compositional boundary layer. Consequently, the rate of upflow in the compositional boundary layer is the same as if the far-field composition were equal to the intermediate viscosity $\tilde{\mu}$. Substituting $\tilde{\mu}$ for μ_∞ in equation (3.2.10), we see that the correct choice for an effective viscosity when both thermal and compositional effects are included is

$$\mu_{\rm eff} = (\mu_w \tilde{\mu})^{1/2} . \tag{3.2.11}$$

This corresponds to an effective nondimensional viscosity

$$\chi_{\rm eff} = \frac{\tilde{\mu}}{\mu_0}\left(\frac{\mu_w}{\tilde{\mu}}\right)^{1/2} , \tag{3.2.12}$$

which suggests that the increase in viscosity due to thermal effects is more important than

the increase in viscosity due to compositional effects. Note, however, that for magmas, composition can have a greater effect upon the viscosity than temperature (Figure 3.1). In the context of differentiation of magmas by fractional crystallization, equation (3.2.11) implies that the relevant viscosity in determining the rate at which the light, fractionated magma rises to the top of the chamber is the geometric mean of the viscosity of the primary magma (*e.g.* basalt) and the fractionated magma (*e.g.* andesite) *measured at their liquidus temperatures.* It is unclear whether the same restriction is likely to apply to magmas fractionating along the tholeiitic trend, as both compositional and thermal buoyancy forces act downwards at the solid/melt interface and so the transport of fractionated fluid is not restricted to the inner compositional boundary layer.

From equation (3.2.11), we see that the nondimensional effective viscosity is

$$\chi_{\text{eff}} = \left(\frac{\mu_w}{\tilde{\mu}}\right)^{1/2} \left(\frac{\tilde{\mu}}{\mu_0}\right) . \tag{3.2.12}$$

If the effective viscosity μ_{eff} successfully describes the boundary layer flow, as suggested by the results of Nilson *et al.* (1985), we may determine the ratio t_{BF}/t_S of timescales for box-filling and solidification. The Prandtl number Pr and the Rayleigh numbers Ra_C and Ra_T are defined in terms of the initial kinematic viscosity μ_0/ρ_0 and so equations (2.3.37) and (2.3.41) imply that

$$\frac{t_{BF}}{t_S} \sim \frac{\mathcal{A}^{1/4} Le^{3/4} {Ra_C}^{-1/4}}{\widehat{St}} \chi_{\text{eff}}^{1/4} = P\, \chi_{\text{eff}}^{1/4} , \tag{3.2.13}$$

where P is defined in Chapter 2 by equation (2.3.41) and $\widehat{St}$ is the modified Stefan number given by equation (2.3.22). The effect of increasing viscosity in the vicinity of the solid/melt interface ($\chi_{\text{eff}} > 1$) is to increase the effective value of P, which corresponds to a decrease in the box-filling rate.

The scaling suggested by (3.2.13) cannot be applied immediately to the solid composition as was done in Chapter 2 for a fluid of constant viscosity. The choice (3.2.11) for an effective viscosity is based upon the numerical results of Nilson *et al.* (1985) for the total upward flux in a steady, counterflowing boundary layer. The total upward flux scales as the product $v\delta_C$ of the upwards velocity in the compositional boundary layer and the

thickness of the compositional boundary layer. It is unclear from the results presented by Nilson *et al.* (1985) whether v and δ_c can individually be described by μ_{eff} or not. The compositional flux is proportional to $1/\delta_c$. Therefore, if δ_c can be determined from μ_{eff} the composition of the solid grown will also depend upon $P\,\chi_{\text{eff}}^{1/4}$ alone.

In the following section we investigate how the box-filling and solid stratification processes are affected by the dependence of the fluid viscosity upon temperature and composition for solidification of a simple eutectic binary alloy from one sidewall. From our numerical calculations, we are able to demonstrate that the solid composition can indeed be described by the parameter $P\,\chi_{\text{eff}}^{1/4}$.

3.3 Numerical results

A number of numerical calculations were performed to study how the convective gravitational separation process is altered by increased viscosity in the thermal and compositional boundary layers at the solid/melt interface. The calculations are summarized in Table 3.1 overleaf. With the exception of the viscosity, all dimensional parameters are the same for all calculations.

The Prandtl number Pr and both Rayleigh numbers, Ra_C and Ra_T, are based on the initial far-field viscosity $\mu_0 = \mu(T_0, C_0)$. Consequently, an increase in the initial viscosity μ_0 is reflected as an increase in the Prandtl number and a decrease in both Rayleigh numbers. However, the products $Pr\,Ra_C$ and $Pr\,Ra_T$ remain constant. The base values of the nondimensional parameters are chosen to reflect magmatic conditions, with the exception of the Prandtl number. The base Rayleigh numbers are $Ra_C = 10^{16}$ and $Ra_T = 10^{15}$ when $Pr = 10$. The base Lewis number $Le = 5 \times 10^3$ and the base Stefan number $St = 0.5$. The aspect ratio of the enclosure is unity. The dynamics of the laminar box-filling process and the solid stratification depend, as in Chapter 2, upon the nondimensional parameters Le, Ra_C, St and $\mathcal{A}$ (see equation (2.3.41) in Chapter 2). In addition, for our choice (3.1.2) of variable viscosity, the dynamics must depend upon the viscosity ratios $\mu_w/\tilde{\mu}$ and $\tilde{\mu}/\mu_0$, which are respectively the viscosity variations due to composition and temperature.

All other physical constants being fixed, the boundary layer dynamics depend upon $\mu_0\chi_{\text{eff}}$ alone. Therefore, the correct nondimensional parameter for describing the effect of variations in viscosity is $Pr\,\chi_{\text{eff}}$. If the Rayleigh number Ra_C is based on μ_0, then from (2.3.41) we see that $P \propto \mu_0^{1/4}$. Therefore, all other physical constants being fixed, $P\,\chi_{\text{eff}}^{1/4} \propto (Pr\,\chi_{\text{eff}})^{1/4}$ and so the dynamics are described by the nondimensional effective viscosity $Pr\,\chi_{\text{eff}}$. The presence here of the Prandtl number $Pr = \mu_0/\kappa_{Tl}$ is purely to provide a suitable nondimensionalisation for the initial (far-field) viscosity μ_0, and does not imply any dependence upon the thermal conductivity κ_{Tl}, which is fixed. Note that the value of $Pr\,\chi_{\text{eff}}$ is the same for Runs 3, 5 and 6, and for Runs 2, 7 and 8. In Table 3.1, the values of $Pr\,\chi_{\text{eff}}$ are listed for the 8 calculations. For numerical convenience, the Lewis number is reduced by a factor of 100 and the Stefan number increased by a factor of 10. This enables us to reduce the Rayleigh numbers Ra_C and Ra_T by a factor of 10^{10}

Run	*Prandtl number* $Pr = \mu_0/\kappa_{Tl}$	*Thermal variation* $\tilde{\mu}/\mu_0$	*Compositional variation* $\mu_w/\tilde{\mu}$	*Nondimensional effective viscosity* $Pr\,\chi_{\text{eff}}$
1	10	33.3	3	577
2	10	10	10	316
3	10	1	100	100
4	10	1	1	10
5	10	10	1	100
6	100	1	1	100
7	100	1	10	316
8	316	1	1	316

Table 3.1. Conditions for numerical calculations. For $Pr = 10$ the base Rayleigh numbers were $Ra_C = 10^{16}$ and $Ra_T = 10^{15}$. For other values of the Prandtl number, the Rayleigh numbers were such that $Pr\,Ra$ remained constant. In all cases, the Lewis and Stefan numbers had base values $Le = 5 \times 10^3$ and $St = 0.5$. For calculation, the base Lewis number was decreased by a factor of 100 and the base Stefan number increased by a factor of 10. This allowed the Rayleigh numbers to be reduced by a factor of 10^{10} (see equation (2.3.41) in Chapter 2). Note that the effective viscosity $Pr\,\chi_{\text{eff}}$ is the same both for Runs 3, 5 & 6 and for Runs 2, 7 & 8.

while still preserving the value of $P\,\chi_{\text{eff}}^{1/4}$.

Contours of liquid composition are plotted after a nondimensional calculation time $t = 0.2$ for Runs 1–4 in Figure 3.3, in which the solidified region is stippled. The nondimensional effective viscosity $Pr\,\chi_{\text{eff}}$ decreases from Run 1 to Run 4. Consequently, the rate at which the upper region of the enclosure fills with stratified fluid is greatest for Run 4 (Figure 3.3(d)) and least for Run 1 (Figure 3.3(a)). In addition, the compositional boundary layer adjacent to the advancing solid/melt interface becomes noticeably thinner as the effective viscosity decreases. The initial (far-field) viscosity μ_0 is the same for all four calculations. In Runs 1–3, the viscosity increases towards the solid/melt interface such that the viscosity μ_w at the solid/melt interface is the same in all three cases ($\mu_w/\mu_0 = 100$). However, the viscosity is essentially thermally determined in Run 1 and wholly compositionally determined in Run 3. Figure 3.3 therefore demonstrates that a given variation in viscosity due to temperature has a much stronger effect upon the bound-

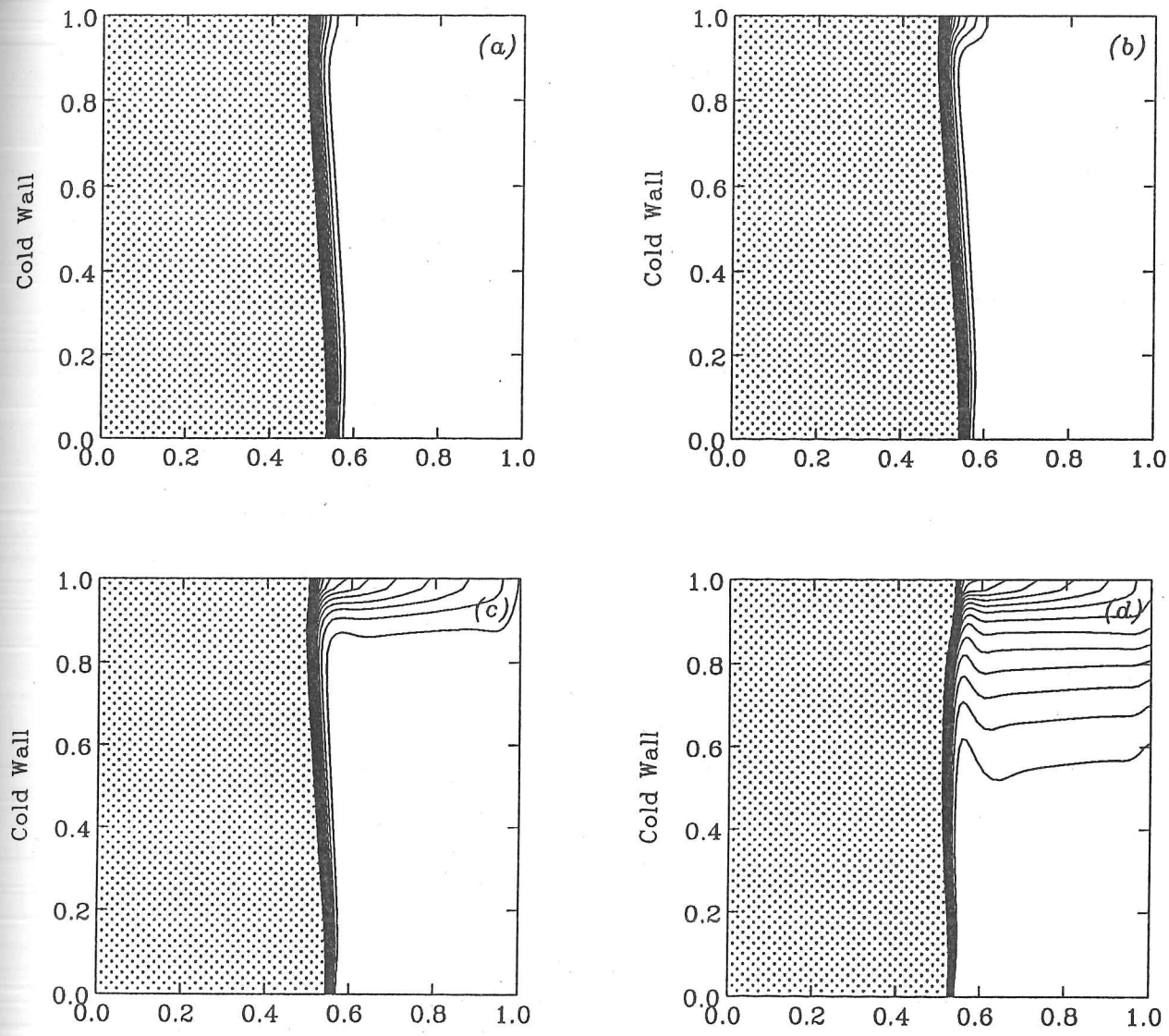

Figure 3.3. Contours of liquid composition for (*a*) Run 1; (*b*) Run 2; (*c*) Run 3; and (*d*) Run 4 (see Table 3.1) after a nondimensional time $t = 0.2$. The effective viscosity μ_{eff} decreases from (*a*) to (*d*). The initial (far-field) viscosity μ_0 is the same in all four cases, and the viscosity μ_w at the solidification front is the same for Runs 1–3. In Run 4, the fluid has constant viscosity. The relative dependence of the viscosity upon temperature compared with its dependence upon composition decreases from (*a*) to (*c*). This leads to more rapid box-filling rates. Note that the compositional boundary layer at the solid/melt interface becomes thinner as μ_{eff} decreases.

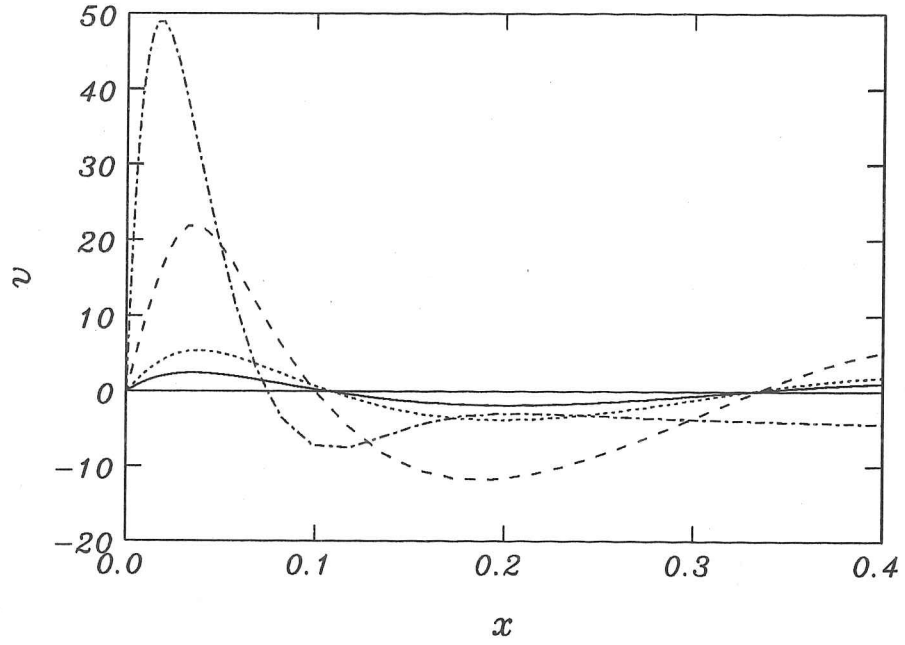

Figure 3.4. Upward velocity v plotted against distance x from the solidification front at the mid-height $y = 0.5$ for —— Run 1; ····· Run 2; – – – Run 3; and – · – Run 4 (see Table 3.1). The velocity v has been scaled by κ_{Tl}/L, where L is the dimensional length of the enclosure. As the effective viscosity μ_{eff} decreases, the influence of the compositional buoyancy forcing over the thermal buoyancy forces increases and consequently the upward flux of light fractionated fluid is enhanced.

ary layer flow than the same viscosity variation when determined by the composition of the fluid.

In Figure 3.4, the vertical velocity profile is shown at the mid-height $y = 0.5$ for the same four calculations. The strength of the upflow when there is no viscosity increase towards the solid/melt interface (– · –) is only about twice as great as when the viscosity increases by a factor of 100 close to the interface due to compositional differences alone (– – –). However, the upflow is reduced by over an order of magnitude if the same viscosity difference is predominantly thermally determined (——). This is because the compositional boundary layer is much narrower than the thermal boundary layer and so the region of upflow is entirely contained within the high-viscosity region.

The effect of variable viscosity upon the solid composition for Runs 1–4 is presented in Figure 3.5. For each calculation, two curves are plotted, the upper curve being the solid

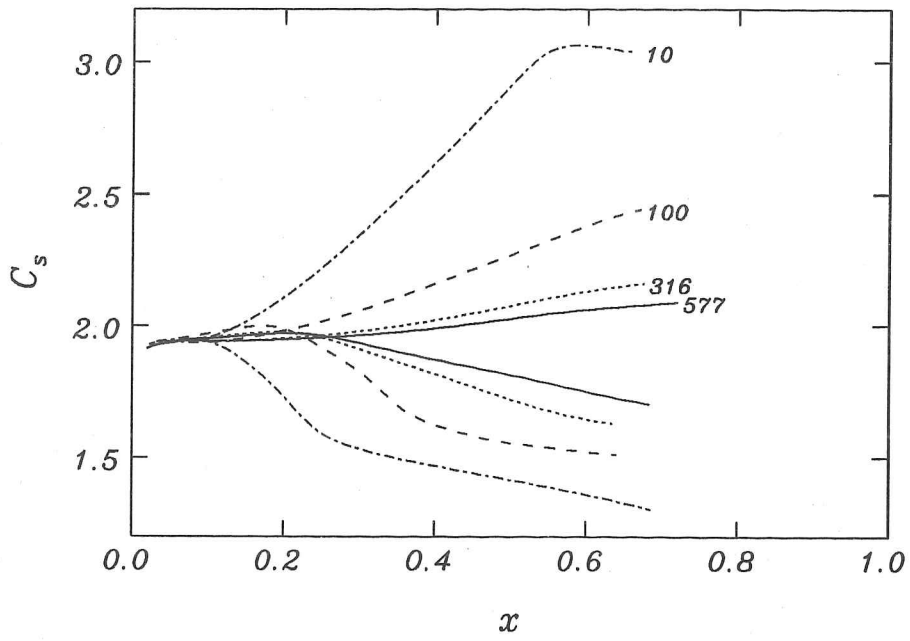

Figure 3.5. Nondimensional solid composition C_s plotted against distance x from the cold wall for —— Run 1; ····· Run 2; – – – Run 3; and – · – Run 4 (see Table 3.1). Two curves are plotted for each calculation, the upper curve corresponding to the base $y = 0$ of the enclosure and the lower curve corresponding to the roof $y = 1$ of the enclosure. The upper curves are labelled by the nondimensional effective viscosity $Pr\,\chi_{\text{eff}}$. The figure demonstrates that the degree of compositional variation observed in the solid as a result of convective fractionation is a strong function of the effective viscosity μ_{eff}.

composition along the base of the tank and the lower curve being the solid composition along the roof of the tank. The upper curves are labelled with the value of $Pr\,\chi_{\text{eff}}$ for each run. The degree of compositional stratification in the solid is represented by the difference between the upper and lower curves for each calculation. The stratification is a decreasing function of the effective viscosity $Pr\,\chi_{\text{eff}}$. This is consistent with the thinning of the compositional boundary layer with decreasing effective viscosity observed in Figure 3.3.

The dependence of the ratio t_{BF}/t_S of box-filling and solidification timescales upon the compound nondimensional parameter $P\,\chi_{\text{eff}}^{1/4}$ has been demonstrated by the boundary layer calculations of Nilson *et al.* (1985), and is discussed in §3.2.2 above. When all nondimensional parameters, with the exception of the dynamic viscosity μ, are held fixed, this translates to a dependence upon $Pr\,\chi_{\text{eff}}$. To determine the applicability of the

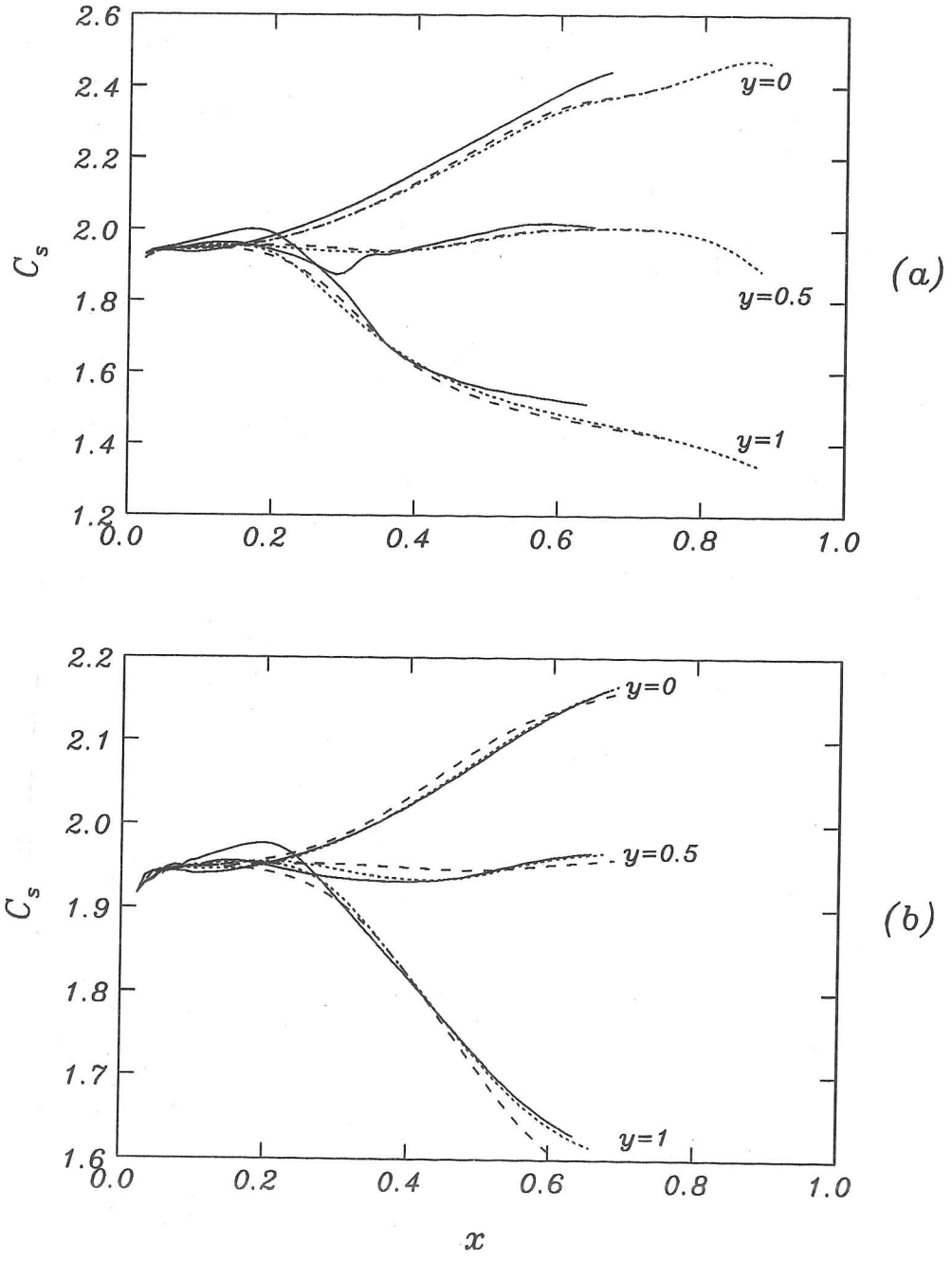

Figure 3.6. Nondimensional solid composition plotted against distance x from the cold wall at heights $y = 0$, $y = 0.5$ and $y = 1$. Figure (a) shows the curves for Run 3 (——), Run 5 (· · · · · ·) and Run 6 (– – –), all of which have the same nondimensional effective viscosity $Pr\,\chi_{\text{eff}} = 100$. Figure (b) shows the results of Run 2 (——), Run 7 (· · · · · ·) and Run 8 (– – –), all of which have $Pr\,\chi_{\text{eff}} = 316$.

effective viscosity μ_{eff} to the compositional flux at the solid/melt interface it is necessary to perform calculations with the same value of μ_{eff}, but with differing weightings between the variation in viscosity due to composition and the variation of viscosity due to temperature. Figure 3.6(a) shows the solid composition plotted at heights $y = 0$, $y = 0.5$ and $y = 1$ for Runs 3, 5 and 6. For all three runs, the nondimensional effective viscosity $Pr\,\chi_{\text{eff}} = 100$. The solid composition for Run 5 ($\cdots\cdots$, $Pr = 10$, $\tilde{\mu}/\mu_0 = 10$) is very close to that for Run 6 ($---$, $Pr = 100$, $\tilde{\mu}/\mu_0 = 1$). This is because the compositional boundary layer is much thinner than the thermal boundary layer. The flow in the compositional boundary layer is therefore essentially the same as if the far-field viscosity were equal to $\tilde{\mu}$. The solid composition for Run 3 (——) agrees reasonably well with Run 5 and Run 6, despite the viscosity at the solid/melt interface being an order of magnitude greater than for Runs 5 and 6. The calculated solid compositions for Runs 2, 7 and 8 ($Pr\,\chi_{\text{eff}} = 316$) are plotted on Figure 3.3(b). Runs 2 (——) and 7 ($\cdots\cdots$) yield similar results, again because they have the same compositional viscosity dependence ($\mu_w/\tilde{\mu} = 10$) and the intermediate viscosity $\tilde{\mu}$ is the same.

Taken together, Figures 3.6 (a) and (b) demonstrate that the effective viscosity (3.2.11) derived for the upwards flow rate also leads to quantitative agreement for the solid composition. This suggests that the compositional stratification due to convective fractionation in a eutectic binary alloy with composition and temperature-dependent viscosity can successfully be modelled by an fluid of constant viscosity by choosing an appropriate average viscosity based upon the viscosity at the solid/melt interface and the viscosity inside the thermal boundary layer.

3.4 Discussion

We have used the numerical model developed in Chapter 2 to investigate how an alloy may become compositionally stratified when its viscosity is dependent both upon its temperature and upon its composition. By appealing to the disparity in scales between the compositional and thermal boundary layers, we are able to separate the effects of composition from those of temperature. This enables us to apply more generally the results of a boundary layer model for a fluid whose viscosity is dependent upon composition alone (Nilson *et al.* 1985). The analysis presented here suggests that the rate of convectional fractionation of light fluid by upflow in the compositional boundary layer can be determined by modelling the fluid as being of a suitably chosen constant effective viscosity. In addition, our numerical calculations demonstrate that our choice (3.2.11) of an effective viscosity enables us to determine the composition of the solid grown.

If the variation in viscosity due to compositional differences $\sim 10^2$, the correct choice of effective viscosity is $\mu_{\text{eff}} = (\mu_w \tilde{\mu})^{1/2}$, which is the geometric mean of the fluid viscosity at the solidification front and the fluid viscosity within the thermal boundary layer, just outside the compositional boundary layer. For a magma, this means that fractionation is controlled by the high viscosity of the fluid within the thermal boundary layer, rather than the low viscosity of the magma in the interior of the chamber. This differs from the conclusions of Nilson *et al.* (1985), who argue that for large variations in viscosity between the bulk fluid and the fluid at the solid/melt interface, the flow is controlled by the smaller viscosity. The difference is for two reasons. Firstly, we argue that since the region of upflow is deep within the thermal boundary layer, the upflow is controlled by the viscosity of the fluid at, or below, its liquidus temperature, rather than the viscosity of the fluid in the interior. This is borne out by the numerical results presented here. Secondly, Nilson *et al.* (1985) based their discussion upon an assumed effective viscosity which is biased towards the lower viscosity. However, we have demonstrated here that an effective viscosity given by the geometric mean of the minimum and maximum viscosities within the thermal boundary layer is more appropriate for modelling the upward flux of fractionated fluid, which is after all the most important physical quantity described by the model of Nilson *et al.* (1985). A weighting towards the smaller viscosity is appropriate for large ($> 10^8$) variations in viscosity (Morris 1982), but the relevant viscosity difference for a thin compositional boundary layer within a thicker thermal boundary layer is the

variation in viscosity *due to compositional effects alone*, which is not as great as the total increase in viscosity across both the thermal and compositional boundary layers.

The apparent success with which the effective viscosity μ_{eff} can also be employed to determine the compositional flux into the solid deserves further investigation. I can see no clear physical reason why the upward flow rate and the thickness of the compositional boundary layer can be modelled by the same average viscosity.

To some extent, the results presented here depend upon our particular choice (3.1.2) for the viscosity. In order that we may treat the thermal boundary layer as effectively having infinite width, the viscosity must be a separable function of temperature and composition. In reality, this is not the case. The viscosity of the fluid will be significantly affected by the presence of suspended crystals. The crystal fraction is likely to be greatest where the magma is coolest, *i.e.* in the thermal boundary layer. Since the freezing temperature of an alloy depends upon its local composition, this means that the thermal and compositional viscosity effects cannot be completely separated. A more important qualification is that the model assumed here for the morphology of the solid/melt interface is highly idealised. In Chapter 2, it was demonstrated that a planar interface model is insufficient to describe fully the evolution of a supereutectic aqueous sodium carbonate solution, except in qualitative terms. It is not possible to observe a solidifying magma chamber directly, and so the morphology of the solid/melt interface for a cooling igneous intrusion remains open to question. However, the planar interface assumption, combined with the dimensional analysis presented in this dissertation, does allow us to analyse numerically parameter regimes appropriate to convecting magmatic systems, and to demonstrate the direct applicability of experiments with constant-viscosity aqueous salt solutions to the crystallization of magma chambers. As such, the work presented here provides a useful insight into some of the physical processes which are important during the formation of igneous rocks within the Earth's crust.

Chapter 4

Thermal erosion by turbulent lava flows

4.1 Introduction

Present-day basaltic lavas are erupted at temperatures in the range 1000–1200 °C (Macdonald 1972) and can have quite a high crystal content. They are relatively viscous (10^2–10^4 Pa s) and consequently exhibit laminar flow. The origin of these lavas is deep in the upper mantle, some 50 km below the Earth's surface, and they are formed by the partial melting of peridotite (Hall 1987). This is a magnesium-rich rock of which most of the Earth's mantle is believed to be composed. In general, ancient volcanic rocks can be recognised as having been formed from similar lavas to those observed today, with the significant exception of the *komatiites*, named after the Komati River in South Africa, in the vicinity of which they were first discovered by Viljoen & Viljoen (1969). Eruption of komatiitic lavas was restricted to the Archaean (2.5–4 $\times$ 10^9 years ago), and the lavas erupted were much richer in magnesium oxide (MgO) than present-day lavas (Nisbet 1987). In addition, komatiites often exhibit a dendritic crystal structure, suggesting that they were formed by rapid quenching of a highly magnesian liquid, rather than by slow freezing of a less picritic (*i.e.* less rich in MgO) basaltic magma (Hall 1987). Komatiites are of great interest to geologists because they offer the best evidence for the composition and temperature of the Archaean mantle. In addition, they are associated with many valuable mineral deposits.

Formation of a highly magnesian lava requires a higher degree of melting of the peridotite at depth, and so erupted komatiitic lavas were much hotter (1300–1600 °C) than present-day lavas. They were also less viscous (0.05–1 Pa s), partly due to their higher temperature and partly due to their composition, particularly their low silica (SiO_2) content. The greater degree of melting which produced the komatiitic melt may well be because the Archaean mantle was hotter than it is today (Nisbet 1987). Alternatively, the melt may have originated from a greater depth, perhaps 150 km below the Earth's surface (McKenzie 1984). Typically, the flow of these lavas was turbulent and accompanied by vigorous thermal convection (Huppert *et al.* 1984). The heat transfer from a hot, turbulent fluid is significantly greater than that from a laminar flow. The melting temperature of the Archaean crust was 850–1200 °C, depending on its local composition, and so the komatiitic lava melted the ground over which it flowed, cutting a channel into the sedimentary surface rocks and the underlying basalt (Huppert *et al.* 1984, Huppert & Sparks 1985*a*). Many komatiitic lavas were erupted on to the Archaean seafloor (Nisbet

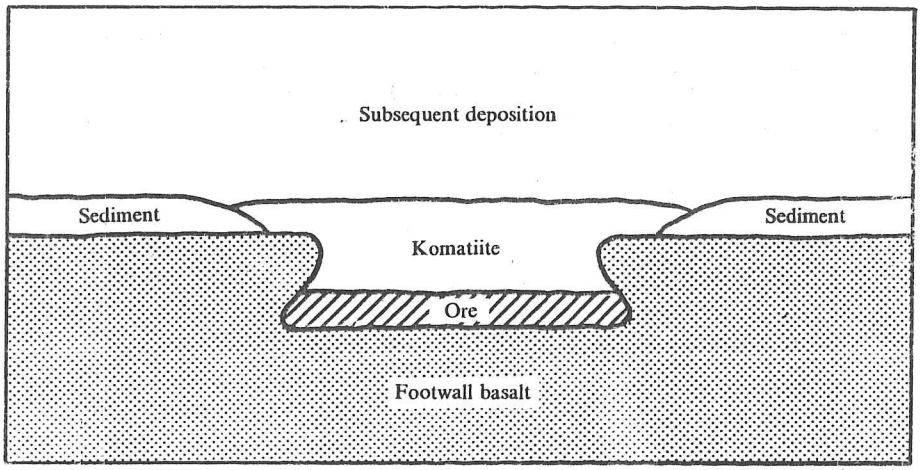

(a)

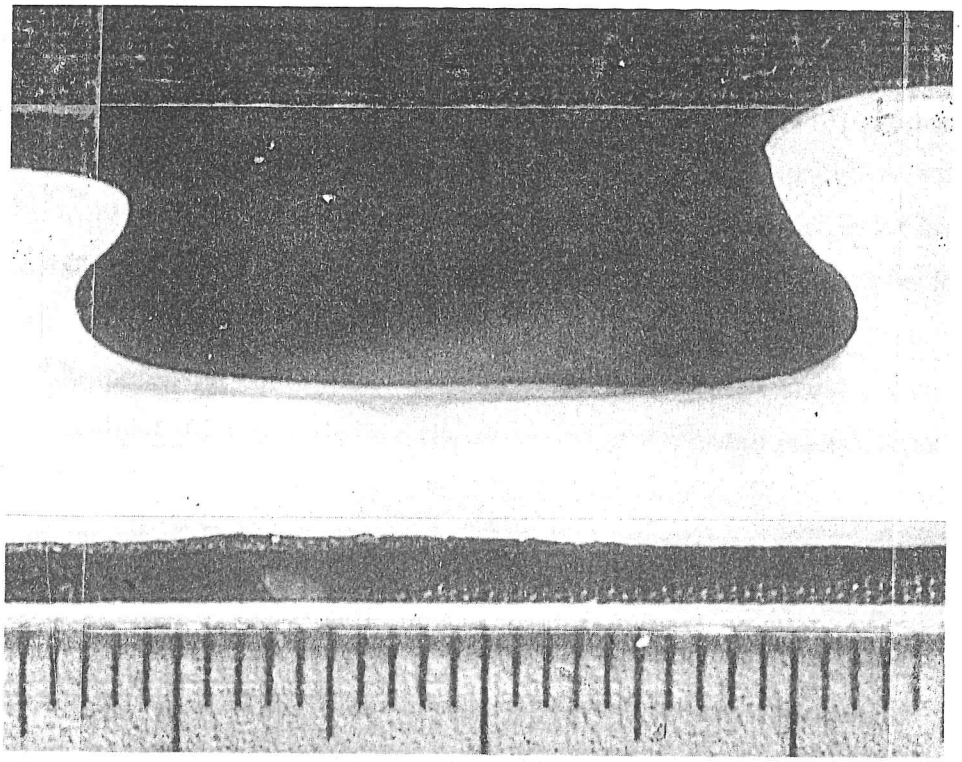

(b)

Figure 4.1. Cross-sections of channels eroded by (*a*) komatiite lavas in Kambalda, Western Australia (from Huppert 1986, after Lesher 1983), and (*b*) hot water flowing down a wax slope (Huppert 1986). Note the similar channel shapes, suggesting that the Kambalda feature is a thermally eroded channel rather than a collapsed lava tunnel or the result of mechanical erosion.

1987), and therefore it is likely that a crust formed on their upper surfaces (Huppert & Sparks 1985*a*). The width of the channel eroded was most likely to be determined either by the length of the fissure from which the lavas erupted, or by existing topographical features. In melting the seafloor, the lava became contaminated by the crustal material — in particular, komatiitic lavas at Kambalda, Western Australia, became enriched in sulphur, which allowed their nickel content to precipitate and crystallize as nickel sulphide ore. Observations (Lesher 1983) reveal that the ore is to be found below the komatiite in long, linear depressions, typically tens of kilometres in length, hundreds of metres in width and tens of metres in depth. Huppert & Sparks (1985*a*) conducted some experiments with hot water flowing down a wax slope. They demonstrated that the cross-sectional geometry of the channels observed in the Kambalda orefields is consistent with the hypothesis that they were formed by thermal erosion (see Figure 4.1).

Similar features have been observed on the Moon. Hulme (1973) proposed that some lunar sinuous rilles in the mare regions were formed by thermal erosion. A typical example, visited by Apollo 15, is the Hadley rille, near the Mare Ibrium, which is 1.2 km wide, 270 m deep and 135 km long (Allaby & Allaby 1990). Hulme constructed a model for the erosion of these channels, based on the assumption that the lava cooled by radiation from its upper surface. The potential contamination of lavas by the seafloor crust presents difficulties for the geochemist if he is to deduce the state of the Archaean mantle from observations of ancient igneous rocks. Huppert *et al.* (1984) and Huppert & Sparks (1985*a*) adapted the earlier model of Hulme (1973) to a seafloor komatiitic eruption, in which the lava flow was fully turbulent and cooled by convective heat transfer to the ground and to the thin crust which formed on its upper surface. They found that the lava could have been contaminated by up to 10%. Contamination is also likely to have occurred in the fissure, as the magma ascended through the crust (Huppert & Sparks 1985*b*). An interesting feature of erosion by hot, turbulent fluids was observed by Huppert & Sparks (1985*a*). On occasion, the channel was observed to split into two as it was eroded, with an island forming in the centre of the stream. Huppert (1986) suggested that this phenomenon was due to variations in melting rate with the local depth of the current. If the fluid were locally shallow, the solid below melts more slowly than the surrounding solid. Therefore, perturbations to the approximately horizontal floor would grow, leading eventually to the formation of islands.

The models of Hulme (1973), Huppert *et al.* (1984) and Huppert & Sparks (1985*a*) were two-dimensional, solving for the channel depth as a function of the distance downstream from the erupting fissure. In these models, the lava flow effectively had infinite width. In this chapter, a new predictive model for the cross-sectional geometry of thermally eroded channels is introduced, which allows us to see how the erosion of a channel of finite width differs from the erosion of a channel of infinite width. In addition, we are able to investigate the stability of the channel geometry to the destabilising influence of current depth-dependent melting rates.

In §4.2, we discuss the physical properties of the lava flow and see how its mean downstream velocity and heat transfer properties vary with cross-sectional geometry. The lava flow is assumed to be turbulent and flowing down a gently sloping seafloor, with a steady state balance between potential energy loss in the lava and friction at its perimeter. We also derive a quasi-steady solution for the melting of a curved surface subject to a constant heat flux per unit area. We show that convex surfaces melt more rapidly than concave surfaces, which provides a mechanism for the damping of perturbations to the channel cross-sectional shape.

In §4.3, the model for the cross-sectional geometry of a thermal erosion channel is formulated. The rate of melting of the solid is dependent upon the temperature of the lava and the intensity of the flow, but if the fluid is assumed to be well-mixed cross-stream, an analytical solution for the channel cross-sectional shape can be found. This solution suggests that the channel geometry depends only upon the total downwards erosion and a single non-dimensional parameter α. The thermal equations of Huppert & Sparks (1985*a*) are then extended for application to the case of a hot, turbulent fluid flowing down a channel of varying cross-section. The model equations are reduced to two first-order partial differential equations, which can be solved numerically along characteristics to find the full time-dependent solution for the thermal erosion of a channel. However, analytical techniques based upon the partial differential equations are preferred for the bulk of this chapter as they lead to greater clarity of argument. A new analytical solution is derived for the lava contamination as a function of lava temperature. As the lava cools, the thermal erosion may be limited either by the lava becoming so viscous that the flow becomes laminar (thus reducing the erosion rate by an order of magnitude), or by the lava freezing when it reaches its solidus temperature. Using the analytical solution for

lava contamination, we are able to see how the maximum lava contamination varies with the melting temperature of the seafloor.

In §4.4, we use the model described in §4.3 to show that for sufficiently narrow channels, the extent of the erosion and the degree of contamination of the lava can differ markedly from the predictions of the model of Huppert & Sparks (1985*a*). Specifically, lava flowing down a narrow channel erodes less deeply, but becomes more contaminated, than a lava flowing in an infinitely wide channel with the same flow rate per unit width. In addition, some algebraic corrections are made to the earlier analyses of Huppert and coworkers, the most important being an increase in the predicted maximum contamination to around 20%. Finally, in §4.5, a more complete model of the thermal erosion is studied, in which the rate of thermal erosion is allowed to vary with the local thickness of the lava flow. It has been suggested by Huppert & Sparks (1985*a*) that cross-stream variations in the ground melting rate can lead to geometrical instabilities, such as the splitting of the erosion channel into two, as observed in their wax melting experiments. If the melting rate is greatest where the lava is deepest, perturbations to the channel shape will grow. Using the model introduced in §4.3 for the channel shape, combined with a parameterised model for the variation in melting rate with lava depth, we are able to predict critical conditions for geometrical instability to occur. We conclude that instability is most likely to occur in lava flows of low cross-sectional aspect ratio and that the fastest growing mode has wavelength approximately equal to the width of the channel.

4.2 Preliminaries

In this section, we discuss the nature of the lava flow and the heat transfer between the fluid and the solid. We then discuss how the local thermal and flow conditions affect the rate of melting of the solid. In addition, we find a solution for the quasi-steady melting of a curved surface, which suggests a mechanism for the damping of perturbations to the cross-sectional shape of the erosion channel.

4.2.1 Magma ascent and lava flow

The viscosity of a magma is strongly dependent upon its temperature T, its composition C and upon its crystal content. For a komatiitic lava, the volume fraction $\phi(T)$ of crystals is approximately linearly dependent on the temperature, with $\phi'(T) = -\frac{1}{625}\ ^{\circ}\mathrm{C}^{-1}$ (Arndt & Nesbitt 1985). An adequate approximation for the viscosity μ (in Pa s) as a function of temperature (in $^{\circ}$C) for a lava of komatiitic composition, including the effects of the crystal content is (Huppert & Sparks 1985*a*)

$$\mu = \exp(34.551 - 0.0226T). \tag{4.2.1}$$

This is the Newtonian shear viscosity. It should be noted that lavas below their liquidus can exhibit non-Newtonian behaviour. It is a commonplace in the geological literature that lavas have a significant yield stress, owing chiefly to the suspension of olivine (Mg_2SiO_4) crystals in the fluid. However, Kerr & Lister (1991) argue that a lava can only have a yield stress if it has a sufficiently high crystal fraction for a connected matrix to form, thus allowing the absorption of small stresses. Otherwise, the fluid must flow subject to even the smallest applied stress. Kerr & Lister (1991) suggest that the prediction of a yield stress originates from the incorrect assumption that silicate lavas behave like Bingham plastics, with a linear relationship between strain and applied stress. However, the available stress/strain data can also be interpreted as evidence that lavas exhibit shear-thinning behaviour, with no yield stress, but a reduction in the apparent shear viscosity (as measured by a viscometer) as the applied stress is increased. Komatiitic lavas were relatively hot and consequently had a relatively low crystal content by comparison with present-day lavas. In the present study, therefore, we consider the flow of komatiitic lavas to have been Newtonian.

The lava is assumed to be erupted from a long, thin fissure of width d. The two-dimensional discharge rate q can be derived from a balance between wall friction and buoyancy as the magma rises up the fissure. An estimate of the wall friction can be obtained by considering empirical relationships for turbulent pipe flows. For a smooth circular pipe of radius r, the balance between friction and buoyancy may be written

$$\frac{\lambda}{2r}\frac{1}{2}\rho u^2 = g\Delta\rho, \tag{4.2.2}$$

where ρ is the density of the magma and $\Delta\rho$ the difference in density between the magma and the Earth's crust. For depths up to 100 km, $\Delta\rho \sim 100\,\mathrm{kg\,m^{-3}}$ (Nisbet & Walker 1982) and $\rho = 2800\,\mathrm{kg\,m^{-3}}$. Here, λ is the nondimensional friction coefficient, which for a circular pipe is (Schlichting 1960):

$$\lambda = 0.32\,Re_{2r}^{-0.25}. \tag{4.2.3}$$

Re_{2r} is the Reynolds number based on the pipe diameter $2r$ and the average streamwise velocity u. Flow is turbulent for $Re \gtrsim 500$. For a non-circular duct, (4.2.3) can be used by substituting the hydraulic radius $R_H = A/P$ for r, where A is the cross-sectional area of the duct and P the wetted half-perimeter. For a rectangular duct very much longer than it is wide, the hydraulic radius $R_H = d$, the width of the fissure. Substituting for R_H and $u = q/d$ in (4.2.2),

$$q = \left(\frac{g\Delta\rho}{\lambda'\rho}\right)^{1/2} d^{3/2}, \tag{4.2.4}$$

where $\lambda' = 0.067\,Re_d^{-0.25}$. The Reynolds number $Re_d = q/\nu$ and $\nu = \mu/\rho$ is the kinematic viscosity of the fluid. Typical values for λ' are 0.002 to 0.01. This differs from the analyses of Wilson & Head (1981) and Huppert & Sparks (1985*a*). Wilson & Head (1981) considered magma rising up a rough-sided fissure, for which the friction coefficient is independent of the Reynolds number, and used $\lambda' = 0.005$. This falls in the above range. However, Huppert & Sparks (1985*a*) chose $\lambda' = 0.03$, which is an order of magnitude greater. Reference to Schlichting (1960) reveals that the expression (4.2.3) for the drag coefficient applies to circular pipes and the drag coefficient λ is defined by the particular drag-buoyancy balance (4.2.2). Application of the empirical relation (4.2.3) to *non-circular* cross-sections can only be made through the hydraulic radius $R_H = d$.

d (m)	q (m^2s^{-1})	u (ms^{-1})	Re
0.3	1.37	4.58	1.3×10^4
1.0	8.37	8.37	7.8×10^4
3.0	43.5	14.5	4.1×10^5
10.0	265	26.5	2.5×10^6

Table 4.1. Flow rates q for the ascent of magma through fissures of various widths d. Flow rates are given by $q = (g\Delta\rho/\lambda'\rho)^{\frac{1}{2}} d^{\frac{3}{2}}$, where $g = 9.8$ ms^{-2}, $\Delta\rho = 100$ $kg\,m^{-3}$, $\rho = 2800$ $kg\,m^{-3}$ and $\lambda' = 0.005$. The eruption velocity $u = q/d$ and the Reynolds number $Re = \rho q/\mu$, where $\mu = 0.3$ Pa s.

Huppert & Sparks (1985*a*) apply the relation $\lambda' = 0.32\, Re_d^{-0.25}$ (in the notation employed here) to (4.2.4), which is incorrect. For convenience, λ' is hereafter chosen to be constant, its order of magnitude given by a typical value of the Reynolds number. Here, the choice $\lambda' = 0.005$ is made (corresponding to $Re_d = 3 \times 10^4$), and corrected values for the flow rate q, Reynolds number Re and velocity u as functions of the fissure width d are presented in Table 4.1 for the ascent of liquid peridotite in a long, thin fissure. Even for the smallest fissure, the Reynolds number Re is sufficiently large for the flow to have been turbulent and two-dimensional flow rates range from around 1 to 250 m^2s^{-1}. Since the corrected Reynolds numbers are higher than the original values obtained by Huppert & Sparks (1985*a*), their conclusion that erupted komatiitic lavas were likely to have exhibited turbulent flow is confirmed.

In this chapter, a submarine eruption is considered. Once erupted, the lava flows out along the seabed, eroding a channel and assimilating the pre-existing rock. Heat is also lost to the water above, leading to the formation of a thin crust (Huppert *et al.* 1984, Huppert & Sparks 1985*a*). The lava flow is therefore enclosed by solid. Two models of the lava flow can be formed, one for frictionless flow over a horizontal plane, and the other for flow down a rough incline. In the two-dimensional analysis of Huppert & Sparks (1985*a*), the former model is employed and the lava flow has a constant thickness upstream from the head of the gravity current. For a steady two-dimensional gravity current of density ρ flowing out over a horizontal plane with two-dimensional flow rate q, the current thickness is (Britter & Simpson 1978)

$$H = \left(\frac{q^2 \rho}{2g\Delta\rho} \right)^{\frac{1}{3}}, \tag{4.2.5}$$

where $\Delta\rho$ is now the difference in density between the gravity current and the overlying water. However, for a lava flow of finite width, the gravity current thins as it erodes outwards and streamwise and cross-stream variations in the extent of the downwards erosion means that the gravity current thickness is constant neither in space nor in time. It is not clear, therefore, how one may model a finite-width lava flow as a frictionless gravity current flowing over a horizontal plane. A turbulent gravity current is also subject to frictional forces. Indeed, Britter & Linden (1980) note that it is not possible to maintain a steady flow for a gravity current flowing down an incline shallower than about 0.3°. For a current flowing down a slope inclined at an angle χ to the horizontal, the boundary friction is balanced by the buoyancy force down the slope for $\chi \gtrsim 0.5°$ (Britter & Linden 1980). Therefore, we may write (*c.f.* (4.2.2))

$$\frac{\lambda}{2R_H} \frac{1}{2} \rho U^2 = g\Delta\rho \sin\chi, \tag{4.2.6}$$

where U is the mean current velocity. The drag coefficient λ is set to be constant, with $\lambda = 0.02$ corresponding to the value used above in modelling the magma ascent. In addition, we must have conservation of mass, and so

$$UA = Q, \tag{4.2.7}$$

where A is the local cross-sectional area of the current and Q the three-dimensional volume flux. Combining (4.2.7) with (4.2.6) and substituting $R_H = A/P$ for the hydraulic radius, where P is the wetted half-perimeter of the current cross-section, we obtain

$$\frac{A^3}{P} = \frac{Q^2 \rho \lambda}{4g\Delta\rho \sin\chi}. \tag{4.2.8}$$

As the channel widens, the wetted half-perimeter P increases and (4.2.8) implies that the cross-sectional area must also increase to maintain the balance between boundary friction and buoyancy. The extent of the lateral erosion decreases with distance downstream of the source as the lava cools. The wetted half-perimeter P therefore decreases with downstream distance, as must the current cross-sectional area A. If the flow rate Q is constant,

equation (4.2.8) is a purely local balance which depends only upon the extent of the erosion at a given distance downstream. In §4.3, we see how this enables us to solve for the channel shape as a function only of the total depth eroded. We show that the degree to which contamination occurs varies with time as the channel geometry changes. There is negligible loss of mass due to the formation of a thin crust as the crust thickness varies little whilst the lava flow is strong (Huppert & Sparks 1985*a*). However, Q must increase with distance downstream from the source as the eroded ground material is assimilated into the current. The flow rate Q becomes a function of downstream distance and of time and so equation (4.2.8) is no longer local, but dependent on upstream erosion. For convenience, therefore, we make the simplifying assumption that Q is constant. This approximation is studied more closely in §4.3.3.

In the limit of current breadth $2W \rightarrow \infty$, $P \sim 2W$ and $A \sim 2WH$ and so (4.2.8) implies that the current has constant thickness $H = (\frac{1}{4}q^2\rho\lambda/g\Delta\rho\sin\chi)^{1/3}$, where $q = Q/2W$ is the equivalent two-dimensional volume flux. Comparison with equation (4.2.5) shows that in the limit $2W \rightarrow \infty$, the predicted current thickness is the same as in the horizontal-plane model used by Huppert & Sparks (1985*a*) if $\lambda = 2\sin\chi$, *i.e.* $\chi = 0.6°$ for $\lambda = 0.02$. To aid comparison of the current model with that of Huppert & Sparks (1985*a*), the drag coefficient λ and seafloor slope χ are assumed here to be such that $\lambda = 2\sin\chi$. For lava flows of low aspect ratio, the downstream velocity of the lava decreases as the channel widens, whether the flow is modelled as a gravity current or by a balance between buoyancy and drag. As the channel widens, a gravity current becomes thinner, leading to a reduction in its mean downstream velocity. For a lava flow controlled by a buoyancy-friction balance, the ratio of buoyancy to frictional forces is approximately equal to the ratio of the cross-sectional area of the flow to the wetted perimeter. The latter ratio decreases as the channel widens, and so the mean downstream velocity of the lava decreases with time at a fixed distance downstream from the source.

4.2.2 Heat transfer and thermal erosion

The heat flux from a turbulent lava flow can be estimated from empirical expressions for turbulent pipe flow. For a smooth pipe of radius r, the heat flux per unit length from a hot gravity current at temperature T_{gc} to the pipe walls at temperature T_m is (Holman

1976),

$$\mathcal{H} = h_T(T_{gc} - T_m), \tag{4.2.9}$$

where

$$h_T = 0.023\frac{k}{2r}Pr^{0.4}Re_{2r}^{0.8}. \tag{4.2.10}$$

Here k is the thermal conductivity of the fluid and Pr its Prandtl number. The Reynolds number Re_{2r} is now based on the cross-sectionally averaged downstream velocity U. For a non-circular duct, the relevant radius is the hydraulic radius R_H. For a lava flow of constant thickness H and breadth $2W$, $R_H = H$ for $h \ll W$ and so $h_T = 0.02(k/H)Pr^{0.4}Re_H^{0.8}$, as used by Huppert & Sparks (1985*a*). For the variable-width channel flow studied here, (4.2.10) becomes, upon substituting for R_H,

$$h_T = 0.02\,\rho c_p \kappa_T^{0.6}\nu^{-0.4}Q^{0.8}\left(\frac{P}{A^5}\right)^{0.2}, \tag{4.2.11}$$

where c_p is the thermal capacity and $\kappa_T = k/\rho c_p$ the thermal diffusivity of the lava. The heat transfer coefficient h_T is therefore dependent upon the temperature (through the kinematic viscosity ν) and the channel geometry (through the cross-sectional area A and the wetted half-perimeter P).

For a constant heat flux applied to a planar erodible bed, the rate of melting of the bed can be determined from the steady state balance between the heat supplied by the melt, the heat conducted into the solid and the latent heat required to melt the solid. The initial value problem for hot, turbulent fluid flowing over an erodible bed has been solved by Huppert (1989), who showed that a steady state is reached very rapidly. For a heat flux $\mathcal{H}$ applied to a solid with melting temperature T_m and far-field temperature T_∞, the rate of melting v is (Hulme 1973, Holman 1976, Huppert *et al.* 1984, Huppert & Sparks 1985*a*):

$$v = v_0 \equiv \frac{\mathcal{H}}{\rho c_p(T_m - T_\infty + Lc_p^{-1})}, \tag{4.2.12}$$

where L is the latent heat of melting of the ground material. For simplicity, the densities of the komatiitic lava and the seabed material are assumed to be equal.

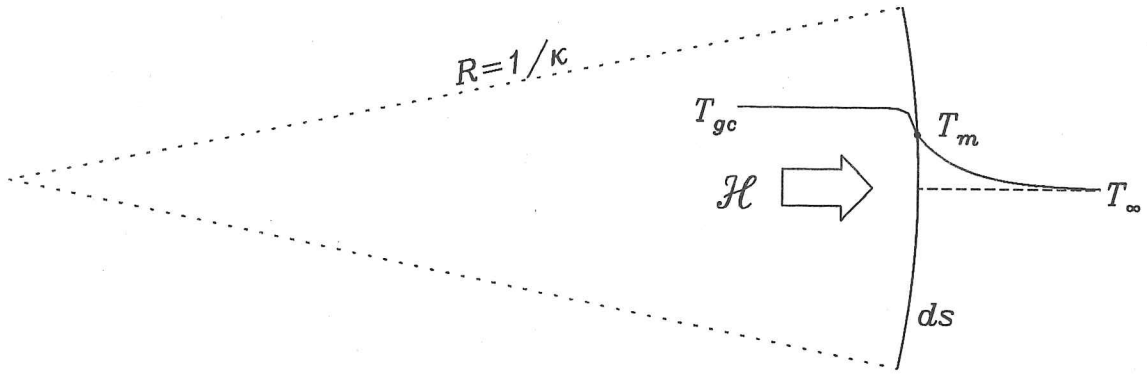

Figure 4.2. Schematic to illustrate idealised problem of a surface of length ds of constant curvature $\mathcal{K}$ (radius of curvature $R = 1/\mathcal{K}$) eroded due to constant heat flux $\mathcal{H}$. A local polar coordinate system is used to solve the steady-state problem.

We can also derive a quasi-steady solution for the rate of melting of a curved surface. Consider a surface whose curvature $\mathcal{K}$ is piecewise constant, *i.e.* composed of a number of circular arcs. The curvature $\mathcal{K}$ should not be confused with the thermal diffusivity $\kappa_T = k/\rho c_p$. For a line segment of length ds, choose a polar coordinate system (r, θ) so that the line segment corresponds to $r = R$, where $R = 1/\mathcal{K}$ is the radius of curvature (see Figure 4.2). For uniform normal melting of the line segment, $dR/dt = v$, the rate of melting. At the channel wall, the heat balance is

$$\mathcal{H} = \rho L v - k \left. \frac{\partial T_s}{\partial r} \right|_{r=R}, \tag{4.2.13}$$

where T_s is the temperature in the solid. For the solid,

$$\rho c_p \frac{\partial T_s}{\partial t} = \frac{k}{r} \frac{\partial}{\partial r} \left(r \frac{\partial T_s}{\partial r} \right). \tag{4.2.14}$$

At $r = R(t)$, $T_s = T_m$ and as $r \to \infty$, $T_s \to T_\infty$. For $dR/dt = v = \text{const.}$, a quasi-steady solution to (4.2.14) may be obtained. Writing $\eta = r - R(t)$, (4.2.14) becomes

$$-\rho c_p v \frac{\partial T_s}{\partial \eta} = \frac{k}{(\eta + R)} \frac{\partial}{\partial \eta} \left((\eta + R) \frac{\partial T_s}{\partial \eta} \right), \tag{4.2.15}$$

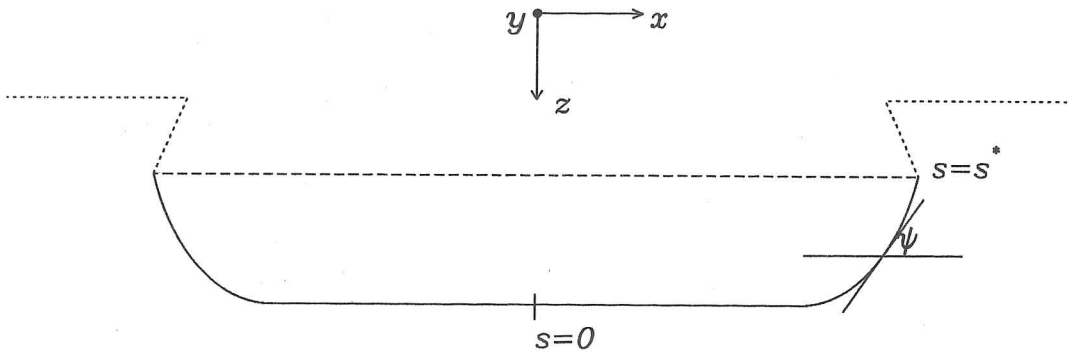

Figure 4.3. Sketch of channel geometry, showing orthogonal (x, y, z) coordinate system and intrinsic (s, ψ) coordinate system. The surface of the lava current meets the channel wall at $s = s^*$.

and so

$$T_s = T_\infty + (T_m - T_\infty)\frac{E_1(\rho c_p v r/k)}{E_1(\rho c_p v R/k)}, \tag{4.2.16}$$

where $E_1(z)$ is the exponential integral (Abramowitz & Stegun 1964). Differentiating (4.2.16) with respect to r and substituting the result into (4.2.13), the heat balance at the channel wall is now

$$\mathcal{H} = \rho L v + \rho c_p v (T_m - T_\infty)\frac{e^{-\zeta}}{\zeta E_1(\zeta)}, \tag{4.2.17}$$

where $\zeta = \rho c_p v/k\mathcal{K}$. If ψ is the inclination to the horizontal of the tangent to the channel wall and s the arc-length, the curvature $\mathcal{K} = \partial\psi/\partial s$ (see Figure 4.3). It is seen in §4.3.1 that the maximum value of ψ_s is $1/vt$, where t is the time elapsed since eruption, and so we may substitute from (4.2.12) for v to obtain an approximate value for ζ, *viz.*

$$\zeta \gtrsim \frac{\rho c_p}{k}\left(\frac{h_T(T_0 - T_m)}{\rho c_p(T_m - T_\infty + Lc_p^{-1})}\right)^2 t, \tag{4.2.18}$$

where T_0 is the eruption temperature of the lava. For a komatiitic lava flowing over a basaltic seafloor, $c_p = 730\ \mathrm{J\,kg^{-1}{}^\circ C^{-1}}$; $k = 1\ \mathrm{W\,m^{-1}{}^\circ C^{-1}}$; $L = 5 \times 10^5\ \mathrm{J\,kg^{-1}}$; $T_0 = 1600\ ^\circ\mathrm{C}$; $T_m = 1200\ ^\circ\mathrm{C}$; $T_\infty = 0\ ^\circ\mathrm{C}$; and typically $h_T \gtrsim 500\ \mathrm{W\,m^{-2}{}^\circ C^{-1}}$ (Huppert *et al.* 1984). Therefore, equation (4.2.18) implies that $\zeta \gg 1$ for $t \gg 3$ mins., a very short time compared with the duration of a typical fissure eruption, which can range from hours to weeks or months.

We can now use (4.2.17) to obtain an explicit expression for the erosion velocity v. For $\zeta \gg 1$, $E_1(\zeta) \sim \zeta^{-1}e^{-\zeta}(1-\zeta^{-1}+\cdots)$ (Abramowitz & Stegun 1964) and so, substituting for $E_1(\zeta)$, (4.2.17) becomes

$$\mathcal{H} = \rho L v + \rho c_p v (T_m - T_\infty)\left(1 - \frac{k\mathcal{K}}{\rho c_p v}\right), \tag{4.2.19}$$

from which we obtain

$$v = \frac{\mathcal{H}}{\rho c_p (T_m - T_\infty + L c_p^{-1})}\left(1 - \frac{k(T_m - T_\infty)}{\mathcal{H}}\mathcal{K}\right). \tag{4.2.20}$$

Equation (4.2.20) has been derived under the assumption that $\mathcal{H}$ is constant. In the two-dimensional model of Huppert & Sparks (1985*a*), $\mathcal{H}$ is indeed constant at a given distance downstream from the source. For the model presented in this chapter, we shall see in §4.3 that the heat flux varies slowly with time because the heat transfer properties of the flow change as the channel widens. In applying (4.2.20) to the case of a slowly-varying heat flux, we will make the approximation that $k(T_m - T_\infty)/\mathcal{H}$ remains constant, and so

$$v(s,t) = v_0(t)(1 - \varepsilon W \psi_s). \tag{4.2.21}$$

Here $\varepsilon = k(T_m - T_\infty)/W\mathcal{H}_0$, where W is the initial channel half-width and $\mathcal{H}_0$ is a typical value for the heat flux $\mathcal{H}$. Using the values above for a komatiite lava, for a channel of the order of 100m wide, $\varepsilon \lesssim 10^{-4}$ and typically $\varepsilon \ll 1$. However, the erosion velocity v given by (4.2.21) is not constant, and so to justify the quasi-steady approximation, we require the timescale for variations in v to be much greater than the adjustment timescale for the thermal boundary layer in the solid. Now, the erosion velocity v is dependent upon the curvature $\mathcal{K}$ and therefore varies over the timescale $1/v\mathcal{K}$. The thermal boundary layer in the solid has thickness $d_T = \kappa_T/v$ and so adjusts over the timescale $(\kappa_T/v)^2/\kappa_T$. We therefore require $1/v\mathcal{K} \gg \kappa_T/v^2$, which is just $\zeta \gg 1$.

From (4.2.21), we deduce that convex surfaces ($\psi_s < 0$) melt more quickly than plane surfaces, while concave surfaces ($\psi_s > 0$) melt more slowly than plane surfaces. Convex surfaces melt more quickly because the heat supplied is concentrated and the solid heats up more rapidly, thus enhancing the melting rate. Conversely, concave surfaces melt

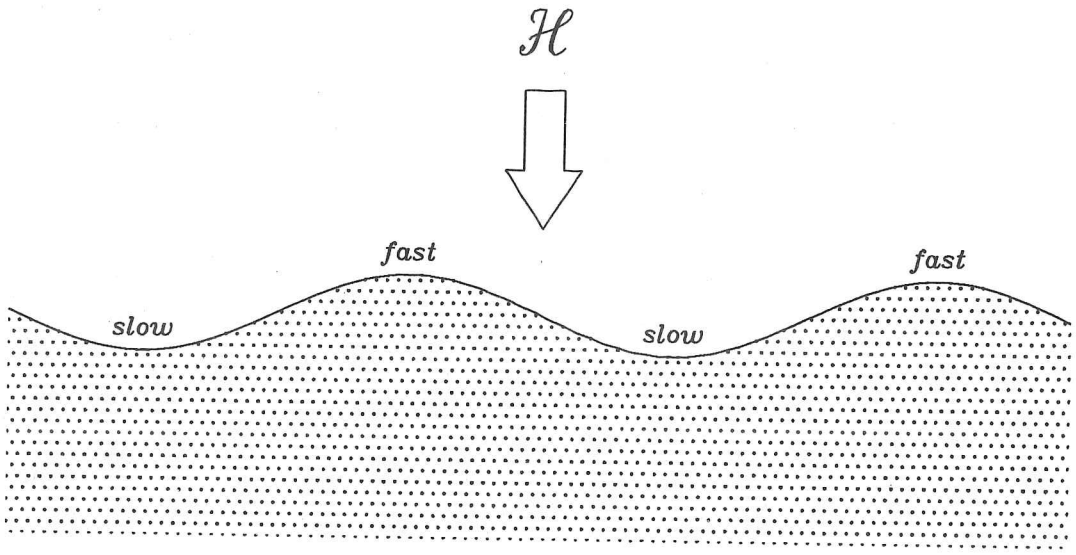

Figure 4.4. Damping of perturbations to a flat channel wall. The crests are convex upwards and so melt more rapidly than the troughs, which are concave upwards.

more slowly because the applied heat is dispersed in the solid and the solid heats up more slowly. Since $\varepsilon \ll 1$, the curvature term in (4.2.21) is usually negligible. However, it has an important role to play in suppressing small perturbations in the channel cross-sectional shape. If the channel shape is perturbed by a wavelike disturbance (see Figure 4.4), the convex crests melt more rapidly than the concave troughs and so the perturbation is damped. This mechanism also prohibits the formation of cusps in the melting interface, which correspond to multi-valued solutions for the channel wall inclination ψ.

4.3 Theoretical model

In this section, a model of the erosion of a channel of finite width by a hot, turbulent lava flow is presented. The channel wall is described by a line moving normal to itself as the channel is eroded. This leads to a nonlinear partial differential equation for the evolution of the tangent angle ψ as a function of the arc-length s, a time variable $\bar{t}$ and a single parameter α, which is related to the initial cross-sectional aspect ratio of the current. Under certain assumptions, this partial differential equation can be solved analytically and the channel geometry obtained as a function of $\bar{t}$ and α alone. The model of Huppert & Sparks (1985*a*) for the downstream evolution of a hot, turbulent, two-dimensional gravity current is then adapted to the case of a lava flow in a channel of varying cross-section. The model equations are cast in a form which permits solution by the method of characteristics. Having formulated the new equations, one of the approximations, namely that the volume of melted solid assimilated into the lava flow is negligible, is examined more closely and is shown *a posteriori* to be justified for typical komatiitic lava flows. From the model equations, we are also able to find a good approximate solution for the degree of contamination of the lava as a function of the temperature of the lava. Finally, we discuss the limiting effects of transition to laminar flow due to the increased viscosity as the lava cools, and the cessation of melting due to the formation of a chill when the lava reaches its freezing temperature.

4.3.1 Channel geometry

The model geometry for the cross-section of a thermal erosion channel at a fixed distance y downstream is shown in Figure 4.3 above. The channel is assumed to be symmetric about its mid-point and so we can define an arc-length s measured from the mid-point. Therefore, the channel is described by the set

$$\Gamma = \{\mathbf{r}(s,t) = (X,Z);\ -s^* < s < s^*\}, \tag{4.3.1}$$

where $s^*(t)$ is the shorter of the arc-length corresponding to the top of the channel and the arc-length corresponding to the position where the top of the current meets the channel wall. The former case applies at early times, when the upper surface of the current still

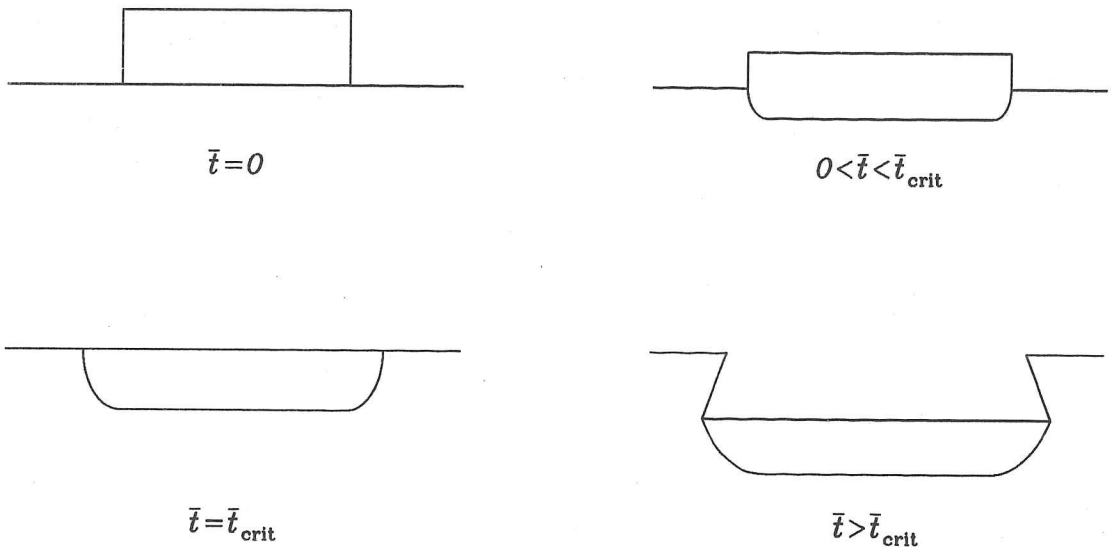

Figure 4.5. Growth of a channel with uniform melting. For $\bar{t} < \bar{t}_{crit}$, the current has not yet fallen entirely below the initial ground level and the channel wall is vertical where it meets the ground level. For $\bar{t} > \bar{t}_{crit}$, the current has fallen below the ground level and the channel walls have become undercut.

lies above the original ground level; the latter case applies once the current has cut a sufficiently deep channel for the fluid level to drop below the original ground level. At time $t = 0$, the current is assumed to be of constant thickness and have finite width $2W$. At all times, the surface of the current is assumed to be level in the cross-stream direction. Figure 4.5 shows the anticipated evolution of the channel cross-section with time. For early times, part of the current remains above the ground level, in an oblong cap of thickness D. As the current level drops below the original ground surface, the channel walls become undercut, as observed in the wax melting experiments of Huppert & Sparks (1985*a*) and the Kambalda ore fields (Lesher 1983).

By definition $ds^2 = \mathbf{dr}.\mathbf{dr}$ and so the tangent vector $\boldsymbol{\alpha} = \dfrac{\partial \mathbf{r}}{\partial s}$ has unit length (*i.e.* $\boldsymbol{\alpha}.\boldsymbol{\alpha} = 1$). Therefore, $\boldsymbol{\alpha}.(\partial\boldsymbol{\alpha}/\partial s) = 0$ and so $\partial\boldsymbol{\alpha}/\partial s$ is normal to the line Γ. We may write (Mathews & Walker 1964):

$$\frac{\partial \boldsymbol{\alpha}}{\partial s} = \kappa\boldsymbol{\beta} \quad \text{and} \quad \frac{\partial \boldsymbol{\beta}}{\partial s} = -\kappa\boldsymbol{\alpha}, \tag{4.3.2}$$

where $\boldsymbol{\beta}.\boldsymbol{\beta} = 1$ and $\boldsymbol{\alpha}.\boldsymbol{\beta} = 0$. κ is the curvature and, if we choose $\boldsymbol{\beta} = \hat{\mathbf{y}} \wedge \boldsymbol{\alpha}$, where $\hat{\mathbf{y}}$ is the unit vector out of the page in Figure 4.3, then $\kappa = \partial\psi/\partial s$, where ψ is the inclination

of the tangent $\boldsymbol{\alpha}$ to the horizontal. That is, $\boldsymbol{\alpha}.\hat{\mathbf{x}} = \cos\psi$ and $\boldsymbol{\beta}.\hat{\mathbf{x}} = -\sin\psi$. The erosion of the channel at a rate $\mathbf{v}$ is analogous to moving the line Γ at velocity $\mathbf{v}$. The distance s_{AB} between the points A and B on a line is

$$s_{AB} = \int_A^B (\mathbf{dr}.\mathbf{dr})^{\frac{1}{2}}. \tag{4.3.3}$$

Therefore, moving the line Γ at velocity $\mathbf{v}$, in time dt, $\mathbf{r} \to \mathbf{r} + \mathbf{v}\,dt$ and $s_{AB} \to s_{AB} + \dot{s}\,dt$. The definition (4.3.3) of s_{AB} implies that

$$\dot{s} = \int_0^s \frac{\partial \mathbf{v}}{\partial s'}.\frac{\partial \mathbf{r}}{\partial s'}\,ds'\,. \tag{4.3.4}$$

The evolution of a point on the line Γ is given by $\mathbf{r}(s + \dot{s}\,dt, t + dt) = \mathbf{r}(s,t) + \mathbf{v}\,dt$. Therefore,

$$\frac{\partial \mathbf{r}}{\partial t} + \dot{s}\frac{\partial \mathbf{r}}{\partial s} = \mathbf{v}. \tag{4.3.5}$$

Differentiating with respect to s and forming the scalar product of the result with $\hat{\mathbf{x}}$, we obtain

$$\frac{\partial \psi}{\partial t} + \dot{s}\frac{\partial \psi}{\partial s} = \boldsymbol{\beta}.\frac{\partial \mathbf{v}}{\partial s}\,. \tag{4.3.6}$$

For the erosion problem studied here, $\mathbf{v} = -v(s,t)\boldsymbol{\beta}$, where $v > 0$, and so

$$\dot{s} = \int_0^s v\frac{\partial \psi}{\partial s'}\,ds', \tag{4.3.7}$$

$$\frac{\partial \psi}{\partial t} + \dot{s}\frac{\partial \psi}{\partial s} = -\frac{\partial v}{\partial s}. \tag{4.3.8}$$

In general, (4.3.7) and (4.3.8) must be solved numerically. An analytical solution can be obtained, however, if we assume the melting to be uniform cross-stream and to be slowly varying in the streamwise direction, *i.e.* $v = v(t)$ alone. In this case, $v(t)$ is given by the relation (4.2.12) for the melting of a planar surface. Writing

$$s = W\sigma \quad \text{and} \quad \bar{t} = \frac{1}{W}\int_0^t v(t')\,dt', \tag{4.3.9}$$

equation (4.3.8) becomes

$$\frac{\partial \psi}{\partial \bar{t}} + \psi\frac{\partial \psi}{\partial \sigma} = 0, \qquad -\sigma^* < \sigma < \sigma^* \tag{4.3.10}$$

which is the nonlinear wave equation. The time $\bar{t}$ is the total amount of erosion relative

to the initial current half-width W. Similarly $\mathbf{r} = (X, Z)$ is rewritten $\mathbf{r} = W(x, z)$, where x and z satisfy

$$\frac{\partial x}{\partial \sigma} = \cos\psi \quad \text{and} \quad \frac{\partial z}{\partial \sigma} = -\sin\psi. \tag{4.3.11}$$

At time $\bar{t} = 0$, $\psi = 0\ \forall \psi$ and the wetted half-length $\sigma^* = 1$. At early times, while the surface of the current still lies above the original ground surface, the channel widens at the same rate as it deepens, and the channel wall is everywhere equidistant from the line segment $-1 < x < 1$, $z = 0$. This implies that the channel wall must meet the level ground at right angles, *i.e.* $\psi = \pi/2$ at $\sigma = \sigma^*$. Under these conditions, equation (4.3.10) has the simple solution

$$\psi(\sigma, \bar{t}) = \begin{cases} (\sigma + 1)/\bar{t} & \text{if } -\sigma^*(\bar{t}) < \sigma < -1; \\ 0 & \text{if } -1 < \sigma < 1; \\ (\sigma - 1)/\bar{t} & \text{if } 1 < \sigma < \sigma^*(\bar{t}). \end{cases} \tag{4.3.12}$$

Note that $\partial\psi/\partial\sigma$ decreases with time $\bar{t}$ and the curvature $\kappa = \partial\psi/\partial s$ has maximum value $1/vt$ for uniform melting rate v. For early times, while the current fills the eroded channel, the maximum arc length $\sigma^*(\bar{t}) = 1 + \pi\bar{t}/2$. The portion of the current lying above the initial ground level is assumed to consist of a cap of thickness D. The channel mid-point lies $\bar{t}$ below the original ground level, and so (4.3.11) and (4.3.12) imply that

$$x(\sigma, \bar{t}) = \begin{cases} -1 + \bar{t}\sin\{(\sigma + 1)/\bar{t}\} & \text{if } \sigma^*(\bar{t}) < \sigma < -1; \\ \sigma & \text{if } -1 < \sigma < 1; \\ 1 + \bar{t}\sin\{(\sigma - 1)/\bar{t}\} & \text{if } 1 < \sigma < \sigma^*(\bar{t}); \end{cases} \tag{4.3.13}$$

$$z(\sigma, \bar{t}) = \begin{cases} \bar{t}\cos\{(\sigma + 1)/\bar{t}\} & \text{if } \sigma^*(\bar{t}) < \sigma < -1; \\ \bar{t} & \text{if } -1 < \sigma < 1; \\ \bar{t}\cos\{(\sigma - 1)/\bar{t}\} & \text{if } 1 < \sigma < \sigma^*(\bar{t}). \end{cases} \tag{4.3.14}$$

The solution (4.3.12)–(4.3.14) is valid for all $\bar{t}$, but the maximum arc length $\sigma^*(\bar{t}) = 1 + \pi\bar{t}/2$ only until the surface of the current falls below the original ground level at some critical time $\bar{t} = \bar{t}_{\text{crit}}$ (see Figure 4.5). Rescaling the cap thickness D, the current depth

H, the current cross-sectional area A and the wetted half-perimeter P according to

$$D = Wd, \quad H = Wh \quad A = W^2 a \quad \text{and} \quad P = Wp, \tag{4.3.15}$$

(4.2.8) becomes

$$\frac{a^3}{p} = \alpha, \tag{4.3.16}$$

where $\alpha = (\frac{1}{4}Q^2\rho\lambda/W^5 g\Delta\rho\sin\chi)$. The initial cross-sectional aspect ratio $H/2W$ of the current is $\frac{1}{2}(\frac{1}{4}\alpha)^{1/3}$. The cross-sectional area of fluid below the level $z(\sigma,\bar{t})$ is $C = W^2 c$, where

$$c(\sigma,\bar{t}) = \begin{cases} (1-\sigma)\bar{t} - 2\bar{t}\cos\{(\sigma+1)/\bar{t}\} & \text{if } -\sigma^*(\bar{t}) < \sigma < -1; \\ \qquad + \frac{1}{2}\bar{t}^2\sin\{2(\sigma+1)/\bar{t}\} & \\ 0 & \text{if } -1 < \sigma < 1; \\ (1+\sigma)\bar{t} - 2\bar{t}\cos\{(\sigma-1)/\bar{t}\} & \text{if } 1 < \sigma < \sigma^*(\bar{t}); \\ \qquad - \frac{1}{2}\bar{t}^2\sin\{2(\sigma-1)/\bar{t}\} & \end{cases} \tag{4.3.17}$$

The breadth of the top of the current is $2x(\sigma^*,\bar{t}) = 2(1+\bar{t})$ and the cross-sectional area of fluid within the channel is $c(\sigma^*,\bar{t}) = 2\bar{t} + \pi\bar{t}^2/2$. For $\bar{t} < \bar{t}_{\text{crit}}$, the wetted half-perimeter $p(\bar{t}) = \sigma^*(\bar{t}) + x(\sigma^*,\bar{t}) + d(\bar{t})$ and so a and p are

$$a = 2\bar{t} + \pi\bar{t}^2/2 + 2d(1+\bar{t}) \quad \text{and} \quad p = 2 + (1+\pi/2)\bar{t} + d\,. \tag{4.3.18}$$

The total current depth $h = \bar{t} + d$. Substituting into (4.3.16), we obtain the following equation for the cap thickness $d(\bar{t})$:

$$\left(\bar{t} + \tfrac{1}{4}\pi\bar{t}^2 + d(1+\bar{t})\right)^3 = \tfrac{1}{8}\alpha(2 + d + (1+\tfrac{1}{2}\pi)\bar{t})\,. \tag{4.3.19}$$

The initial cap thickness $d(0)$ is equal to the thickness of a two-dimensional current flowing down a slope with the same two-dimensional flow rate $q = Q/2W$. For constant three-dimensional flow rate Q, the current thickness decreases ($dh/d\bar{t} < 0$) as the channel widens. The solution given by (4.3.19) is valid until the cap thickness d becomes zero,

i.e. the current level falls below the original ground level. This occurs at $\bar{t} = \bar{t}_{\rm crit}$, where $\bar{t}_{\rm crit}$ is the only positive root of

$$\bar{t}^3(1+\tfrac{1}{4}\pi\bar{t})^3 = \tfrac{1}{4}\alpha(1+\tfrac{1}{2}(1+\tfrac{1}{2}\pi)\bar{t}). \tag{4.3.20}$$

For $\bar{t} > \bar{t}_{\rm crit}$, the current surface lies below the original ground level. Now $1 < \sigma* < 1 + \pi\bar{t}/2$, with the current cross-sectional area $a = c(\sigma^*, \bar{t})$ and wetted half-perimeter $p = \sigma^* + x(\sigma^*, \bar{t})$. Again substituting from (4.3.13) and (4.3.17) into (4.3.16), $\sigma^*(\bar{t})$ is the root of

$$\left((\sigma+1)\bar{t} - 2\bar{t}\cos\{(\sigma-1)/\bar{t}\} - \tfrac{1}{2}\bar{t}^2\sin\{2(\sigma-1)/\bar{t}\}\right)^3 = \alpha\left(\sigma + 1 + \bar{t}\sin\{(\sigma-1)/\bar{t}\}\right), \tag{4.3.21}$$

and the current thickness $h = \bar{t} - z(\sigma^*, \bar{t})$.

After time $\bar{t}_{\rm max} > \bar{t}_{\rm crit}$, the channel wall is only partly wetted: for a given depth z below the original ground level, erosion ceases once the surface of the hot current has fallen below z, *i.e.* the unwetted portion of the channel is described parametrically by $(x(\pm\sigma^*(\bar{t}), \bar{t}), z(\pm\sigma^*(\bar{t}), \bar{t}))$ for $\bar{t}_{\rm crit} < \bar{t} < \bar{t}_{\rm max}$. Therefore the channel is described by the union of three sets:

$$\begin{aligned}
&\{\mathbf{x} = (x(-\sigma^*(\bar{t}), \bar{t}), z(-\sigma^*(\bar{t}), \bar{t}))\,;\ \bar{t}_{\rm crit} < \bar{t} < \bar{t}_{\rm max}\} \\
&\cup \{\mathbf{x} = (x(\sigma, \bar{t}_{\rm max}), z(\sigma, \bar{t}_{\rm max}))\,;\ -\sigma^*(\bar{t}_{\rm max}) < \sigma < \sigma^*(\bar{t}_{\rm max})\} \\
&\cup \{\mathbf{x} = (x(\sigma^*(\bar{t}), \bar{t}), z(\sigma^*(\bar{t}), \bar{t}))\,;\ \bar{t}_{\rm crit} < \bar{t} < \bar{t}_{\rm max}\}\,.
\end{aligned} \tag{4.3.22}$$

The second set in (4.3.22) describes the wetted portion of the channel at $\bar{t} = \bar{t}_{\rm max}$, while the first and third sets describe the two unwetted parts. The inclination of the unwetted part of the channel wall to the vertical is

$$\Pi(\bar{t}) = \tan^{-1}\left(\frac{dx(\sigma^*(\bar{t}), \bar{t})}{d\bar{t}} \Big/ \frac{dz(\sigma^*(\bar{t}), \bar{t})}{d\bar{t}}\right). \tag{4.3.23}$$

The function Π can be determined at the top of the channel ($\bar{t} = \bar{t}_{\rm crit}$) and as $\bar{t} \to \infty$ by

analysing equation (4.3.21). After some algebra, we obtain

$$\frac{\sigma^* - 1}{\bar{t}} = \frac{\pi}{2} - \frac{(\bar{t} - \bar{t}_{\rm crit})}{\bar{t}_{\rm crit}} \cdot \frac{1 + \frac{1}{3}(1+2\pi)\bar{t}_{\rm crit} + \frac{5}{48}\pi(2+\pi)\bar{t}^2_{\rm crit}}{1 + \frac{1}{3}(4+\pi)\bar{t}_{\rm crit} + \frac{1}{24}(12+5\pi)\bar{t}^2_{\rm crit}} \qquad \text{for} \quad \bar{t} - \bar{t}_{\rm crit} \ll \bar{t}_{\rm crit} \tag{4.3.24}$$

and

$$\frac{\sigma^* - 1}{\bar{t}} = \left(\frac{27\alpha}{4}\right)^{\frac{1}{8}} \bar{t}^{-\frac{5}{8}} \qquad \text{as} \quad \bar{t} \to \infty. \tag{4.3.25}$$

Therefore, differentiating (4.3.13) and (4.3.14) with respect to $\bar{t}$ and substituting the result into (4.3.23), we have

$$\Pi(\bar{t}_{\rm crit}) = \tan^{-1}\left(\frac{1 + \frac{1}{3}(4+\pi)\bar{t}_{\rm crit} + \frac{1}{24}(12+5\pi)\bar{t}^2_{\rm crit}}{1 + \frac{1}{3}(1+2\pi)\bar{t}_{\rm crit} + \frac{5}{48}\pi(2+\pi)\bar{t}^2_{\rm crit}}\right) \tag{4.3.26}$$

and

$$\Pi(\bar{t}) \to \frac{3}{8}\left(\frac{27\alpha}{4}\right)^{\frac{1}{8}} \bar{t}^{-\frac{5}{8}} \qquad \text{as } \bar{t} \to \infty. \tag{4.3.27}$$

The inclination $\Pi(\bar{t}_{\rm crit})$ of the top of the channel wall to the vertical is a monotonically decreasing function of $\bar{t}_{\rm crit}$, and so (4.3.26) implies that the angle the top of the channel makes with the vertical lies between $\Pi(\bar{t}_{\rm crit} = \infty) = 34.5°$ and $\Pi(\bar{t}_{\rm crit} = 0) = 45°$. Equation (4.3.27) implies that as $\bar{t} \to \infty$, the channel walls tend towards the vertical (*i.e.* $\Pi \to 0$).

Solutions for the channel geometry are presented in Figure 4.6 for three different values of α. Larger values of α correspond to narrower channels, or higher volume fluxes, or flow down shallower slopes. The cross-sectional shapes in Figure 4.6 have been scaled by the initial current width. The relative extent of the subsequent erosion in the horizontal direction, compared with the downwards erosion, is greatest for the largest value of α. This reflects the greater depth of fluid compared with the channel width. Comparison of the photograph of one of the wax melting experiments of Huppert & Sparks (Figure 4.1(*b*)) with Figure 4.6 suggests that the experimental value of α was of the order of 0.1. Comparisons cannot be drawn with Figure 4.1(*a*), which shows the channel eroded by a komatiitic lava flow, as it is only schematic. The channel shapes observed in the field and in experiments are smoother than those calculated here. In practice the sharp corners

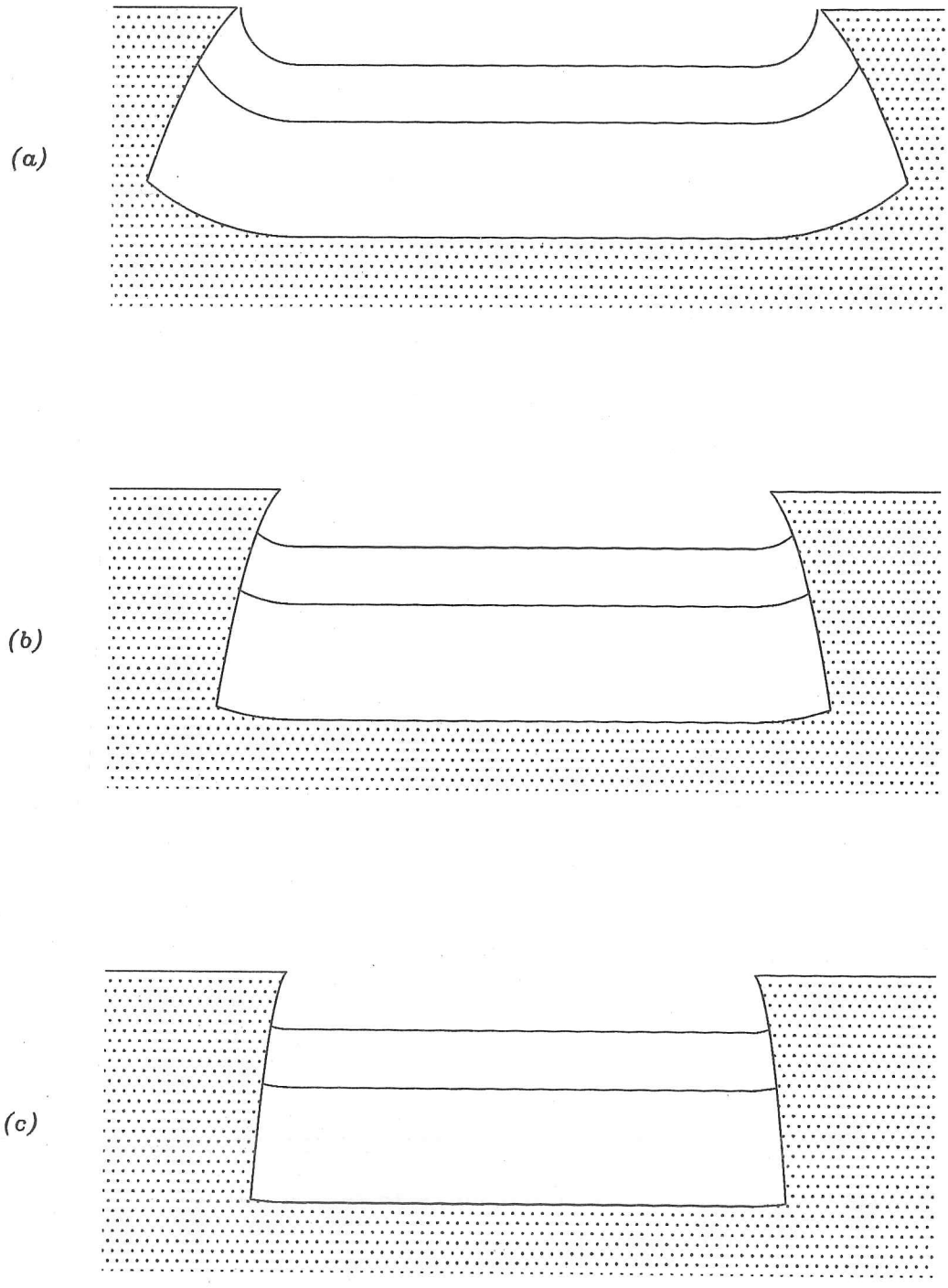

Figure 4.6. Solutions for the channel geometry after $\bar{t} = 1$ for (a) $\alpha = 0.1$, (b) $\alpha = 0.001$ and (c) $\alpha = 0.00001$. The stippled region is solid which has not yet been eroded after time $\bar{t} = 1$ and the two horizontal lines within the channel represent the extent of the erosion after times $\bar{t} = 0.25$ and $\bar{t} = 0.5$. Note that the horizontal extent of the erosion is greatest for the highest value of α.

in the channel shape predicted at the top of the channel and at the point where the top of the current meets the channel wall will be smoothed out by the combined effects of fluctuating flow rates and radiative heating of unwetted parts of the channel walls.

In this subsection, we have constructed a solution for the channel geometry as a function of the total erosion $\bar{t}$ alone. In general, this can be achieved for any $v(s,t)$ which can be separated into $v(s,t) = F(t)G(s,\psi,\psi_s)$. Writing $G(s,\psi,\psi_s) = g(\sigma,\psi,\psi_\sigma)$, ψ satisfies

$$\frac{\partial\psi}{\partial\bar{t}} + \left\{\int_0^\sigma g\frac{\partial\psi}{\partial\sigma'}\,d\sigma'\right\}\frac{\partial\psi}{\partial\sigma} = -\frac{dg}{d\sigma}\,, \tag{4.3.28}$$

where $\bar{t}$ is now defined as $\bar{t} = \dfrac{1}{W}\displaystyle\int_0^t F(t')\,dt'$. In §4.5, we briefly discuss an example of non-uniform erosion in which v is a function of s and $\bar{t}$. In this case also, the evolution equation (4.3.8) for the channel wall inclination ψ can be reduced to the form (4.3.28).

4.3.2 Thermal evolution

As the lava flows out along the seabed, heat is lost both to the water above and to the ground below. Above the current, a thin crust forms, its thickness determined by a balance between the heat transferred from the fluid and the heat conducted away through the solid. At the base of the lava flow, solid is melted if the heat transfer is sufficiently high. If the crust thickness is δ_c, the water temperature T_w and the liquidus temperature of the komatiitic lava T_f, then $\delta_c = k(T_f - T_w)/\mathcal{H}$, where $\mathcal{H} = h_T(T_{gc} - T_f)$ (Huppert 1986). If a crust does not form, as in the wax experiments of Huppert & Sparks (1985*a*) and the lunar rille model of Hulme (1973), heat is lost through the upper surface chiefly by convection in the air (in the wax experiments) or by radiation (in the lunar rille model).

The formation of a crust means that the lava is entirely enclosed by solid, with a contact temperature T_f, the freezing temperature of the lava, on its upper surface and a contact temperature T_m, the melting temperature of the solid, on its lower surface. The aspect ratio of the lava flow is very small — it is very much wider than it is thick — and so the relationships (4.2.4) for the eruption rate q and (4.2.11) for the heat transfer coefficient h_T are not as accurate as they would be for an aspect ratio closer to 1, but are still adequate (Hulme 1973, Wilson & Head 1981). Equation (4.2.10) for h_T is for

a fully developed hot, turbulent flow down a pipe of fixed temperature, and so (4.2.11) is most accurate when the liquidus temperature of the komatiite is equal to the melting temperature of the ground, *i.e.* $T_f = T_m$.

In addition to the heat lost through convective transfer through the crust and ground, heat is also lost in bringing the temperature of the newly-eroded ground material up from T_m to T_{gc}, the temperature of the current. Furthermore, as the lava cools, the crystal content of the lava increases and latent heat is released upon crystal formation. Therefore, if the melting is uniform and given by (4.2.12), the temperature T_{gc} of the current satisfies (*c.f.* Huppert & Sparks 1985*a*)

$$\rho c_p A\left(\frac{\partial T_{gc}}{\partial t} + U\frac{\partial T_{gc}}{\partial y}\right) = -2Ph_T(T_{gc} - T_m) - 2s^*\frac{h_T(T_{gc} - T_m)^2}{(T_m - T_\infty + Lc_p^{-1})} + 2Xh_T(T_f - T_m) + \rho AL_c\phi'(T_{gc})\left(\frac{\partial T_{gc}}{\partial t} + U\frac{\partial T_{gc}}{\partial y}\right), \quad (4.3.29)$$

where L_c is the latent heat of fusion of the crystals, X is the half-width of the crust formed on the upper surface of the lava flow and $\phi(T_{gc})$ is the crystal fraction. A similar expression for the thermal evolution is presented by Hulme (1973), but in that model, cooling is dominated by radiative heat loss through the top of the lava flow. Writing $T_{gc} = T_m + (T_0 - T_m)\theta$, where T_0 is the temperature of the lava on eruption ($T_0 > T_m$, $T_0 > T_f$), and $\Gamma = 1 - L_c\phi'(T)/c_p$ (since $\phi'(T)$ is modelled as a constant), (4.3.29) becomes, upon substituting for $U = Q/A$ and rescaling A, P and s^*,

$$\frac{\rho c_p aW\Gamma}{2h_T}\left(\frac{\partial\theta}{\partial t} + \frac{Q}{aW^2}\frac{\partial\theta}{\partial y}\right) = -p\theta - 2\beta\sigma^*\theta^2 + x\gamma, \quad (4.3.30)$$

where $\beta = \dfrac{\frac{1}{2}(T_0 - T_m)}{T_m - T_\infty + Lc_p^{-1}}$ and $\gamma = \dfrac{(T_f - T_m)}{(T_0 - T_m)}$. The parameter β is the ratio of the specific heat of the erupted lava to the heat required to raise the ground to its melting temperature and melt it, and can be considered to be a measure of the thermal energy of the lava flow (Huppert 1986). The constant Γ is a measure of the influence of crystallization in the melt and increases when either the latent heat released upon fusion or the rate of crystallization with cooling is increased.

The energy equation (4.3.29) is valid only while the flow is turbulent and the floor is melting. The flow remains turbulent so long as its Reynolds number remains sufficiently

high. As the lava cools, it becomes more viscous and its Reynolds number decreases. If the Reynolds number becomes sufficiently small (~ 500) for the flow to become laminar, the heat transfer from the lava flow decreases by an order of magnitude (Huppert & Sparks 1985*a*) and significant erosion ceases. This is termed Reynolds number limitation and is discussed further in §4.3.4 below. The behaviour of the lava flow also differs according to whether the lava freezing temperature T_f is above or below the ground melting temperature T_m. If $T_f \leq T_m$, equation (4.3.29) is valid until $T_{\rm gc} = T_m$, at which time erosion ceases, but the lava continues to cool and eventually freezes when $T_{\rm gc} = T_f$. Since we are only interested in processes up until the cessation of erosion, this second stage is not modelled here. If $T_f > T_m$, the lava reaches its freezing temperature T_f while still sufficiently hot to cause significant thermal erosion. However, at $T_{\rm gc} = T_f$, the lava must begin to solidify at the floor of the channel. Experiments and analysis by Huppert (1989) demonstrated that the ground may continue to melt below a chill layer of frozen lava. After some time, the ground material trapped under the chill layer refreezes. The shielding of the melt region from the lava flow by the chill layer means that there is no further contamination of the lava. Although the ground continues to melt, contamination is limited by the lava reaching its freezing temperature and so analysis of the flow for $T_{\rm gc} < T_f$ need not be conducted.

The heat transfer coefficient h_T is not constant, but dependent upon the lava temperature, the flow velocity and the channel geometry. We define an equivalent two-dimensional flow rate q by dividing the three-dimensional flow rate Q by the initial current width, *i.e.* $Q = 2Wq$. We also introduce an as yet undefined reference half-width W_0, and corresponding values p_0 and a_0 for the nondimensional wetted half-perimeter and cross-sectional area respectively at $\bar{t} = 0$ for a channel of half-width W_0. By applying (4.2.11) at the source temperature T_0, we obtain a base heat transfer coefficient $h_T^{(0)} = 0.02\rho c_p \kappa_T^{0.6} \nu(T_0)^{-0.4} (2q)^{0.8} (p_0/a_0^5)^{0.2} W_0^{-1}$. Therefore, h_T may be written

$$h_T = h_T^{(0)} \exp\{-0.009(T_0 - T_m)(1-\theta)\} \left(\frac{p}{p_0}\right)^{0.2} \left(\frac{a_0}{a}\right) \frac{W_0}{W} \equiv h_T^{(0)} f(\theta, \bar{t}). \qquad (4.3.31)$$

It is convenient to rescale time t and distance y downstream from the source as follows,

$$t = \frac{\rho c_p W_0}{2\beta h_T^{(0)}} \tau \quad \text{and} \quad y = \frac{\rho c_p q \Gamma}{h_T^{(0)}} \eta \,. \qquad (4.3.32)$$

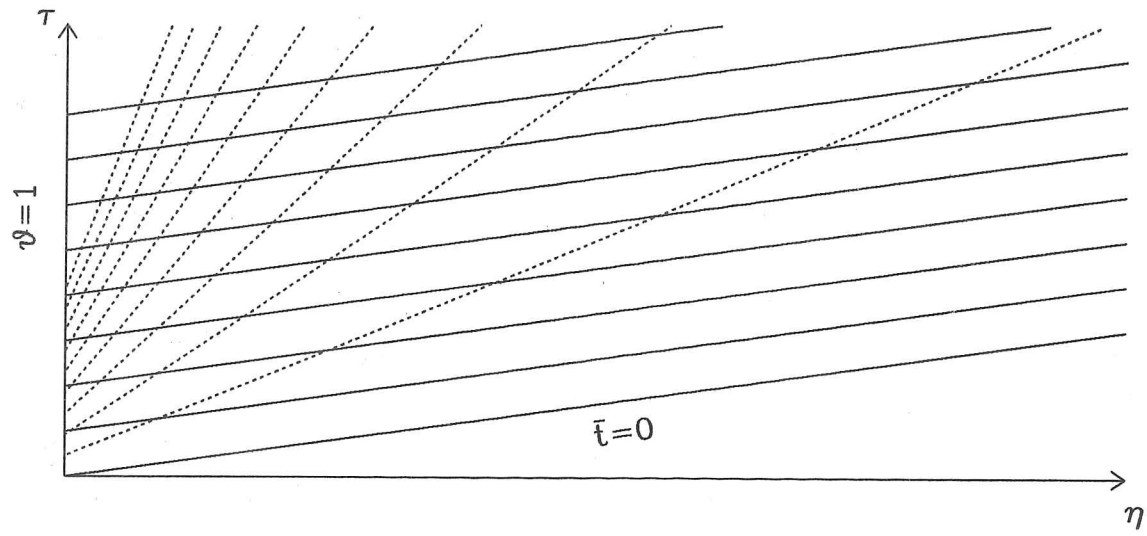

Figure 4.7. Characteristics for the ordinary differential equations (4.3.35)–(4.3.36). The solid lines represent derivatives taken moving with the lava flow. The dashed lines are contours of equal erosion $\bar{t}$. $\bar{t}$ increases with time τ and decreases with downstream distance η.

The nondimensional form of the heat equation (4.3.30) in terms of the nondimensional independent variables τ and η is

$$\frac{\beta\Gamma W}{W_0}a(\bar{t})\frac{\partial\theta}{\partial\tau}+\frac{\partial\theta}{\partial\eta}=-(p(\bar{t})\theta+2\beta\sigma^*(\bar{t})\theta^2-\gamma x(\bar{t}))f(\theta,\bar{t}). \qquad (4.3.33)$$

If a, p, x and σ^* are all evaluated at $\bar{t}=0$ and $W_0=W$, the initial channel half-width, equation (4.3.33) is the same as the heat equation derived by Huppert *et al.* (1984) and Huppert & Sparks (1985*a*) for a two-dimensional lava flow. If $\bar{t}_{\max}$ is the maximum value of the erosion variable $\bar{t}$, the three-dimensional flow model described here approaches the two-dimensional model of Huppert *et al.* (1984) and Huppert & Sparks (1985*a*) as $\bar{t}_{\max}\to 0$. The main difference between equation (4.3.33) and the heat equation of Huppert and co-workers is that (4.3.33) is dependent on time, through the erosion variable $\bar{t}$. Consequently, we anticipate variations in erosion rates, *etc.*, as the eruption progresses.

For uniform melting $v=v(t)$ given by (4.2.12), and upon rescaling of time, $\bar{t}$ is defined implicitly by

$$\bar{t}(\eta,\tau)=\frac{W_0}{W}\int_{\tau_0}^{\tau}\theta f(\theta,\bar{t})\,d\tau' , \qquad (4.3.34)$$

where τ_0 is the time at which the lava first reaches a distance η downstream from the

source. Equations (4.3.33) and (4.3.34) can be written

$$\frac{d\theta}{d\eta} = -(p(\bar{t})\theta + 2\beta\sigma^*(\bar{t})\theta^2 - \gamma x(\bar{t}))f(\theta,\bar{t}) \qquad \text{on} \quad \frac{d\tau}{d\eta} = \frac{\beta\Gamma W}{W_0}a(\bar{t}) \tag{4.3.35}$$

$$\frac{d\bar{t}}{d\tau} = \frac{W_0}{W}\theta f(\theta,\bar{t}) \qquad \text{on} \quad \eta = \text{const.} \tag{4.3.36}$$

Integrating along $d\tau/d\eta = \beta\Gamma W a(\bar{t})/W_0$ is equivalent to solving in a frame moving with the fluid. At the head of the lava flow, $(\eta = \eta_{\text{head}}(\tau))$, $\bar{t} = 0$ and at the source $(\eta = 0)$, $\theta = 1$. The head of the lava flow is given by $\eta_{\text{head}}(0) = 0$ and $d\eta_{\text{head}}/d\tau = W_0/\beta\Gamma W a(0)$. The non-dimensional wetted half-perimeter $p(\bar{t})$ and the half-arc length $\sigma^*(\bar{t})$ are both monotonically increasing functions of $\bar{t}$ and so the rate of cooling increases as the channel is eroded. Therefore, $\theta(\eta,\tau)$ is a monotonically decreasing function of τ for a fixed distance η downstream from the source.

For an eruption of nondimensional duration τ_{erupt} and constant volume flux Q, the system (4.3.35)–(4.3.36) can be solved numerically for θ and $\bar{t}$ along each of the characteristics $d\tau/d\eta = \beta\Gamma W a(\bar{t})/W_0$ in turn, starting at $\eta = 0$ where $\theta = 1$, for $\tau = 0$ up to $\tau = \tau_{\text{erupt}}$ (see Figure 4.7). A simple explicit Forward Euler scheme is sufficient, with timestep $d\tau = 0.01$ and downstream spatial increment $d\eta = 0.03$. The geometrical problem need only be solved once, for $0 < \bar{t} < \bar{t}_{\max}$, where $\bar{t}_{\max} = W_0\tau_{\text{erupt}}/W$, creating a table of values for $p(\bar{t})$, $\sigma^*(\bar{t})$ and $a(\bar{t})$ for, say, 1000 evenly-spaced values of $\bar{t}$. Values at arbitrary $\bar{t}$ can then obtained by linear interpolation. Computation times for a typical solution (up to $\tau = 1$ and $\eta = 3$) were less than 10 cpu seconds on an IBM 3084 mainframe.

4.3.3 Contamination

As the ground is melted, it is assimilated into the lava flow. Thus far, for convenience, it has been assumed that the consequent increase in volume flux Q with distance downstream is negligible. Otherwise, the geometric solution is no longer dependent on $\bar{t}$ alone, but also on η. This adds to the complexity of the solution, especially when an analytical solution for the channel geometry is not available, as the parameter α (see (4.3.16)) is no longer a constant, and so x, p, σ^* and a must be calculated from (4.3.19) or (4.3.21) at each (η,τ). In this subsection, we will first neglect the increase in Q due to contamination, as

in the two-dimensional model of Huppert & Sparks (1985*a*). We will then briefly consider a more complete model in which the increase in Q with distance downstream is included, and determine a parameter range for which downstream variations in Q may be neglected.

Assuming the density of melted solid is the same as that of the lava, the volume flux $Q(y)$ is

$$Q(y) = Q_0 + \int_0^y 2s^* v(y,t)\, dy\ , \tag{4.3.37}$$

where the integral is taken travelling with the lava flow and Q_0 is the volume flux at the source, that is at the erupting fissure. Substituting from (4.2.12) for the erosion rate v, and casting the result in terms of nondimensional variables, equation (4.3.37) becomes

$$Q(\eta) = Q_0 \left(1 + 2\beta\Gamma \int_0^\eta \sigma^*(\bar{t})\theta f(\theta,\bar{t})\, d\eta'\right), \tag{4.3.38}$$

where the integral is taken along $d\tau/d\eta = Wa(\bar{t})/W_0$, *i.e.* moving with the fluid. The relative contamination $\mathcal{C}$ is given by

$$\mathcal{C} = 2\beta\Gamma \int_0^\eta \sigma^*(\bar{t})\theta f(\theta,\bar{t})\, d\eta'. \tag{4.3.39}$$

A solution for the contamination $\mathcal{C}$ can be obtained as a function of the temperature θ by making the approximation

$$p(\bar{t}) \sim 2\sigma^*(\bar{t}) \qquad \text{and} \qquad x(\bar{t}) \sim \sigma^*(\bar{t})\,. \tag{4.3.40}$$

In the two-dimensional model of Huppert *et al.* (1984) and Huppert & Sparks (1985*a*), (4.3.40) holds exactly. Figure 4.8 demonstrates that for a typical solution to the geometric problem (with $\alpha = 10^{-4}$), the relative error $\delta = (p - 2\sigma^*)/p$ in p for the approximation (4.3.40) is no more than 2% and is less than 0.5% for $\bar{t} > 0.1$. In general, the maximum relative error occurs at $\bar{t} = 0$ and is $\delta_{\max} = H/2W$, where H is the initial depth of the current. Solving (4.3.19) for the cap thickness at $\bar{t} = 0$ and noting that $H = Wd$ at $\bar{t} = 0$, we obtain $\delta_{\max} \simeq \frac{1}{2}(\frac{1}{4}\alpha)^{1/3}$. The error in $x(\bar{t})$ is the same order of magnitude as the error in $p(\bar{t})$.

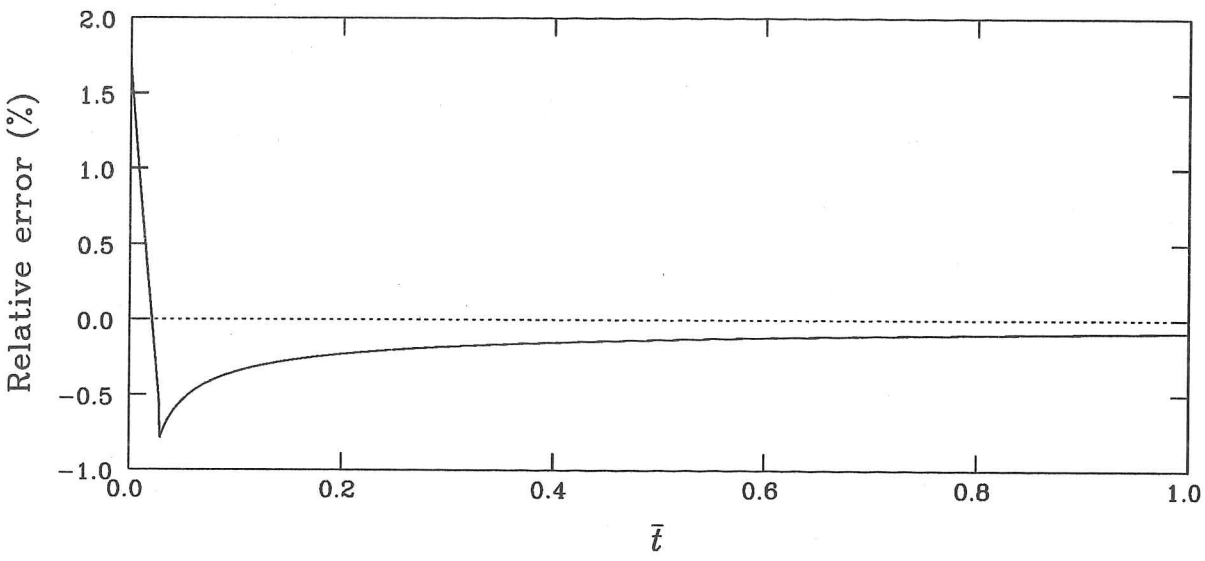

Figure 4.8. Relative error $\delta = (p(\bar{t}) - 2\sigma^*(\bar{t}))/2\sigma^*(\bar{t})$ in the approximation (4.3.40). The cusp at $\bar{t} \sim 0.05$ corresponds to the change in solution regime at $\bar{t} = \bar{t}_{\text{crit}}$.

If (4.3.39) is rewritten

$$\frac{d\mathcal{C}}{d\eta} = 2\beta\Gamma\sigma^*(\bar{t})\theta f(\theta, \bar{t}) \qquad \text{on} \quad \frac{d\tau}{d\eta} = \frac{\beta\Gamma W}{W_0} a(\bar{t}), \tag{4.3.41}$$

then we may divide (4.3.41) by (4.3.35) and integrate the result to obtain a solution for $\mathcal{C}$ as a function of θ alone, with the initial condition $\mathcal{C}(1) = 0$ corresponding to zero contamination at the source. Dividing (4.3.41) by (4.3.35) (with the approximation (4.3.40)), we obtain

$$\frac{d\mathcal{C}}{d\theta} = -\frac{2\beta\Gamma\theta}{(2\theta + 2\beta\theta^2 - \gamma)}. \tag{4.3.42}$$

Writing $z = 1 + 2\beta\theta$ and $E^2 = 1 + 2\beta\gamma$, equation (4.3.42) becomes

$$\frac{d\mathcal{C}}{dz} = -\Gamma\frac{(z-1)}{(z^2 - E^2)}, \tag{4.3.43}$$

where $\mathcal{C} = 0$ at $z = 1 + 2\beta$. By integrating (4.3.43) and substituting for z, the solution is obtained for the relative contamination $\mathcal{C}$ as a function of nondimensional temperature

θ, namely

$$C(\theta) = \frac{\Gamma}{2} \ln \left[\left(\frac{1 + 2\beta - E}{1 + 2\beta\theta - E} \right)^{1-\frac{1}{E}} \left(\frac{1 + 2\beta + E}{1 + 2\beta\theta + E} \right)^{1+\frac{1}{E}} \right]. \qquad (4.3.44)$$

The equations (4.3.35), (4.3.36) and (4.3.41) have been solved numerically for typical parameter values, and the solution (4.3.44) was indistinguishable from the numerical solution. In the special case $T_f = T_m$, the parameter $E = 1$ and (4.3.44) reduces to

$$C(\theta) = \Gamma \ln \left(\frac{1 + \beta}{1 + \beta\theta} \right). \qquad (4.3.45)$$

If the lava is allowed to flow an infinite distance from the source, the lava cools and $\theta \to 0$ as $\eta \to \infty$. The maximum contamination is $C(0) = \Gamma \ln(1 + \beta)$, independent of time. For $\Gamma = 1$, this is the same as the expression derived by Huppert (1986) for a simplified model in which the lava viscosity μ and the heat transfer coefficient h_T are constants. For an actual komatiite eruption, it is unlikely that the lava flow will have been able to flow a sufficient distance away from its source for the lava to cool to $\theta = 0$ while still flowing turbulently. Therefore, the contamination is unlikely to have reached its theoretical maximum (Huppert & Sparks 1985*a*). More likely, the lava will have experienced adverse topography, perhaps ponding in a depression and cooling there. In determining the contamination of an erupted lava from field observations, one therefore must consider the level of contamination at a fixed distance downstream from the source. Unfortunately, it is difficult to tell how far individual solid remnants of komatiitic flows are from the erupting fissure, as the evidence now lies under many layers of sediment and the remnants of more recent eruptions.

It may seem surprising that the lava contamination is related to the lava temperature by the simple expression (4.3.44). This is a natural consequence, however, of the approximation (4.3.40), which implies that the total heat flux from the lava is always equal to the wetted half-perimeter P, multiplied by the heat transfer coefficient h_T, divided by the mean downstream velocity U and multiplied by a function of the lava temperature alone. Consequently, the rate of cooling of the lava with distance downstream is equal to Ph_T/AU multiplied by a function of the lava temperature, where A is the cross-sectional area of the lava flow. Similarly, the rate at which ground material is assimilated into the flow with distance downstream is equal to Ph_TU multiplied by a function of the lava

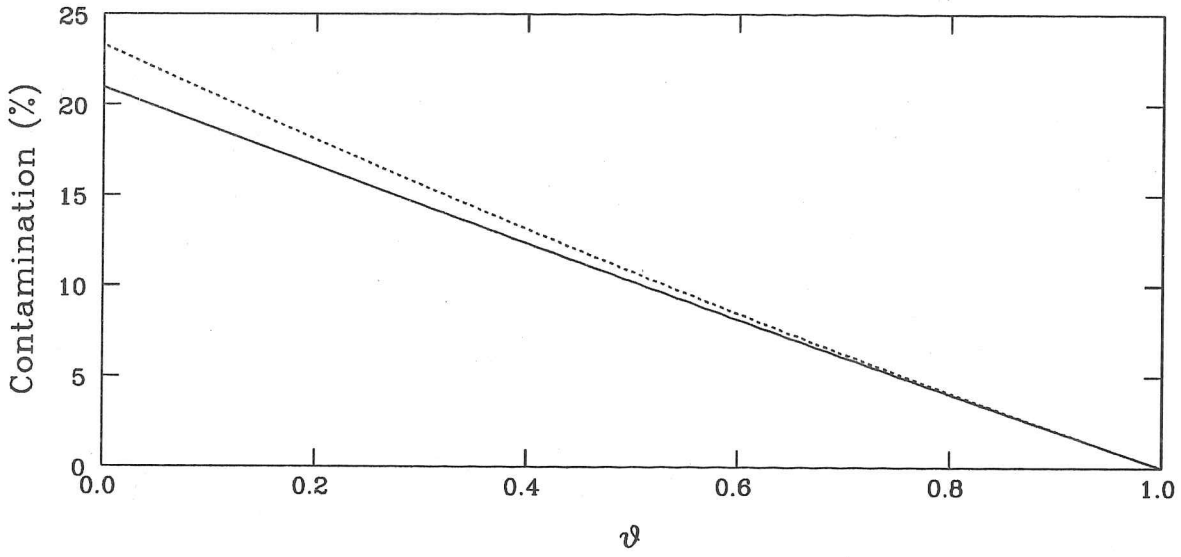

Figure 4.9. Contamination $\mathcal{C}$ as a function of nondimensional temperature θ for (——) increase in flow rate Q with distance downstream neglected and (· · · · · ·) increase in flow rate Q with distance downstream included ($\Gamma = 2.1$, $\beta = 0.1$, $\gamma = 0$).

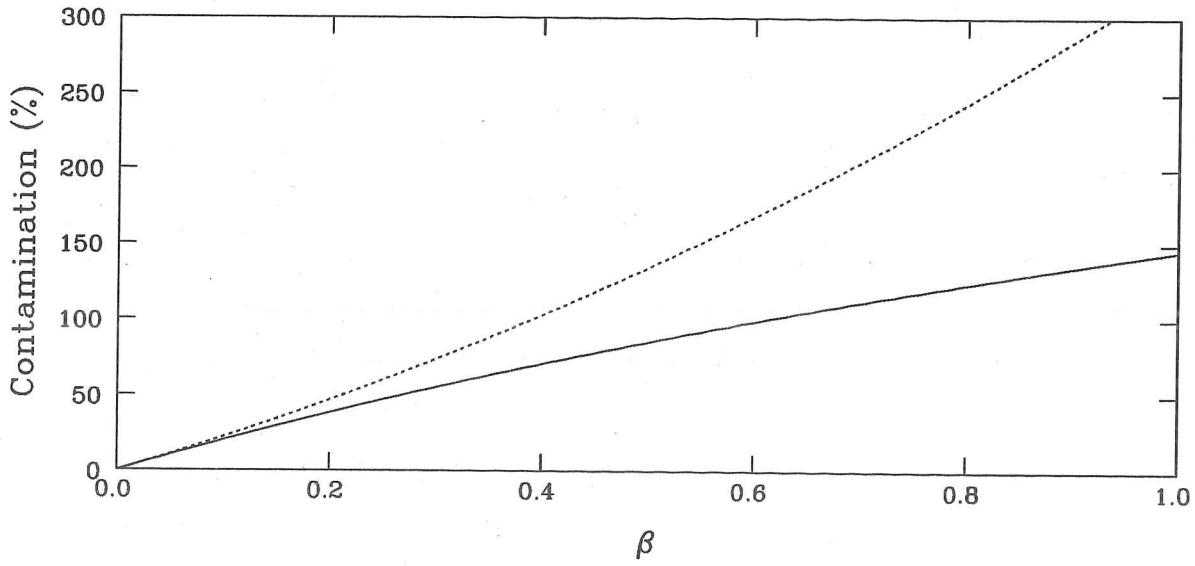

Figure 4.10. Maximum contamination $\mathcal{C}(0)$ for (——) increase in flow rate Q with distance downstream neglected and (· · · · · ·) increase in flow rate Q with distance downstream included ($\Gamma = 2.1$, $\gamma = 0$).

temperature and so the rate at which contamination increases with distance downstream is also equal to Ph_T/AU multiplied by some function of the lava temperature. Therefore, as long as (4.3.40) is satisfied, the relative contamination in the lava must be a function of the lava temperature alone.

We shall now include the increase in volume flux Q with distance downstream from the source. In neglecting the increase in Q, but including the heat required to heat the newly-melted ground to the temperature of the current in equation (4.3.29), we introduced a spurious heat loss. This is corrected by including the increase in Q. Since Q is no longer constant, we must redefine our downstream length scale (see (4.3.32)) by replacing q with q_0, where $q_0 = Q_0/2W$. In addition, the heat transfer coefficient is affected by the variation in Q, and so (4.3.35), (4.3.36) and (4.3.41) become

$$\frac{d\theta}{d\eta} = -(p(\bar{t},\mathcal{C})\theta + 2\beta\sigma^*(\bar{t},\mathcal{C})\theta^2)\frac{\tilde{f}(\theta,\bar{t},\mathcal{C})}{1+\mathcal{C}} \qquad \text{on} \quad \frac{d\tau}{d\eta} = \frac{\beta\Gamma W}{W_0}\frac{a(\bar{t},\mathcal{C})}{1+\mathcal{C}}\,; \tag{4.3.46}$$

$$\frac{d\bar{t}}{d\tau} = \frac{W_0}{W}\theta\tilde{f}(\theta,\bar{t},\mathcal{C}) \qquad \text{on} \quad \eta = \text{const.}\,; \tag{4.3.47}$$

$$\frac{d\mathcal{C}}{d\eta} = 2\beta\Gamma\sigma^*(\bar{t},\mathcal{C})\theta\tilde{f}(\theta,\bar{t},\mathcal{C}) \qquad \text{on} \quad \frac{d\tau}{d\eta} = \frac{\beta\Gamma W}{W_0}\frac{a(\bar{t},\mathcal{C})}{1+\mathcal{C}}\,, \tag{4.3.48}$$

where $\tilde{f}(\theta,\bar{t},\mathcal{C}) = (1+\mathcal{C})^{0.8}\,f(\theta,\bar{t})$. The inclusion of the variation in volume flux Q leads to a decrease by a factor of $(1+\mathcal{C})$ in the downstream rate of cooling $d\theta/d\eta$ and an increase by a factor of at least $(1+\mathcal{C})^{0.8}$ in the erosion $\bar{t}$ and contamination $\mathcal{C}$ as functions of η. The change in $\mathcal{C}$ as a function of θ is therefore a good guide to whether or not the variation in volume flux with distance downstream may be neglected. If we proceed as before by dividing equation (4.3.48) by equation (4.3.46) and making the approximation (4.3.40), we obtain an expression similar to (4.3.42), the only difference being an additional factor $1/(1+\mathcal{C})$ on the left-hand side. Therefore, in (4.3.44), we need only replace $\mathcal{C}$ by $\ln(1+\mathcal{C})$ on the left-hand side to recover the solution for $\mathcal{C}$. In general, therefore, the neglect of the increase in volume flux Q with distance downstream is justified if and only if $\mathcal{C} \ll 1$. In the special case $T_f = T_m$, the contamination $\mathcal{C}$ is now given by

$$\mathcal{C}(\theta) = \left(\frac{1+\beta}{1+\beta\theta}\right)^{\Gamma} - 1\,. \tag{4.3.49}$$

The maximum contamination is $\mathcal{C}(0) = (1+\beta)^{\Gamma} - 1$. As $\beta \to 0$, both (4.3.45) and (4.3.49) reduce to $\mathcal{C}(\theta) = \beta\Gamma(1-\theta)\,(1+O(\beta))$. Figure 4.9 shows (4.3.45) (solid line)

and (4.3.49) (dotted line) for $\beta = 0.1$, which corresponds to a lava erupted at 1600 °C over a seafloor with melting temperature 1200 °C. The parameter β is smaller for lavas erupted at lower temperatures, but larger if the melting temperature T_m of the seafloor is lower. The inclusion of the downstream increase in volume flux Q leads to higher values of the contamination $\mathcal{C}$ as a function of temperature θ, but the difference is not significant given the simplicity of the model presented here. The variation in the two expressions for the limiting value $\mathcal{C}(0)$ is presented in Figure 4.10 for a range of values of the parameter β. For $\beta \ll 1$, the inclusion of the downstream variation in Q makes little difference, but for larger values of β, there is a significant increase in the predicted contamination, and the neglect of the downstream increase in Q is not justified. For a komatiite eruption, the eruption temperature was not likely to have exceeded 1600 °C and the melting temperature of the seafloor no lower than 850 °C (Huppert & Sparks 1985*a*). Therefore, the maximum value of β for a komatiite eruption is about 0.25, and the increase in volume flux with distance downstream can reasonably be neglected. In the remainder of this chapter, therefore, Q is considered to be constant.

4.3.4 Reynolds number and thermal limitation

The model presented here is only valid while the lava flow is turbulent. For $Re < 500$, the crystals suspended in the fluid sediment out, forming an insulating layer at the base of the lava flow. This dramatically reduces the heat transfer into the seafloor and melting rates become negligible (Huppert & Sparks 1985*a*). The Reynolds number is based here upon the hydraulic radius $R_H = A/P$. Substituting from (4.2.1) for the dynamic viscosity μ into $Re = \rho U R_H/\mu$ and noting that $UA = Q = 2Wq$ and $P = Wp$, we obtain

$$Re = \left(\frac{\rho q}{\mu_0}\right) \frac{1}{\frac{1}{2}p(\bar{t})} \exp(-\omega(1-\theta)), \tag{4.3.50}$$

where $\mu_0 = \exp(34.551 - 0.0226T_0)$ and $\omega = 0.0226(T_0 - T_m)$. The temperatures T_0 and T_m are measured in °C. Variations in the Reynolds number due to the decrease in $p(\bar{t})$ with distance downstream are negligible compared with variation due to the decrease in temperature θ and so the Reynolds number Re decreases with distance downstream.

Defining $Re_0 = \rho q/\mu_0$, the Reynolds number $Re = Re_{\text{crit}}$ (where $Re_{\text{crit}} = 500$) when

$$\frac{Re_0}{Re_{\text{crit}}} = \tfrac{1}{2} p(\bar{t}) \exp\left(\omega(1-\theta)\right). \tag{4.3.51}$$

The erosion may also be thermally limited. Two forms of thermal limitation exist. If the lava freezing temperature T_f is less than the ground melting temperature T_m, the lava temperature can fall below the melting temperature of the ground and thermal erosion ceases. Alternatively, if $T_f > T_m$, the lava temperature reaches its freezing temperature and the lava begins to solidify against the channel walls. Both Reynolds number limitation and the first type of thermal limitation were discussed by Huppert & Sparks (1985*a*), but the second form of thermal limitation is new. The first form of thermal limitation limits only the downstream extent of the erosion — the theoretical maximum contamination given by (4.3.44) for $\theta = 0$ is still attained, independent of flow rate. Also, the second form of thermal limitation is perhaps the more relevant of the two, since the freezing temperature of komatiitic lavas is approximately 1200°C, whilst the melting temperatures of typical Archaean floor rocks are (Huppert & Sparks 1985*a*): tholeiitic basalt 1200°C; sediment/andesite 1000°C; and acid gneiss 850°C. Combining all three limiting processes, the minimum nondimensional lava temperature at which thermal erosion may continue is

$$\theta_{\text{lim}} = \max\left\{0, \frac{T_f - T_m}{T_0 - T_m}, 1 - \frac{1}{\omega}\ln\frac{Re_0}{Re_{\text{crit}}}\right\}. \tag{4.3.52}$$

The limiting temperature θ_{lim} can then be substituted into the solution (4.3.44) for the contamination $\mathcal{C}$ as a function of θ to obtain the maximum contamination $\mathcal{C}_{\text{max}}$. In deriving (4.3.52), we have made the approximation $p(\bar{t}) \sim 2$, which holds best at $\bar{t} = 0$ and is exact when applied to the two-dimensional model of Huppert & Sparks (1985*a*). For $\bar{t} > 0$, $p(\bar{t}) > 2$, and so, under conditions of Reynolds number limitation, equation (4.3.51) implies that θ_{lim} increases with time and consequently the maximum contamination $\mathcal{C}_{\text{max}}$ decreases. The contamination predicted by substituting the expression (4.3.52) for θ_{lim} into equation (4.3.44) therefore represents a maximum value of the maximum contamination.

For a given two-dimensional volume flux q, only one of the two main limitation mechanisms, *i.e.* Reynolds number limitation and the second form of thermal limitation, can

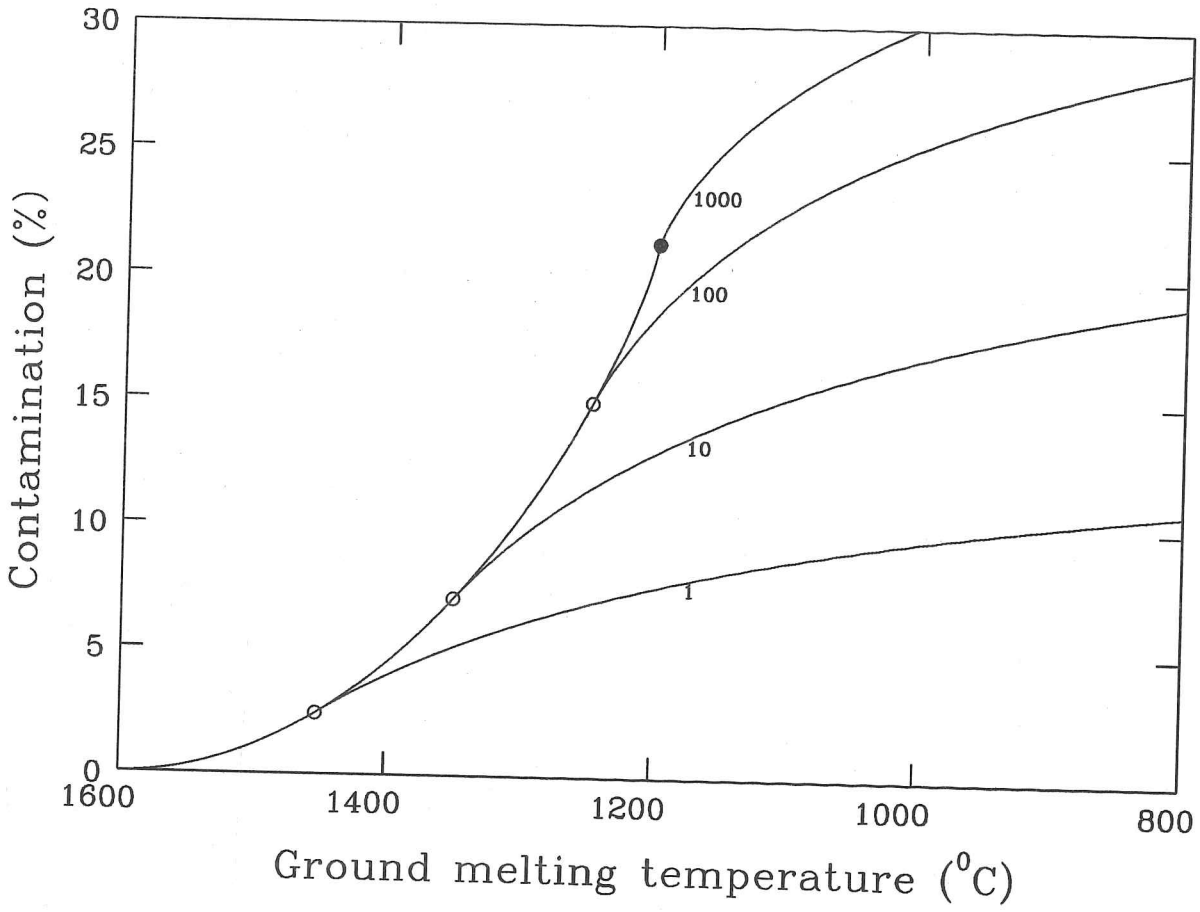

Figure 4.11. Maximum contamination when erosion is subject to Reynolds number and thermal limitation. Curves are plotted for two-dimensional flow rates q=1, 10, 100 and 1000 m^2s^{-1}. In all cases the lava temperature on eruption is $T_0 = 1600°C$ and the lava freezing temperature is $T_f = 1200°C$. The Reynolds number Re is related to the flow rate q through $Re = \rho q/\mu_0$, where $\mu_0 = \exp(34.551 - 0.0226T_0)$ (in Pa s) and $\rho = 2800$ kg m^{-3}. Significant erosion, and therefore contamination, ceases once $Re < Re_{crit}$, where $Re_{crit} = 500$. For high values of ground melting temperature T_m, the erosion is limited by the lava temperature becoming lower than T_m. As T_m decreases, the downstream extent of the erosion, and hence the lava contamination, becomes limited either by the flow becoming laminar (o), or by the lava reaching its freezing temperature (•). Note that the curve for $q = 1000$ m^2s^{-1} would be the same for any $q > q_{crit} = 300$ m^2s^{-1}.

occur. If the viscosity of the lava at its freezing temperature is too large for turbulent flow, we will have Reynolds number limitation. However, if the viscosity of the lava at its freezing temperature is such that the flow remains turbulent, Reynolds number limitation will not occur, and the thermal erosion will be limited by the lava reaching its freezing

temperature. From the definition $Re_0 = \rho q/\mu_0$ and the expression (4.2.1) for the lava viscosity, we see that Reynolds number limitation occurs only when $q < q_{\text{crit}}$, where

$$q_{\text{crit}} = \frac{Re_{\text{crit}}}{\rho} \exp\left(34.551 - 0.0226 T_f\right) \tag{4.3.53}$$

and ρ is in kg m^{-3}, T_f is in °C and q_{crit} is in m^2 s^{-1}. The critical flow rate q_{crit} is a decreasing function of the lava freezing temperature T_f and so Reynolds number limitation is more likely for lavas with low freezing temperatures. For a lava with freezing temperature $T_f = 1200$°C and density 2800 kg m^{-3}, the critical flow rate is $q_{\text{crit}} = 300$ m^2 s^{-1}.

In Figure 4.11, the maximum contamination, obtained by substituting (4.3.52) into (4.3.44), is plotted against ground melting temperature for a lava erupted at temperature $T_0 = 1600$°C with freezing temperature $T_f = 1200$°C. For flow rates $q = 1$, 10 and 100 m^2 s^{-1}, the erosion is subject to Reynolds number limitation, and the ground melting temperature T_m for which limitation occurs is a decreasing function of flow rate. For the flow rate $q = 1000$ m^2 s^{-1}, the erosion is subject to the second form of thermal limitation for $T_m < T_f$. On Figure 4.11, the onset of Reynolds number limitation is marked by a circle (o) and the onset of the second form of thermal limitation by a bullet (•). Figure 4.11 is similar to a figure presented by Huppert & Sparks (1985*a*), in which numerically calculated results are presented for the maximum contamination when Reynolds number limitation is taken into account. The values for contamination given here differ by a factor of about two from those calculated by Huppert & Sparks (1985*a*). The reason for the discrepancy is discussed below. Taking the factor of two into account, the numerical calculations of Huppert & Sparks (1985*a*) provide excellent confirmation of the analytical solution obtained here. When Reynolds number and thermal limitation are considered, the maximum contamination is no longer independent of the flow rate q, as was suggested by equation (4.3.44), but increases with q for $q < q_{\text{crit}}$. This is because a faster-flowing lava flow is able to cool further, and thereby become more contaminated, before the flow becomes laminar and significant erosion ceases. However, for $q > q_{\text{crit}}$ the flow rate q is unimportant, and the erosion is limited by the lava cooling to its freezing temperature and freezing. Therefore, the curve plotted for $q = 1000$ m^{2}s^{-1} would be the same for any $q > q_{\text{crit}} = 300$ m^{2}s^{-1}.

In the following section, we investigate how the erosion of a channel of finite width

differs from the erosion of a channel of infinite width, as studied by Huppert *et al.* (1984) and Huppert & Sparks (1985*a*). In particular, we see how the ground melting rate and lava contamination vary with channel width and with time. In §4.5, the model for the channel geometry, presented in §4.3.1, is refined to include variations in erosion rate with local current thickness. This enables us to see how the channel-splitting instability, observed by Huppert & Sparks (1985*a*) in their experiments with water flowing down a wax slope, may have arisen.

4.4 Erosion of a channel of finite width

Previous theories (Hulme 1973, Huppert *et al.* 1984, Huppert & Sparks 1985*a*) have assumed that the essential dynamics of thermal erosion of channels can be described by a two-dimensional model, effectively setting the channel width to infinity. For a lava flow, the channel width is likely to be determined by the length of the fissure from which the lava erupts and the pre-existing topography. Channelling of a lava flow into a valley can lead to two-dimensional flow rates higher than those predicted in Table 4.1 (Huppert & Sparks 1985*a*). In this section, we first see how the erosion of a channel of finite width differs from that for a channel of infinite width, and then briefly see how channelling of lava flows by topography alters the previous conclusions.

As the channel erodes, it widens. For a fixed volume flux, this leads to a thinning of the current and therefore its heat transfer properties alter, through equation (4.2.12). In addition, the surface area over which the current is cooled increases, and so the current cools more rapidly. Both the thinning of the current and the increase in downstream cooling rate result in the temperature, and therefore the rate of melting, at a given distance downstream decreasing with time. For a very wide current, the change in the channel width is negligible compared with the initial channel width and so the current thickness and surface area may be considered constant, as in the studies of Huppert *et al.* (1984) and Huppert & Sparks (1985*a*). In this section, we examine how wide the current must be for such an approximation to be accurate, and investigate the effect of finite width upon the thermal erosion of a channel and the level of contamination in the lava.

The variation in eroded channel depth with distance downstream and with eruption duration for two-dimensional volume flux $q = 10\ \mathrm{m^2\,s^{-1}}$ is presented in Figure 4.12. Results were calculated using the method of characteristics as described in §4.3. In comparing channels of two different initial widths, it is the initial value of the two-dimensional flux q based on the initial channel widths which must be the same, rather than the three-dimensional volume flux Q. However, as each channel is eroded, it is Q which remains constant and so the thickness of the current at a given distance η downstream from the source decreases with time as the channel widens. The solid line in Figure 4.12 is for a current of initial half-width 100 m and the dotted line is for a current of infinite width, *i.e.*

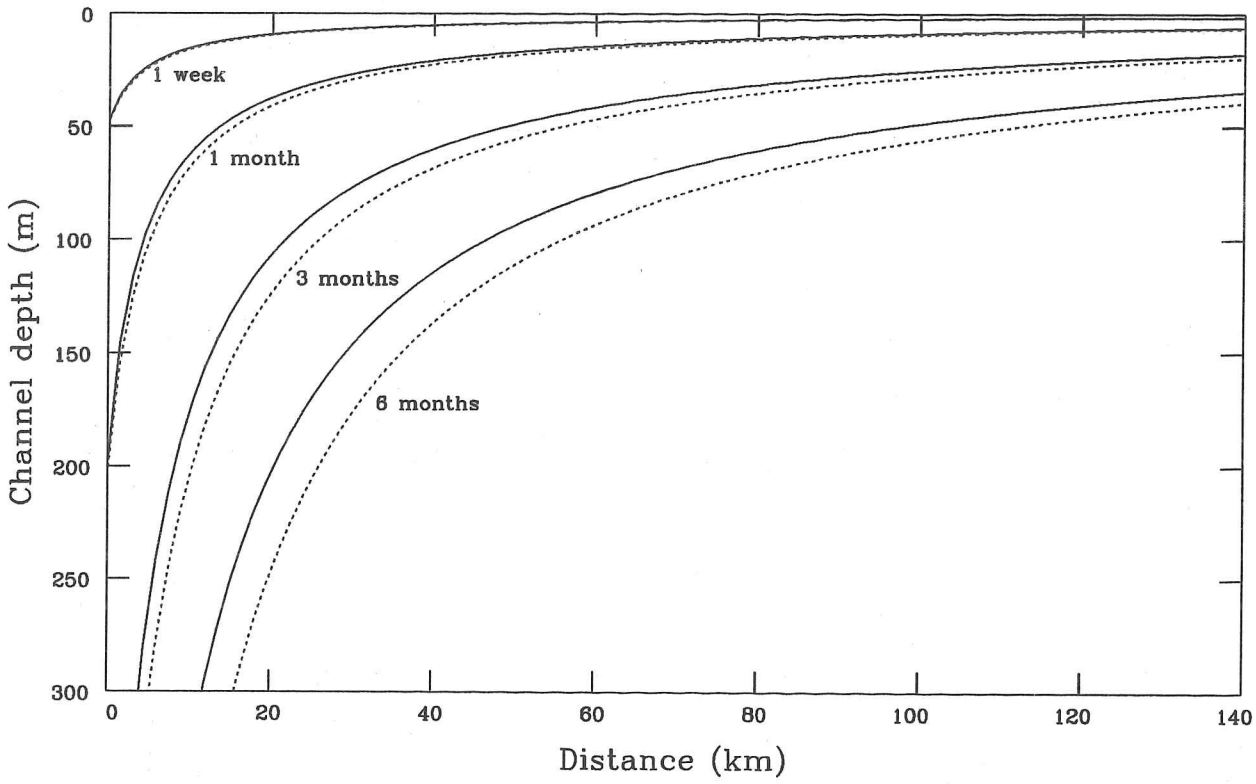

Figure 4.12. Variation in channel depth with distance downstream for eruptions of various durations and two-dimensional flow rate $q = 10\ \mathrm{m^2\,s^{-1}}$. Results for two channels are presented: —— initial half-width $W = 100\,\mathrm{m}$ and ····· $W \to \infty$. The effects of Reynolds number limitation have been neglected here. The Reynolds number falls below 500 about 110 km from the source.

a two-dimensional current. For an eruption of length one week, there is little difference in the downstream erosion, but for longer eruptions, we see that the narrower current erodes downwards more slowly. The rate of erosion decreases with distance downstream as the lava cools and its viscosity increases (Huppert *et al.* 1984, Huppert & Sparks 1985*a*).

Figure 4.12 is similar to a figure presented in Huppert & Sparks (1985*a*), and the physical values used in their calculation are the same as those employed here (taking the two different models of the fluid flow into account). However, it should be noted that the predicted channel depths in the present calculation are approximately twice as great as those predicted by Huppert & Sparks (1985*a*). At the source ($\eta = 0$), the rate of melting here is approximately $7\ \mathrm{m\,day^{-1}}$. This is the same as that calculated by Huppert *et al.* (1984) and Huppert & Sparks (1985*a*) for a lava in which no crystallization occurs

(*i.e.* $\Gamma = 1$). Huppert and co-workers then proposed that the rate of melting at the source is decreased when crystallization effects are included. In Huppert *et al.* (1984), there is some disparity between the figures and the text. In Figure 2*A* of Huppert *et al.* (1984), the rate of melting ($\dot{S}$ in their notation) is the same at the source, whether or not crystallization effects are included. However, Table 3 of Huppert *et al.* (1984) suggests a decrease in source melting rate when crystallization effects are included. The figure is correct and the table and text wrong. The rate of melting at the source is dependent only upon the source temperature T_0 and is given by substituting $\mathcal{H} = h_T(T_0 - T_m)$ into (4.2.13) to give $v(0) = 2\beta h_T/\rho c_p$, which is independent of Γ. Indeed, further downstream, the rate of erosion at a fixed distance downstream is *increased* by crystallization as the release of latent heat reduces the rate of cooling of the lava with distance downstream. Therefore, the contamination at a fixed distance downstream is increased by crystallization effects. Equation (4.3.45) shows that the maximum contamination when $T_f = T_m$ is $\mathcal{C}(\theta = 0) = \Gamma \ln(1+\beta)$, where $\Gamma = 2.1$ when crystallization effects are included and $\Gamma = 1$ when crystallization effects are neglected. The maximum contamination is independent of channel geometry and width. For $\Gamma = 2.1$ and $\beta = 0.106$, the maximum contamination is 21.2%. This again differs from the results of Huppert *et al.* (1984) and Huppert & Sparks (1985*a*), who find that the maximum contamination is 10.4%, whether or not crystallization occurs. We argue that crystallization effects must lead to increased contamination because the lava is everywhere hotter, with the exception of the source. The cause of the difference is most likely to be a minor algebraic error in the analyses of Huppert *et al.* (1984) and Huppert & Sparks (1985*a*). In equation (22) of Huppert & Sparks (1985*a*), which gives the amount of ground assimilated into the lava flow, a factor $[1 - L_x c_l^{-1} x'(T)]$ (equal to Γ in our notation) has been omitted. The same error appears to have been carried over into their numerical analysis for flows with temperature-dependent viscosity. In Huppert & Sparks (1985*a*), all presented results for melting rate, channel depth and contamination should be multiplied by $\Gamma = 2.1$. With the exception of their discussion of the effects of crystallization and the minor quantitative errors outlined here, the papers of Huppert and co-workers remain fundamentally correct.

An important feature of thermal erosion is that the greater erosion close to the source can lead to an adverse gradient in the channel floor and thence lead to ponding of the lava in the neighbourhood of the fissure (Huppert & Sparks 1985*a*). Ponding is possible once

the rate of decrease of channel depth with distance away from the source equals $\tan\chi$, where χ is the inclination of the seafloor to the horizontal. The rate of decrease of channel depth is greatest close to the source, and an approximate criterion for ponding can be obtained from (4.3.9), (4.3.34) and (4.3.35). From (4.3.9), we see that the dimensional eroded depth is $S = W\bar{t}$, and so if $f(\theta,\bar{t})$ is assumed to be approximately constant, $S \simeq W_0\theta f(\theta,\bar{t})\tau$. If we assume that $p \simeq 2$ and $\sigma^* \simeq 1$, then using (4.3.32) to obtain S in terms of dimensional variables, (4.3.35) implies that

$$\left.\frac{dS}{dy}\right|_{y=0} = 4\beta(1+\beta)\left(\frac{h_T^{(0)}}{\rho c_p}\right)^2 \frac{T_{\mathrm{erupt}}}{q}, \tag{4.4.1}$$

where y is the dimensional distance downstream from the source. Taking typical values for a komatiitic lava flow over a basaltic seabed, with $h_T^{(0)} = 1000\ \mathrm{W\,m^{-2}\,{}^{\circ}C^{-1}}$, $\rho = 2800\ \mathrm{kg\,m^{-3}}$ and $c_p = 730\ \mathrm{J\,kg^{-1}\,{}^{\circ}C^{-1}}$, (4.4.1) implies that the maximum channel floor inclination is 1.6° for an eruption lasting 30 days with flow rate $q = 10\ \mathrm{m^2\,s^{-1}}$; 0.04° for an eruption lasting 7 days with $q = 100\ \mathrm{m^2\,s^{-1}}$; and 28.6° for an eruption lasting 60 days with flow rate $q = 1\ \mathrm{m^2\,s^{-1}}$. In general, ponding is least likely for short, high volume eruptions. Ponding close to the source does not result in the lava flow ceasing further downstream. Once an adverse gradient has been eroded, the lava will fill the resulting depression. The continuous supply of lava from the fissure ensures that the fluid level rises above the lip of the depression and flow continues down the slope. However, the erosion dynamics close to the source will be significantly altered, as the heat transfer properties of a deep, ponded lava differ markedly from those of a thin, turbulent flowing lava. Therefore, care must be taken in interpreting results obtained from this model, and previous models, for the contamination of lavas extruded in long, low volume eruptions.

Figure 4.13 shows how the lava temperature and the relative contamination vary with distance downstream from the source for an eruption which has lasted one month. The lava temperature decays more rapidly with distance downstream for the finite-width channel. This is because the surface area over which the current cools increases as the channel widens and the current thins, an effect which is greater for narrower channels and longer eruptions. If the lava temperature and relative contamination were plotted for a much shorter eruption, say 1 day, the two lines would be indistinguishable. Conversely, the difference would be greater for a longer eruption. If the lava is allowed to flow

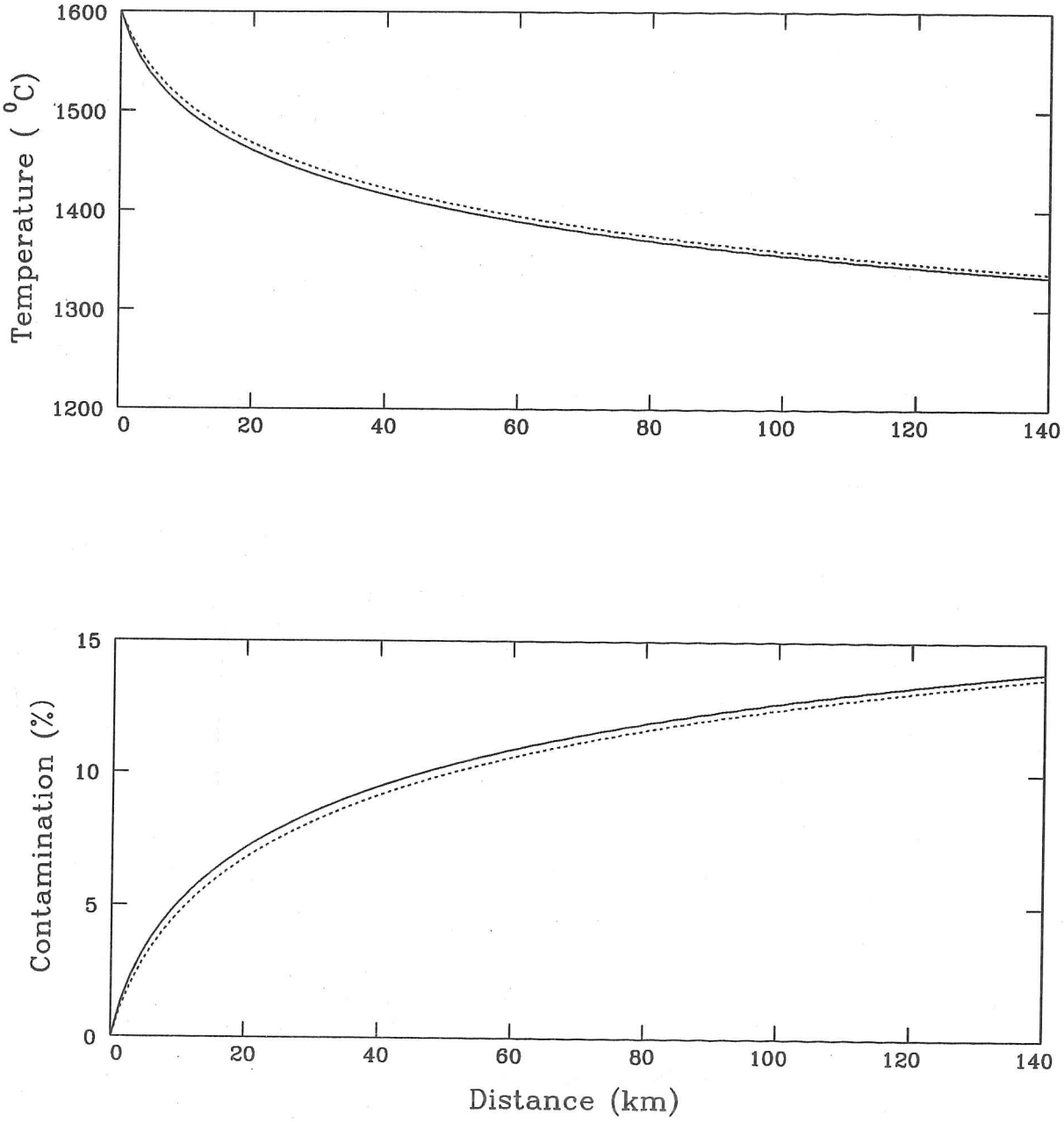

Figure 4.13. Temperature and relative contamination for an eruption of duration 1 month and two-dimensional flow rate $q = 10\ \mathrm{m^2\,s^{-1}}$. Results for two channels are presented: —— initial half-width $W = 100\,\mathrm{m}$ and ····· $W \to \infty$. The effects of Reynolds number limitation have been neglected here. The Reynolds number falls below 500 at around 110 km.

far from the source, over 100 km say, the width of the channel has little effect on the contamination. However, it is likely that topography will constrain the lava to pond at some fixed distance downstream. If the lava is emplaced 40 km from the source, the contamination is noticeably greater for the narrower channel. From (4.3.44), we see that contamination is a function of lava temperature. In the following analysis, therefore, the effect of finite width is quantified by the *cooling range*, *i.e.* the lengthscale over which the lava temperature falls with distance downstream from the source. If the cooling range is high, the lava temperature falls slowly with distance away from the source and the contamination at a given distance downstream is relatively low. Conversely, if the cooling range is low, contamination at a given distance downstream is relatively high. For very low ranges, we may expect that the contamination at even a moderate distance downstream approaches the theoretical maximum $\Gamma \ln(1+\beta)$.

First, let us define a suitable reference half-width W_0. If the dimensional eruption duration is T_{erupt}, we define W_0 to be equal to the maximum depth of erosion in time T_{erupt}. The ratio $R = W_0/W$ is therefore a measure of the deviation of the current cross-section from its initial state. In the limit $R \to 0$, the current cross-section varies little over the duration of the eruption and the two-dimensional model may be expected to hold. However, as $R \to \infty$, the channel cross-section has a high aspect ratio. Significant sideways erosion occurs, which modifies the thermal evolution of the lava and the melting process itself. From the definition (4.3.9) for $\bar{t}$ and the expression (4.2.13) for the melting velocity v, we see that W_0 is given by

$$W_0 = \frac{2\beta h_T^{(0)}}{\rho c_p} T_{\text{erupt}}. \tag{4.4.2}$$

Note that $h_T^{(0)}$ is a function of W_0 and (4.4.2) is therefore an implicit expression for W_0. If the current thickness $H = (q^2\rho/g\Delta\rho)^{1/3} \ll W_0$,

$$W_0 \simeq 0.05\beta\kappa^{3/5}\nu(T_0)^{-2/5}\left(\frac{g\Delta\rho}{\rho}\right)^{1/3} q^{2/15} T_{\text{erupt}}. \tag{4.4.3}$$

Therefore, the reference half-width W_0 is an increasing function of eruption time T_{erupt}. Comparison of (4.4.2) with (4.3.32) shows that with this choice of W_0, the dimensional timescale is the eruption duration T_{erupt}, and so $0 < \tau < 1$. The lengthscale over which

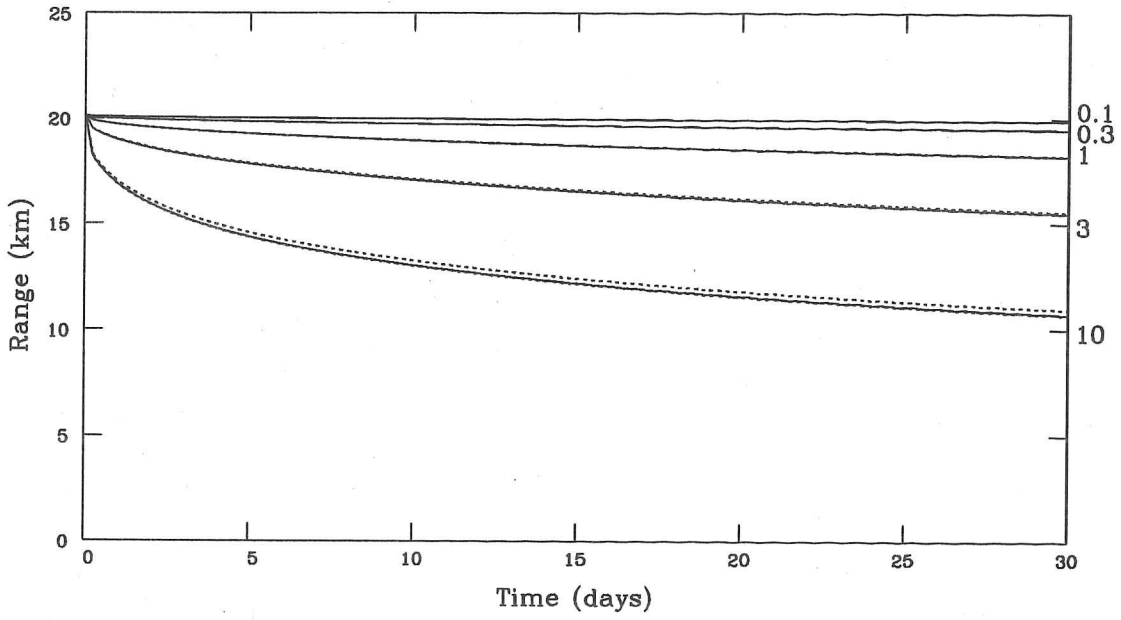

Figure 4.14. Range over which lava temperature decays away from the source plotted against eruption duration for channels of varying widths, with $R = W/W_0$ taking the values 0.1, 0.3, 1, 3 and 10. The reference channel half-width $W_0 \sim 260$ m for two-dimensional volume flux $q = 10\ \mathrm{m^2\,s^{-1}}$. The dotted lines (almost indistinguishable from the solid lines) represent the maximum and minimum values of the range as given by equation (4.4.7).

the temperature decays away from the source is $(-d\theta/d\eta)^{-1}$ measured at $\eta = 0$, where $\theta = 0$. At $\eta = 0$, under the approximation (4.3.40), equations (4.3.35) and (4.3.36) reduce to

$$\left.\frac{d\theta}{d\eta}\right|_{\eta=0} = -2(1+\beta)\,\sigma^*(\bar{t};\alpha_0 R^3)\,g(\bar{t},R;\alpha_0 R^3) \tag{4.4.4}$$

and

$$\left.\frac{d\bar{t}}{d\tau}\right|_{\eta=0} = R\,g(\bar{t},R;\alpha_0 R^3)\,, \tag{4.4.5}$$

where $\alpha_0 = q^2\rho/2g\Delta\rho W_0^3$ is the value of α evaluated for channel half-width W_0 and

$$g(\bar{t},R;\alpha_0 R^3) = R\left(\frac{\sigma^*(\bar{t};\alpha_0 R^3)}{\sigma^*(0;\alpha_0)}\right)^{0.2}\frac{a(0;\alpha_0)}{a(\bar{t};\alpha_0 R^3)}. \tag{4.4.6}$$

At $\bar{t} = 0$, $a(0; \alpha_0 R^3) = 2HW_0/R$, where H is the initial dimensional current thickness, and $\sigma^*(0; \alpha_0 R^3) = 1$. Therefore, $g(0, R; \alpha_0 R^3) = 1$. The function $g(\bar{t}, R; \alpha_0 R^3)$ is a slowly decreasing function of $\bar{t}$ and so (4.4.5) implies that $\bar{t} < R\tau$ at $\eta = 0$. Consequently the minimum value of g is $\hat{g} = g(R, R; \alpha_0 R^3)$. Therefore, as $\sigma^*(\bar{t}; \alpha_0 R^3)$ is an increasing function of $\bar{t}$,

$$\sigma^*(\hat{g}R\tau; \alpha_0 R^3)\, g(R\tau, R; \alpha_0 R^3) < \frac{1}{2(1+\beta)} \left| \frac{d\theta}{d\eta} \right|_{\eta=0} < \sigma^*(R\tau; \alpha_0 R^3)\, g(\hat{g}R\tau, R; \alpha_0 R^3). \quad (4.4.7)$$

In Figure 4.14 the range over which the lava temperature decays away from the source is plotted against eruption duration for different values of R. The two-dimensional volume flux $q = 10\ \mathrm{m^2\,s^{-1}}$ and the reference half-width $W_0 \simeq 260$ m. The results are obtained by evaluating σ^* and g at $\bar{t} = R\tau$. The upper and lower limits given by (4.4.7) are represented in Figure 4.14 as dotted lines, almost indistinguishable from the approximate solution. As $R \to 0$, and for short eruptions, the cooling range is just under 20 km. However, for $R = 10$, which corresponds to a channel about 50 m wide, the cooling range falls to just over 10 km after 30 days. It is apparent that under the latter conditions, the simple two-dimensional model of Huppert *et al.* (1984) and Huppert & Sparks (1985*a*) is insufficient to describe the growth of the lava channels. Figure 4.14 demonstrates that the cooling range decreases with initial channel width for a given two-dimensional volume flux q. Consequently, the lava temperature at a given distance downstream is lower for a narrower channel and therefore the erosion is slower everywhere. Intuitively, therefore, one might expect the contamination in the lava to decrease with initial channel width. However, the contamination increases as the initial channel width decreases. This is because the relative area of ground in contact with the lava increases as the eruption progresses and the channel becomes wider. For a given eruption duration, this effect is more marked for an initially narrower channel.

The cooling range is also dependent on the parameter α_0, which is a function of the two-dimensional flow rate q. In Figure 4.15, the cooling range is plotted against $2W$, the channel width, for two-dimensional flow rates varying from 1 to 100 $\mathrm{m^2\,s^{-1}}$. The range increases with flow rate q because the lava velocity is higher for large flow rates. For the largest flow rate ($q = 100\ \mathrm{m\,s^{-1}}$), the range varies by an order of magnitude from

At $\bar{t} = 0$, $a(0; \alpha_0 R^3) = 2HW_0/R$, where H is the initial dimensional current thickness, and $\sigma^*(0; \alpha_0 R^3) = 1$. Therefore, $g(0, R; \alpha_0 R^3) = 1$. The function $g(\bar{t}, R; \alpha_0 R^3)$ is a slowly decreasing function of $\bar{t}$ and so (4.4.5) implies that $\bar{t} < R\tau$ at $\eta = 0$. Consequently the minimum value of g is $\hat{g} = g(R, R; \alpha_0 R^3)$. Therefore, as $\sigma^*(\bar{t}; \alpha_0 R^3)$ is an increasing function of $\bar{t}$,

$$\sigma^*(\hat{g}R\tau; \alpha_0 R^3)\, g(R\tau, R; \alpha_0 R^3) < \frac{1}{2(1+\beta)} \left| \frac{d\theta}{d\eta} \right|_{\eta=0} < \sigma^*(R\tau; \alpha_0 R^3)\, g(\hat{g}R\tau, R; \alpha_0 R^3). \quad (4.4.7)$$

In Figure 4.14 the range over which the lava temperature decays away from the source is plotted against eruption duration for different values of R. The two-dimensional volume flux $q = 10\ \mathrm{m^2\,s^{-1}}$ and the reference half-width $W_0 \simeq 260$ m. The results are obtained by evaluating σ^* and g at $\bar{t} = R\tau$. The upper and lower limits given by (4.4.7) are represented in Figure 4.14 as dotted lines, almost indistinguishable from the approximate solution. As $R \to 0$, and for short eruptions, the cooling range is just under 20 km. However, for $R = 10$, which corresponds to a channel about 50 m wide, the cooling range falls to just over 10 km after 30 days. It is apparent that under the latter conditions, the simple two-dimensional model of Huppert *et al.* (1984) and Huppert & Sparks (1985*a*) is insufficient to describe the growth of the lava channels. Figure 4.14 demonstrates that the cooling range decreases with initial channel width for a given two-dimensional volume flux q. Consequently, the lava temperature at a given distance downstream is lower for a narrower channel and therefore the erosion is slower everywhere. Intuitively, therefore, one might expect the contamination in the lava to decrease with initial channel width. However, the contamination increases as the initial channel width decreases. This is because the relative area of ground in contact with the lava increases as the eruption progresses and the channel becomes wider. For a given eruption duration, this effect is more marked for an initially narrower channel.

The cooling range is also dependent on the parameter α_0, which is a function of the two-dimensional flow rate q. In Figure 4.15, the cooling range is plotted against $2W$, the channel width, for two-dimensional flow rates varying from 1 to 100 $\mathrm{m^2\,s^{-1}}$. The range increases with flow rate q because the lava velocity is higher for large flow rates. For the largest flow rate ($q = 100\ \mathrm{m\,s^{-1}}$), the range varies by an order of magnitude from

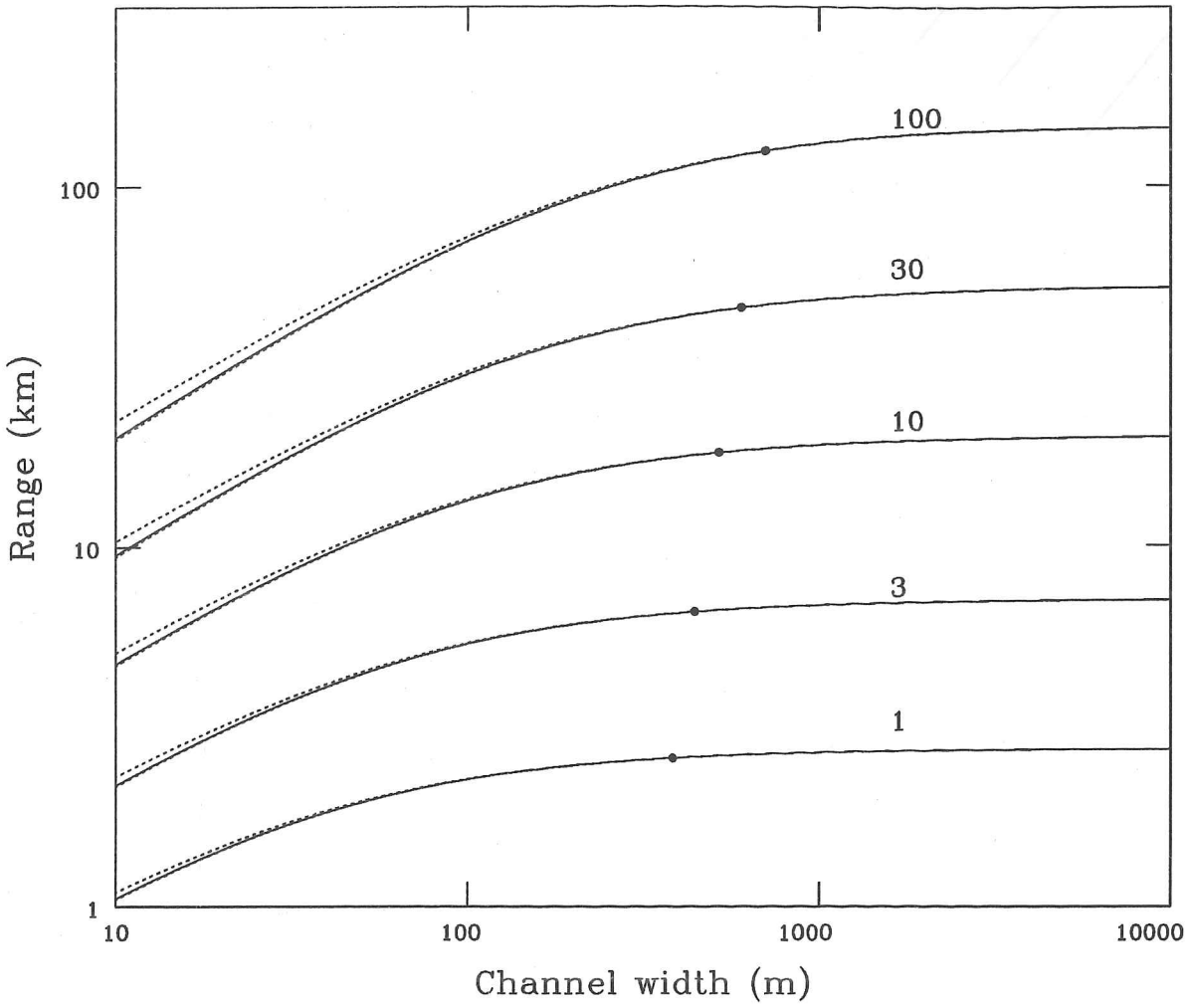

Figure 4.15. Range over which lava temperature decays away from the source plotted against channel width for different values of the initial two-dimensional volume flux. The flux q takes the values 1, 3, 10, 30 and 100 $m^2 s^{-1}$. The reference channel width $2W_0$ is marked as a bullet (•) on each curve. As in Figure 4.14, the dotted lines represent minimum and maximum values of the range.

the lowest channel width of around 10 m to the largest channel width of 10 km. The reference channel width $2W_0$ is marked on Figure 4.15 as a bullet for each q. We see that the infinite-width approximation of Huppert *et al.* (1984) and Huppert & Sparks (1985*a*) is accurate only for $W > W_0$.

Thus far, we have compared the growth of channels of varying initial widths $2W$ by constraining the initial two-dimensional volume flux q to be the same for all channel widths. Thereafter, it must be the three-dimensional volume flux $Q = 2Wq$ which remains

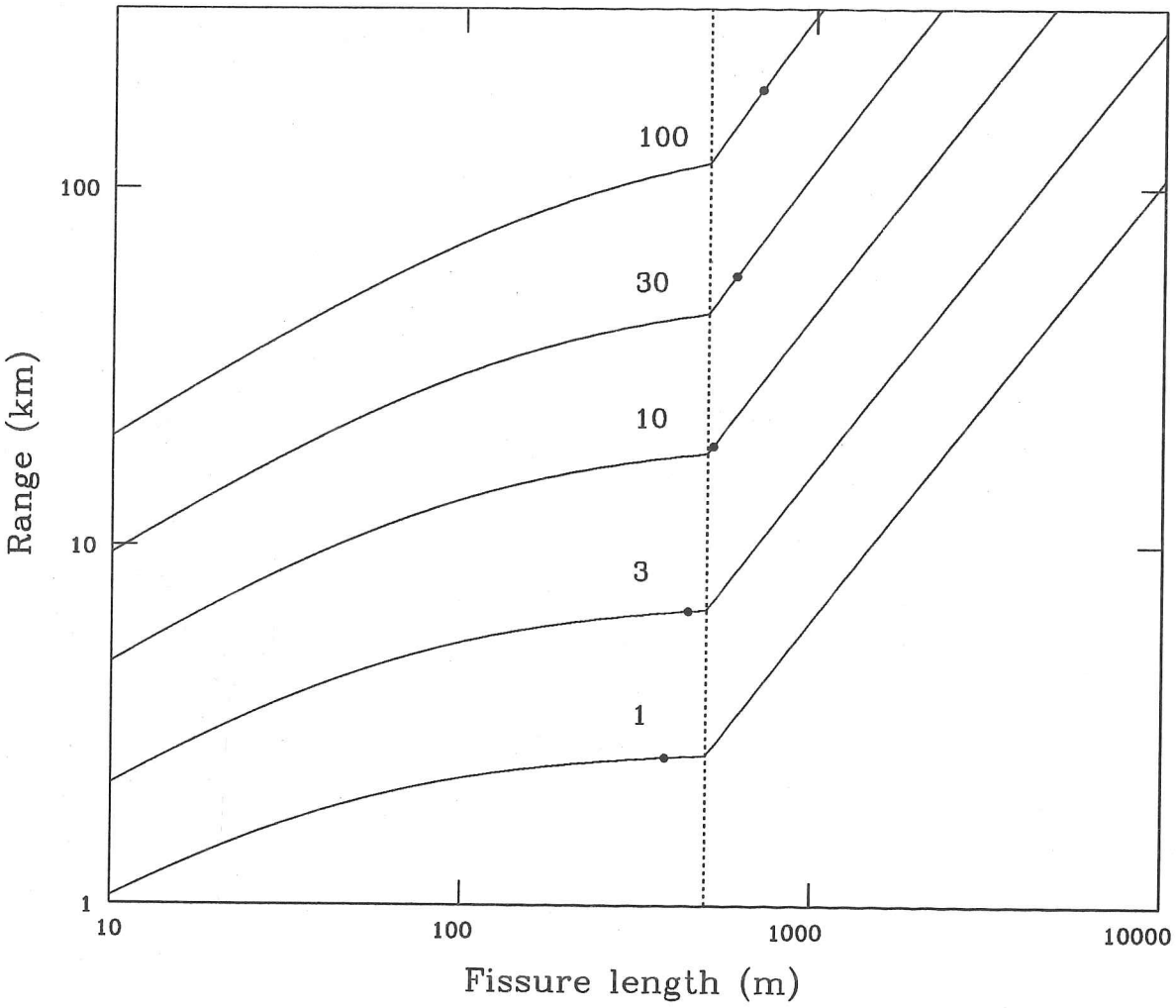

Figure 4.16. Range over which lava temperature decays away from the source plotted against fissure length for different values of two-dimensional flux q per unit length of fissure. The flux q takes the values 1, 3, 10, 30 and 100 $m^2 s^{-1}$. The fissure is modelled as being at the head of a valley 500 m wide. For longer fissures, the lava flow is focussed into the valley and the range increases markedly as the volume flux per unit width of channel increases. The reference channel width $2W_0$ is marked as a bullet (•) on each curve.

constant. In practice, the channel width is likely to be determined by topography, such as a valley, down which the lava flows. Figure 4.16 shows the range as a function of fissure length for lava flowing into a valley of width 500 m for a constant two-dimensional volume flux q per unit fissure length. Lavas erupted from fissures narrower than 500 m are assumed to flow down channels with an initial width equal to the fissure length. Lavas erupted from fissures longer than 500 m are focussed into a channel of initial width

500 m, with a consequent increase in initial two-dimensional flow rate. For fissure lengths greater than 500 m, there is a significant increase in cooling range with fissure length, implying that lava flows focussed by topography are likely to exhibit much lower levels of contamination than those allowed to flow freely from the fissure.

The behaviour described here is to some extent dependent upon our models for the flow and heat transfer properties of the lava. The rate of cooling of the lava with time is proportional to Ph_T/A (from equation (4.3.29)), and the heat transfer coefficient h_T is proportional to $P^{1/5}/A$ (from equation (4.2.11)). Therefore, the rate of cooling of the lava with time is proportional to $P^{6/5}/A^2$. The mean downstream velocity U is proportional to $1/A$, as the volume flux Q is modelled as constant, and so the rate of decrease of lava temperature with distance downstream from the source is proportional to $P^{6/5}/A$. As the channel is eroded sideways, the wetted half-perimeter P must increase. However, the evolution of the cross-sectional area A depends upon our choice of flow model. From equation (4.2.8), we see that A is proportional to $P^{1/3}$ for friction-controlled flow down a slope, and so A increases as the channel widens. Therefore, the rate of cooling of the lava with time is proportional to $P^{8/15}$. In addition, the mean downstream velocity is proportional to $P^{1/3}$, and so the rate of decrease of lava temperature with distance downstream from the source is proportional to $P^{13/15}$.

There are two physical processes which determine the manner in which the rate of cooling of the lava varies with time. First, as the channel widens, the ratio of cross-sectional area to wetted perimeter decreases, and so the ratio of the heat stored in the lava flow to the heat flux through the surface of the lava decreases with time and the rate of cooling of the lava with time increases. This process is complicated by the change in the heat transfer coefficient h_T as the channel geometry alters, but this is a secondary effect which is is relatively small ($h_T \propto P^{-2/15}$). Second, the rate of cooling with distance downstream is increased further because the lava flow becomes slower as it widens. In the flow model discussed here, this is also due to the decrease in the ratio of cross-sectional area to wetted perimeter as P increases, which increases the influence of boundary friction over negative buoyancy. For a flow model based on a gravity current flow along a horizontal plane, the mean downstream velocity would also decrease with channel width. This is because the lava flow becomes thinner and so the upstream head of pressure decreases.

For the main conclusions of the section to be invalid would require either that the ratio of cross-sectional area to wetted perimeter increases as the channel widens, or that the lava flow becomes more rapid as it thins. Neither of these requirements are physically likely, and so we conclude that the rate of cooling of the lava with distance downstream from the source must increase as the channel widens. Consequently, the lava contamination increases as the channel widens since the contamination is a decreasing function of the lava temperature. The main reason for this phenomenon is the decrease in the ratio A/P of cross-sectional area to wetted half-perimeter as the channel widens, and therefore the effect is most marked when the lateral extent of the thermal erosion is significant compared with the initial channel width. This occurs when the eruption is long-lived or the initial channel width is small.

4.5 Non-uniform erosion

The analytical solution for the channel cross-sectional geometry presented in §4.3.1 depends upon the assumption that melting is uniform. This relies upon the current being well-mixed across its width. The heat flux is then a function of the fluid temperature T_{gc} and the area A and wetted half-perimeter P of the current cross-section. This is a reasonable assumption if the aspect ratio $H/2W$ of the current cross-section is close to unity. However, for the flows studied here the cross-sectional aspect ratio is much less than unity, ranging from no more than 0.1 in the laboratory experiments to less than 0.01 for typical komatiite lava flows. If the current is very much thinner than it is wide, the lateral mixing of the lava current will not be perfect and the heat transfer $\mathcal{H}$ will partially depend upon the local current thickness H. In their experiments with hot water flowing down a wax slope, Huppert & Sparks (1985*a*) noted that on occasion the thermally-eroded channel would split into two, with an island formed in the stream (Figure 4.17). Huppert (1986) suggested that this may have arisen because the melting rate is an increasing function of the local thickness of the current. If the melting interface were to become perturbed, the melting rate would continue to decrease for regions of slower melting because the lava flow would be thinner locally. Similarly, the melting rate would increase for regions of more rapid melting. Eventually, an island forms and the flow is split into two currents. This instability mechanism is local and one would therefore expect the position of the island relative to the centre of the channel to be random. However, Huppert & Sparks (1985*a*) observed that most islands formed near to the centre of the channel (H.E. Huppert, personal communication), which suggests that a wavelength equal to the width of the channel is favoured by the instability mechanism responsible for the channel splitting.

In this section, we first formulate a parameterised model for the variation of melting rate with local depth. We then see how the curvature mechanism for stabilising perturbations, introduced in §4.2, may combine with the depth-dependence instability mechanism to produce a preferred wavelength for the instability equal to the width of the thermal erosion channel.

4.5.1 Depth-dependent melting rate

For a current of constant thickness H with two dimensional volume flux $\hat{q}$, the expression

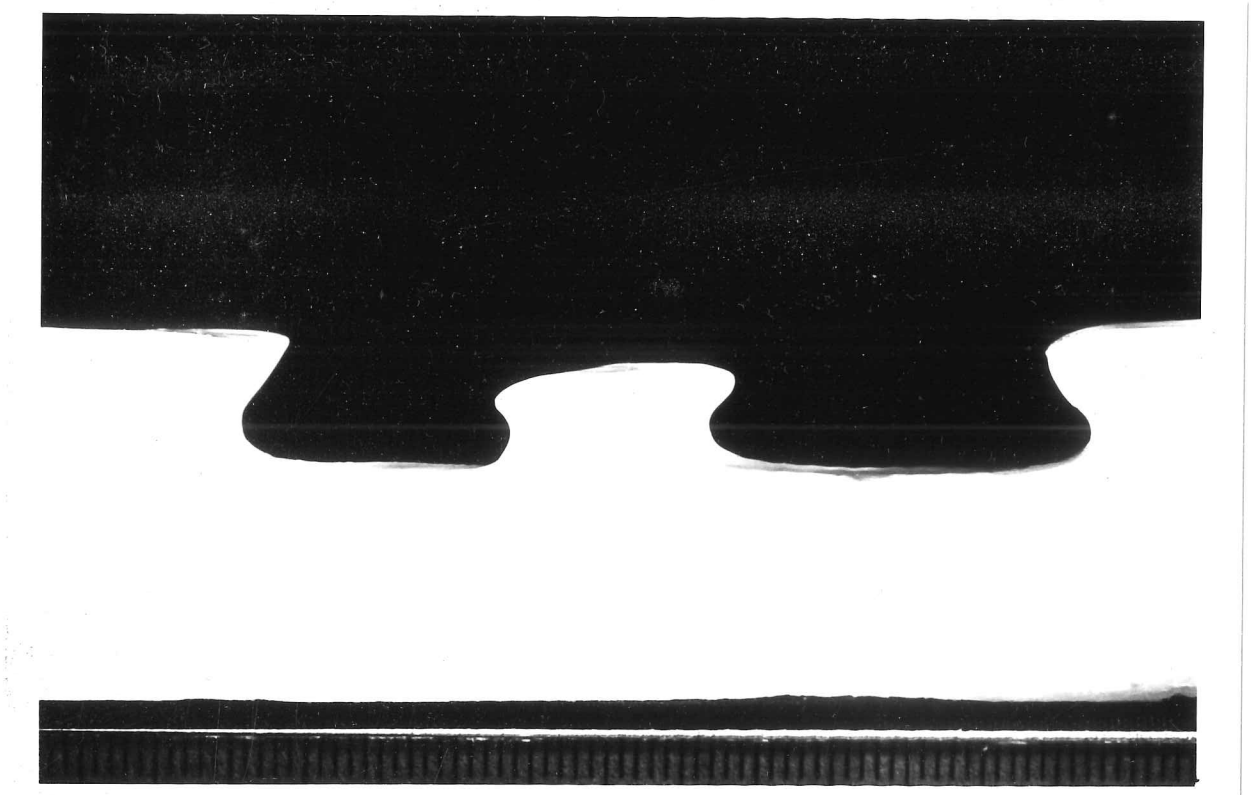

Figure 4.17. Cross-section of a channel eroded in wax by the turbulent flow of hot water, demonstrating the channel splitting instability. The flow has split into two, leaving an exposed island near the centre of the channel. Note that the two sub-channels each continue to evolve as a single channel, with undercutting of the banks (from Huppert & Sparks 1985*a*).

(4.2.11) for the heat transfer coefficient h_T becomes

$$h_T = 0.02\rho c_p \kappa_T^{0.6} \nu^{-0.4} \hat{q}^{0.8} H^{-1} . \tag{4.5.1}$$

For a lava flow of constant thickness H, substituting $A = 2WH$, $P = 2W$ (as $H \ll 2W$) and $Q = 2W\hat{q}$ into (4.2.8), we obtain

$$H^3 = \left(\frac{\rho\lambda}{4g\Delta\rho \sin\chi} \right) \hat{q}^2 . \tag{4.5.2}$$

Substituting for $\hat{q}$ from (4.5.2) into (4.5.1), we see that

$$h_T = 0.02\rho c_p \kappa_T^{0.6} \nu^{-0.4} \left(\frac{\rho\lambda}{4g\Delta\rho \sin\chi} \right)^{-0.4} H^{0.2} \tag{4.5.3}$$

for a lava flow of constant thickness H. Equation (4.5.3) demonstrates that the heat transfer from a thin current is less than that from a thick current. For a current with variable thickness in the cross-stream x-direction, (4.5.3) may be applied locally if $dh/dx \ll h/W$. Unfortunately, this cannot apply at the margins of the current, where $h \to 0$. In addition, the fluid velocity must vary across the width of the current, with the effect of boundary friction being felt most where the current is thin. In any case, direct application of (4.5.3) to the model presented in the preceding section is not straightforward. If one is to admit the possibility of variations in heat transfer and downstream velocity across the width of the current, a full three-dimensional solution should be calculated, with suitable treatment of cross-stream mixing processes. This is not attempted here. Instead the effect of variations in current thickness across the stream are parameterised in the following expression for the erosion rate v,

$$v(s,t) = v_0(t)\left\{\mathcal{M} + (1-\mathcal{M})\left(\frac{H}{H_0}\right)^{\lambda}\right\}, \tag{4.5.4}$$

where $v_0(t)$ is given by (4.2.12), $\mathcal{M}$ is a parameter describing the efficiency with which fluid is mixed across the stream, and H_0 is the thickness of the current at the centre of the channel. The exponent λ (> 0) represents the degree of variation in erosion rate with current depth. If $\mathcal{M} = 1$, the lava flow is perfectly mixed and there is no variation in melting rate with current thickness. Alternatively, if $\mathcal{M} = 0$, the current is poorly mixed across-stream and the heat transfer coefficient h_T is proportional to H^{λ}, where H is the local current thickness, as suggested by (4.5.3). An omission from (4.5.4) is the cross-stream variation in temperature and downstream velocity which would follow from inefficient lateral mixing. For a current of constant thickness H, equation (4.5.2) implies that the downstream velocity $u = \hat{q}/H$ is proportional to $H^{0.5}$. The cooling rate $-D\theta/Dt$ is proportional to h_T (from equation (4.3.29)). Equation (4.5.3) therefore implies that the rate of cooling with distance downstream is proportional to $H^{-0.3}$. Hence, at a given distance downstream from the source, the fluid is coolest where the current is thinnest. The choice $\lambda = 0.2$ therefore represents a conservative estimate of the variation in ground melting rate with current depth.

Writing $H = Wh$ and $H_0 = Wh_0$, the evolution equation (4.3.8) for the channel wall

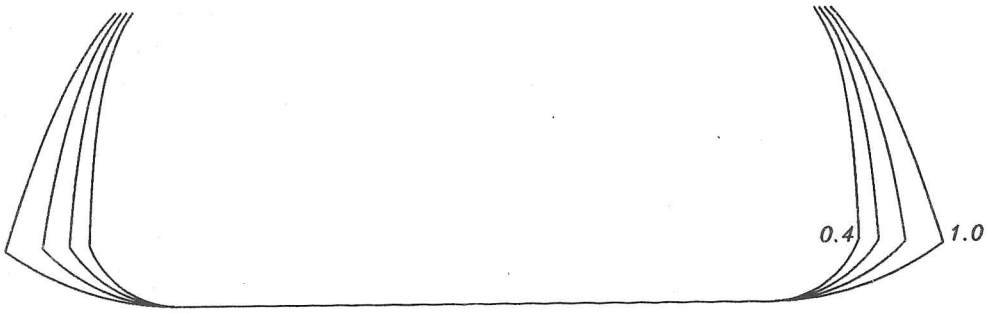

Figure 4.18. Channel cross-section after $\bar{t} = 1$ for 4 different values of the lateral mixing efficiency parameter $\mathcal{M}$, namely 0.4, 0.6, 0.8 and 1. The lateral extent of the erosion is greatest for $\mathcal{M} = 1$ and least for $\mathcal{M} = 0.4$. For all curves the parameter $\alpha = 0.05$.

inclination ψ may be written (*c.f.* (4.3.28))

$$\frac{\partial \psi}{\partial \bar{t}} + \left\{ \int_0^\sigma g \frac{\partial \psi}{\partial \sigma'} \, d\sigma' \right\} \frac{\partial \psi}{\partial \sigma} = -\frac{\partial g}{\partial \sigma}, \tag{4.5.5}$$

where $g(\sigma, \bar{t}) = \mathcal{M} + (1 - \mathcal{M})(h/h_0)^\lambda$ and $h_0 = h(0, \bar{t})$. The current thickness is given by

$$h(\sigma, \bar{t}) = \int_\sigma^{\sigma^*(\bar{t})} \sin\psi \, d\sigma + d(\bar{t}), \tag{4.5.6}$$

where $d(\bar{t})$ is the cap thickness when the upper surface of the current has not yet fallen below the original ground level, as described in §4.3.1. To avoid a singularity on the right-hand side of (4.5.5) when $h \to 0$, while keeping λ as close to 0.2 as possible, the choice $\lambda = 1$ is made. Equation (4.5.5) cannot be solved analytically (except when $\mathcal{M} = 1$), and so an explicit pseudo-spectral method was used (see Appendix).

The results of a typical calculation are presented in Figure 4.18. The lateral extent of the thermal erosion is significantly diminished when depth-dependent erosion is considered. This is because the current is thinnest at the margins of the current and therefore has less erosive power. It has been suggested (Hulme 1973) that the lava flow may freeze at its margins because it is so thin. While it is true that the local flow Reynolds number is lower at the channel margins, one cannot determine whether it becomes subcritical without solving for the cross-stream variation in flow. Nevertheless, one would certainly expect that freezing of the lava flow would occur first at its margins, and later towards the centre of the stream.

4.5.2 Channel splitting instability

Using the parameterisation described in §4.5.1, it is possible to investigate the channel splitting mechanism described by Huppert & Sparks (1985*a*) and Huppert (1986). For instability to occur, the instability mechanism provided by the parameterisation (4.5.4) must dominate the stability mechanism provided by the variation in melting rate with curvature, discussed in §4.2.2. Using equation (4.2.21) for the rate of melting of a curved surface, we now write

$$v(s,t) = v_1(t)\left\{\mathcal{M} + (1-\mathcal{M})\left(\frac{H}{H_0}\right)^{\lambda}\right\}, \tag{4.5.7}$$

where $v_1(t) = v_0(t)(1-\varepsilon W\psi_s)$. The evolution equation for ψ may still be written in the general form (4.5.5), where now

$$g(\sigma,\bar{t}) = (1-\varepsilon\psi_\sigma)\left\{\mathcal{M} + (1-\mathcal{M})\left(\frac{h}{h_0}\right)^{\lambda}\right\}. \tag{4.5.8}$$

Here h_0 is chosen to be a typical constant current thickness. In the linear stability calculations below, h_0 is chosen to be the average current depth, and in the numerical calculations performed later in this subsection for a thermal erosion channel, h_0 is chosen to be the current thickness at $\bar{t} = 0$. The latter choice avoids the singularity in (4.5.8) which would otherwise arise if the current thickness h were to vanish at the centre of the channel. When substituting (4.5.8) into (4.5.5), the curvature correction $\varepsilon\psi_\sigma$ leads to a diffusive term on the right-hand side. In particular, when $\mathcal{M} = 1$, equation (4.5.5) becomes

$$\frac{\partial\psi}{\partial\bar{t}} + \psi\frac{\partial\psi}{\partial\sigma} = \varepsilon\left(\frac{\partial^2\psi}{\partial\sigma^2} + \frac{\partial\psi}{\partial\sigma}\int_0^\sigma\left(\frac{\partial\psi}{\partial\sigma'}\right)^2 d\sigma'\right). \tag{4.5.9}$$

This is similar in appearance to Burgers' equation ($\psi_T + \psi\psi_X = \varepsilon\psi_{XX}$), which is well-known in the field of nonlinear acoustics. The additional integral term on the right-hand side is of the same magnitude everywhere as the diffusive $\varepsilon\psi_{\sigma\sigma}$ term and makes (4.5.9) insoluble analytically. However, the essential physics are unaltered. In Burgers' equation, the diffusive term limits wave steepening so that multi-valued solutions for ψ cannot arise. Here, a multi-valued solution for ψ corresponds to a cusp in the channel wall. The

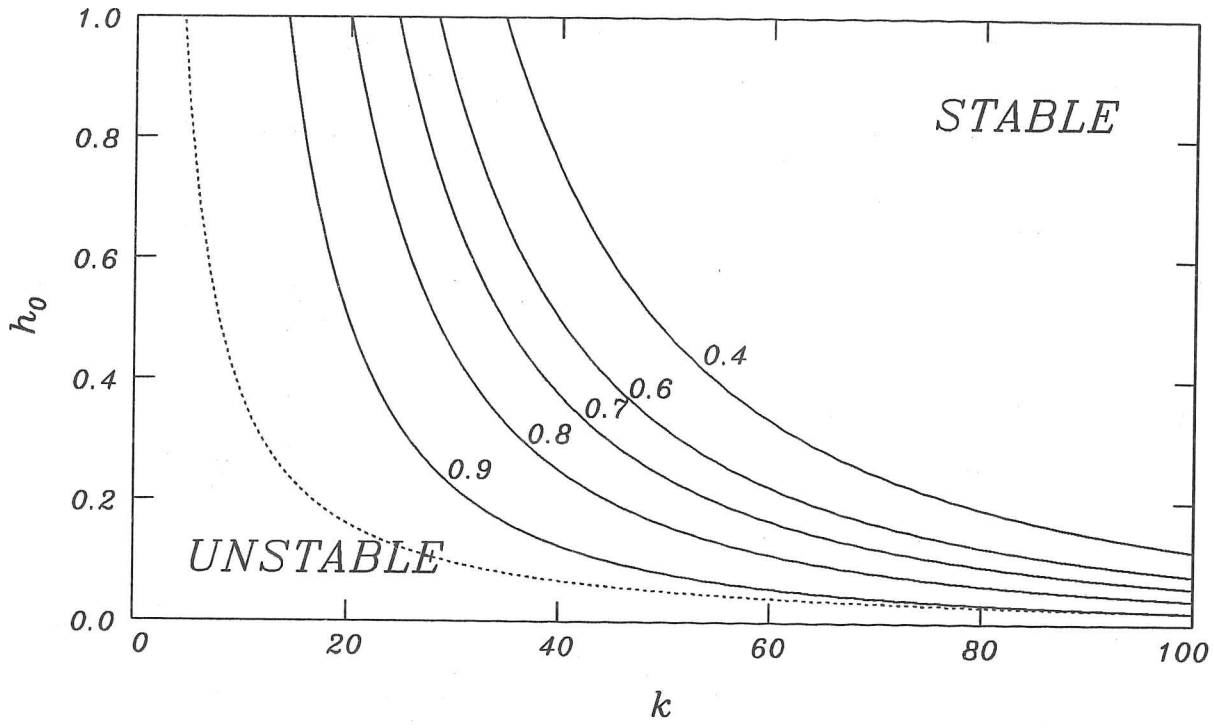

Figure 4.19. Marginal stability curves for wavenumber k against nondimensional current depth h_0 for various values of the lateral mixing efficiency parameter $\mathcal{M}$. The curvature coefficient $\varepsilon = 0.0001$, the exponent $\lambda = 0.2$ and $\mathcal{M}$ takes the values 0.9, 0.8, 0.7, 0.6 and 0.4. Growth rates decrease as k or h_0 increase. Also plotted ($\cdots\cdots$) is the marginal stability curve for the choice $\mathcal{M} = 1-(1-\mathcal{M}_0)\exp(-h_0 k)$, where $\mathcal{M}_0 = 0.2$. The maximum growth rate is $p_{\max} = \lambda(1-\mathcal{M})/h_0$.

curvature term in (4.5.9) prevents this and the solution for ψ remains single-valued. In §4.2, it was shown that, for a typical komatiitic lava flow, $\varepsilon \lesssim 10^{-4}$.

To demonstrate the competition between curvature and depth-dependence effects, we now perform some linear analysis. Consider a flat, infinite surface which is perturbed so that

$$\psi = \tilde{\psi}\, e^{p\bar{t}} \sin k\sigma\,, \tag{4.5.10}$$

where $\tilde{\psi} \ll 1$. If h_0 is the average depth of fluid above the surface, then the local depth h of the fluid is

$$h = h_0 - \int_{\sigma_0}^{\sigma} \sin\psi \, d\sigma'\,, \tag{4.5.11}$$

where $h = h_0$ at $\sigma = \sigma_0$. Over a number of wavelengths, the depth h averages h_0. For

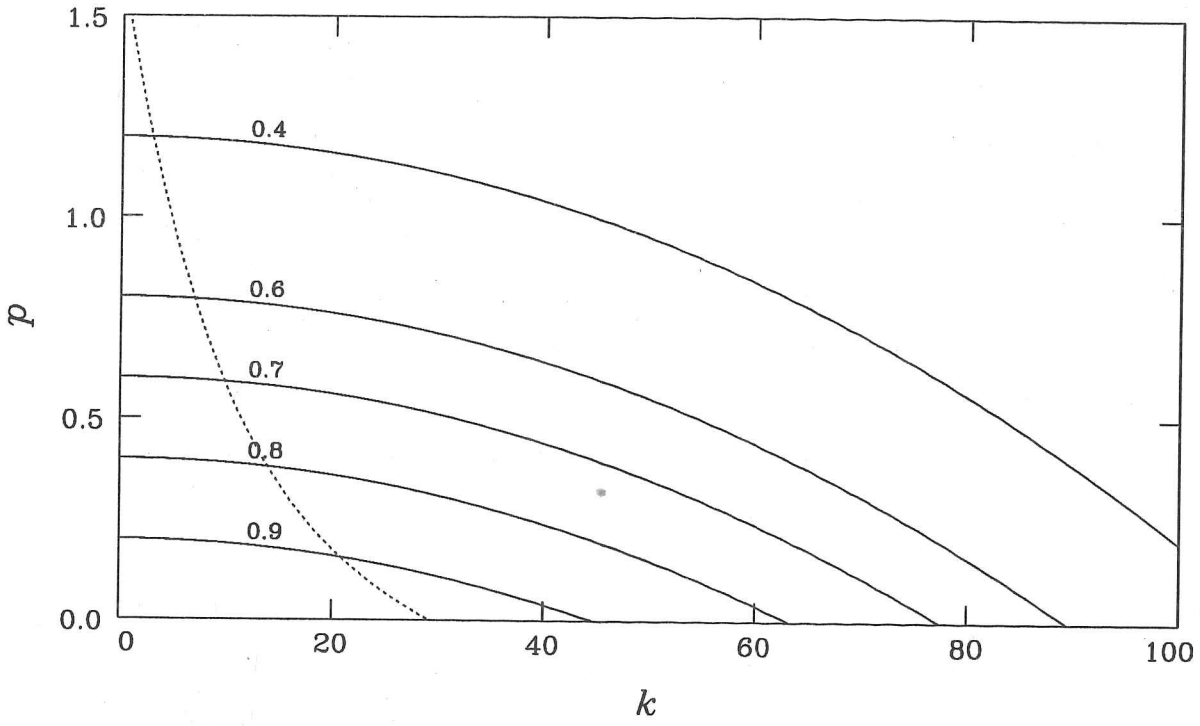

Figure 4.20. Linear growth rate p as a function of wavenumber k for various values of the lateral mixing efficiency parameter $\mathcal{M}$. The curvature coefficient $\varepsilon = 0.0001$, the exponent $\lambda = 0.2$ and the nondimensional current depth $h_0 = 0.1$. The parameter $\mathcal{M}$ takes the values 0.9, 0.8, 0.7, 0.6 and 0.4. Also plotted (· · · · ·) is the linear growth rate for the choice $\mathcal{M} = 1 - (1 - \mathcal{M}_0)\exp(-h_0 k)$, where $\mathcal{M}_0 = 0.2$. The growth rate tends to its maximum value $p_{\max} = \lambda(1 - \mathcal{M})/h_0$ as $k \to 0$.

$\tilde{\psi} \ll 1$, equation (4.5.8) becomes

$$g(\sigma, \bar{t}) = 1 - \varepsilon\psi_\sigma - \frac{\lambda(1-\mathcal{M})}{h_0}\int_{\sigma_0}^{\sigma} \sin\psi \, d\sigma' + O(\tilde{\psi}^2). \tag{4.5.12}$$

Substituting the expression (4.5.12) for the melting rate $g(\sigma, \bar{t})$ into the evolution equation (4.5.5) and linearising, the following dispersion relation between the perturbation growth rate p and the wavenumber k is obtained

$$p = -\varepsilon k^2 + \frac{\lambda(1-\mathcal{M})}{h_0}. \tag{4.5.13}$$

The marginal stability curves are plotted for wavenumber against current depth for a number of values of $\mathcal{M}$ in Figure 4.19. The liquid/solid interface is stable to perturbations

for large wavenumbers (short wavelengths), efficient lateral mixing ($\mathcal{M} \rightarrow 1$) and currents of large aspect ratio ($h_0 \rightarrow \infty$). Shorter wavelengths are more stable because they have higher curvature ψ_σ. Note that the channel depth has been scaled by the channel half-width W, and so h_0 represents the cross-sectional aspect ratio of the lava flow. For $\varepsilon = 0$, all perturbations are linearly unstable, while for $\mathcal{M} = 1$, all perturbations are linearly stable. For the bottom of an erosion channel, $-1 < \sigma < 1$ and $h_0 << 1$, and so perturbations are unstable up to quite high wavenumbers. However, the lateral mixing efficiency parameter $\mathcal{M}$ has been modelled as constant in this section, whereas it should depend upon the aspect ratio given by the channel depth and the perturbation wavelength, namely $h_0 k$. In general, $\mathcal{M}$ should increase as the channel becomes deeper and increase with wavenumber, because the lateral mixing is more efficient over shorter lengthscales. The marginal stability curve for the choice $\mathcal{M} = 1-(1-\mathcal{M}_0)\exp(-h_0 k)$, where $\mathcal{M}_0 = 0.2$ is shown on Figure 4.19 as the dotted line. When the lateral mixing efficiency parameter is dependent upon $h_0 k$ in this manner, we see that the higher wavenumbers only become unstable when h_0 is very small. In Figure 4.20, the growth rate p is plotted against wavenumber k. The growth rate tends to its maximum $p_{\max} = \lambda(1 - \mathcal{M})/h_0$ as $k \rightarrow 0$. The growth rates increase and more modes become unstable as the aspect ratio h_0 decreases. Note that the maximum in growth rate at $k = 0$ is more marked when the choice $\mathcal{M} = 1 - (1 - \mathcal{M}_0)\exp(-h_0 k)$ is made (dotted line). We see, therefore, that the fastest growing mode is the mode with the lowest wavenumber consistent with the model geometry. For a channel of half-width wW, where W is the initial half-width of the channel, the lowest wavenumber possible corresponds to $\lambda = 2w$, *i.e.* $k = \pi/w$. Therefore, as the channel widens, instability becomes more likely because the minimum geometrically possible wavenumber decreases.

In short, two conclusions can be drawn from the linear analysis. First, geometric instability is most likely for lava flows of low aspect ratio because they exhibit less efficient lateral mixing. Second, the instability has a preferred wavelength which is equal to the width of the channel. The latter effect has been observed experimentally by Huppert & Sparks (1985*a*).

To demonstrate how a perturbation in the floor of the channel evolves, three sample calculations will be described. All calculations started from a solution for ψ which was perturbed from a solution calculated up to $\bar{t} = 0.5$ with $\varepsilon = 0$. Consequently $\psi = 0$ for

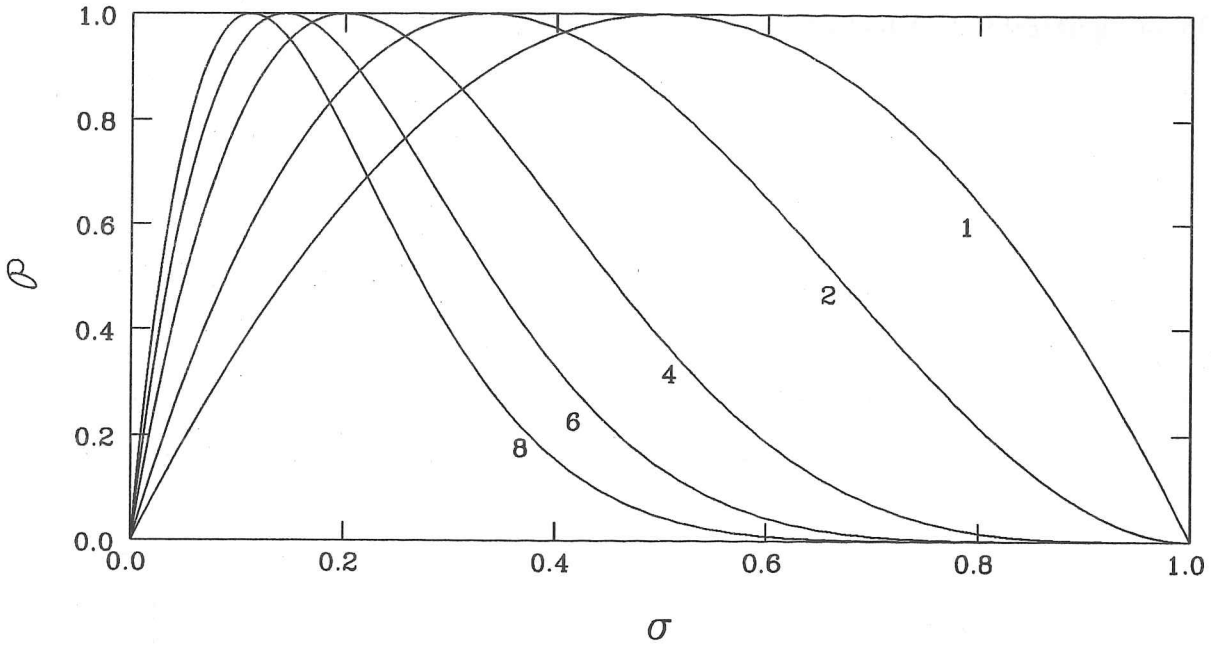

Figure 4.21. Family of perturbation functions $\mathcal{P}^{(\gamma)}$ for $\gamma = 1, 2, 4, 6$ and 8. Note that as γ increases, the perturbation becomes more biased towards $\sigma = 0$

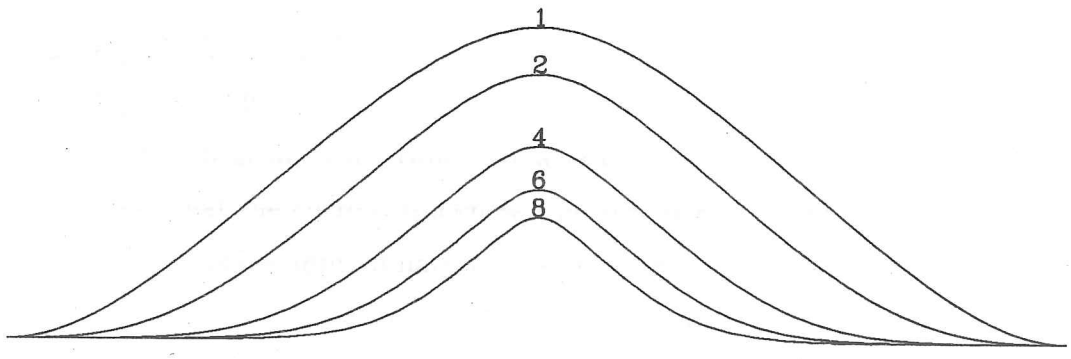

Figure 4.22. Shape of channel floor for perturbations $\mathcal{P}^{(\gamma)}$ with $\mathcal{P}_0$=1. The parameter γ takes the values 1, 2, 4, 6 and 8. The width of the central bump is a decreasing function of γ and the height of the bump is an increasing function of $\mathcal{P}_0$.

$0 < \sigma < 1$. The solution for $0 < \sigma < 1$ was then perturbed by subtracting one of the following family of perturbations from ψ:

$$\mathcal{P}^{(\gamma)}(\sigma) = \mathcal{P}_0 \frac{(1+\gamma)^{1+\gamma}}{\gamma^\gamma} \sigma(1-\sigma)^\gamma, \tag{4.5.14}$$

where $\mathcal{P}_0 < \pi/2$ is the maximum value of the perturbation in ψ. The constant $\gamma > 1$ represents a bias towards the centre of the channel, so that as γ increases, the maximum in $\mathcal{P}$ moves closer to $\sigma = 0$. The shapes of the functions $\mathcal{P}^{(\gamma)}$ are shown in Figure 4.21, and the resulting perturbations to the flat part of the bottom of the channel shown in Figure 4.22. For a given maximum perturbation $\mathcal{P}_0$ in ψ, the 'bump' in the centre of the channel is highest and widest for $\gamma = 1$, becoming smaller and narrower as γ increases. The constant γ is therefore a measure of the narrowness of the perturbation. The family of perturbations given by (4.5.14) was specifically chosen to enable us to see how perturbations of varying wavelengths may evolve.

In the calculations, the curvature coefficient $\varepsilon = 10^{-2}$ for computational convenience. The thickness of a shock described by Burgers' equation is $\delta_s = \varepsilon$, and so at least 10^4 collocation points would be required for the pseudo-spectral solution of (4.5.5) if ε were equal to 10^{-4}. This is too expensive computationally. The possibility of a shock-like solution in equation (4.5.5) arises because $\psi_\sigma < 0$ close to $\sigma = 0$ when the channel shape has been perturbed.

In Figure 4.23, the channel wall inclination ψ is plotted against σ for three cases. First, in Figure 4.23(a), the efficiency parameter $\mathcal{M} = 0.6$ and the bias $\gamma = 8$. The perturbation in ψ, close to $\sigma = 0$ grows with time. At a later time than plotted, the perturbation becomes so great that the current thickness vanishes at $\sigma = 0$ and an island forms. Note that the slope ψ_σ remains approximately constant at $\sigma = 0$. Without the curvature term, the slope would grow until the solution for ψ became multi-valued (corresponding to a cusp in the channel wall), at which point the numerical calculation would break down. For the same bias $\gamma = 8$, but with $\mathcal{M} = 1$ (Figure 4.23(b)), the perturbation decays with time and no island forms. This is because the solid/liquid interface is convex upwards at the centre of the channel. The heat flux becomes concentrated there and melting increases locally. This is the same effect as that predicted by equation (4.2.21). These two cases represent two extremes — growth due to the dependence of melting rate upon

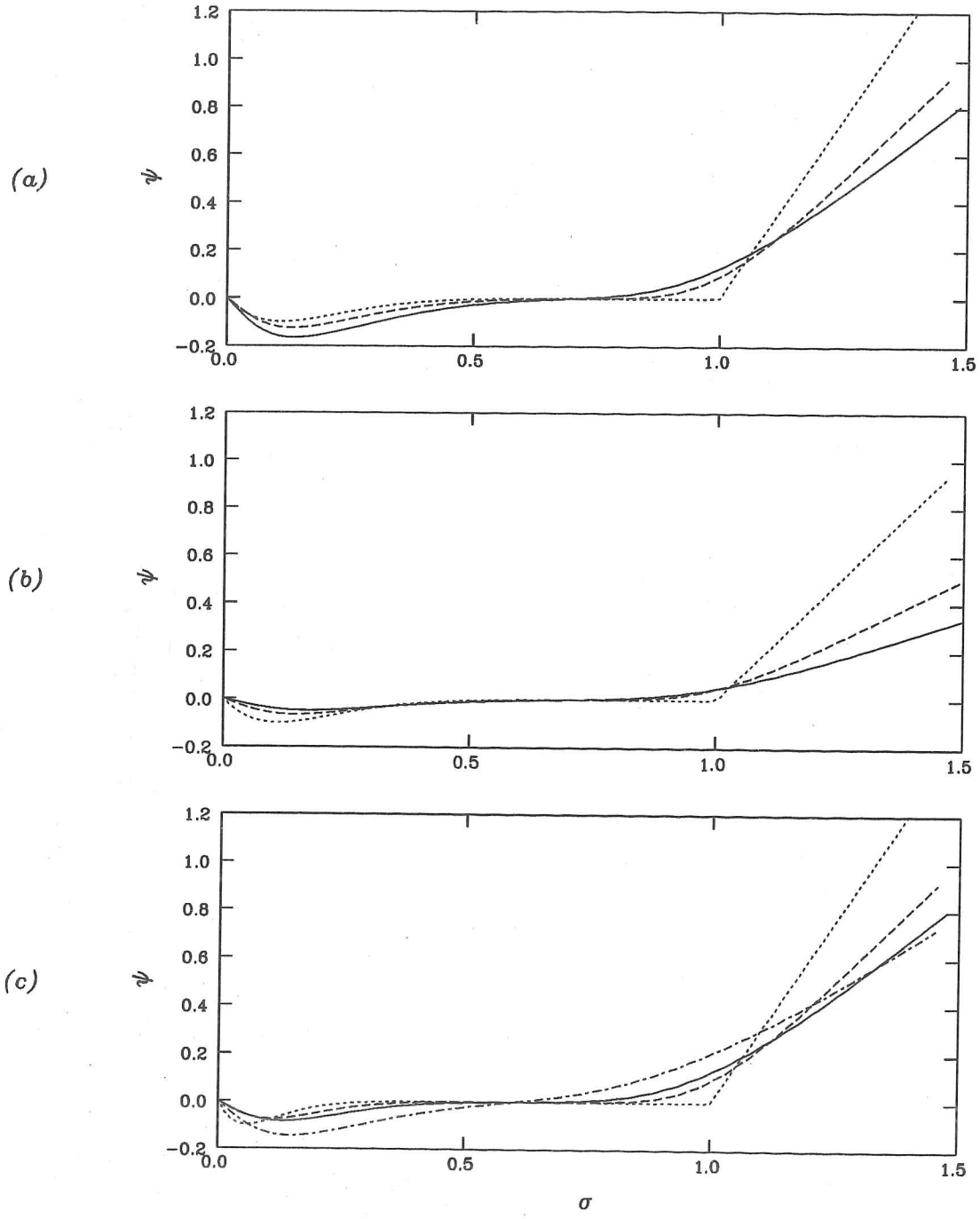

Figure 4.23. Evolution of the channel wall inclination ψ for three cases: (a) $\mathcal{M} = 0.6, \gamma = 8$; (b) $\mathcal{M} = 1$, $\gamma = 8$; and (c) $\mathcal{M} = 0.6, \gamma = 16$. For all three figures, the perturbation magnitude $\mathcal{P}_0 = 1$. The channel floor is first perturbed at $\bar{t} = 0.5$ ($\cdots\cdots$), and curves are drawn thereafter for $\bar{t} = 0.75$ ($- - -$) and $\bar{t} = 1$ (——). In figure (c), an additional curve is drawn for $\bar{t} = 1.5$ ($- \cdot -$).

current thickness, and decay due to curvature effects. In Figure 4.23(c), the growth of the perturbation is shown for the case $\mathcal{M} = 0.6$, $\gamma = 16$. Here, the perturbation has a shorter characteristic wavelength, and so is damped initially. However, the longer-wavelength components of the disturbance grow and so the perturbation grows, with a longer characteristic wavelength, as the melting continues. This is because the short-wavelength components of the perturbation are stabilised by curvature effects, whereas the long-wavelength components are destabilised by depth-dependence effects.

The response of the channel geometry to perturbations is clearly very complex. It is possible that nonlinear interaction between modes is occurring in the case shown in Figure 4.23(c). This is beyond the scope of the present study, especially when one considers the simplicity of the parameterisation (4.5.4). However, the success of the simple model presented here is encouraging, and would suggest that a more complete investigation of lateral mixing in thin lava flows, coupled with the model presented here for the evolution of the channel geometry, would lead to interesting results.

4.6 Discussion

In this chapter, a new model has been presented for the thermal erosion of channels by hot, turbulent lava flows. In particular, an analytical solution for the channel cross-sectional geometry has been found under certain simplifying conditions. The main conclusions of this study are that sideways erosion is greatest for the largest flow rates and that narrower lava flows exhibit less downwards erosion, but greater contamination, than wider flows. In addition, it has been shown that inefficient lateral mixing of the fluid can lead to lower melting rates in shallower parts of the channel. This leads to reduced erosion at the margins of the channel and also provides a mechanism for the splitting of the lava flow into two.

By describing the melting channel wall at a given distance downstream from the source as a moving line, evolution equations have been found for the inclination of the channel wall to the horizontal. For a lava flowing down a shallow slope, a condition was obtained for the point along the channel wall at which the top of the current must meet the wall, and for a uniform erosion rate (at a given distance downstream), the channel cross-sectional shape was shown to be a function of the single parameter α. The amount of sideways erosion relative to downwards erosion is an increasing function of flow rate and drag coefficient, and a decreasing function of channel width and seafloor inclination. The extent of the sideways erosion determines the deviation of the model presented here from the original two-dimensional model of Huppert *et al.* (1984) and Huppert & Sparks (1985*a*). The most notable feature of the solutions for the channel cross-section is the undercutting of the channel walls as the fluid level falls below the original ground level. This feature has been observed in experiments (Huppert & Sparks 1985*a*) and in the field (Lesher 1983).

The equations of Huppert & Sparks (1985*a*) for the cooling of the lava downstream were then extended to the case of a general channel cross-section and two new analytical solutions were found, for the lava contamination as a function of lava temperature, and for the maximum lava contamination when Reynolds number limitation is considered. The solution for the contamination as a function of temperature allowed most of the conclusions drawn from the model to be made without recourse to numerical solutions of the thermal evolution equations. In the process, some corrections were made to the

earlier analyses of Huppert and co-workers. In particular, the maximum contamination (with or without Reynolds number limitation) was shown to be strongly dependent on the latent heat released when crystals form, and are suspended, within the cooling lava. Consequently, the maximum possible contamination for a lava erupted at 1600 °C onto a seafloor with melting temperature 1200 °C was shown to be greater than 20%, rather than the value of 10% suggested by Huppert *et al.* (1984) and Huppert & Sparks (1985*a*). Their main conclusion, that komatiites can exhibit a high degree of crustal contamination, is unaffected.

The variation in erosive behaviour and lava contamination with channel width was then addressed. For channels narrower than a reference width $2W_0$, the downwards erosion was noticeably less, and the lava contamination at a given distance downstream greater, than predicted by the earlier two-dimensional models. The reference half-width W_0 increases linearly with eruption time. The conclusion that narrower lava flows exhibit less downwards erosion but experience greater contamination is perhaps counter-intuitive, but is a natural consequence of the dependence of contamination upon temperature. For a narrow channel, the sideways erosion is greater and so the current becomes thinner and the surface area over which it cools becomes greater. Hence, the cooling rate of the lava increases and the temperature of the lava at a given distance downstream from the source falls. This results in a reduction in erosion rate, but an increase in contamination. It is then simple to see how focussing of a lava flow by topography affects the level of contamination in the lava. The focussed flow exhibits a two-dimensional flow rate which is higher than the volume erupted per unit length of fissure. Consequently the lava flows faster and the rate of decrease of temperature with distance downstream is lower. At a fixed distance downstream from the source, the lava temperature is therefore higher and the contamination lower.

In the final section, the possible effects of inefficient lateral mixing of the lava were discussed. It was argued that the heat transfer at the margins of the channel is less than in the centre, which leads to a reduction in the sideways extent of the erosion. It was then briefly shown that the channel splitting instability observed by Huppert & Sparks (1985*a*) could have been due to variations in erosion rates with current thickness. In §4.2.2, a calculation was presented for the melting of a curved surface, and a stabilising mechanism proposed for small-wavelength perturbations to the shape of the channel-

cross section. By combining these two mechanisms and conducting a linear analysis of the evolution equation for the channel geometry, we were able to show that the channel shape is least stable to perturbations for low aspect ratios, in which the lava flow is much wider than it is deep, and that the fastest growing mode corresponds to a disturbance with wavelength equal to the width of the channel. This is consistent with the experimental observations of Huppert & Sparks (1985*a*). Representative numerical calculations using the full erosion model were then performed to demonstrate the growth of long-wavelength perturbations and the decay of short-wavelength disturbances.

The model presented here is in many ways idealised. Many complicating factors are neglected, such as contamination of the lava during ascent (Huppert & Sparks 1985*b*) and the full three-dimensional nature of the lava flow. Unfortunately, it is also difficult to see how many of the results may be applied directly to field observations. While it is possible to make predictions based on a single eruption, it is more likely that a succession of eruptions of varying length occurred. The channel created by the first eruption will have been a natural route for lavas erupted from later eruptions and so the previously emplaced komatiite or komatiitic basalt will have been melted again and partially assimilated into the later flows. This may explain why some komatiitic remnants exhibit very little contamination (Nisbet 1987).

One means of confirmation may come from experiments with crystallizing lunar olivine basalt (Donaldson 1982). The shape and size of olivine crystals depends strongly on the cooling rate and supercooling at the time of crystallization. Predictions for cooling rate can certainly be made directly from this model if the volume flux is known (equation (4.3.35)), but the extent of supercooling is less easy to determine. If the emplacement temperature of an individual lava can be determined by comparison with Donaldson's experiments, then equation (4.3.44) provides an estimate of the degree of contamination of that lava. If the composition of the crustal material is known, one then has an estimate for the composition of the erupted komatiitic lava. Another possible approach would be to compare the cross-sectional channel shape of a channel eroded by a komatiite lava with the theoretical shapes presented in Figure 4.6. This provides an estimate of the volume flux of the eruption which led to the channel being formed. In this chapter, we have presented many ways in which different flow conditions and material properties can lead to different channel geometries, lava emplacement temperatures, degrees of downwards

erosion and levels of contamination. By presenting a full picture of the physical processes involved in the erosion of thermal channels, it may prove possible to deduce some of the unknown flow parameters and material properties from the field evidence.

Appendix. Numerical methods

To solve the general evolution equation for the channel wall tangent angle ψ, the pseudo-spectral method is used. Pseudo-spectral methods work well when applied to nonlinear problems which are periodic and whose solutions exhibit rapid variations over short lengthscales. Conventional finite difference schemes would require a very fine mesh size to resolve sharp features such as shock waves, commonly observed in nonlinear wave theory, especially if there is little *a priori* information as to the exact location of the shock.

To apply the pseudo-spectral method, the domain $-\sigma^*(\bar{t}) < \sigma < \sigma^*(\bar{t})$ is first mapped onto $-1 < \xi < 1$ through the transformation $\sigma = \xi\sigma^*(\bar{t})$, $\mathcal{T} = \bar{t}$. Equation (4.5.6) then becomes

$$\frac{\partial\psi}{\partial\mathcal{T}} = -\frac{1}{\sigma^*}\left\{\int_0^\xi \hat{g}\frac{\partial\psi}{\partial\xi'}\,d\xi' - \xi\sigma^*_{\mathcal{T}}\right\}\frac{\partial\psi}{\partial\xi} - \frac{1}{\sigma}\frac{\partial\hat{g}}{\partial\xi}, \qquad (4.A.1)$$

where σ^* is now a function of $\mathcal{T}$ and $\hat{g}(\xi,\mathcal{T}) = g(\sigma,\bar{t})$. The angle ψ is not a periodic function of ξ (as $\psi(-\sigma^*,\bar{t}) = -\psi(\sigma^*,\bar{t}) \neq 0$), and so the ξ-domain is extended to $|\xi| < 1+\phi$, where $\phi > 0$. At each new timestep, the solution for ψ at the previous timestep is extended into the domain $-1-\phi < \xi < 1+\phi$ by fitting a trigonometric function into the ranges $1+\phi > |\xi| > 1$ to ensure that ψ is smooth and periodic over the whole domain $|\xi| < 1+\phi$. The parameter ϕ is chosen so that the total number of collocation points is an integral power of 2. This maximises the efficiency of the Fast Fourier Transform (FFT) algorithm used in the pseudo-spectral method. For example, if 200 evenly-spaced points are required to resolve ψ over the range $-1 < \xi < 1$, ϕ is chosen so that the total number of points is 256, *i.e.* $\phi = 0.28$.

Since ψ is now periodic, the integrals on the right-hand side of (4.5.7) can be evaluated by taking FFTs of their integrands, dividing the nth Fourier coefficient by ik_n and performing the inverse transforms. Derivatives may be calculated in a similar manner. Having evaluated the right-hand side of (4.A.1) by Fourier techniques, the solution is marched forward in time by a simple explicit Forward Euler scheme. A good description of pseudo-spectral methods as applied to nonlinear, periodic equations is provided by Peyret & Taylor (1983). Absolute stability criteria for pseudo-spectral methods have not yet been identified. One suggested criterion, for solution of inviscid problems by Adams-Bashforth time integration with spatial resolution by Chebyshev expansions, is

$\Delta\mathcal{T} \lesssim 8/N^2$, where N is the number of spectral terms (Gottlieb & Orszag 1977). For $N = 256$, this corresponds to $\Delta\mathcal{T} \lesssim 10^{-4}$. For viscous problems, such as we have in §4.5.2 when the effect of channel curvature (as given by equation (4.2.21)) is included, the timestep is also restricted to be less than the viscous timescale. The nondimensional viscous timescale for equation (4.5.7) is $1/\varepsilon \gg 1$. Viscosity therefore has no role to play in determining the stability criterion.

For the problem studied here, it was found that 200 points were sufficient to describe the solution for ψ with a timestep $d\mathcal{T} = 10^{-4}$. A typical calculation, up to $\mathcal{T} = 1$, took around 5 minutes on a Convex C210 vector computer, the most expensive part of the calculation being the FFT algorithm.

To solve (4.A.1), we must determine the rate of increase of arc length $\sigma^*_{\mathcal{T}}$. At early times, while the top of the current is still above the ground level, σ^* is determined by the condition that the top of the channel wall is at ground level, *i.e.* $z(1,\mathcal{T}) = 0$. The rate of deepening of the channel at its centre is $g(0,\mathcal{T})$, and so (4.3.11) implies that σ^* must satisfy

$$-\int_0^{\mathcal{T}} g(0,\mathcal{T})\, d\mathcal{T} + \sigma^* \int_0^1 \sin\psi \, d\psi = 0. \tag{4.A.2}$$

Differentiating (4.A.2) with respect to $\mathcal{T}$ and substituting from (4.A.1) for $\psi_{\mathcal{T}}$, we obtain after some algebra

$$\frac{\partial\sigma^*}{\partial\mathcal{T}} = \int_0^1 g\frac{\partial\psi}{\partial\xi}\, d\xi + g\cot\psi\Big|_{\xi=1}. \tag{4.A.3}$$

The cross-sectional area of fluid below the original ground level is

$$c(\mathcal{T}) = 2{\sigma^*}^2 \int_0^1 \sin\psi \int_0^\xi \cos\psi \, d\xi' \, d\xi\,, \tag{4.A.4}$$

and so the cross-sectional area of the current is

$$a(\mathcal{T}) = c(\mathcal{T}) + 2\Delta{\sigma^*}^2 \int_0^1 \cos\psi \, d\xi \tag{4.A.5}$$

and the wetted half-perimeter is

$$p(\mathcal{T}) = \sigma^*\left(1 + \int_0^1 \cos\psi \, d\xi + \Delta\right). \tag{4.A.6}$$

Here, Δ is the cap thickness ($d = \sigma^*\Delta$) and is obtained by substituting (4.A.5) and

(4.A.6) into (4.3.16) and solving the resulting cubic equation. The cap thickness Δ is a decreasing function of $\mathcal{T}$ and becomes zero when the top of the current reaches the initial ground level at $\mathcal{T} = \mathcal{T}_{\text{crit}}$, say. For $\mathcal{T} > \mathcal{T}_{\text{crit}}$, Δ is fixed at zero and now σ^* is determined by (4.3.16), *i.e.*

$$8{\sigma^*}^5 \left(\int_0^1 \sin\psi \int_0^\xi \cos\psi \; d\xi' \; d\xi \right)^3 = \alpha \left(1 + \int_0^1 \cos\psi \; d\xi \right) . \tag{4.A.7}$$

Differentation of (4.A.7) with respect to $\mathcal{T}$ and substitution from (4.A.1) for $\psi_{\mathcal{T}}$ now leads to

$$\frac{\partial \sigma^*}{\partial \mathcal{T}} = I_4 + \frac{I_1(g\sin\psi + I_4) + 3(I_2+1)(gI_2\cos\psi - I_3)}{3I_2(I_2+1)\sin\psi - I_1(1+\cos\psi)}, \tag{4.A.9}$$

where g and ψ are evaluated at $\xi = 1$ and

$$\begin{aligned} I_1 &= \int_0^1 \sin\psi \int_0^\xi \cos\psi \; d\xi' \; d\xi \, ; \\ I_2 &= \int_0^1 \cos\psi \; d\xi \, ; \\ I_3 &= \int_0^1 g \; d\xi \, ; \\ I_4 &= \int_0^1 g \frac{\partial \psi}{\partial \xi} \; d\xi \, . \end{aligned} \tag{4.A.10}$$

Although σ^* could be obtained directly from (4.A.7), the expression for $\sigma^*_{\mathcal{T}}$ thus obtained is very sensitive to errors in ψ due to the numerical method used. The expression (4.A.9) is found to be much more robust.

Chapter 5

Concluding remarks

In this dissertation, we have studied two cases in which fluid dynamical processes play a dominant role in determining the composition of igneous rocks. First, in a magma chamber undergoing fractional crystallization from the side, where convective redistribution of the various components of the magma can lead to complex patterns of compositional stratification in the solidified igneous intrusion. Second, a turbulently flowing komatiitic lava erupted on the seafloor which can erode a channel and become significantly contaminated by the oceanic crust.

Fractional crystallization in a magma chamber cooled from the sides has been modelled by a eutectic binary alloy solidifying from one side of a two-dimensional rectangular cavity. Fluid motions are driven by the density anomaly between the residual melt adjacent to the advancing solidification front and the bulk fluid in the interior of the enclosure. The fractionated melt either rises or falls in a boundary layer next to the solid/melt interface, the direction of flow being determined by the relative density of the residual melt. The composition of the solid grown is affected by convective fluid motions in two distinct ways. Entrainment of bulk fluid means that the compositional boundary layer becomes thicker in the direction of flow. For convection dominated by compositional effects, the streamwise variation in the boundary layer thickness leads to vertical stratification in the solid in which heavy elements predominate at the floor of the chamber. The rate of growth of the solid phase decays with time and so, if the bulk fluid is largely homogeneous, the solid composition tends towards the appropriate equilibrium end-member as the alloy solidifies inwards. However, for a chamber of finite size, the fractionated fluid collects at the floor or roof of the chamber, where it forms a stably stratified region. The fractionated zone grows as solidification proceeds until the melt is everywhere compositionally stratified. The melt composition evolves towards the eutectic composition, a trend which is followed by the solid composition. Therefore the layering observed in the final solid product is characterised by a vertical stratification in which light components overly heavier components and a horizontal stratification in which the solid composition first approaches one of the equilibrium end-members, and then evolves back towards the eutectic composition.

The relative duration of these two styles of layering depends primarily upon the ratio of timescales for the solidification of the alloy and for the growth of the region of fractionated melt. In Chapter 2, we demonstrated that for a solidifying alloy of con-

stant viscosity, growing with a planar solid/melt interface, both the style of layering and the degree of stratification are described by the same compound nondimensional parameter. This same scaling analysis allows the modelling of high-Reynolds-number, high-Lewis-number magmatic and experimental systems by numerical calculations performed at substantially lower Reynolds and Lewis numbers. Comparison between calculations and experiments performed with aqueous sodium carbonate solutions (Leitch 1985, 1987, Huppert *et al.* 1987) showed that the model calculations provide an accurate description of the experimental results when the solidification front is planar, but is rather less accurate when the morphology of the solid/melt interface is more complicated.

In Chapter 3, the crystallization model was extended to fluids whose viscosity is dependent upon both temperature and composition. This is particularly relevant to magmas, whose viscosity may vary by several orders of magnitude across the thermal and compositional boundary layers adjacent to the growing solid. By analysing previous calculations for the boundary layer flow in a fluid of constant viscosity, we argued that the compositional layering in the solid can be qualitatively described by the scaling theory presented in Chapter 2, provided a suitable effective viscosity is chosen. We then proceeded to show numerically that the same effective viscosity provides a quantitative description of the solid stratification. Our analysis demonstrated that the effective viscosity may well be relatively high, as the flow is determined by the geometrical mean of the viscosities of the primary magma and the fractionated magma measured at their liquidus temperatures.

The geological relevance of the models presented in Chapters 2 and 3 depends primarily upon two considerations. First, it was demonstrated in Chapter 2 that the quantitive accuracy of the model is strongly dependent upon the assumption that the solid/melt interface is planar. The direct application of the model therefore depends upon the particular morphology of the advancing solidification front. Extension of the present study to dendritic growth of a binary alloy is one possibility for future investigations, perhaps coupled with suitable experiments to determine the morphology of the solid/melt interface for a convecting magmatic melt. The second important assumption of the model is that the complicated segregation behaviour of a multicomponent melt can be reasonably described by a binary eutectic alloy. It would be interesting to see how the results presented here would differ for other types of binary alloy, such as the plagioclase system, or for ternary and quaternary systems.

A contrasting style of igneous rock formation was studied in Chapter 4. Lavas extruded on the surface of the Earth can flow many kilometres from their source before freezing to become solid rock. Komatiitic lavas, which were erupted in the Archaean, were relatively inviscid and exhibited turbulent flow. They were sufficiently energetic thermally to melt the ground over which they flowed. Consequently, komatiites may exhibit contamination from the Archaean crust. The mixing of the lava and crust provides an interesting problem for the geologist who wishes to interpret komatiites and obtain an insight into the Archaean crust and mantle.

In Chapter 4, a new model was presented for the cross-sectional geometry of channels eroded by hot, turbulently flowing komatiitic lava. This adds significantly to earlier models (Huppert *et al.* 1984, Huppert & Sparks 1985), which considered only downwards erosion. It was demonstrated that the lateral extent of erosion increased with the flow rate of lava per unit width. By incorporating the model for the cross-sectional geometry into a pre-existing two-dimensional model for the downwards thermal erosion by a hot, turbulently flowing lava, we were able to find a solution for the relative contamination of the lava as a function of temperature alone, independent of flow parameters. Studies of crystal morphologies can provide some information about thermal conditions in a komatiitic lava flow (Donaldson 1982), from which it may now be possible to infer the degree of crustal contamination. We then proceeded to study how the erosion of a finite channel differs from that of a channel of effectively infinite width. It was demonstrated that significant departures from the original two-dimensional model occur for narrow channels or for long continuous eruptions. Lava flowing down a narrow channel becomes more contaminated, but erodes less deeply, than does an infinitely wide lava flow with the same two-dimensional flow rate. It was also shown that a lava flow channelled by topography will have undergone significantly less contamination than a lava emplaced the same distance away, but allowed to flow freely from its source.

An interesting phenomenon occurs when hot water flows turbulently down an erodible wax slope. On occasion, the channel is observed to split into two, with an island forming near the centre of the stream (Huppert & Sparks 1985*a*). It has been suggested (Huppert 1986) that this instability can be explained by the rate of melting of the solid being dependent upon the local current thickness. We propose that depth-dependent melting rates can arise due to inefficient lateral mixing of the current, which therefore provides a

mechanism for geometrical instability in the channel cross-section. At small wavelengths, perturbations to the cross-sectional geometry are damped by curvature effects, as a concave surface melts more slowly than a convex surface. This means that the most unstable mode for the geometrical instability is that which has wavelength equal to the width of the channel, which is consistent with observations of the formation of islands near the centre of the flow.

Extensions to the thermal erosion problem presented here are not obvious. By decoupling the geometric problem from the thermal problem, we have been able to employ largely analytical methods to solve for the channel shape, channel depth and lava contamination. Further theoretical investigations may well have to rely upon numerical simulation, which is a somewhat less penetrating approach. More valuable would be a survey of known examples of thermally eroded channels to determine the validity or otherwise of the model presented here. Equally interesting would be a more detailed experimental investigation of the types of instability reported by Huppert & Sparks (1985*a*) and discussed in this dissertation.

References

Abramowitz, M. & Stegun, I.A. 1964 *Handbook of Mathematical Functions.* US Government Printing Office, Washington.

Allaby, A. & Allaby, M. (eds.) 1990 *The Concise Oxford Dictionary of Earth Sciences.* Oxford.

Arndt, N.T. & Nesbitt, R.W. 1985 Magma mixing in komatiitic lavas from Munro Township, Ontario. In *Archaean Geochemistry* (eds. G. Hansen, A. Kröner & A.W. Goodwin), 99—114. Springer.

Beckermann, C. & Viskanta, R. 1988 Double-diffusive convection during dendritic solidification of a binary mixture. *PhysicoChem. Hydro.* **10**(2), 195–213.

Bennon, W.D. & Incropera, F.P. 1987*a* A continuum model for momentum, heat and species transport in binary solid-liquid phase change systems – I. Model formulation. *Int. J. Heat Mass Transfer* **30**, 2161–2170.

Bennon, W.D. & Incropera, F.P. 1987*b* A continuum model for momentum, heat and species transport in binary solid-liquid phase change systems – II. Application to solidification in a rectangular cavity. *Int. J. Heat Mass Transfer* **30**, 2171–2187.

Bottinga, Y. & Weill, D.F. 1972. The viscosity of magmatic silicate liquids: a model for calculation. *Am. J. Sci.* **272**, 438–475.

Britter, R.E. & Linden, P.F. 1980 Motion of the front of a gravity current travelling down an incline. *J. Fluid Mech.* **99**, 531–543.

Britter, R.E. & Simpson, J.E. 1978 Experiments on the dynamics of a gravity current head. *J. Fluid Mech.* **88**, 233–240.

Carslaw, H.S. & Jaeger, J.C. 1959 *Conduction of Heat in Solids.* Oxford.

Chen, C.F. & Turner, J.S. 1980 Crystallization in a double-diffusive system. *J. Geophys. Res.* **85**, 2573–2593.

Crank, J. 1984 *Free and Moving Boundary Problems.* Oxford.

Donaldson, C.H. 1982 Spinifex-textured komatiites: a review of textures, mineral compositions and layering. In *Komatiites* (eds. N.T. Arndt & E.G. Nisbet), 213–244. Allen & Unwin.

Elder, J.W. 1965 Turbulent free convection in a vertical slot. *J. Fluid Mech.* **23**(1), 99–112.

Gottlieb, D. & Orszag, S.A. 1977 *A Numerical Analysis of Spectral Methods.* SIAM, Philadelphia.

Hall, A. 1987 *Igneous Petrology.* Longman.

Hebditch, D.J. 1975 Contribution concerning the solidification problem. In *Moving Boundary Problems in Heat Flow and Diffusion* (ed. J.R. Ockendon and W.R. Hodgkins). Oxford.

Hess, P.C. 1989 *Origins of Igneous Rocks.* Harvard.

Hieber, C.A. & Gebhart, B. 1971 Stability of vertical natural convection boundary layers: expansions at large Prandtl number. *J. Fluid Mech.* **49**(3), 577–592.

Hills, R.N., Loper, D.E. & Roberts, P.H. 1983 A thermodynamically consistent model of a mushy zone. *Q. J. Mech. Appl. Math.* **36**, 505–539.

Ho, C.-J. & Viskanta, R. 1984 Heat transfer during melting from an isothermal vertical wall. *Trans. ASME C: J. Heat Transfer* **106**, 12–19.

Holman, J.P. 1976 *Heat Transfer.* McGraw-Hill.

Hulme, G. 1973 Turbulent lava flow and the formation of lunar sinuous rilles. *Modern Geology* **4**,107–117.

Huppert, H.E. 1986 The intrusion of fluid mechanics into geology. *J. Fluid Mech.* **173**, 557–594.

Huppert, H.E. 1989 Phase changes following the initiation of a hot turbulent flow over a cold solid surface. *J. Fluid Mech.* **198**, 293–319.

Huppert, H.E. 1990 The fluid mechanics of solidification. *J. Fluid Mech.* **212**, 209–240.

Huppert, H.E. & Sparks, R.S.J. 1980 The fluid dynamics of a basaltic magma chamber replenished by influx of hot, dense ultrabasic magma. *Contrib. Mineral. Petrol.* **75**, 270–289.

Huppert, H.E. & Sparks, R.S.J. 1985*a* Komatiites I: eruption and flow. *J. Petrology* **26**(3), 694–725.

Huppert, H.E. & Sparks, R.S.J. 1985*b* Cooling and contamination of mafic and ultramafic magmas during ascent through continental crust. *Earth Planet. Sci. Lett* **74**, 371–386.

Huppert, H.E., Sparks, R.S.J., Turner, J.S. & Arndt, N.T. 1984 Emplacement and cooling of komatiite lavas. *Nature* **309**, 19–22.

Huppert, H.E., Sparks, R.S.J., Wilson, J.R., Hallworth, M.A. & Leitch, A.M. 1987 Laboratory experiments with aqueous solutions modelling magma chamber processes II. Cooling and crystallization along inclined planes. In *Origins of Igneous Layering* (ed. I. Parsons), pp. 539–568. Reidel.

Huppert, H.E. & Worster, M.G. 1985 Dynamic solidification of a binary melt. *Nature* **314**, 703–707.

Kerr, R.C & Lister, J.R. 1991 The effects of shape on crystal settling and on the rheology of magmas. *J. Geol.* (in press).

Kerr, R.C., Woods, A.W., Worster, M.G. & Huppert, H.E. 1989 Disequilibrium and macrosegregation during solidification of a binary alloy. *Nature* **340**, 357–362.

Koyaguchi, T., Hallworth, M.A., Huppert, H.E. & Sparks, R.S.J. 1990 Sedimentation of particles from a convecting fluid. *Nature* **343**, 447–450.

Langer, J.S. 1980 Instabilities and pattern formation in crystal growth. *Rev. Mod. Phys.* **52**(1), 1–28.

Leitch, A.M. 1985 Laboratory models of magma chambers. Ph.D. Thesis, Australian National University.

Leitch, A.M. 1987 Various aqueous solutions crystallizing from the side. In *Structure and Dynamics of Partially Solidified Systems* (ed. D.E. Loper), pp. 37–57. Nijhoff.

Lesher, C.M. 1983 Localization and genesis of Fe–Ni–Cu sulphide mineralization at Kambalda, Western Australia. Ph.D. Thesis. University of Western Australia.

Lowell, R.P. 1985 Double-diffusive convection in partially molten silicate systems: its role during magma production and in magma chambers. *J. Volcanol. Geotherm. Res* **26**, 1–24.

McBirney, A.R. 1980 Mixing and unmixing of magmas. *J. Volcanol. Geotherm. Res.* **7**, 357–371.

McBirney, A.R., Baker, B.H. & Nilson, R.H. 1985 Liquid fractionation. Part I: basic principles and experimental simulations. *J. Volcanol. Geotherm. Res.* **24**, 1–24.

McBirney, A.R. & Murase, T. 1984 Rheological properties of magmas. *Ann. Rev. Earth Planet. Sci.* **12**, 337–357.

McBirney, A.R. & Noyes, R.M. 1979 Crystallization and layering of the Skaergaard intrusion. *J. Petrol.* **20**, 487–554.

Macdonald, G.A. 1972 *Volcanoes.* Prentice-Hall.

McKenzie, D.P. 1984 The generation and compaction of partially molten rock. *J. Petrol.* **25**, 713–765.

McKenzie, D.P. 1985 The extraction of magma from the crust and mantle. *Earth Planet. Sci Lett.* **74**, 81–91.

Marsh, B.D. 1981 On the crystallinity, probability of occurrence, and rheology of lava and magma. *Contrib. Mineral. Petrol.* **78**, 85–98.

Martin, D. & Nokes, R. 1988 Crystal settling in a vigorously convecting magma chamber. *Nature* **332**, 534–536.

Mathews, J. & Walker, R.J. 1964 *Mathematical Methods of Physics.* Benjamin Cummings.

Morris, S. 1982 The effects of strongly temperature dependent viscosity on slow flow past a sphere. *J. Fluid. Mech.* **124**, 1–26.

Morse, S.A. 1980 *Basalts and phase diagrams.* Springer

Mullins, W.W. & Sekerka, R.F. 1964 Stability of a planar interface during solidification of a dilute binary alloy. *J. Appl. Phys.* **35**, 444–451.

Murase, T. 1962 Viscosity and related properties of volcanic rocks at 800° to 1400°C. *J. Fac. Sci. Hokkaido Univ. (Ser. VII)* **1**, 487–584.

Murase, T. & McBirney, A.R. 1973 Properties of some common igneous rocks and their melts at high temperatures. *Bull. Geol. Soc. Am.* **84**, 3563–3592.

Nilson, R.H. 1985 Countercurrent convection in a double-diffusive boundary layer. *J. Fluid Mech.* **160**, 181–210.

Nilson, R.H., McBirney, A.R. & Baker, B.H. 1985 Liquid fractionation. Part II: fluid dynamics and quantitative implications for magmatic systems. *J. Volcanol. Geotherm. Res.* **24**, 25–54.

Nisbet, E.G. 1987 *The Young Earth.* Allen & Unwin.

Nisbet, E.G. & Walker, D. 1982 Komatiites and the structure of the Archaean mantle. *Earth Planet. Sci. Lett.* **60**, 103–113.

Patterson, J. & Imberger, J. 1980. Unsteady natural convection in a rectangular cavity. *J. Fluid Mech.* **100**, 65–86.

Peaceman, D.W. & Rachford, H.H. 1955 The numerical solution of parabolic and elliptic differential equations. *J. Soc. Indust. Appl. Maths* **3**, 28–41.

Peyret, R. & Taylor, T.D. 1983 *Computational Methods for Fluid Flow.* Springer.

Porter, D.A. & Easterling, K.E. 1981 *Phase Transformations in Metals and Alloys.* Van Nostrand Reinhold.

Ramachandran, N., Gupta, J.P. & Jaluria, Y. 1981 Two-dimensional solidification with natural convection in the melt and convective and radiative boundary conditions. *Num. Heat Transfer* **4**, 469–484.

Schlichting, H. 1960 *Boundary Layer Theory.* McGraw-Hill.

Shaw, H.R. 1972 Viscosities of magmatic silicate liquids: an empirical method of prediction. *Am. J. Sci.* **272**, 870–893.

Sonneveld, P., Wesseling, P. & de Zeeuw, P.M. 1985 Multigrid and conjugate gradient methods as convergence acceleration techniques. In *Multigrid Methods for Integral and Differential Equations* (ed. D.J. Paddon and H. Holstein), pp. 117–167. Oxford.

Sparks, R.S.J., Huppert, H.E. & Turner, J.S. 1984 The fluid dynamics of evolving magma chambers. *Phil. Trans. Roy. Soc. Lond.* **A310**, 511–534.

Spera, F.J., Yuen, D.A. & Kirschvink, S.J. 1982 Thermal boundary layer convection in silicic magma chambers: effects of temperature dependent rheology and implications for thermogravitational chemical fractionation. *J. Geophys. Res.* **87**, 8755–8767.

Thompson, M.E. & Szekely, J. 1987 Double-diffusive convection during solidification at a vertical wall. In *Structure and Dynamics of Partially Solidified Systems* (ed. D.E. Loper), pp. 59–77. Nijhoff.

Thompson, M.E. & Szekely, J. 1988 Mathematical and physical modelling of double-diffusive convection of aqueous solutions crystallizing at a vertical wall. *J. Fluid Mech.* **187**, 409–434.

Turner, J.S. 1979 *Buoyancy Effects in Fluids.* Cambridge.

Turner, J.S. & Gustafson, L.B. 1981 Fluid motions and compositional gradients produced by crystallization or melting at vertical boundaries. *J. Volcanol. Geotherm. Res.* **11**, 93–125.

Turner, J.S., Huppert, H.E. & Sparks, R.S.J. 1986 Komatiites II: experimental and theoretical investigations of post-emplacement cooling and crystallization. *J. Petrol.* **27**, 397–437.

Viljoen, M.J. & Viljoen, R.P. 1969 Evidence for the existence of a mobile extrusive peridotite magma from the Komati Formation of the Onverwacht Group. In *The Upper Mantle Project*, 87–112. Geological Society of South Africa Special Publication **2**.

Wager, L.M. & Brown, G.M. 1968 *Layered Igneous Rocks.* Oliver and Boyd.

Weast, Q.C. (ed.) 1971 *Handbook of Chemistry and Physics.* Cleveland: C.R.C.

Wilson, L. & Head, J.W. 1981 Ascent and eruption of basaltic magma on the Earth and Moon. *J. Geophys. Res.* **86**, 1971–3001.

Wilson, M. 1989 *Igneous Petrogenesis.* Unwin Hyman.

Woods, A.W. 1989 Geophysical fluid flows. Ph.D. Thesis, University of Cambridge.

Woods, A.W. & Huppert, H.E. 1989 The growth of compositionally stratified solid above a horizontal boundary. *J. Fluid Mech.* **199**, 29–54.

Worster, M.G. 1986 Solidification of an alloy from a cooled boundary. *J. Fluid Mech.* **167**, 481–501.

Worster, M.G. & Leitch, A.M. 1985 Laminar free convection in confined regions. *J. Fluid Mech.* **156**, 301–319.